Politecnico di Torino

INGEGNERIA ELETTRONICA (ELECTRONIC ENGINEERING)
Collegio di Ingegneria Elettronica, delle Telecomunicazioni e Fisica (ETF)

Codice Classe LM-29 (DM270)

Electronic micro and nanosystems

A.a. 2022/2023

Sessione di Laurea Ottobre 2023

Redesign of 180nm CMOS-MEMS sensors and interface for bioinspired processing

Relatori:

Matteo Cocuzza
Daniel Fernández Martínez
Jordi Madrenas Boadas

Candidato:

Leonardo Santoro

Title of the thesis: Redesign of 180nm CMOS-MEMS sensors and interface for bioinspired processing

Author: Leonardo Santoro

Advisor: Daniel Fernández Martínez

Co-advisors: Jordi Madrenas Boadas, Matteo Cocuzza

Abstract

CMOS-MEMS capacitive resonant pressure sensors and accelerometers are a state-of-the-art technology in the field of pressure and acceleration sensing, which have demonstrated superior performance compared to other types of sensors. Their development faces challenges related to BEOL integration and manufacturability, which require careful design and fabrication processes. Despite these challenges, CMOS-MEMS sensors offer a number of advantages, such as high sensitivity, low power consumption, and compatibility with standard CMOS processes. They have been implemented in a variety of applications, including atmospheric pressure or acceleration sensing, and are expected to continue to be refined and optimized in the future. This work has the aim to discuss the most important and general aspects related to sensors made with CMOS-MEMS technology, leading the way through the most interesting design characteristics of the CMOS-MEMS Capacitive resonant pressure sensor. A good prominence will be dedicated also to the Accelerometer CMOS-MEMS design characteristics. The following chapters offer a review of the most important aspects of these sensors, from their simulations with COMSOL to the ease of the migration process from one technology to another. Particularly, chapter 1 provides a general introduction stating the state of the art of CMOS-MEMS sensors. Chapter 2 covers the most general aspects of the resonant pressure sensors and accelerometer, from their integration to the manufacturing issues related to the BEOL with emphasis on their theoretical behaviour; some initial simulations performed in COMSOL 5.5 will be carried out on the 250 nm IHP resonant pressure sensor design developed by Diana Mata-Hernandez et. al. (2016-2017) [2], with the aim to set a methodological approach for the development and characterization of further simulations that will be performed on the other aforementioned sensors; subsequently, both the 180nm TSMC (Taiwan Semiconductor Manufacturing Company) resonant pressure sensor [1] and the accelerometer designs already

developed in the past will be migrated in UMC (United Microelectronics Corporation) technology, hence demonstrating the versatility of CMOS integrated MEMS; additionally, in order to check the reliability of the new born designs, the DRC (Design Rule Check) related to the UMC technology will be performed and the concept of expected errors from the DRC, layout grid technology limitations, and even more, will be deepen in Chapter 3. Chapters 4, 5 and 6 detail the implementation and the simulation of the pressure sensor and the accelerometer performed in COMSOL 5.5; different conditions are discussed for each sensor, distinguishing from the post and pre-fabrication case of each sensor and detailing the analysis with the effect of the squeeze film damping which acts on the central resonators of the various structures. In particular, the fringing fields effect on the accelerometer is briefly discussed in chapter 6. Chapter 7 provides a comparison between the mechanical differences present between the two sensors, hence giving answers to the different behaviours between the structures. An alternative design of the accelerometer with new arrangement of springs made in UMC technology and the consequent sensing properties are proposed in Chapter 8. Finally, in Chapter 9 an overview of the electronic read-out dedicated to the front end of the sensors is analysed. More in details, the comparison between the different transistors belonging to the different technologies will be then exploited for the migration of one operational amplifier from TSMC to UMC. For the latter, the UMC schematic and its correspondent layout have been made from scratch, with the principal aim to obtain the most similar characteristics in terms of Loop gain, noise, phase margin and power consumption with respect its TSMC counterpart. Finally, both the DRC and the LVS check will be performed on the UMC operational amplifier in order to validate its functionality and its implementation in possible future utilizations, specifically destined for Address Event Representation (AER), an asynchronous approach where events are transmitted and processed in real-time as they occur and that is inspired by the way biological nervous systems process information.

To my family. To the people I hope to help during my life journey.

Politecnico di Torino

Acknowledgements

I am deeply grateful for the unwavering encouragement and support I have received mainly from Daniel Fernández and Jordi Madrenas, my advisor and co-advisor from UPC, who have played pivotal roles, and that deserve my utmost appreciation. I thank them for giving me the opportunity to enter the world of CMOS-MEMS design as an initial approach. It has been an honour and privilege to have their esteemed guidance and supervision during my master work. Special thanks to Matteo Cocuzza, my supervisor from Politecnico di Torino, who has always supported me expressing satisfaction and encouraging me to achieve satisfactory results and to grow professionally. I owe a special debt of gratitude to Angel Rodriguez for his unwavering assistance and insightful conversations from the beginning of my experience at UPC, the discussions we had together inspired me to gradually deepen and improve my practice. Finally, I thanks all the people met at UPC and Politecnico di Torino in particular Matteo, Valerio, Federico M. e Federico C. with whom I have spent unforgettable periods of professional and personal growth. To my parents and my sisters, the most beautiful people on heart who make me feel loved daily and who always offer me the best perspective of the world.

Revision history and approval record

Revision	Date	Purpose
0	01/07/2023	Document creation
1	28/08/2023	Document revision
2	10/10/2023	Document revision

Written by:		Reviewed and approved by:	
Date	01/07/2023	Date	01/09/2023
Name	Leonardo Santoro	Name	Daniel Fernández Martínez
Position	Project Author	Position	Project Advisor

Table of contents

Abstract ... *1*

Acknowledgements ... *4*

Revision history and approval record ... *5*

List of Figures ... *8*

List of Tables ... *14*

Work objectives ... *16*

1. Introduction ... *17*

2. Theoretical and manufacturing aspects of the CMOS-MEMS sensors ... *19*

2.1. Resonant Capacitive Pressure sensor ... 19

2.2. Accelerometer ... 24

2.3. CMOS-MEMS integration ... 29

2.4. The post processing approach ... 29

2.5. Manufacturing issues of BEOL CMOS-MEMS ... 31

2.6. Generic simulation in COMSOL 5.5 Resonant Capacitive Pressure sensor 250nm ... 33

3. Migration of Resonant Capacitive Pressure Sensor and Accelerometer Layout from TSMC to UMC 180nm Technology: A comparative analysis using Klayout and Cadence Virtuoso ... *37*

3.1. Resonant Capacitive Pressure sensor migration from TSMC to UMC 180nm technology 38

3.2. Expected DRC errors ... 46

3.3. Dummy Layers ... 46

3.4. Hierarchy ... 47

3.5. Accelerometer migration from TSMC to UMC 180nm technology ... 48

4. Pressure sensor 180nm TSMC COMSOL Multiphysics characterization ... *51*

4.1. Pressure sensor Central Resonator TSMC characterization ... 54

4.2. Simulation on the theoretical Pre-Fabricated Capacitive Resonant Pressure sensor 180nm TSMC ... 59

4.3. Comments on the spring stiffness ... 67

4.4. Squeeze film damping study on pre-fabrication Pressure sensor resonant central plate ... 70

4.5. Simulations on the theoretical Post-Fabricated Capacitive Resonant Pressure sensor 180nm TSMC *(based on [Ref. 1])* ... 74

4.6. External pressure applied, Bias Voltage sweep ... 80

4.7. Squeeze film damping study Post-Fabrication Pressure sensor ... 85

4.8. Spring Stiffness computation for the post-fabrication device ... 87

4.9. Composite Central resonator capacitive pressure sensor UMC characterization ... 88

5. Accelerometer 180m, TSMC COMSOL Multiphysics Characterization ... 92

5.1. Central Resonator TSMC characterization Accelerometer ... 93

6. Accelerometer Technical implementation in COMSOL ... 102

6.1. Fringing fields effect ... 103

6.2. Simulations on the theoretical Pre-Fabrication Capacitive Accelerometer ... 104

6.3. Simulations on the theoretical Post-Fabrication Capacitive Accelerometer 180nm TSMC 110

6.4. Simulation Pull-in as if the accelerometer is a simple parallel plate ... 114

6.5. Vertical Squeeze film damping study on Accelerometer resonant central plate ... 117

7. Mechanical differences Pressure sensor vs Accelerometer ... 124

8. Alternative design of the post-fabrication Accelerometer ... 127

8.1. New springs configuration and new arrangement of fixed electrodes ... 127

9. Electronics read-out: comparison between TSMC and UMC ... 135

9.1. Introduction ... 135

9.2. Comparison between UMC and TSMC transistors ... 135

9.3. UMC transistors width modulation to get same TSMC transistors performance ... 146

9.4. TSMC Operational amplifier migration to UMC ... 150

9.5. UMC layout design operational amplifier ... 158

10. Conclusions and recommendations ... 163

References ... 165

Glossary ... 169

List of Figures

Figure 1 ASIC optical microphotograph of the pressure sensor and its associated front-end electronics [Ref. 5] ... 17
Figure 2 Schematic of spring-mass damped resonator ... 19
Figure 3 Lumped model of the two plate CMOS-MEMS resonator [Ref. 1] ... 20
Figure 4 SEM image of the manufactured prototype and the cross-section of it after the post-CMOS realization based on an isotropic wet etching. Source: "Resonant MEMS Pressure Sensor in 180 nm CMOS Technology Obtained by BEOL Isotropic Etching" Diana Mata-Hernandez et. Al. [Ref. 1] ... 24
Figure 5 Crab flexure configuration (left) and Serpentine flexure configuration (right) reproduced in Klayout ... 28
Figure 6 Cross-section view of ASIC/MEMS etching process [Ref. 8] ... 29
Figure 7 CMOS-MEMS cross-section after post-processing release and cavity sealing. Source: "Manufacturing issues of BEOL CMOS-MEMS devices" [Ref. 4] ... 31
Figure 8 a) Curling of beams made of a single metal layer. b) Via detachment, similar behaviour can be expected for the resonant pressure sensor [Ref.4] ... 31
Figure 9 COMSOL simulation of the resonant capacitive pressure sensor 250nm technology IHP, computation of the resonance frequency and successive modes of the modified structure with eliminated mass ... 33
Figure 10 COMSOL simulation of the resonant capacitive pressure sensor 250nm technology IHP, computation of the resonance frequency and successive modes ... 33
Figure 11 Bias Voltage (from 10V to 60V with a step of 10V) vs Maxwell Capacitance (in Farad) trend. For 0V the capacitance is equal to 0F, while increasing the Bias this last one increases exponentially from 88fF at 10V up to 94fF at 60V. However, even if it is not shown above 60V of Bias the structure gets close to the pull in condition [6] which would result in a diverging capacitance and a short circuit of the structure, breaking the device ... 35
Figure 12 Bias Voltage (from 0V to 60V with a step of 10V) vs Displacement of the central resonator (in um) trend. Also in this case, increasing the Bias the displacement shows an exponential behaviour going from 0um at 0V to 0.24um at 60V ... 35
Figure 13 Displacement with 0V of bias applied ... 36
Figure 14 Displacement with 60V of bias applied ... 36
Figure 15 Klayout view prototype-A1 Resonant Capacitive Pressure sensor TSMC 180nm layout with all its layers identified by different colours and stipples. Based on Ref. [1], design made by Daniel Fernandez et. Al. ... 38
Figure 16 Klayout view prototype-A1 Resonant Capacitive Pressure sensor UMC 180nm layout with all its layers identified by different colours and stipples. Faithful migration of the TSMC design compliant with UMC technology. ... 39
Figure 17 Top view TSMC (left) and UMC (right) Via5 and Metal6 outlined in black ... 43
Figure 18 Top view zoomed section of the UMC central resonator. The pattern of Vias (Bright Blue) is shown in the central resonator made of Metal 6 and Metal 5 (superimposed). On the left the single spring made exclusively of Metal 6 layer ... 43
Figure 19 TSMC (left) and UMC (right) Metal6 dimensions and passivation layers ... 44
Figure 20 Single Springs dimensions TSMC-UMC ... 45

Figure 21 UMC 180nm Pressure sensor dummy layers representation: Metal dummy fill layers and PadMark (layer defined by the light blue contour that covers the resonator) above the physical layers of the sensor are showed 46
Figure 22 Klayout view Hierarchy UMC Pressure sensor 180nm design, from left to right the lowest to the highest level of hierarchy view 47
Figure 23 Klayout TOP view Accelerometer UMC 180nm layout with all its layers identified by different colours and stipples. 48
Figure 24 UMC 180nm Accelerometer layout zoomed, output sensing nodes 49
Figure 25 COMSOL view entire 3D structure recreated resonant capacitive pressure sensor 51
Figure 26 Exploded view Central Resonator Pressure sensor TSMC 180nm section. From left to right: Metal5-Dielectric/Via5-Metal6 with the correct thickness required by the technology 53
Figure 27 Homogeneous central resonant plate of the pressure sensor (in blue) zoomed and mounted on the entire pressure sensor (in grey). 55
Figure 28 Composite central resonant plate of the pressure sensor zoomed and separated from the rest of the structure. The outer vias pattern and the air spaces (non-physical volume) nearby those are visible. 55
Figure 29 Composite central resonant plate of the pressure sensor zoomed with metal 6 layer hidden. In yellow are represented the vias and the filling dielectric domains respectively on the left and the right representations. 56
Figure 30 pre-fabrication Pressure sensor dimensions built in COMSOL 5.5 59
Figure 31 Maxwell Capacitance vs Bias Voltage of pre-fabrication resonant pressure sensor TSMC 180nm (no external pressure variation applied) 66
Figure 32 Total displacement central resonator vs Bias Voltage pre-fabrication resonant pressure sensor (no external pressure variation applied) 67
Figure 33 Parameters set for the simulation of the Squeeze film damping pre-fabrication pressure sensor 71
Figure 34 Relative film pressure on the central resonant movable plate pre-fabrication with no perforation 72
Figure 35 Relative film pressure on the central resonant movable plate pre-fabrication with Bao's Model (perforations not explicitly modelled) 72
Figure 36 Relative film pressure on the central resonant movable plate pre-fabrication with perforations and zero relative pressure in the etch holes P=0 73
Figure 37 Damping coefficient extrapolated from the three cases 73
Figure 38 Thicknesses of the springs (Metal6) and the central resonator of the post fabricated case of the resonant capacitive pressure sensor TSMC 76
Figure 39 Maxwell Capacitance vs Bias Voltage of post-fabrication resonant pressure sensor TSMC 180nm (no external pressure variation applied) 77
Figure 40 Maxwell capacitance between the movable (Grounded) and the fixed electrode (Biased) with respect the bias voltage range 2.5V-10V 78
Figure 41 Total displacement central resonator vs Bias Voltage post-fabrication resonant pressure sensor (no external pressure variation applied) 79

Figure 42 RMS displacement of the movable plate (Grounded) in the frequency range post-fabrication pressure sensor 79
Figure 43 Total displacement of the movable plate of the pressure sensor at 30V of Biasing with respect the variation of the external pressure from 0Pa to 50kPa 80
Figure 44 Total displacement of the movable plate of the pressure sensor at 5V of Biasing with respect the variation of the external pressure from 30kPa to 50kPa 81
Figure 45 Von Mises stresses on the movable plate of the pressure sensor at 5V of Biasing with 50000Pa of external variation of pressure 82
Figure 46 Maxwell Capacitance between the movable and the fixed plate at 5V of Biasing with respect the variation of the external pressure 83
Figure 47 Maxwell Capacitance between the movable and the fixed plate at 30V of Biasing with respect the variation of the external pressure. Less points of step have been exploited; therefore, the plot does not show a good quality 84
Figure 48 Maxwell Capacitance between the movable and the fixed plate at 30V of Biasing with respect the variation of the external pressure zoomed around 0Pa 84
Figure 49 Relative film pressure on the central resonant movable plate post-fabrication with no perforation 85
Figure 50 Relative film pressure on the central resonant movable plate post-fabrication with Bao's Model (perforations not explicitly modelled) 86
Figure 51 Relative film pressure on the central resonant movable plate post-fabrication with perforations and zero relative pressure in the etch holes P=0 86
Figure 52 Damping coefficient extrapolated from the three cases. The Bao model result is extremely similar to the actual experimental results related to a 6x6 perforation structure analysed in Bao's work 87
Figure 53 Central Vias pattern for UMC technology (left) and TSMC technology (right) design zoomed 90
Figure 54 Central Dielectric pattern for UMC technology (right) and TSMC technology (left) design zoomed 91
Figure 55 transparent view of the supporting outermost block for the springs that carries the central resonator proof mass. It can be clearly seen the path of the Vias below the Metal6 94
Figure 56 clear prospective of the vias by means of transparent side view of the supporting outermost block for the springs that carries the central resonator proof mass. In sequence from the bottom there is metal4-Via4-Metal5-Via5-Metal6, between the vias there is the presence of oxide 94
Figure 57 Single Fixed sense electrode, underlined in blue colour the Vias4 and Vias5 from the bottom to the top, between the vias the presence of oxide 95
Figure 58 General view of the Central resonator proof mass part of the CMOS-MEMS Accelerometer 95
Figure 59 Zoomed Clipping plane view of the Central resonator proof mass part of the CMOS-MEMS Accelerometer. In blue is underlined the oxide layer that must exist within the metal layers and between the Vias. The thickest top layer is the Metal6 while the thin bottom layer is Metal 5 96

Figure 60 Zoomed top view of the Central resonator proof mass part of the CMOS-MEMS Accelerometer with hidden TOP Metal6 layer. Underlined in blue the Vias (Vias5) that exist between Metal6 and Metal5, while in red the bottom Metal5 layer 96
Figure 61 Composite central resonator proof mass 97
Figure 62 Homogeneous central resonator proof mass 97
Figure 63 General homogeneous accelerometer structure 101
Figure 64 Fringing fields effect on a capacitance 103
Figure 65 The blue areas are the surfaces that actively contribute to the sensed capacitance. These must be added to the ones on the other side of the accelerometer if acceleration/deceleration along x is the one to be estimated 106
Figure 66 Pre-fabrication accelerometer displacement of a point belonging to one movable finger vs acceleration at +-0.5mV of Biasing. From it the mechanical sensitivity can be estimated 106
Figure 67 Optimized mesh localized in the region for the sensing of surface charge density performed with a block of air. As can be observed the vertical mesh is less complex with respect to the horizontal one.. 108
Figure 68 Pre-fabrication accelerometer, effect of fringing fields at 50g and +-0.5mV of bias 109
Figure 69 Post-fabrication accelerometer displacement of one movable finger vs acceleration at +-0.5mV of biasing 111
Figure 70 Post-fabrication accelerometer, effect of fringing fields at 50g and +-0.5mV of bias 112
Figure 71 Post-fabrication accelerometer, effect of fringing fields at 50g and +-0.5mV of bias zoomed on the movable finger 112
Figure 72 Exponential increase in displacement. It can be observed that at 450V a displacement of 0.55um (≅1/3 of the gap) is achieved 114
Figure 73 Linear pull-in in the pre-fabricated accelerometer, as clear the pull-in occurs at 0.5um, thus at 1um of remaining gap 115
Figure 74 Displacement of sensor at 450V applied to one only of the fixed electrodes in both sides in scale 116
Figure 75 Displacement of sensor at 450V applied to one only of the fixed electrodes in both sides in scale zoomed 116
Figure 76 Relative film pressure on the central resonant movable plate pre-fabrication with no perforation 118
Figure 77 Relative film pressure on the central resonant movable plate pre-fabrication with Bao's Model (perforations not explicitly modelled).................................... 118
Figure 78 Relative film pressure on the central resonant movable plate pre-fabrication with perforations and zero relative pressure in the etch holes P=0 119
Figure 79 Relative film pressure on the central resonant movable plate pre-fabrication with perforations and zero relative pressure in the etch holes P=0 zoomed.......... 119
Figure 80 Damping coefficient extrapolated from the three cases pre-fabrication ... 120
Figure 81 Relative film pressure on the central resonant movable plate post-fabrication with Bao's Model (perforations not explicitly modelled) 121

Figure 82 Relative film pressure on the central resonant movable plate comparison pre and post-fabrication with Bao's Model (perforations not explicitly modelled). On the left the pre-fabrication case, on the right the post fabrication case. They are practically identical. 121
Figure 83 Relative film pressure on the central resonant movable plate pre-fabrication with Bao's Model (perforations not explicitly modelled), with prescribed displacement only along y and x with z=0 122
Figure 84 Relative film pressure on the central resonant movable plate post-fabrication with perforations and zero relative pressure in the etch holes P=0 zoomed, with prescribed displacement only along y and x with z=0 122
Figure 85 TSMC layout with Metal6, Metal5 and Metal4 layers respectively of pressure sensor and accelerometer designs 124
Figure 86 Klayout view metal6 layer of the new design of the post-fabrication accelerometer UMC 180nm 128
Figure 87 Klayout view metal6 layer of the new design of the accelerometer UMC 180nm zoomed. The dimensions are explicit. 129
Figure 88 Displacement of the point belonging to the movable finger of the new geometry vs External Acceleration 130
Figure 89 Maximum Total Displacement of the new geometry under 50g of external acceleration and $\pm 0.5mV$ of bias voltage 130
Figure 90 Vertical Von Mises stresses on the new version design of the accelerometer 180nm with vertical acceleration of 50g 132
Figure 91 Horizontal Von Mises stresses on the new version design of the accelerometer 180nm with horizontal acceleration of 50g 132
Figure 92 Fringing fields effect of the new design accelerometer with 0.5mV of Biasing at 50g 133
Figure 93 UMC transistors under test schematic representation with Cadence default sizes. From left to right and up to down: N_18_MM, N_LV_18_MM, N_ZERO_18_MM and P_18_MM, P_LV_18_MM. The operating bias points of each transistor can be appreciated 138
Figure 94 TSMC transistors under test schematic representation with Cadence default sizes. From left to right: nmos2v, pmos2v and nmosnvt2v. The operating bias points of each transistor can be appreciated 139
Figure 95 N_18_MM width required to get the same vgs of the correspondent nmos2v TSMC 148
Figure 96 N_ZERO_18_MM width required to get the same vgs of the correspondent nmosnvt2v TSMC (since it should reach the value of 222.421mV, correspondent to the TSMC gate-source voltage of the nmosnvt2v, the achievable gate-source voltage results to be close to this, but still, it is not possible for this UMC transistor to obtain the same gate source voltage only by changing its width) 148
Figure 97 P_18_MM width required to get the same vgs of the correspondent pmos2v TSMC 149
Figure 98 Operational amplifier TSMC schematic Cadence view 150
Figure 99 test bench operational amplifier TSMC Cadence view 151

Figure 100 V2 generator parameters Cadence window view 152
Figure 101 UMC operational amplifier characteristics in terms of Open and Closed loop gain, phase margin, power consumption, with transistors with identical sizes with respect the one used in TSMC operational amplifier 153
Figure 102 Operational amplifier UMC schematic Cadence view. The chosen width, length and multiplier are visible on each transistor 154
Figure 103 Optimized UMC operational amplifier total results 155
Figure 104 TSMC operational amplifier noise.. 156
Figure 105 UMC operational amplifier noise 156
Figure 106 TSMC operational amplifier dynamic in DC 157
Figure 107 UMC operational amplifier dynamic in DC 157
Figure 108 UMC operational amplifier time analysis for slew rate computation. In green line the output signal, in pink the input signal 158
Figure 109 UMC operational amplifier Layout design complete view 160
Figure 110 UMC operational amplifier Layout design higher level of hierarchy 161
Figure 111 LVS results log file of the UMC operational amplifier optimization 162

List of Tables

Table 1 Parameters 180nm TSMC capacitive resonant pressure sensor prototype-A1 post-fabrication [1] 52
Table 2 Parameters 180nm TSMC capacitive resonant pressure sensor prototype-A1 pre-fabrication [1]... 52
Table 3 Parameters 180nm TSMC Accelerometer prototype-A1 pre-fabrication 93
Table 4 Mechanical differences between Pressure sensor and Accelerometer in the pre and post-fabrication cases 125
Table 5 Horizontal resonance frequency and stiffness for the pre and post-fabrication accelerometer 126
Table 6 Dimensions Accelerometer new springs and electrodes arrangement 129
Table 7 - Differences on the horizontal and vertical resonance frequency and stiffness for the old and new designs of the accelerometer 131
Table 8 Minimum length and width size (the same colour on columns has been used for a direct comparison between transistors) 140
Table 9 Standard technology sizes 141
Table 10 Sizes ten times the minimum ones 142
Table 11 Default Cadence sizes 143
Table 12 Minimum sizes, width variation to get same vgs of the TSMC version 146
Table 13 Standard technology, width variation to get same vgs of the TSMC version 146
Table 14 Ten times sizes, width variation to get same vgs of the TSMC version 147
Table 15 Default Cadence sizes, width variation to get same vgs of the TSMC version 147
Table 16 Width, length and multiplier chosen for the transistors dedicated to the UMC version of the operational amplifier 155

Disclaimer

I have the personal responsibility to ensure any confidentiality agreements or restrictions imposed by the manufacturer regarding the sharing of proprietary information, including design rule checks. No specific details, rules or exact dimensions values will be included in this work without proper authorization. Industry-standard design rules or other publicly available references that provide general guidelines for design rule considerations may be present in the following sections.

Work objectives

The principal objectives of this work are: to assess the feasibility and advantages of transferring the existing CMOS-MEMS pressure sensors and accelerometers design from TSMC technology to UMC technology, considering factors such as process compatibility and performance improvement; to demonstrate the ease of the migration process that characterize the CMOS-MEMS fabrication technology; to analyse the compatibility of the UMC fabrication process with the required CMOS-MEMS structures, ensuring that the migrated design can be accurately and reliably manufactured within the UMC process constraints; to modify the accelerometer design to adapt to the new UMC technology with the aim to enhance its performance characteristics, such as sensitivity and resolution; to utilize COMSOL simulations to model the behaviour of both pressure sensors and accelerometers; to validate the simulation results against expected performance metrics and experimental results to ensure accuracy and reliability; to conduct a comprehensive comparison between the performance of different pressure sensors and accelerometers designs and devices between TSMC and UMC; to assess the migrated designs' robustness and reliability, considering factors like process variations and stresses; to create general guidelines outlining the migration process, design modifications, simulation methodologies using COMSOL, and best practices for future CMOS-MEMS projects intending to switch technologies or to simulate sensors; to provide a comparative analysis between the devices belonging to the two different technologies and to exploit them for the migration of a fundamental element destined for the read-out of a sensor; to share insights gained from the migration process and simulations using COMSOL in order to contribute to the broader understanding of CMOS-MEMS technology, helping researchers and engineers make informed decisions about similar topics.

1. Introduction

CMOS technology is widely used in electronic circuits, it allows for the integration of digital and analog circuits. On the contrary, MEMS technology enables the fabrication of mechanical structures characterized by high reliability, accuracy, excellent mechanical properties of single crystal silicon and batch manufacturability. CMOS-MEMS represents the combination of these two technologies, which is able to provide high-performance sensing and actuation capabilities with low power consumption. MEMS-electronics integration allows to determine the most important specification parameters together with the electronics. This grants the design of both the electronics and the MEMS at the same time, hence shortening the design cycle and reducing the time-to-market. The significant growth we see today in the MEMS sensor market is powered mainly by the increasing demand of wearables, human-interface devices and applications used by the consumers. Particularly, two of the most interesting CMOS-MEMSs used nowadays are the resonant pressure sensors and the accelerometers, which are exploited in different fields such as automotive, aerospace, medical devices, computer and general industries applications. Their structure is mainly based on a capacitive or piezoresistive diaphragms that is monolithically integrated with CMOS circuitry, a characteristic that has indeed paved the way for the integration of sensors and electronics in a single chip, thus allowing the immediate read out of pressure, or more generally of the external physical perturbation, sensed by means of electronics i.e., a system on chip designed on a digital platform (Figure 1).

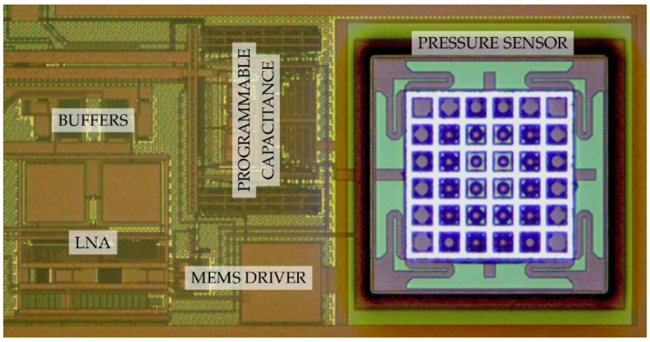

Figure 1 ASIC optical microphotograph of the pressure sensor and its associated front-end electronics [Ref. 5]

Pressure sensors generally operate based on the detection of pressure-induced changes in the resonant frequency or on the quality factor of a micro-mechanical structure, which is integrated with CMOS electronics, similarly, accelerometers are based on the external excitation force that moves a central floating movable resonator plate that provokes changes of the stress distribution within the resonator modifying its resonant frequency; the capacitance change between fixed and movable fingers electrodes can be detected in both the sensors. However, in order to gain a sufficient quality factor often the necessity of a vacuum packaging may represent an important limitation in these kinds of devices. The manufacturing of all the sensors and their electronics in the same silicon die show distinct advantages, such as the reduction of area, package volume and cost, while improving the overall sensor performance. Indeed, neither pads nor bonding wires are required between them, therefore noise and parasitic effect are greatly reduced. Different techniques can be used for achieving the monolithic integration [3, 4], but the considerations that will be analysed in this work focus mainly on the CMOS-MEMS backend-of-line (BEOL) micromachining. This state-of-the-art technique uses the metallization interconnection layers of the CMOS process as structural layers for the MEMS device by just performing a release step where the silicon oxide surrounding the metallization interconnection layers is selectively removed, hence giving the structure the possibility to move freely in the presence of external stimuli. A standard passivation of the CMOS process serves as a blocking layer for the release of the movable parts; thus, no additional masks are required, reducing the cost of manufacturing MEMS in CMOS. As in most of the case both the pressure sensors and accelerometers do not require the addition of new materials or complex manufacturing postprocesses, they have the possibility to be directly exploited in the CMOS-MEMS scenario. The present work is based on previous studies which involved specifically the quality factor sensing for the pressure sensor [1, 2] and the capacitive sensing for the accelerometer. A catalyst aspect of CMOS-MEMS technology, is that it provides the possibility for an easy migration from one technology to another due to the compatibility with standard CMOS process. The different technologies, impose different Design Rules Checks [1](DRCs), thus a modification of the original design must be performed in order to be conformed with the new technology of interest. Overall, if compared with the standard MEMS fabrication design and manufacturability process, the CMOS-MEMS represents the perfect trade-off between sensing reliability and manufacturability costs.

[1] Design rules are a set of specifications and constraints dictated by the manufacturer which specify how different (or equal) layers and interconnections in an electronic layout design should be laid out to ensure proper functionality, manufacturability, and reliability. When a design violates any of the predefined rules, DRC tools flag these violations as DRC violations.

2. Theoretical and manufacturing aspects of the CMOS-MEMS sensors

2.1. Resonant Capacitive Pressure sensor

The resonant pressure sensor can be at first modelled as a spring-mass damped vibrating system (Figure 2), thus it can be described by Newton's second law of motion:

$$m\ddot{x} + c_{total}\dot{x} + kx = \sum F_{external}$$

(1)

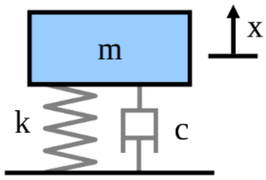

Figure 2 Schematic of spring-mass damped resonator

Where $\ddot{x}$, $\dot{x}$ and x are respectively the acceleration, velocity and position of the proof mass, $\sum F_{external}$ is the sum of the external forces applied to the proof mass, m is the effective mass, which is a contribution of the mass of the diaphragm plus any added mass due to the enclosed fluid, c_{total} is the total damping coefficient and k is the spring constant, which is a measure of the stiffness of the diaphragm and it is dependent on its dimensions and material properties. By applying a single initial force to the proof mass, the system starts to oscillate at its fundamental frequency, also known as eigenfrequency (or natural frequency) which is defined as:

$$f_r = \frac{1}{2\pi}\sqrt{\frac{k}{m}}$$

(2)

However, with no external forces applied to the system the damping mechanism cancels the vibrations of the system itself. A condition of resonance is instead achieved when an external harmonic force is applied to the resonator (the movable membrane) with the same frequency as the resonator's natural frequency, thus, allowing the amplitude of the vibrations of the system to increase with respect to the previous case, but at the same time to settle at a certain level as a consequence of the presence of damping. The actual sensing of the variation of the external pressure is performed by observing the variation of the quality factor or of the shifting of the resonance frequency of the structure: as the surrounding pressure changes, the diaphragm deflects, and the effective mass changes, resulting in a change in the resonant frequency. To measure this change, the sensor is excited by applying an AC voltage (the quoted harmonic force) to the diaphragm, causing it to vibrate at its resonant frequency, and therefore creating an attractive electrostatic force among the plates (see Figure 3). However, during the COMSOL simulations carried out in this work, only a DC is applied, hence no shift in resonance frequency is simulated, but only the movement of the central mass not dependent on time, thus the variation of the capacitance that occurs between the two electrodes at different displacement. Indeed, when a voltage is applied to the movable membrane, the electrostatic force reduces the plate separation between the movable membrane and fixed bottom metal plate from z_0 to $z_0 - z$, where z is representing the displacement of the proof mass. The electrostatic voltage is countered by the spring force $F = -kx$ at small voltages, however, as the voltage is increased, the plates eventually snap together leading to the known pull-in effect [6], where the electrostatic spring constant can exceed the elastic spring constant leading to the possible destruction of the device (see section 4.2). The resulting displacement of the diaphragm is detected by measuring the capacitance between the fixed electrode, the ground, and the diaphragm, which is instead driven by a certain power supply. The capacitance is dependent on the distance between the diaphragm and the fixed electrode; hence, it varies due to the displacement of the diaphragm.

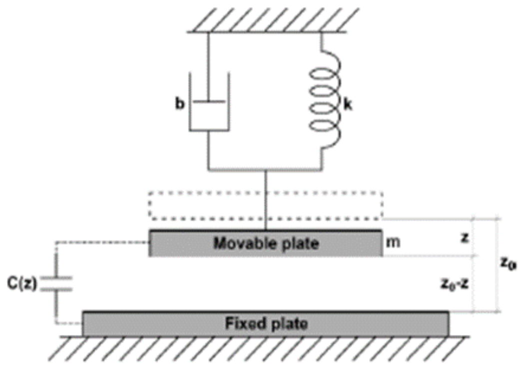

Figure 3 Lumped model of the two plate CMOS-MEMS resonator [Ref. 1]

This variation on the capacitance is then converted into an electrical signal and processed by the integrated circuitry. The resonance frequency can be correlated with the applied surrounding pressure by means of the Knudsen number $\boldsymbol{k_n}$, a dimensionless parameter which characterizes the rarefaction of gases and that is defined as the ratio of the mean free path of the molecule to the surrounding pressure:

$$k_n = \frac{\lambda}{h_0} = \frac{k_b T}{\sqrt{2}\pi P_a \sigma^2 \, h_0} = \frac{0.0068}{P_a h_0}$$

(3)

In the proposed definition k_b is the Boltzman constant, T is the ambient temperature, P_a is the ambient pressure, σ is the diameter of the air molecules, h_0 is the length of flow of the device and it depends on the air gap between the movable plate and the fixed substrate, λ is the mean free path covered by the gas molecule before colliding with another molecule. As quoted, another possibility to sense pressure exploiting a CMOS-MEMS resonant pressure sensor is by observing the variations in the quality factor (Q-factor) of the resonant cavity. This parameter is primarily dependent on the viscosity (a measure of a fluid's resistance to deformation under shear stress) and it measures the energy stored per cycle of oscillation with respect to the energy lost per cycle. In vacuum, the Q-factor is primarily determined by the internal losses of the resonator, such as mechanical damping and material losses. On the contrary, in a gas, such as for atmospheric pressure sensing, the Q-factor is also influenced by the squeeze film gas damping effect, which arises due to the interaction of gas molecules with the resonator surface and that is described by means of the Knudsen number itself.

$$Q = \frac{Energy\ stored}{Energy\ dissipated\ per\ cycle} = \frac{m\, w_r}{c_{total}} = \frac{\sqrt{m\, k}}{c_{total}} \tag{4}$$

Therefore, pressure sensing is performed by the trend of the quality factor with the variation of the Knudsen number which in turn depends on pressure, hence in damping effects. Based on k_n the fluid flow may be classified in four different regimes: continuum flow, slip flow, transition flow and molecular flow. As pressure reduces, the mean free path increases and becomes comparable to the characteristic flow length i.e., the air gap between the electrodes, resulting in an increment of the Knudsen number.

- In the continuum flow regime (high pressure) $P_a > 272000\, Pa$ and $k_n < 0.01$ air damping is essentially independent of the surrounding pressure, since the mean free path is very low and the molecules collide imminently among each other.

- In the slip flow regime $272000\, Pa > P_a > 27200\, Pa$, $0.01 < k_n < 0.1$ phenomena such as temperature jump and velocity slip occur due to change in the boundary conditions.

In these two regimes the Q-factor of the resonator is inversely proportional to the pressure of the gas, and it follows the Stokes' law, which states that the damping force is proportional to the gas viscosity and inversely proportional to the radius of the resonator; hence, the Q-factor decreases as the pressure of the gas increases.

- In the transition regime (very low pressures) $27200\, Pa > P_a > 272\, Pa$, $0.1 < K_n < 10$, the mean free path λ is comparable to the air gap between the fixed and the movable plate of the device; the consequence is that both the structural effects (the factors related to the geometry, the materials and the mechanical properties of the resonator structure itself) and the film damping effects (the collision between gas molecules and structural molecules) contribute equally to the computation of the overall damping coefficient.

- In the free molecular flow regime $P_a < 272\,Pa$, $k_n > 10$ the individual gas-molecules structure collisions become the dominant gas loss mechanism and air stops behaving like a viscous fluid. At very low pressures the density of the gas molecules is reduced, therefore the effect of collisions between the gas molecules and the resonator surface is reduced, which it means that the squeeze film damping is the less dominant with respect to the structural damping.

The corresponding Laplace transform notation of the entire spring-mass damped system can be converted into a second order transfer function and expressed by means of all the quoted parameters as follows:

$$\frac{X(s)}{F(s)} = \frac{1}{s^2 + s\frac{c_{total}}{m} + \frac{k}{m}}\frac{1}{m} = \frac{1}{s^2 + s\frac{2f_r\pi}{Q} + (2f_r\pi)^2}\frac{1}{m} \tag{5}$$

Nowadays, the most frequent geometry used in CMOS-MEMS to design the resonating mass of the pressure sensors is the one made of a square-perforated oscillating membrane composed of several metal layers which are electrically and mechanically connected by vias compatible with CMOS technology as shown in the SEM picture provided by the work of Dana Mata et. al. reported in Figure 4 [1]. This kind of geometry is also fundamental for the improvement of the gas flow around the diaphragm, where the gas squeeze film damping effect on the resonator decreases, resulting in an enhancement of the Q-factor and frequency response of the resonator. However, an asymmetric flow pattern of gas due to squeeze film flow must be taken into account around the internal perforations near the boundary of the structure when analysing the parameters of the sensor. For this purposes, different models can be used; among all, the Reynolds equation is fundamental to make an estimation of the net damping coefficient and it states that the pressure distribution in a fluid film is a function of the viscosity, velocity, and geometry of the surfaces, as well as the applied load. Moreover, the validity of the Reynolds model is derived under the assumption of continuum flow or slip flow regimes, where pressure is high, while in rarefied gasses (gasses at low pressure), where the mean free path of the gas molecules is comparable to or larger than the air gap between the plates, this model may not be the most appropriate, and the gas behaviour is better described by the Boltzmann equation or other rarefied gas models. In such cases, the resonant frequency of a resonant cavity may not be directly proportional to the pressure applied, and more complex models may be required to accurately predict the sensor response. In general, due to its relatively high density and viscosity at ambient conditions, the behaviour of air can be considered as continuum flow in most engineering applications, therefore the Reynolds equation is the proper model to be exploited for the computation of the damping coefficient in a CMOS-MEMS resonant atmospheric pressure sensor. For more detailed considerations regarding this topic, the study conducted by Pandey et. Al. analyses the modified Reynolds equation specifically for MEMS structure [7].

The two most important contributions that must be taken into account for the overall computation of damping in the pressure sensor that affects the resonant structure are reported in equations 6, 7 and 8.

$$c_{squeeze} = \frac{16\sigma P_a L^2}{\pi^6 w_r h_0} \sum_{m,n=odd} \frac{\left[\left(\frac{\Gamma^2}{\pi^2}\right) + m^2 + n^2\right](4 - f_{perforation})}{(mn)^2[\left(\frac{\Gamma^2}{\pi^2}\right) + m^2 + n^2]^2 + \frac{\sigma^2}{\pi^4}}$$

(6)

$$c_{perforation} = 8\pi\mu\left(\frac{T_p}{q_{th}} + \Delta_E b\right) x N_h$$

(7)

$$C_{tot} = c_{squeeze} + c_{perforation}$$

(8)

Therefore, the total damping effect is expressed respectively by the damping coefficient due to squeeze film damping and the one due to loss through perforation of the resonator. Particularly, m,n are the harmonic nodes, L is the length of the resonator, σ is the squeeze number, Γ is a constant that captures the perforation effect, $f_{perforation}$ is the force through each perforation, μ is the viscosity, Q_{th} is the relative flow rate, T_p is the thickness of the resonator, Δ_E is the relative elongation of the perforation length and N_h is the total number of perforations in the movable plate. The final goal of the optimization process of the design of a resonance pressure sensor that works at atmospheric pressure ($1atm$ which correspond to be around $100kPa$, thus targeted to operate in the slip flow regime), consists into minimizing the damping while optimizing the quality factor and the sensitivity of the device without affecting negatively the sensed device capacitance.

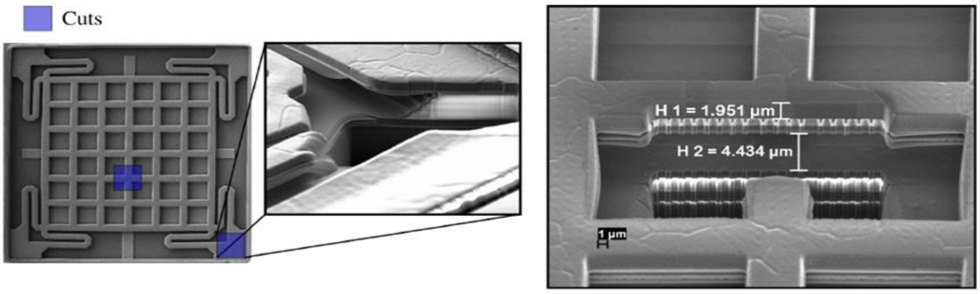

Figure 4 SEM image of the manufactured prototype and the cross-section of it after the post-CMOS realization based on an isotropic wet etching. Source: "Resonant MEMS Pressure Sensor in 180 nm CMOS Technology Obtained by BEOL Isotropic Etching" Diana Mata-Hernandez et. Al. [Ref. 1]

In conclusion, several additional approaches with respect the already quoted ones may be used for the production of pressure sensor, on which its functionality will also depend and these are: the Pirani sensing, in which pressure can be estimated by heating-up a filament and measuring its thermal loss, proportional to the molecules colliding with it; the membrane-deformation sensing, which relies on the air pressure difference between the external and internal pressures of a vacuum-sealed cavity and which causes the deformation of a membrane; the resonant-frequency sensing, which, as stated, is based on the observation of the resonant-frequency shift that acquires at different pressures due to the mechanical stress of the movable part of the MEMS and finally, the quality-factor sensing, based on a resonator quality factor (Q) change with pressure.

2.2. Accelerometer

Accelerometer fundamental behaviour is based on the movement of a proof mass anchored to a series of springs which can be arranged in different ways depending on the wanted characteristics of the sensor. The accelerometer sensing typologies can be distinguished in: piezoresistive sensing, in which the movement of the proof mass is detected by the change of electrical resistance of a piezoresistive material attached to a suspension; resonant sensing, in which the movable mass works as a frequency-tuning element in an oscillator; tunneling sensing, in which nanometer gaps placed between the movable mass and an electrode detect the tunneling current; thermal sensing, in which thermocouple are exploited to sense the position of a movable bubble of heated air eventually sealed in the cavity of the sensor; capacitive sensing, in which the movement is detected by sensing the capacitance between a movable electrode attached to the proof mass and a fixed electrode. However, all of quoted typologies share the purpose to increase the sensitivity of the sensor, which is defined by the ratio between the mass of the movable part and the stiffness of the suspensions that anchor the movable part to the fixed one. Similarly with respect to the resonant pressure sensor, the accelerometer is modelled as a simple second order mass spring-damper system (Figure 2), hence defined by equation (1). The dynamic behaviour of the accelerometer is represented also in this case by the quality factor, defined in equation (4); depending on Q, different conditions are possible for the system [26, 27]:

- $Q \leq 0.5$: over-damped or critically-damped ($Q = 0.5$) system in which the step response is an exponentially decreasing function of time, and it approaches the steady state value asymptotically.
- $Q > 0.5$: under-damped (resonant) system in which the step response is a sinusoidal function with exponentially decreasing amplitude with respect to time.

The device shows the widest flat bandwidth and the fastest settling time if characterize by a critical damping. Higher values of Q could enhance noise optimization, however vacuum encapsulation is required.

Since we are dealing with parallel plate devices, the estimation of the capacitance both for the pressure sensor and for the accelerometer depends on the displacement of the movable released part of the resonator (see Figure 3), hence the capacitance can be defined as follows:

$$C(z) = N\frac{\varepsilon A}{z_0 + z}$$

(9)

where A is the capacitor area (overlapping area between movable and fixed electrodes), ε is the product of the vacuum permittivity and the permittivity of the medium between the plates (air) and N is the number of fingers (number of parallel plates). However, most accelerometers rely also on the change of the area instead of the gap, thus defining the comb-finger version of the devices where the capacitance can be estimated instead as:

$$C(l_0) = N\frac{\varepsilon l_0 t}{d}$$

(10)

where l_0 is the length, t is the thickness of the single finger and d is the fixed gap between the electrodes. Due to the intrinsic behaviour of the accelerometer the displacement of the proof mass directly depends on the external acceleration:

$$z \sim \frac{m}{k}a_{ext} = \frac{1}{w_0^2}a_{ext}$$

(11)

where a_{ext} represents the external acceleration acting on the proof mass and w_0 is the angular frequency of resonance characterizing the device which also defines its mechanical sensitivity as $1/(w_0^2)$; therefore, an important trade-off between the bandwidth and the sensitivity must be taken into account. Furthermore, even in accelerometers the application of voltages to the electrodes produces an electrostatic force. Depending if device is a parallel plate or comb-finger, the formulas defining the electrostatic forces are respectively reported in equation (12) and (13) which can be obtained simply substituting accordingly equations (9) and (10) to the capacitance in the definition of the electrostatic force.

$$F_{el}(z,V) = \frac{\partial \mathrm{E}}{\partial \mathrm{z}} = \frac{\partial}{\partial \mathrm{z}}\frac{\mathrm{CV}^2}{2} = \frac{V^2}{2}\frac{\partial \mathrm{C}(\mathrm{z})}{\partial \mathrm{z}} = \frac{N}{2}\ \varepsilon\ \mathrm{A}\frac{\mathrm{V}^2}{(z_0+z)^2}$$

(12)

$$F_{el}(l_0,V) = \frac{\partial \mathrm{E}}{\partial l_0} = \frac{\partial}{\partial l_0}\frac{\mathrm{CV}^2}{2} = \frac{V^2}{2}\frac{\partial \mathrm{C}(l_0)}{\partial l_0} = N\ \varepsilon\ \mathrm{t}\frac{\mathrm{V}^2}{2\ \mathrm{d}}$$

(13)

In this work the analysed accelerometer is based on the change of the gap. However, two main geometries that define the configuration between the electrodes must be distinguished:

- Proof mass and single stator:
  So far, this classic configuration has been discussed, hence the electrostatic force can be determined using equation (12) or (13) depending on the parallel or comb-drive arrangement respectively. As quoted for the pressure sensor in section 2.1, this case may be affected by pull-in when the electrostatic force exceeds the elastic one.

- Proof mass electrode between two stators electrodes:
  In this case two capacitors are changing their value in opposite directions in response to the mass displacement provoked by the external acceleration. This topology gives the possibility to acknowledge a better sensing and it also provides the feasibility of applying electrostatic force towards both top and bottom plates. The electrostatic force in this case is computed as follows:

$$F_{el}(z,V) = \frac{1}{2}\ \varepsilon\ \mathrm{A}\left(\frac{V_{top}^2}{\left(d_{top}-z\right)^2} - \frac{V_{bottom}^2}{(d_{bottom}-z)^2}\right)$$

(14)

V_{top} and V_{bottom} represent respectively the voltage applied between the finger of the movable plate and the first stator and the voltage applied between the finger of the movable plate and the second stator with d_{top} and d_{bottom} as the correspondent formed gaps. With this addition of another stator electrodes nearby the proof mass, it is formed the interdigitated comb structure of the accelerometer, which can generally be affected as well by pull-in. This configuration of accelerometer will be the one simulated in further sections using COMSOL Multiphysics.

To sum up, an accelerometer can be modelled as a simple mass-spring-damper system, and the estimation of the sensing capacitance is performed through different models. At this point, to obtain the desired design, the main working parameters such as density, Young’s Modulus, spring constant, capacitance and capacitance sensitivity to acceleration, thickness dimensions and composition of each layer, need to be estimated exploiting a first rule of thumb. The mechanical parameters are the first to be estimated starting from the suspensions and the beam deflection. An initial approach requires the discussion of the different possible beam deflections formula for the most general boundary conditions: fixed-free, fixed-guided and fixed-fixed case terminals. For each case the maximum deflection for a concentrated load F or a distributed load f applied on a suspension have been minutely analysed in the E. J. Hearn’s work “Mechanics of Materials 1: The mechanics of elastic and plastic deformation of solids and structural materials”, Butterworth-Heinemann, 1997, vol. 1. [28], which also describes in detail the Castigliano method, used whenever a more precise approach is required for suspension modelling. An important relation to consider regarding the mechanical parameters is the one between Young’s modulus E, shear modulus G (which describes the material's response to shear stress) and Poisson’s ratio ν, defined as follows:

$$G = \frac{E}{2(1 + \nu)}$$

(15)

Regarding the stiffness characterizing the device, this depends hugely on the arrangement of the springs that suspend the resonating proof mass. Different typologies of arrangement have been studied in the past, however the most common springs architectures are the crab (Figure 5 left configuration) or serpentine (Figure 5 right configuration) flexures.

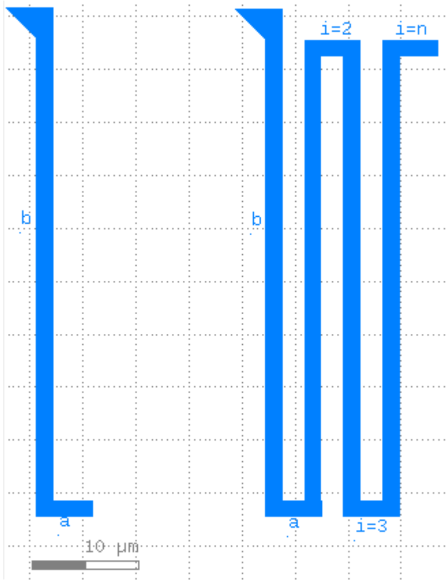

Figure 5 Crab flexure configuration (left) and Serpentine flexure configuration (right) reproduced in Klayout

Depending on whether the deflection occurs in-plane or out-of-plane, different formulas are used for estimating the spring constant [30]. The ideal formula corresponding to the in-plane spring constant, where deflection occurs in the xy plane only, is defined in equation (16).

$$k_x = \frac{12mEI_{zzb}((\bar{a}+b)n-b)}{b^2(n-1)((3\bar{a}^2+4\bar{a}b+b^2)n+3\bar{a}^2-b^2)}$$

(16)

In this formula, a and b represent respectively the segment pitch and the length of the spring, n is the number of segments while m is the number of parallel serpentines, E is the Young's modulus, I_{zzb} is the second moment of area of the beam cross-section b around the vertical neutral axis zz (in this case exiting from the paper), which in this case is the axis in which the material ideally does not change its length during the bending, and finally $\bar{a}$, which is defined as:

$$\bar{a} = a\frac{I_{zzb}}{I_{zza}}$$

(17)

This represents a possible first raw approach for the computation of the spring stiffness, however, in further sections the computation of the stiffness will be generally performed basing on the results obtained from the FEM COMSOL simulations on the resonance frequency or other mechanical parameters, hence implicitly exploiting these formulas.

2.3. CMOS-MEMS integration

The integration of MEMS devices with CMOS technology offers significant advantages, leveraging standardized and state-of-the-art processing techniques to enhance performance, reduce the time-to-market, and improve manufacturing costs. This integration brings together the strengths of both technologies, allowing for a more efficient and streamlined approach. By incorporating both technologies into the same fabrication process, MEMS devices can benefit from the use of CMOS feature sizes. This opens up opportunities for designing smaller and more flexible structures and it allows for the creation of thinner membranes and smaller gaps, enhancing overall device performance and leading to an improvement in the device sensitivity. The share of the same die between MEMS and CMOS components also provides a significant reduction in parasitic capacitances which could instead negatively impact device performance and power consumption. Additionally, the most important CMOS-MEMS fabrication process steps completely eliminate the need for separate packaging for each technology, resulting in streamlined and more cost-effective packaging options. An additional advantage lies in the fact that CMOS foundries have greater production capacity and infrastructure, enabling higher volume production of MEMS devices. This integration allows for the scaling up of MEMS production without the need of specialized and often more expensive manufacturing processes associated with standard MEMS foundries. Overall, the integration of CMOS and MEMS technologies in a single manufacturing process addresses the difference in economies of scale between CMOS and MEMS. On the other hand, the integration process increases the risk of defects and failures, which can affect the device itself and the overall yield of it, this is the reason why the reliability of both CMOS and MEMS components becomes critical, requiring stringent quality control measures. Finally, the exploitable materials with CMOS processing techniques and their thermal, mechanical, and electrical properties represent a fundamental aspect to take into consideration during the design and fabrication of these kind of devices, their unwanted effects and the limited choice can have a serious effect on the final result.

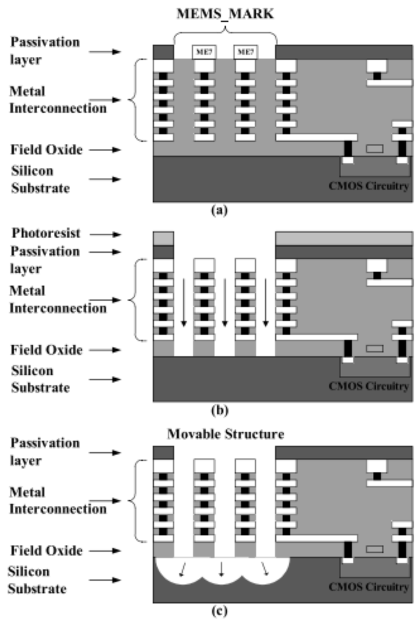

Figure 6 Cross-section view of ASIC/MEMS etching process [Ref. 8]

2.4. The post processing approach

A CMOS processing technology consists of two main phases: the Front-End-of-Line (FEOL) and the Back-End-of-Line (BEOL). The FEOL involves principally the formation of transistors, while the BEOL focuses on creating the wiring interconnections. The technological process is characterized by the minimum feature size allowed and the different FEOL and BEOL layers. Integrating MEMS devices with CMOS technology can be achieved by modifying the CMOS process or by the use of "CMOS post-processing," which involves utilizing micromachining techniques to release a MEMS structure that has already been manufactured using the CMOS process and it minimizes the number of additional steps required in standard CMOS manufacturing. A simple example of the release steps of a CMOS-MEMS with all the layers involved is reported in Figure 6. In the latter process, the BEOL layers are particularly suitable for serving as the MEMS structural layer where no need for deep etching is required and silicon oxide present between the metal layers is used as a sacrificial layer. During the release process, a resonator can be formed within metal walls, and if necessary, a top-cavity can be sealed, as it can be observed in Figure 7. In most cases, both top and bottom metal plates are needed. The top-most metal layer contains holes that allow the etching agent to penetrate the cavity, while the bottom-most metal layer protects a doped-silicon oxide layer below. By employing CMOS post-processing, MEMS structures can be efficiently integrated with CMOS technology, leveraging the existing CMOS manufacturing capabilities while introducing minimal modifications. This approach is particularly advantageous for achieving cost-effective integration and streamlining the production of CMOS-MEMS devices. The Back-End-of-Line processes involves the use of multiple metal layers and vias for interconnection. In the case of resonators, a common approach is to combine metal layers, which are made typically in aluminium (Al) and copper (Cu), with tungsten (W) vias. This multilayer structure serves several purposes; for instance, it allows for the creation of thick structures with smaller radius of curvature, hence resulting in higher overall stiffness. The combination of metal layers and unreleased silicon oxide (SiO2) between them, contributes to the overall structural robustness particularly when the silicon oxide comes into contact with the metal lines. However, there are challenges in achieving the desired stability and repeatability for mass-scale production. Residual stress and the difference in thermal expansion coefficients during high-temperature processes can cause deformation of the structures, such as curling in beams (Figure 8). Careful control of time-dependent thermal processes is necessary, including the elimination of residues resulting from reactions between passivation materials and release agents. Another concern is the potential detachment of the structure if the vias do not provide sufficient robustness to hold the metal layers together. The presence of unreleased oxide in contact with the metal helps to maintain the integrity of the structure and it prevents detachment, that is the main reason why SiO_2 is present between the vias that compose the central resonator proof mass.

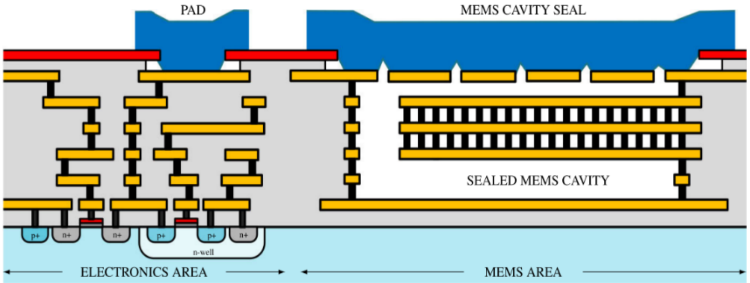

Figure 7 CMOS-MEMS cross-section after post-processing release and cavity sealing. Source: "Manufacturing issues of BEOL CMOS-MEMS devices" [Ref. 4]

The CMOS technology used in semiconductor manufacturing may involves stringent geometrical constraints to ensure accurate translation of the layout design onto the wafer during photolithography. However, since these design rules may be too restrictive for MEMS (Microelectromechanical Systems) designs, a collaborative agreement between the MEMS designer and the CMOS foundry is needed. For example, the strict design rules may prohibit the development of straight vertical metal walls since they require metal layers to extend beyond the edges of vias. In such cases, adjustments need to be made either to the MEMS geometry or by accepting certain violations of the design rules by the foundry, depending on the specific requirements of the MEMS design. Moreover, this collaboration between the MEMS designer and the CMOS foundry involves finding a balance between adhering to the necessary CMOS design rules while accommodating the unique requirements and constraints of the MEMS device. By reaching an agreement, the design can be optimized for manufacturability and functionality, allowing for the successful fabrication of CMOS-MEMS devices.

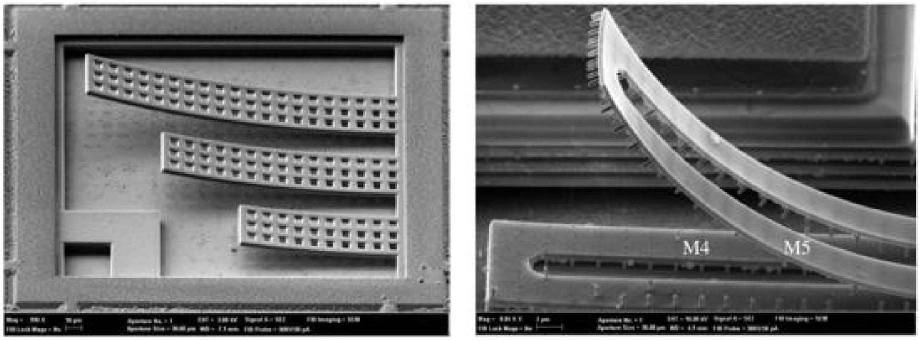

Figure 8 a) Curling of beams made of a single metal layer. b) Via detachment, similar behaviour can be expected for the resonant pressure sensor [Ref.4]

2.5. Manufacturing issues of BEOL CMOS-MEMS

In the Back-End-of-Line (BEOL) CMOS-MEMS approach, once the CMOS processing is completed, the MEMS structure is released using either dry or wet etching techniques.

Isotropic [2]wet etching with Silox-Vapox III [1, 3] is a cost-effective solution suitable for device prototyping. However, it may lead to device stiction, a phenomenon caused by capillary forces during the etching and drying process. Dry etching, on the other hand, offers the advantage of preventing stiction-related failures, making it a potential choice for high-volume CMOS-MEMS production. Vapor-phase hydrofluoric acid (Vapor-HF) is commonly used in dry etching for silicon-oxide etching due to its high repeatability and selectivity with respect to the metals present in the BEOL layers. The different deposition techniques used in the manufacturing process can result in non-uniformity in SiO_2 composition along the BEOL layers. Additionally, each oxide layer consists of two sub-layers with different densities, creating a heterogeneous oxide structure with varying etching rates. This phenomenon has serious implications for design considerations. The oxide layer below the bottom-most metal layer, known as the pre-metal dielectric (PMD), is partially doped and highly reactive to Vapor-HF. To address this, a bottom metal layer is exploited. Moreover, to prevent electrical shorting in enclosed metal cavities, interleaved anchor structures may be employed. These structures guide the vapor-HF to move up and down across the silicon oxide layers until it is exhausted, leaving behind unetched silicon oxide. This isolation of the top and bottom metal plates ensures electrical separation while maintaining mechanical integrity. A standard CMOS passivation layer, which is typically composed of silicon nitride (Si_3N_4), is employed to protect the die from moisture and contaminants and openings are made in this layer in order to provide contact between the top-metal layers and the pad area for external connections. The same passivation opening technique is used for the release process, with appropriate hole sizes, to ensure repeatability, and sufficient separation in order to prevent passivation breaking due to undercutting. If the layer has a sufficient silicon content, it can act as a release mask, simplifying the processing steps. However, if only standard Si_3N_4 is available, a layer of photoresist may be utilized on top of the passivation [9]. Moreover, to allow proper sealing of the cavity where the MEMS is placed, an additional metallization step is required. One feasible option that does not increase the overall production cost in excess is the use of aluminium sputtering[3] to seal the cavity in the passivation openings [9, 10]. Sealing is necessary in order to prevent contamination, to provide a suitable pressure environment and to allow wafer handling and packaging. Deposition conditions need to be optimised for proper sealing and film adhesion, while not compromising the structure with high temperatures. Also, the interleaved anchor structures used to isolate the top and bottom metal walls can be used as columns to provide mechanical consistency to the top-metal plane and support the sealing. The holes of this metal layer, as mentioned, allow Vapor-HF penetration. The size of the holes should neither be too small to avoid proper patterning nor too big to avoid proper sealing; it is also likely that the suitable size will not pass the standard design-

[2] Isotropic etching method involves in the removal of material in all directions at an equal rate from a substrate via a chemical process using an etchant substance. Its counterpart is represented by the anisotropic etching method.

[3] Sputtering is a physical process in which the vaporization of a solid material occurs by bombarding it by ion energy. This technique is exploited mainly for the deposition of metals layers.

rule checking (DRC). In conclusion, depending on the characteristics of the sensor, a thermal annealing to be performed before the sealing might be necessary in order to decrease the pressure inside the cavity.

2.6. Generic simulation in COMSOL 5.5 Resonant Capacitive Pressure sensor 250nm

As a simple overview introduction to COMSOL Multiphysics a design of the pressure sensor made in $250nm$ technology IHP [2] with a resonator part responsible for sensing can be characterize in terms of displacement, stiffness of the structure and resonance frequency. The resonator measures $140x140\ um^2$ respectively for width and length, has a thickness of $8\ um$, a density of $8943.75\ [kg/m^3]$ (chosen for the best optimization in terms of quality factor and sensitivity), Young's Modulus of $197.88\ [GPa]$ and Poisson's ratio equal to 0.32375. After having created the desired geometry made of $6x6$ perforations to enhance the damping effect in COMSOL, it is possible to make an estimation of the stiffness of the structure by applying an arbitrary small force of $1\mu N$ on a particular point of the resonator and observing the displacement occurred in that point. For instance, we can find a theoretical stiffness of about $k = F/x = 1\mu N/0.0024556um = 407.23\ [N/m]$.

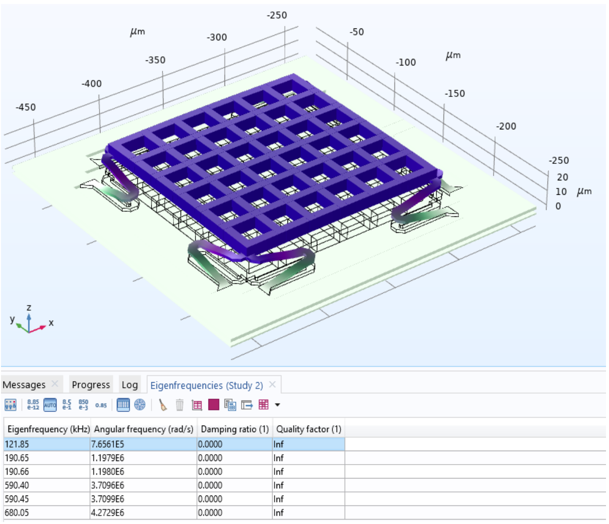

Figure 10 COMSOL simulation of the resonant capacitive pressure sensor 250nm technology IHP, computation of the resonance frequency and successive modes

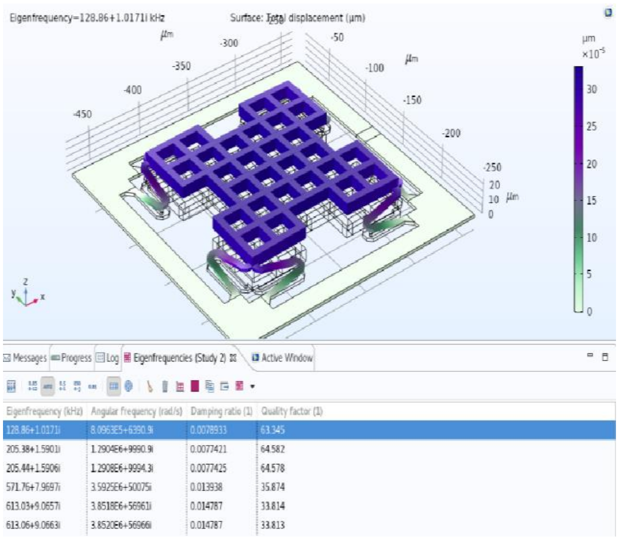

Figure 9 COMSOL simulation of the resonant capacitive pressure sensor 250nm technology IHP, computation of the resonance frequency and successive modes of the modified structure with eliminated mass

Defining the material properties and dimensions we can compute the mass of the central part of the structure, hence of the effective resonator, directly in COMSOL and which approximately correspond in this case to $7.97 * 10^{-10} kg$. Therefore, the estimation of the resonance frequency of the structure under study is theoretically equal to $f_r = 1/2\pi \sqrt{k/m} = 114\, kHz$. Performing in COMSOL an eigenfrequency study that is able to detect the resonance frequency and all the successive modes of the structure, if the proper boundary conditions have been correctly set, it is clearly visible in Figure 10 that the actual resonance frequency is around $120\, kHz$, which is very close to the theoretical estimation and to the experimental value which is equal to $100 kHz$ [2]. In particular, it must be underlined that the precision of results in COMSOL depend on the mesh that has been used on the structure, indeed a very precise mesh leads to a higher computation time for the simulation to compute, as well does a more complex structure, but better results are provided. Since this design is not the one of interest for this work, generic simulations have been performed in order to check the validity and to define the methodology to use in the tool for the best advancement. From the simulation has been observed that the actual quality factor of the structure for each frequency is ideally infinite due to the fact that no damping has been included in the simulation, thus showing an infinite response, sensitivity and quality factor at the resonance. Indeed, including this last-mentioned parameter we expect a slight reduction of the resonance frequency, since it is inversely proportional with the damping and as a consequence of this a convergence of the quality factor. An interesting aspect can be analysed also by modifying the structure itself. For instance, in further simulations some of the perforations have been completely eliminated. As a result of this change the new resonance frequency results to be equal to $128.9\, kHz$ as clear from Figure 9, so it has increased with respect to the original square shaped structure. Indeed, eliminating some parts of the structure has affected the mass in an important way, decreasing it. On the contrary, the stiffness is slightly decreased as well, showing a value of $387.07\, N/m$. However, its effect on the resonance frequency is not as important as the one due to the decrement of the mass. For this second case, the reported Figure 9 shows that the resonance frequency and all the successive modes have an imaginary part, the reason for this is that an eligible damping factor has been added to the structure based on the Rayleigh damping analysis. This is defined by two parameters that for the current simplified study have been set to be equal to $\alpha = 8107.3[Hz]$, $\beta = 7.13e^{-9}[s]$ in order to simulate the structure to show a quality factor around 60, as the experimental results has proven. It is clear in fact that the quality factor results to be around 63 which as well it represents a close value to the experimental one. A decrement of resonance frequency occurs instead if some springs belonging to the resonator are eliminated. In this case, both an important decrease of mass and change in the overall stiffness occur. However, oppositely with respect to the previous quoted case the modification in stiffness is the dominant effect that modifies the resonance frequency with respect the modification in mass. The new stiffness in fact results to be equal to $1\mu N/0.0047131 um = 212.2[N/m]$, with a new mass approximately equal to $7.655e^{-10} kg$. These results confirm that a small decrease of the mass and higher decrease of stiffness has occurred with respect to the original case with all the springs present, leading then to a much lower resultant resonance frequency which is now equal to $80\, kHz$. This result is due to the fact that a higher elasticity characterizes the structure, allowing it to be more flexible, therefore to resonate more slowly. Different displacement for each mode could be represented. A last simulation of interest is based on the observation on how the central resonant membrane deflects if a certain amount of voltage is applied to the fixed bottom metal. Particularly, applying the ground to the resonator and a sweep of voltage bias to the bottom fixed electrode, an electrostatic force arises across the two electrodes exactly as a capacitive sensor. The two plates start to attract each other in a nonlinear way, meaning that the closer they are in space, the higher the electrostatic force is, hence obtaining an exponential behaviour of the trend of both the Bias Voltage vs. Capacitance (Figure 11) and the Bias Voltage vs. displacement (Figure 12) curves. The two mentioned behaviours have been plotted, considering the Maxwell capacitance in $Farad$ and the displacement in um:

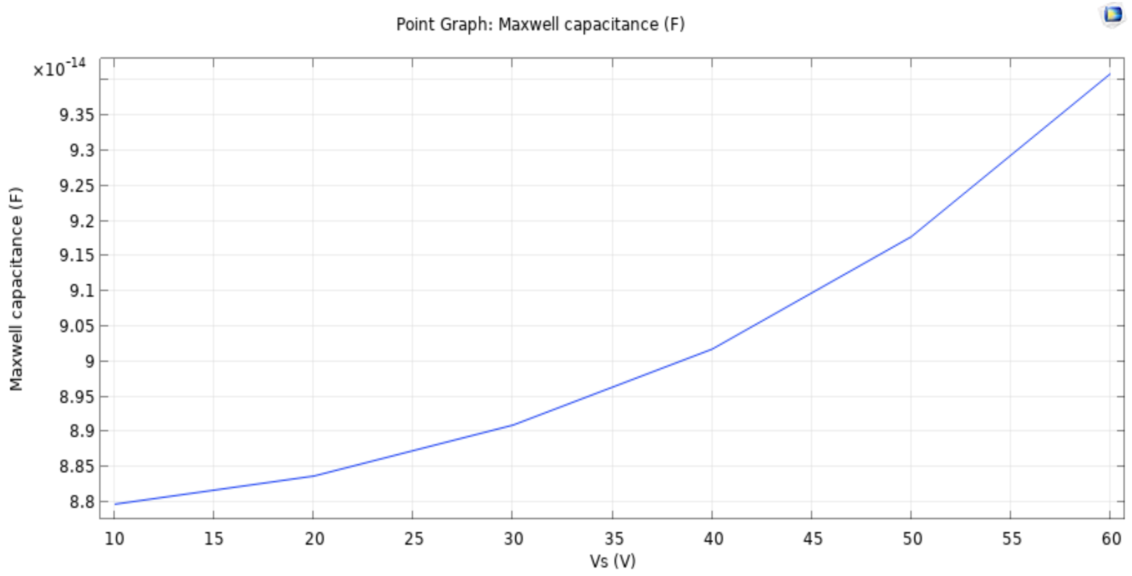

Figure 11 Bias Voltage (from 10V to 60V with a step of 10V) vs Maxwell Capacitance (in Farad) trend. For 0V the capacitance is equal to 0F, while increasing the Bias this last one increases exponentially from 88fF at 10V up to 94fF at 60V. However, even if it is not shown above 60V of Bias the structure gets close to the pull in condition [6] which would result in a diverging capacitance and a short circuit of the structure, breaking the device

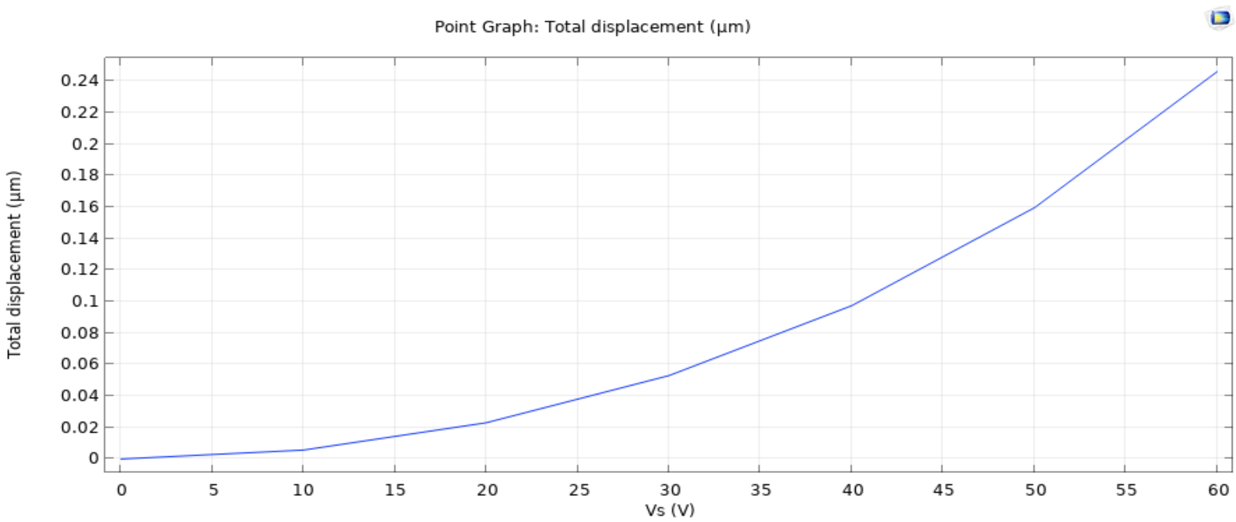

Figure 12 Bias Voltage (from 0V to 60V with a step of 10V) vs Displacement of the central resonator (in um) trend. Also in this case, increasing the Bias the displacement shows an exponential behaviour going from 0um at 0V to 0.24um at 60V

The visual inspection of the actual displacement that occurs during the application of the electrostatic force depending on the Bias is reported in the following figures both at $0V$ (Figure 13) and $60V$ (Figure 14) applied.

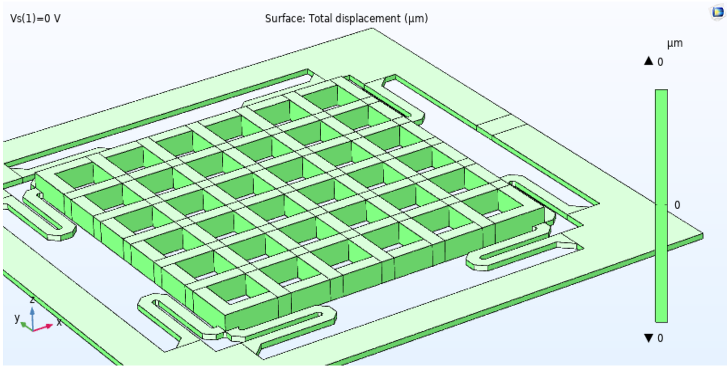

Figure 13 Displacement with 0V of bias applied

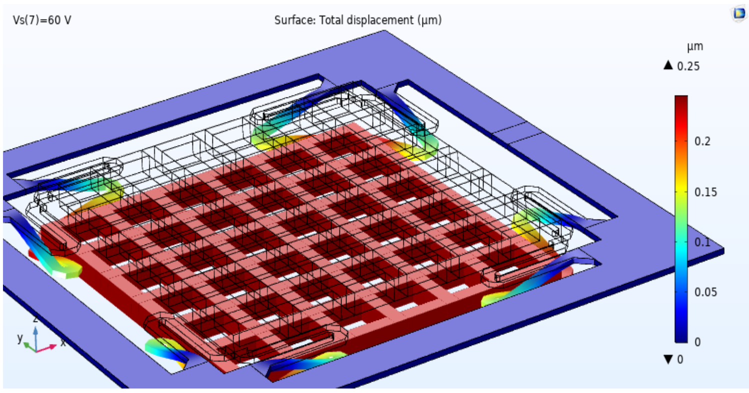

Figure 14 Displacement with 60V of bias applied

The two pictures report respectively the (not-in-scale) shift of the central resonator, with a legend placed on the right that shows the correct value of the displacement. It is clear how the plate tends forward the bottom fixed electrode (hidden for a better visualization) whenever a Bias voltage is applied, which in this case is $60V$ (Figure 14). On the contrary, it remains stationary when no Bias is applied (Figure 13), thus with a null resultant displacement. All these concepts will be applied to the desired structure of the Resonant capacitive pressure sensor $180nm$ TSMC and similarly to the accelerometer, providing more details depending on various scenarios and different conditions. More details will be provided both in terms of implementation and results obtained from COMSOL in the following paragraphs.

3. Migration of Resonant Capacitive Pressure Sensor and Accelerometer Layout from TSMC to UMC 180nm Technology: A comparative analysis using Klayout and Cadence Virtuoso

In the quest for optimal device performance, cost-effectiveness, and compatibility with fabrication processes, is often considered the migration from one fabrication technology to another. The presented section is focalised on the migration of the prototype-A1 of the layout designs of the Resonant Capacitive Pressure sensor [1] and the prototype-A1 of the Accelerometer from TSMC (Taiwan Semiconductor Manufacturing Company) to UMC (United Microelectronics Corporation) made in $180nm$ technological node. Different prototypes depending on the composition of the central resonator proof mass are analysed in the studied conducted by Diana Mata-Hernandez et al. [1]. The present section has the aim to provide a detailed comparative analysis of the migration process using the tools *Cadence Virtuoso* and *KLayout* for both the quoted layouts. Challenges and considerations involved in adapting the designs to the UMC $180nm$ technology will be discussed, including device dimensions and material compatibility. In conclusion, the Design Rule Check (DRC) using *Cadence Virtuoso* and how it ensures compliance with the fabrication technology's specific rules and constraints, will be analysed for both the sensors. The migration of layout designs from one fabrication technology to another requires a careful analysis of various factors, such as process compatibility, design considerations, and also tool compatibility. *Cadence Virtuoso* and *KLayout* are two tools widely used to facilitate the migration process. The former provides a comprehensive environment for designing integrated circuits, giving the possibility to easily create and modify layouts of MEMS devices and general circuits and that allows a detailed analysis and verification of the layout designs, including design rule checking (DRC). On the other hand, KLayout is a powerful open-source layout viewer and editor which permits to provide variations on the geometry dimensions in an extremely easy way. Despite both of the tools may be used separately, this study exploits both of them in order to speed up the migration, however the importing and exporting procedure of layouts may results challenging and if the grid properties used during the design of a device in one tool does not properly match the ones of the other some errors may appear, therefore particular attention must be paid during these secondary procedures. Those migrations will start from already existing designs made in TSMC $180nm$ technology both for the pressure sensor and the accelerometer, that will represent the base for a comparison on dimensions and for the optimization in the UMC versions depending on the design rules that the manufacturer impose. Therefore, by undertaking this migration analysis, the feasibility of transitioning the layout designs of the sensors from TSMC to UMC technology will be seeked. The final insights gained from this study will aid in making informed decisions regarding the fabrication process, performance optimization, and cost-effectiveness of these MEMS devices in the future.

3.1. Resonant Capacitive Pressure sensor migration from TSMC to UMC 180nm technology

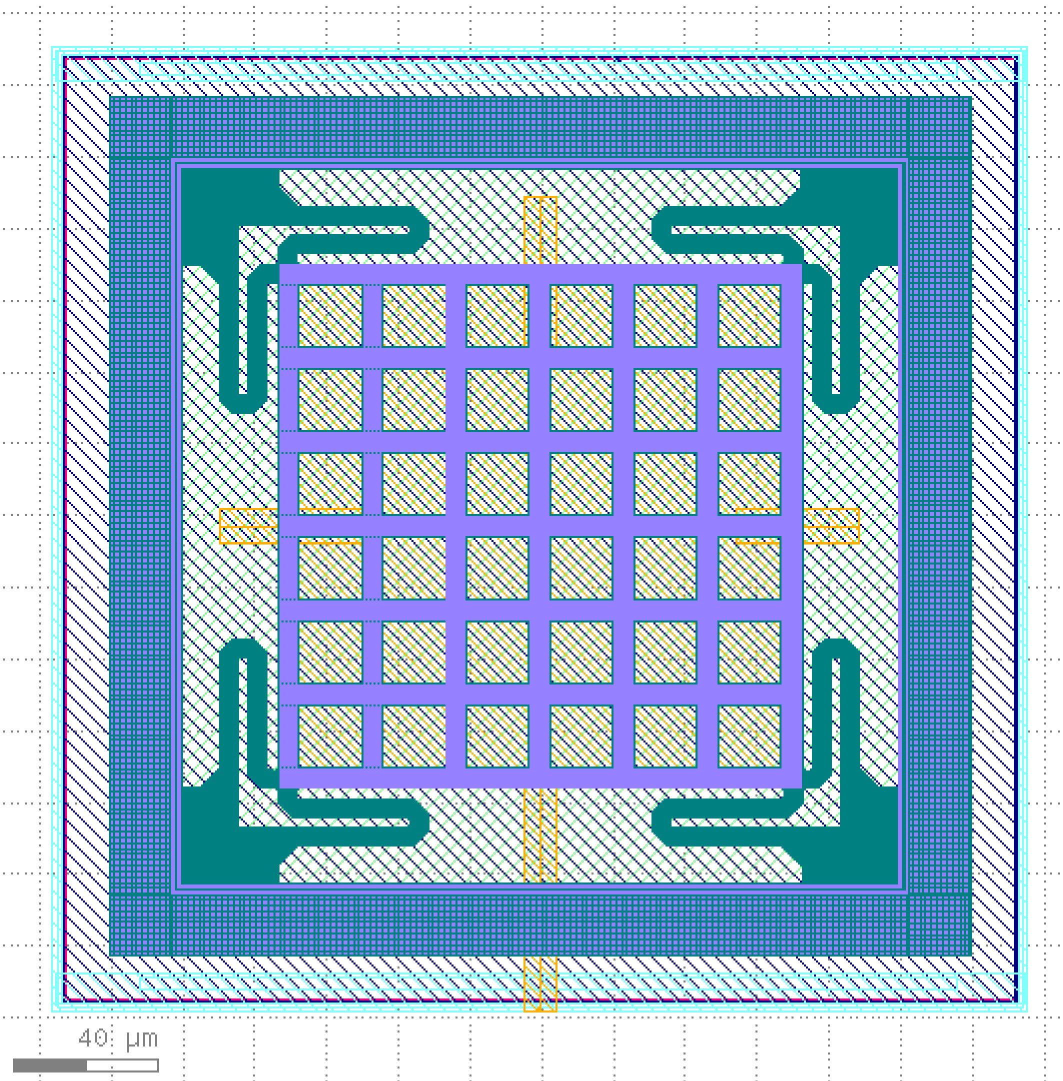

Figure 15 Klayout view prototype-A1 Resonant Capacitive Pressure sensor TSMC 180nm layout with all its layers identified by different colours and stipples. Based on Ref. [1], design made by Daniel Fernandez et. Al.

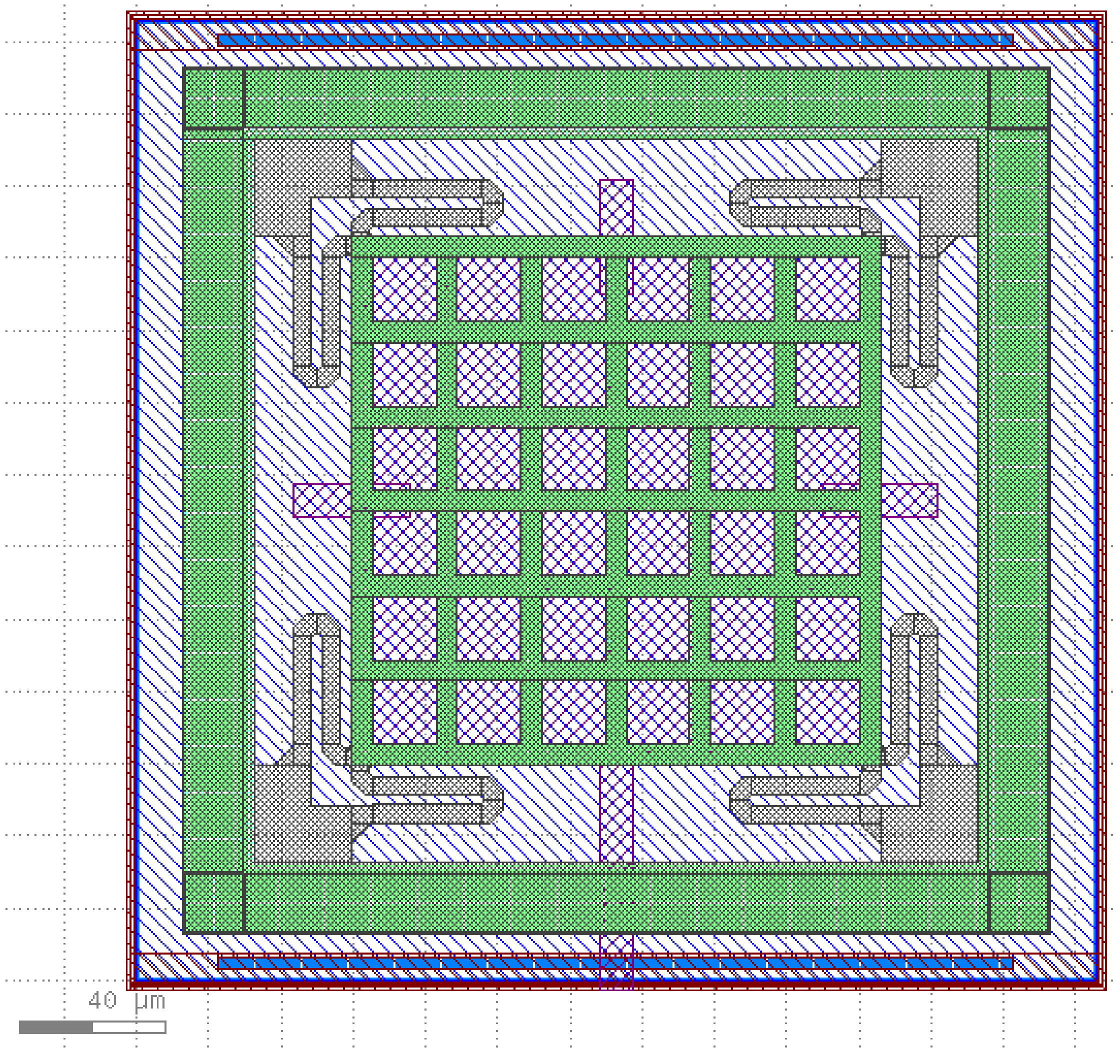

Figure 16 Klayout view prototype-A1 Resonant Capacitive Pressure sensor UMC 180nm layout with all its layers identified by different colours and stipples. Faithful migration of the TSMC design compliant with UMC technology.

As already mentioned, a CMOS-MEMS device is built in the BEOL (Back end of line) through several metal layers which are usually made of aluminium. Tungsten vias interconnect the different metals among each other, and within those, a layer of dielectric material made of silicon oxide (sacrificial layer) is deposited in order to be then selectively removed in some parts with the aim of creating a gap between the central movable resonator part (rotor) and the fixed part of the structure (stator). During the design in Cadence and Klayout a silicon nitride passivation layer is created, which means to create on the top of the structure an opening draw performed in order to delimit the etching area and to protect the surrounding CMOS circuitry. The Figure 15 and Figure 16 show the layouts of the pressure sensor composed in all its layers respectively in TSMC and UMC technology. Since it has been made and manufactured with the design rules of the standard analog designs Industry-Compatible 180nm CMOS technology, its layout can be easily migrated into different manufacturers, hence proving its versatility as an IP-block. This and the further designs that will be discussed in this section are *1P6M* type of process technology, therefore one polysilicon layer, which is used as gate, interconnects and six metal layers are present in the process. For this and the following migration designs the top metal layer thickness is the standard $20KÅ$ $(2um)$. The metal layers are used for interconnecting various components and nodes in the IC design. The principal layers that compose the BEOL CMOS compatible MEMS prototype-A1 (Figure 15) are the following (from the bottom to the top surface):

-Thin Oxide for device and interconnection

-P+ S/D implantation

-Contact hole between Metal1 and thin oxide

-Metal1

-Via1 between Metal1 and Metal2

-Metal2

-Metal3

-Metal4

-Via4 between Metal4 and Metal5

-Metal5

-Via5 between Metal5 and Metal6

-Metal6

-Passivation Pad opening

Due to the fact that the migration in this case include only the MEMS and not the electronic CMOS part, the steps necessary for the migration in UMC do not involve in this case the schematic migration, the transistor models, the place and route and the simulation setups, since no transistors are present. Indeed, the most important steps performed for the defining of the UMC design have been the following:

- Preparation and Design Analysis:
  Fundamental step is to carefully examine the existing design files such as Design Rules Manuals of both the technologies involved in the migration, including layout dimensions, minimum and maximum tolerances among layers and limiting constraints.

- Technology Characterization:
  Understand the most important differences between TSMC and UMC $180nm$ process technologies. For this purpose, a content table describing all the characteristics and dimensions of each technology has been created to ease the

process. The first fundamental difference to report is the grid size of each technology. In fact, the grid size, also called grid spacing or resolution, defines the minimum distance between points or objects that can be placed on the layout. This represents an essential parameter for maintaining design consistency, adhering to manufacturing constraints and it represent the first parameter to properly set in the design tool before starting to draw the layers. UMC is characterize by a grid size higher if compared to the TSMC's, hence a lower "degree of freedom" can be used with UMC technology. Both in Cadence and in Klayout it is of a pivotal importance to properly set the grid size before any change on the layout design.

- Layout Migration:
  The new-created UMC $180nm$ library must be used to reproduce faithfully the layout of the CMOS-MEMS TSMC design. This involves manually drawing shapes of different layers according to the design and ensuring adherence to UMC's design rules. During this step is fundamental to specify also the signals pin, which in the case of the pressure sensor have been called $Vsense$, $Vdrive$ and VSS which are associated to Metal 6, Metal 3 and Metal 1 respectively.

- Layout Verification:
  Design rule check (DRC) verification must be performed to ensure that the layout matches the schematic and adheres to the design rules of the technology. For the MEMS migration there is no need of layout vs. schematic (LVS) verification since no schematic is present at this point.

- Design Verification:
  The MEMS system, including the CMOS circuitry (readout) if present, can be simulated and tested before manufacturing in order to verify the overall functionality and performance of the design. To simulate the MEMS, an approach based on its description made in Verilog A may be performed (for major information see references 2, 11 and 12). In this work no simulation using Verilog A has been carried out on the sensors.

- GDSII Generation:
  The GDSII layout file represents the final layout representation used for chip manufacturing, hence once the layout design is completed the GDSII file must be generated to be sent to the manufacturer.

- Process Compatibility Check:
  Validate the layout against UMC's process design rules and guidelines. Any issues that may arise during this compatibility check must be analysed and fixed.

The quoted steps may vary depending on the errors and kind of implementation exploited. If errors are encountered during the DRC of the layout, the design needs to be carefully checked and properly fixed.

Depending on the desired central mass weight and general characteristics in terms of stiffness, resonance frequency and damping coefficient, additional via layers (such as Via2 and Via3), thus additional metals, can be included in the central movable proof mass of the pressure sensor. This choice will change the release time during the etching of the silicon oxide during the manufacturing step, thus providing important mechanical and electrical variations with respect the ones expected from the prototype-A1. The main different TSMC prototypes with the correspondent characteristics for each and possible implementations have been already studied and tested in reference [1]. It is clear how the migration process may be performed similarly for each prototype adding proper layers or modifying accordingly the design. For the current analysed prototype-A1 the only physical layers that will contribute to the definition of the suspended mass are Metal5, Via5 and Metal6, therefore possible variations in terms of thicknesses, or integration of a different number of Vias may affect the device characteristics in an important way depending on the kind of change. During the COMSOL simulations, variations in terms of thicknesses will be discussed in future paragraphs. Vias are fundamental as vertical interconnects, they allow signals to be transmitted from one metal to another, facilitating the routing in a CMOS process and compacting complex circuit. Specifically for a CMOS-MEMS integration, vias contribute in the reduction of the parasitic resistance and capacitance, therefore enhancing the performances. Those are important also as supports for the suspended mechanical structures, providing stability and robustness to the device. The pad layers with the proper pad mark layer specified in the design tool must be included in the layout in order to underlined where the etching, thus the creation of the movable part, will occur. Particularly, the migration from TSMC to UMC was carried out trying as much as possible to leave the planar dimensions of the structure unchanged. On the contrary, the thicknesses are mainly decided by the manufacturers, but as quoted, for both the TSMC and the UMC the standard top metal thickness of $20K\AA$ has been used. During the migration, a significant variation from the first to the second technology was found in the width of the vias. In fact, since this parameter is strongly dependent on the manufacturer, it has been found out that a greater integration of vias is possible in the second technology, maintaining the width of metal6 and metal5 almost unchanged with respect to the TSMC design, especially for those placed under the metal6 and which contribute to the moving mass of the sensor. The following pictures clarify this concept, where it can be observed that the UMC design allows for a higher integration of Vias with respect the TSMC one (Figure 17, Figure 18); metal 6/metal5 are delimited by the black coloured outline.

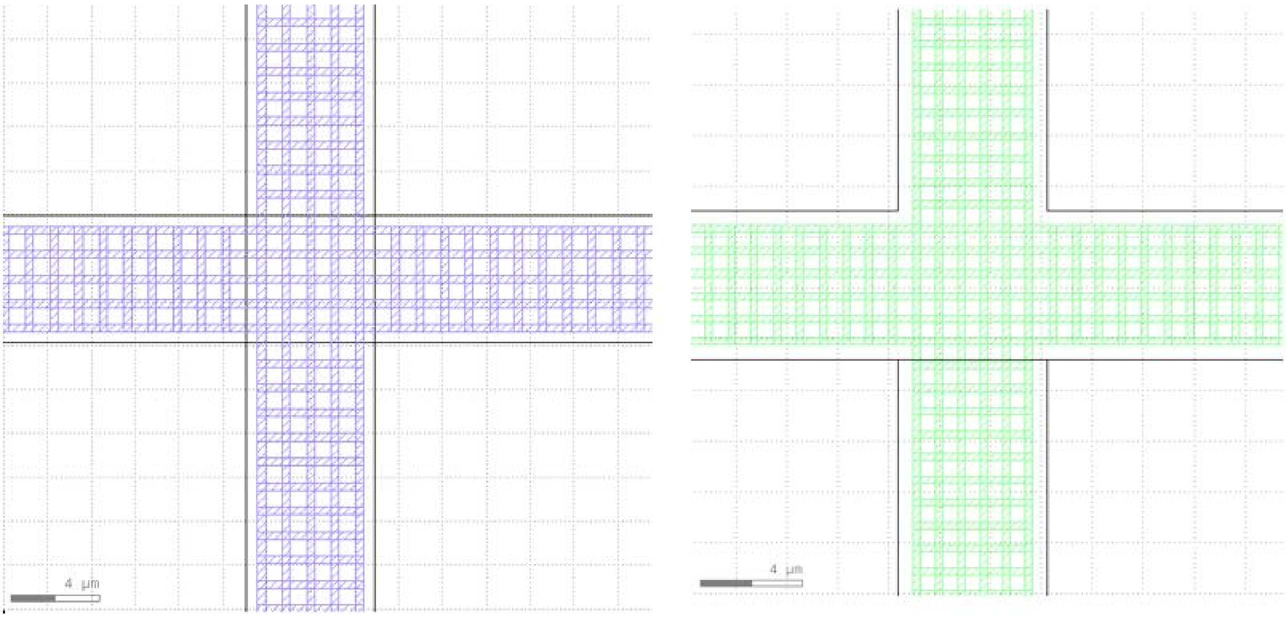

Figure 17 Top view TSMC (left) and UMC (right) Via5 and Metal6 outlined in black

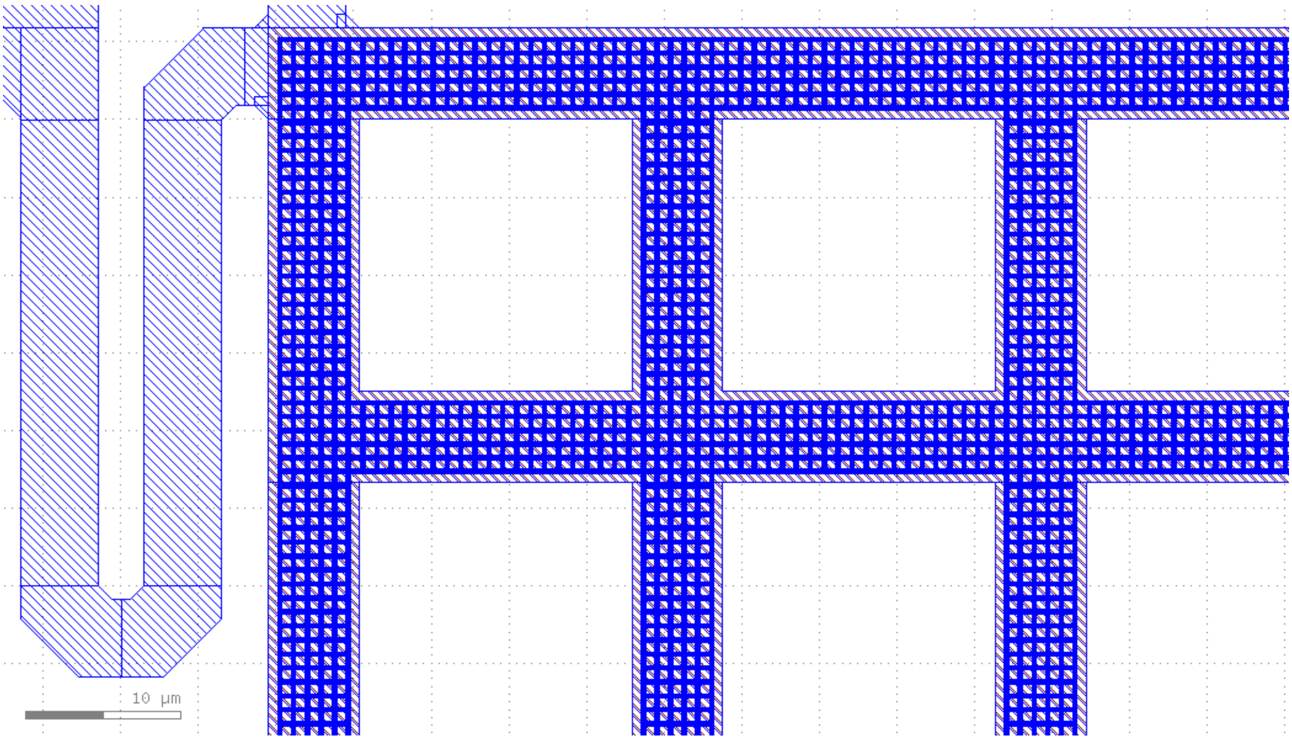

Figure 18 Top view zoomed section of the UMC central resonator. The pattern of Vias (Bright Blue) is shown in the central resonator made of Metal 6 and Metal 5 (superimposed in the central resonator block). On the left the single spring made exclusively of Metal 6 layer

Considering the general resonator structure, the length of both the Metal6 and Metal5 that contribute to the central resonator proof mass has been slightly changed from TSMC to UMC with the exclusive aim to get a more uniform integration of Via5 in the pattern and because of difference in the layout grids of the two technologies. As a consequence, the two designs overall dimensions are slightly different as visible in Figure 19, however this variation is practically negligible. This higher integration of vias does not change significantly the characteristics of the sensor, this will be demonstrated also during the simulations of the design in the following sections. However, it is likely to suppose that a better robustness can be achieved for the UMC design once fabricated.

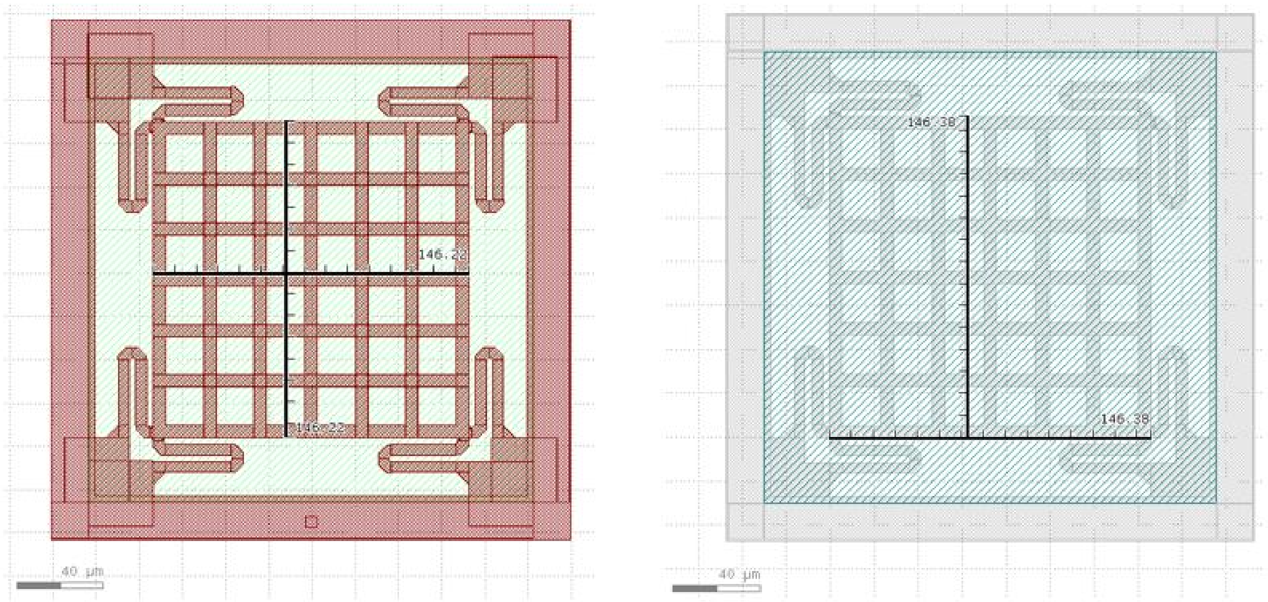

Figure 19 TSMC (left) and UMC (right) Metal6 dimensions and passivation layers

Klayout is useful to draw the design in a fast way and in a user-friendly environment, however, it may be easy to perform a DRC in Cadence Virtuoso, that is why it is of interest to import the design into this second tool. As quoted, it is important to check that the design rule layout grid exploited in both the designs are compatible with the one provided by the manufacturer itself, if not, some grid errors may be encountered during the DRC.

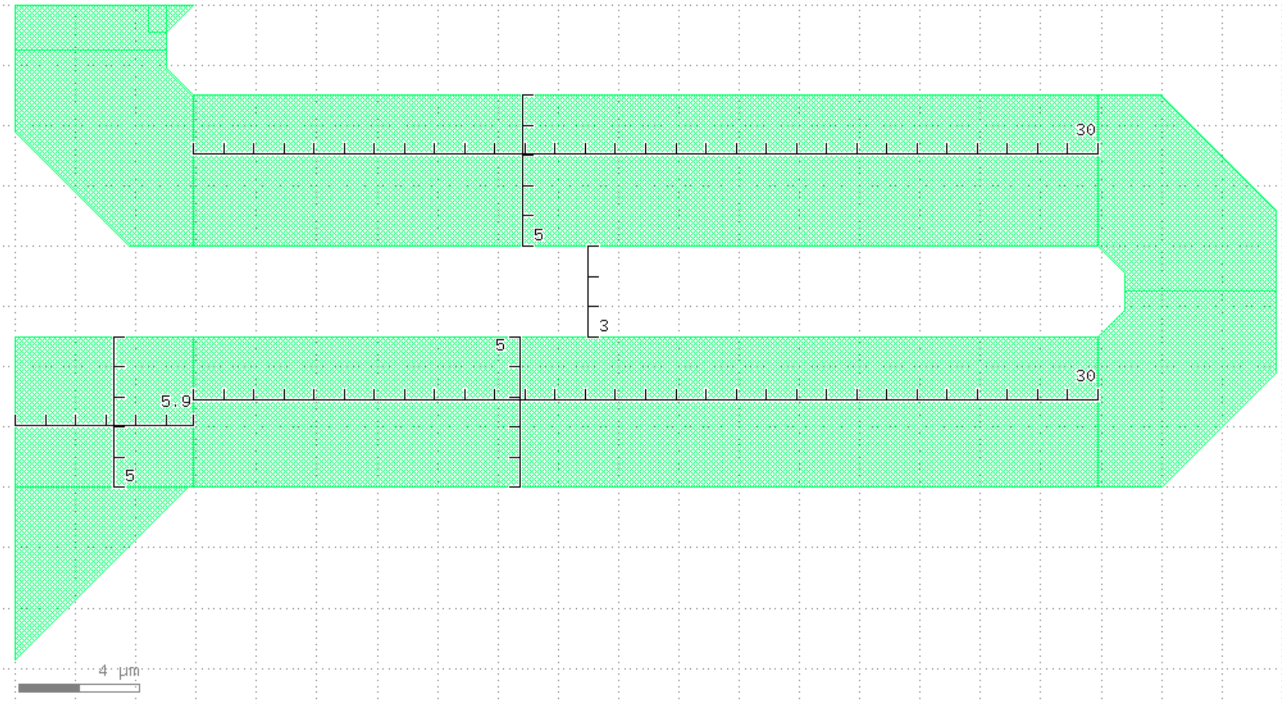

Figure 20 Single Springs dimensions TSMC-UMC

From the layout design of the Resonant Pressure sensor, it can be observed the arrangement and the dimensions of the single spring (Figure 20). These represents one of the most important components of the sensor that will define the stiffness of the entire structure, hence of the resonance frequency. The same exact dimensions have been used between the two-manufacturing process since the rules of the two were not in contrast among each other, hence giving the possibility to replicate the springs structures. In this design the springs are made with Metal 6 only.

Moreover, the same exact springs dimensions will be exploited for the prototype-A1 of the accelerometer TSMC and UMC designs, however further consideration regarding the stiffness of the structure must be analysed since the arrangement of those tends to change with respect the pressure sensor, hence a variation in terms of stiffness between the two sensors is expected. This, as well as the mass of the central resonator, will affect the resonance frequencies that characterize the two sensors leading to differences independently on the technology used.

3.2. Expected DRC errors

Once the TSMC geometry has been replicated in UMC technology, following the rules provided by the manufacturer, the Design Rule Check has been performed on the layout. Some expected errors occurred. More in detail, the main encounter errors were related to the length of the Vias. For instance, the central resonator plate of the pressure sensor must have very long vias that run across the length of the plate (see Figure 18), in order to provide stabilization to the structure. Since the manufacturer usually provide a limitation in the width of the vias, making a vias longer than this limit may be reported as an error. However, this error was expected and no direct action on the design have been taken. An additional expected error hides in missing slotting metal. When no passivation opening is provided in the layout, it may arise this error that states that the width and the length of a certain metal should be limited. Slots on the metal itself could easily solve these issues, however since those occurred for the Metal1 and Metal3, that are metal layers that belong to the bottom plate and bottom cavity seal respectively, those errors were expected and no direct action were taken on the design.

3.3. Dummy Layers

Some dummy layers have been added in the layout. Those additional layers do not represent any active circuitry or functional elements and are required for several important purposes such as protective barrier during fabrication processes, electromagnetic isolation, maintenance of uniformity among adjacent layers and preservation of planarity and flatness of the whole layout. Examples of added dummy layers are: the RF layers, which permit to the DRC to verify the functionality of the layout as an RF application circuit, hence to test correctly the associated rules; the metal blocker dummy layers (metal fill layers), which are important as alignment marks for the lithography process or to prevent irregularities in the structure, hence guaranteeing smooth surfaces or also to fill up open spaces and gaps between active metal layers uniformly distributing the metal in order to reduce stress and mechanical deformations caused by the mismatch of materials or different thermal expansions or even to inform the foundry to be aware which space not to fill. In the proposed design each six metal layers have

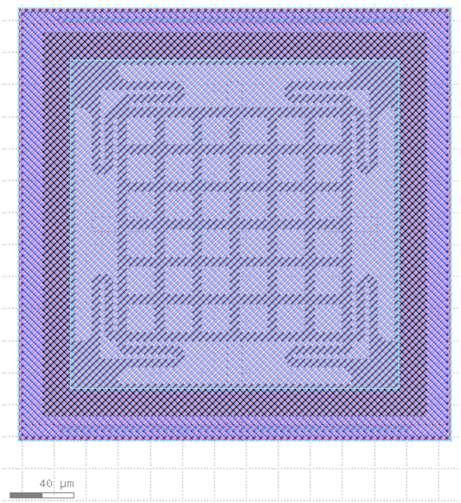

Figure 21 UMC 180nm Pressure sensor dummy layers representation: Metal dummy fill layers and PadMark (layer defined by the light blue contour that covers the resonator) above the physical layers of the sensor are showed

been characterized with additional dummy fill layers. In Figure 21 is reported the pressure sensor layout Cadence view with the superimposed dummy layers.

3.4. Hierarchy

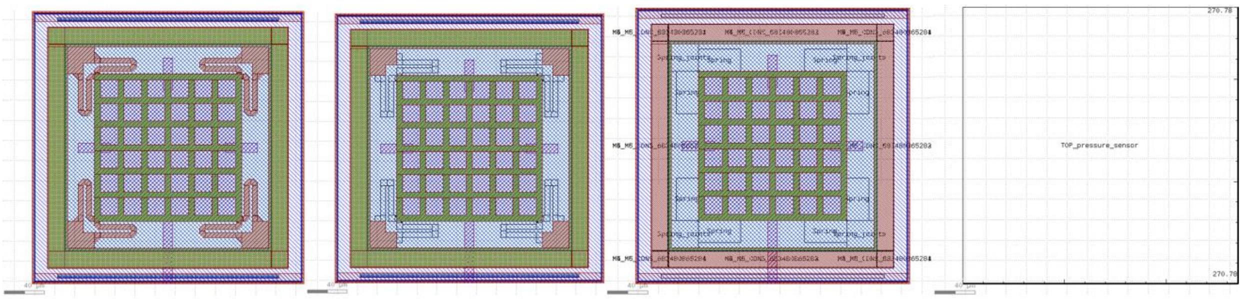

Figure 22 Klayout view Hierarchy UMC Pressure sensor 180nm design, from left to right the lowest to the highest level of hierarchy view

Despite the pressure sensor layout has been made for an easy understanding, the concept of hierarchy has been exploited during the UMC design. Indeed, hierarchy allows for a well organization of the design and it helps to navigate better in complex structures improving the clarity of them. Common blocks can be easily re-used in other different designs if the dimensions properly match, hence saving time for the creation and the verification of the layout. Additionally, single block check can be performed independently from the others giving the possibility to speed up the process of validation with DRC. For the presented UMC $180nm$ Pressure sensor layout several levels of hierarchy have been exploited; those include the springs blocks, fixed supporting blocks, vias and top view (highest level of hierarchy) which are all visible in Figure 22.

3.5. Accelerometer migration from TSMC to UMC 180nm technology

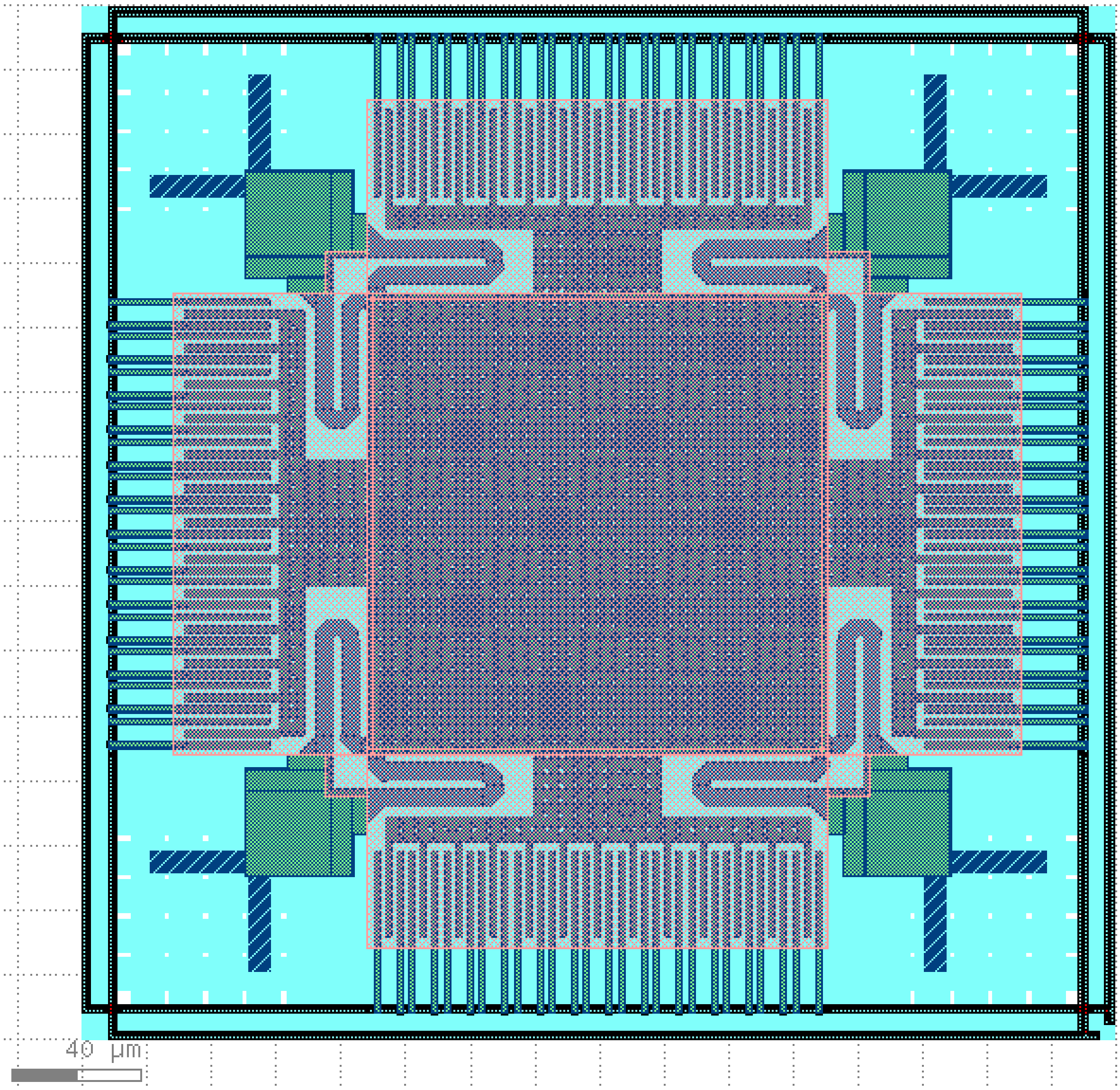

Figure 23 Klayout TOP view Accelerometer UMC 180nm layout with all its layers identified by different colours and stipples.

An identical approach exploited for the pressure sensor has been used also for the migration from TSMC to UMC $180nm$ accelerometer. The various layers have been translated and faithfully reproduced in the new technology. In particular, it is possible to observe in Figure 23 the passivation layer in pink, which covers the central resonator which includes the movable fingers on the sides. Furthermore, the metal 1 (sky blue coloured) that closes and encapsulates the sensor is characterized by slots (white slots) to comply with stringent rules (see section 3.2). The metal layer 4 that runs along the edges (in dark blue colour) represents the metal in which capacitance sensing is performed by the external circuit. In fact, knowing that the accelerometer is an interdigitated comb structure it is possible to observe in detail the bottom right part of the layout: the total differential capacity measured by the fixed electrodes on the right and left sides of the layout (looking at the top view design in Figure 23) and which are placed above with respect the movable plate, and the one measured with the fixed electrodes placed below the floating structure, go to the output via two separate tracks and through different pins related to metal 4 (Figure 24-A). Similarly, the same happens for the sensing that takes place in the fingers located on the top and bottom sides of the layout, which show further different tracks for measuring the output (Figure 24-B). The pin labelled as "*DR*" is representing the pin of Metal1.

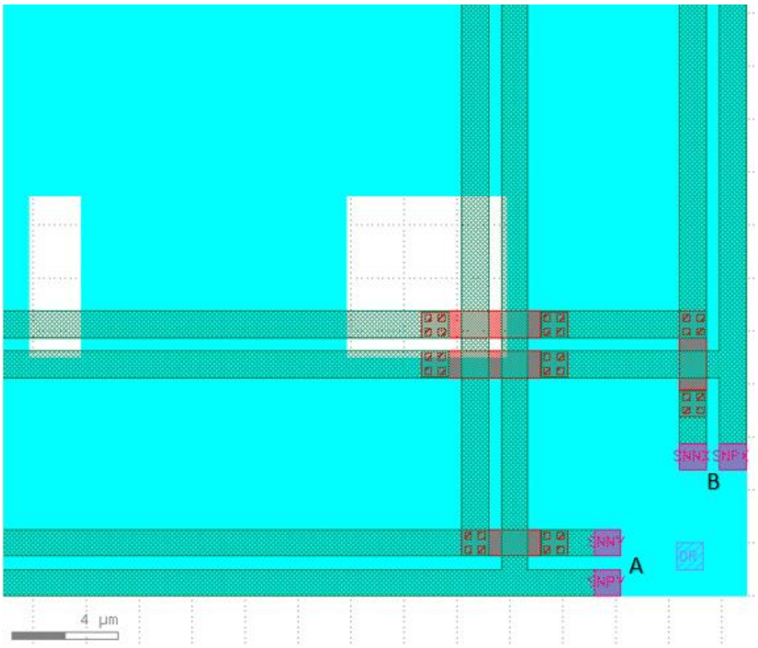

Figure 24 UMC 180nm Accelerometer layout zoomed, output sensing nodes

During the migration, the dimensions with respect the TSMC design were maintained practically unchanged, however due to different vias dimensions between the technologies, in some parts of the design it has been required to change the width of the external track of metal 4, thus adjusting metal 3 accordingly. This change in width metal is not expected to variates significantly the overall characteristics of the sensor.

In conclusion, both the designs have been migrated from TSMC to UMC without huge differences in terms of dimensions. UMC design rules are generally more stringent with respect the ones of the original technology, however, with the proper adjustment in term of spacing these can be easily overcome. The DRC's of both the pressure sensor and the accelerometer made in UMC have been checked with successful results presenting exclusively expected errors, such as the limitation on the length of the Vias, something to be managed directly with the manufacturer. At a theoretical prospect the design layout works, however from the simple design is not straight forward that the MEMS will behave exactly as expected, that is the reason why some numerical simulations must be performed, or by the exploitation of an equivalent model of the sensor made in Verilog A or by Multiphysics FEM simulations. The next sections of the document analyse the behaviour of the sensors under realistic conditions and scenarios.

4. Pressure sensor 180nm TSMC COMSOL Multiphysics characterization

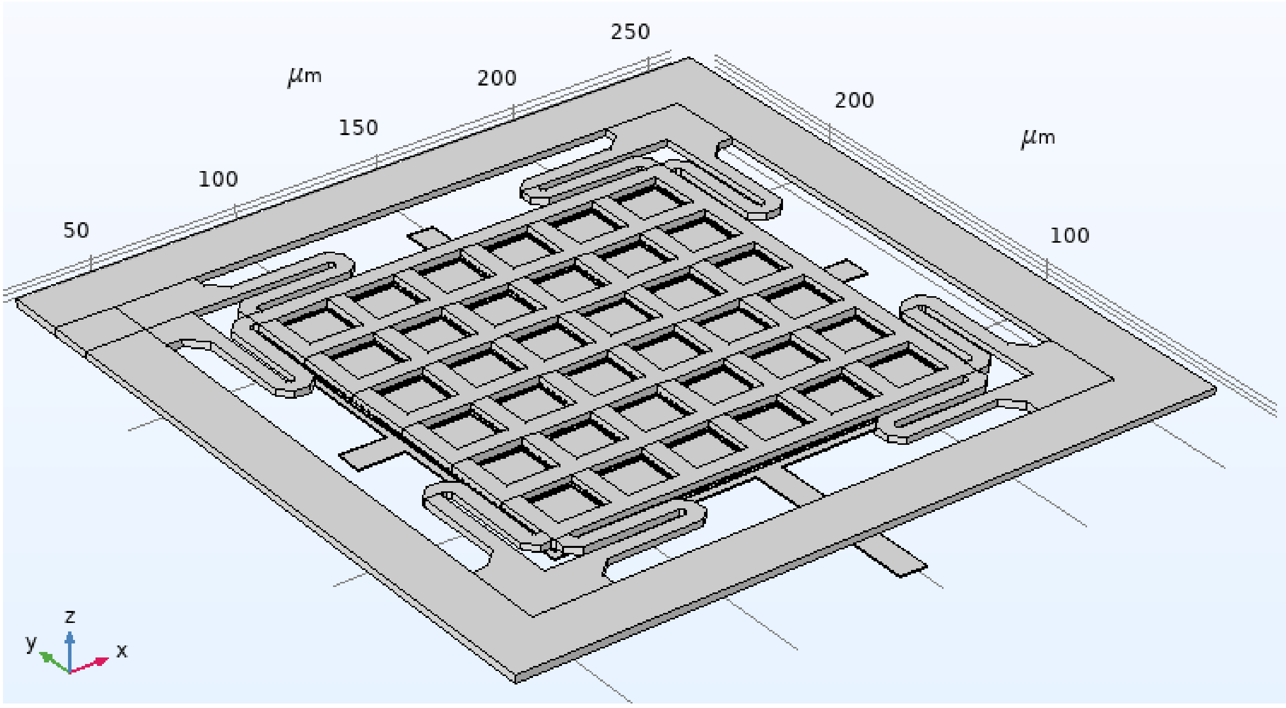

Figure 25 COMSOL view entire 3D structure recreated resonant capacitive pressure sensor

Simulations of sensors represent a pivotal role on a design, allowing to predict the behaviour of the sensor under various conditions depending on several factors such as materials, external stresses, dimensions and geometric composition of the layers used. The COMSOL Multiphysics tool provides the possibility to easily build the desired geometry in all its characteristics and dimensions (Figure 25 shows COMSOL *Graphic window* of the entire pressure sensor) and to specify the quoted features and even more in a very user-friendly environment also giving the chance to use different mathematical methods and FEM computations[4]; it is a very powerful tool to simulate any kind of structure if the proper boundary conditions are well defined. Particularly, in this section greater prominence will be given to the mechanical properties of the sensors, hence the resonance frequency and its importance in the definition of the stiffness that characterizes the structure (or vice-versa) will be analysed in different scenarios. If not underlined differently, all the simulations carried out in the following paragraphs characterize the TSMC version of the $180nm$ sensors. Two main designs regarding the pressure sensor have been carried out, these will be referred as the pre-fabrication and the post-fabrication case of study. The following simulations analyse the already fabricated pressure sensor (post-fabrication case) based on the work of Diana Mata-Hernandez, Daniel Fernández, Saoni Banerji and Jordi Madrenas

[4] Numerical methods dedicated to solve partial differential equations in two or three space variables subdividing a large system into smaller and simpler parts called finite elements.

[1], which currently does not present any characterization made with COMSOL. However, to start with, the theoretical (ideal) pressure sensor structure in terms of expected dimensions and characteristics (pre-fabrication case) will be discussed; the differences found between the pre and post case of the pressure sensor have made possible to suppose an ideal, constant variation introduced by the manufacturing process which can also be applied to the accelerometer itself, which has not been released at the moment, thus this hypothetical approach may be of interest for further sensors fabrication. Regarding the pressure sensor, the stiffness of the structure, the mass of the central resonator, the resonance frequency and other parameters are reported in Ref. [1]. At first, the two designs of the resonant capacitive pressure sensor have been faithfully recreated in COMSOL in all their dimensions, where both the characteristics of the pre-fabrication version and the post-fabrication version have been analysed willing to foresee what could have been the reasons in terms of thickness and mass variations of the central resonator from the theoretical pre-fabricated case to the actual real post-fabricated device. In order to simplify the analysis, the composite layered central resonator structure has been studied separately in terms of mechanical properties and it has been used in both the cases. From the experimental results obtained from the study made by Hernandez et. Al. [1], the $180nm$ TSMC sensor has shown the following common parameters in the structural design:

Table 1 Parameters 180nm TSMC capacitive resonant pressure sensor prototype-A1 post-fabrication [1]

$W = 146.22um$	Width central resonator plate
$L = 146.22um$	Length central resonator plate
$L_h = 17.56um$	Perforation length
$s = 5.86um$	Spacing between perforations
$h_0 = 2.23um$	Air gap
$T_p = 3.38um$	Thickness central plate resonator
$m = 1.53x10^{-10}kg$	Mass central plate resonator
$Q = 87.65$	Quality factor
$f_r = 135kHz$	Resonance frequency
$b = 1.48x10^{-6}\ Ns/m$	Damping coefficient
$k = 110.08\ N/m$	Stiffness constant

As a matter of fact, the pre-fabricated (theoretical) dimensions of this structure differ mainly for the thickness of the central plate resonator:

Table 2 Parameters 180nm TSMC capacitive resonant pressure sensor prototype-A1 pre-fabrication [1]

$W = 146.22um$	Width central resonator plate
$L = 146.22um$	Length central resonator plate
$L_h = 17.56um$	Perforation length
$s = 5.86um$	Spacing between perforations
$h_0 = 2.23um$	Air gap
$T_p = 3.87um$	Thickness central plate resonator

With an undefined mass of the central resonator. The variation in the thickness of the central resonating part of the pressure sensor may acquire because of several reason during the fabrication step; this parameter it is the one most of interest since it affects directly the volume, hence the density of the central resonator and all the parameters that derive from it such as the resonance frequency itself and it will be the main parameter to evaluate the variations introduced by the fabrication process. In fact, the theoretical thickness of the metals and vias are of $0.53um$ for Metal5, $1um$ for the Vias5 and $2.34um$ for the TOP Metal6, which are respectively the layers that compose the central plate resonator and which shows in fact a total thickness of $3.87um$. An exploded view of the central plate composition has been reported in Figure 26.

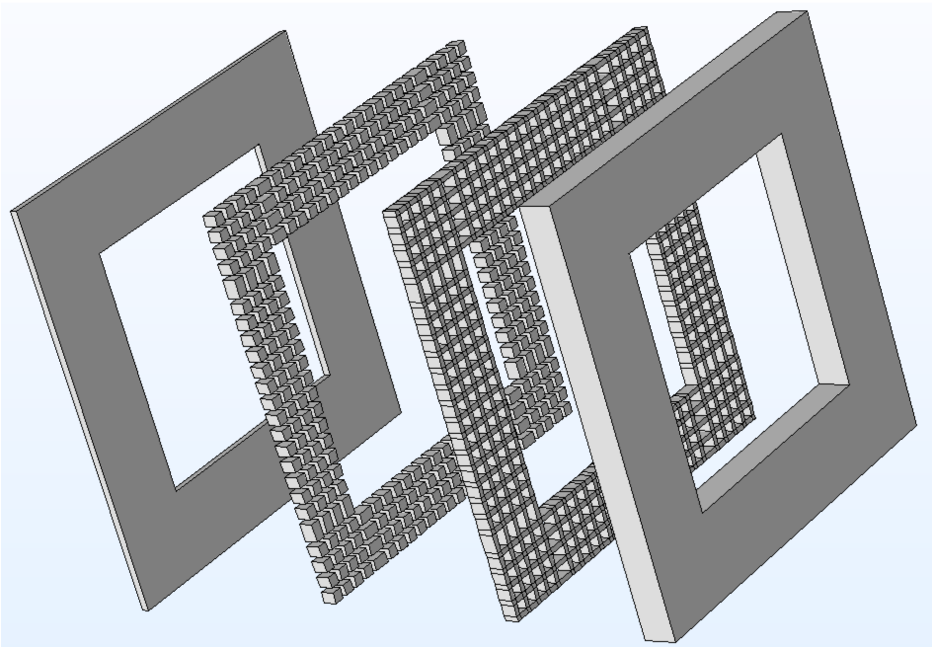

Figure 26 Exploded view Central Resonator Pressure sensor TSMC 180nm section. From left to right: Metal5-Dielectric/Via5-Metal6 with the correct thickness required by the technology

Moreover, the mechanical properties such as Young's modulus, Poisson's ratio, mass and density, and also the electrical properties such as permittivity of the parts composing the pressure sensor, have been analysed in detail and they have been distinguished between the pre and the post fabrication case. Therefore, in order to emulate this variation contributions a detailed simulation on the geometry has been carried out starting from the central resonant plate diaphragm only.

4.1. Pressure sensor Central Resonator TSMC characterization

As a first step, a simplification on the central resonant structure has been performed. In fact, the central composite resonant plate, exploiting CMOS technology, is made sequentially by Metal5-Vias5-Metal6, were Aluminium (Al) and Tungsten (W) are the materials used for the metal and the vias respectively. Since with this total layered structure the computational effort performed by COMSOL resulted to be huge, due to the presence of many patterned vias and blocks of dielectrics present between the two metal layers, a separate characterization of the theoretical resonant central part with respect the total pressure sensor has been performed. The principal aim of this simulation is to extract a unique value for each of the most important parameters (Young's modulus E, Poisson's ratio v, relative permittivity ε, density ρ and electrical conductivity σ) of the central structure, thus to create a single homogeneous layer that would englobe all the parameters and characteristics of each single layer of the composite structure. This choice allows for a faster computation time and a diverging solution once applied the boundary conditions to the total sensor. Therefore, once extrapolated these values during the separate analysis of the central resonator, these will be substituted in a homogeneous block in the entire structure in order to provide a faster computation. Indeed, despite this simplification may lead to a slightly different geometry characterization in terms of volume of the central plate with respect the actual one, the computational effort results to be definitely less heavy. Furthermore, using COMSOL it must be taken into account that it is possible to rely on the simulated results only if a proper mesh is defined both in the separate characterization of the composite central resonant part and the total structure made of a homogeneous central resonant part. It is important to be aware about the fact that the difference between the simplified (homogeneous) and total structure (composite) of the central resonator relies mainly on the variation among the volumes of those, this as a consequence of choosing a single homogeneous block: in fact, the total structure does not include in the volume the spaces present next to the outermost vias, which indeed are represented by air as a consequence of the etching procedure; on the contrary, the simplified version includes this spaces in its geometry due to the intrinsic simplification as a single block layer. The Figure 27, Figure 28 and Figure 29 clarify these concepts.

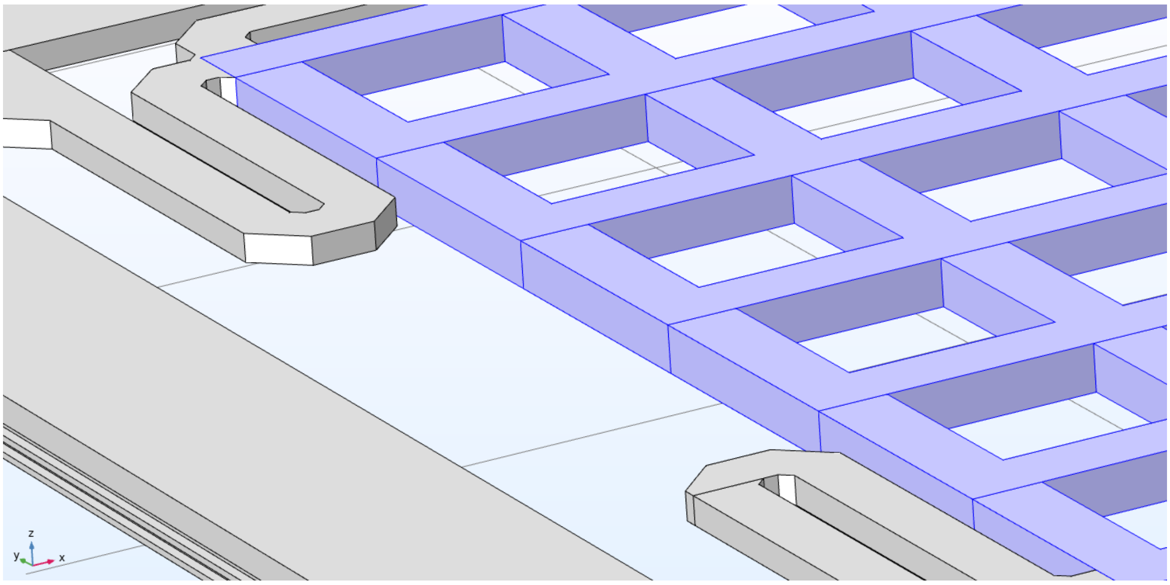

Figure 27 Homogeneous central resonant plate of the pressure sensor (in blue) zoomed and mounted on the entire pressure sensor (in grey).

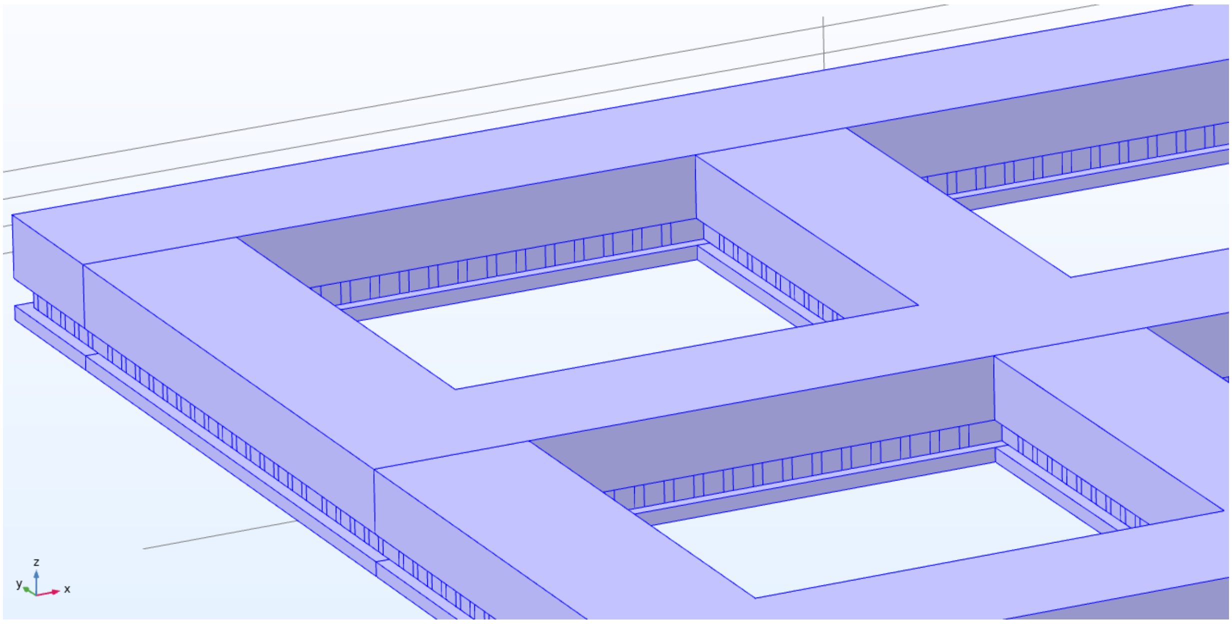

Figure 28 Composite central resonant plate of the pressure sensor zoomed and separated from the rest of the structure. The outer vias pattern and the air spaces (non-physical volume) nearby those are visible.

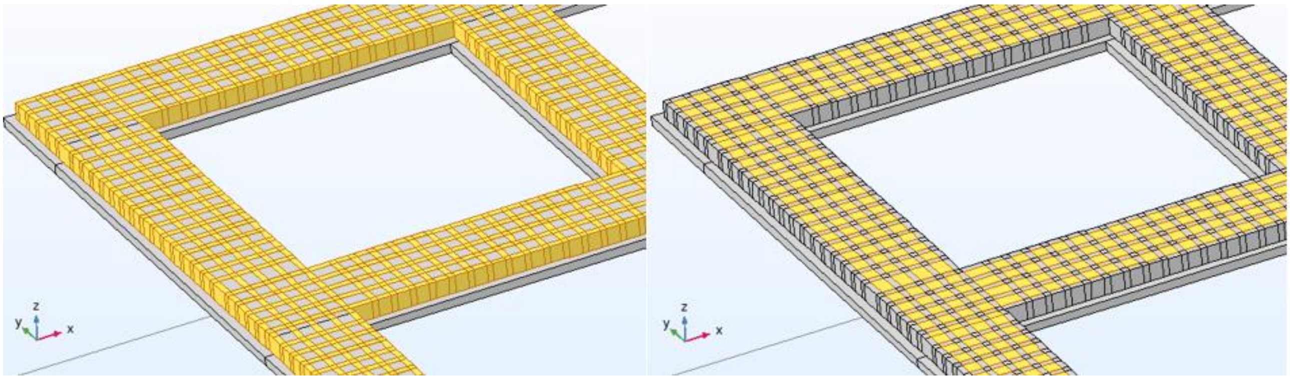

Figure 29 Composite central resonant plate of the pressure sensor zoomed with metal 6 layer hidden. In yellow are represented the vias and the filling dielectric domains respectively on the left and the right representations.

Specifically, Figure 27 reports the homogeneous central resonant plate with the same mechanical property of the composite one "mounted" on the total structure. On the contrary, Figure 28 reports the composite (M5-Vias5+SiO_2-M6) central resonant plate were clearly no volume nearby the most external vias is present. Nevertheless, the density of the two is the same, therefore a very small variation on the resonance frequency with respect the one that is obtained from the simulation should be taken into account due to this simplification, mainly due to the effect of damping acting on the perforated structure. In order to clarify the layered structure, Figure 29 highlights the difference between the vias and the dielectric layers. Once created the structure in COMSOL with the proper thickness and dimensions and elevations, this have been simulated according to different possible choices of simulation. The following statements describe not only the most important quoted characteristics of the sensors and the central resonator, but also the methodologies and the steps that have been used in COMSOL in order to obtain that specific result. It is possible that in some sections more space will be given to the COMSOL 5.5 implementation, from the model chosen to the boundary conditions, the physics and model used for a specific simulation. Since the COMSOL implementation is not the main topic of this work, for any more detailed information please refer to the Reference Manual [13, 14] or User Guide of the specific quoted module.

Analysing the composite plate, the proper materials for each layer were set, hence each characterized by their own density, Young's modulus and Poisson's ratio which are already defined in COMSOL by default depending on the specified material. The correspondent total volume and mass resulted to be the following:

$$Volume_{composite} = 38170.0\ um^3 = \ 3.817\ 10^{-14}\ m^3 \tag{18}$$

$$mass_{composite} = 1.824\ 10^{-10}\ kg \tag{19}$$

Once defined the proper boundary conditions, a *Solid Mechanics* Physic simulation has been run in COMSOL exploiting an *iterative* method in order to find the mechanical properties of the entire geometry. The following parameters were extrapolated:

$$Density_{composite} = \rho_{composite} = \frac{m}{V} = \frac{1.824088112 * 10^{-10} kg}{3.817 * 10^{-14}\, m^3} = 4778.85\ kg/m^3$$

(20)

$$E_{composite} = \frac{0.0043361\, J * m^3}{3.817 * 10^{-14}\, m^3} = 113.59\ GPa$$

(21)

$$v_{composite} = \frac{1.1742 * 10^{-14}\, m^3}{3.817 * 10^{-14} m^3} = 0.308$$

(22)

Particularly, the values at the numerator of the Young's modulus (E) and Poisson's ratio (v) have been obtained in COMSOL under the *results* section performing a *global evaluation* and, more specifically, a *volume integration.* Therefore, their values are obtained integrating the volume of the composite structure and indeed they are reported in m^3, that is the reason why, in order to obtain the correct parameters, they must be divided by the volume of the structure itself. It must be underlined that the volume used for this calculation is exclusively the one of the composite geometry and not the homogeneous one. The composite one is indeed the most faithful to use for the most reliable depiction of the ideal, pre-fabricated central resonant plate diaphragm since it will be used for all the future simulations of the pre and post fabrication pressure sensor.

Regarding the electrical parameters, the *Electrostatic* physic interface in COMSOL allows to determine the electrical conductivity and the relative permittivity (dielectric constant), which is the property that characterizes the ability of the material to store electrical energy in an electric field w.r.t the vacuum. Metals like tungsten do not have a well-defined relative permittivity, in fact they have relatively high electrical conductivity, but low relative permittivity, hence they are likely to be considered as electrically conducting materials rather than dielectrics. Therefore, since the dielectric constant of the tungsten is likely to be very close with respect to the one of vacuum or air, a value of 1 has been used for the simulation. The respective standard relative permittivity of SiO_2 and Aluminium has been exploited in the simulation. The overall dielectric constant ε (hence normalized w.r.t. vacuum) for the composite central resonator resulted to be equal to:

$$\varepsilon_{composite} = \frac{1.4175 * 10^{-13} m^3}{3.817 * 10^{-14} m^3} = 3.714$$

(23)

To ease the simulating process even more, isotropic values of permittivity has been considered, however a permittivity matrix can be obtained from COMSOL, thus it can be substitute in the material properties for the characterization of the homogeneous layer in the overall pressure structure. Similarly, the value of the electrical conductivity σ that characterize the central resonator of the pressure sensor has been found performing an *average* evaluation among the whole geometry with the exploitable formula "*material.def.sigma_iso*", which in COMSOL defines the isotropic value of the electrical conductivity. The correspondent value resulted to be equal to:

$$\sigma_{composite\ avarage} = 3.170 * 10^{7} S/m$$

(24)

While the maximum value of the electrical conductivity is the one corresponding to aluminium, hence equal to:

$$\sigma_{composite\ max} = 3.774 * 10^{7} S/m$$

(25)

Also in this case, for a more precise computation, the anisotropic values could be found. The obtained mechanical and electrical parameters, allow the definition of the new homogeneous material that can now be mounted in the general geometry of the resonant capacitive pressure sensor as the central perforated plate, hence hugely facilitating the computational process for all the following simulations.

Leaving unchanged the dimensions in terms of length, thickness, width and spacing with respect the composite one, the volume and the mass of the homogeneous central structure with original theoretical thickness results to be respectively equal to:

$$Volume_{homogeneous} = 3.975 * 10^{-14}\ m^{3}$$

(26)

$$mass_{homogeneous} = 1.8995 * 10^{-10} kg$$

(27)

Thus, they are clearly higher with respect the composite ones (equations (18), (19)), due to the inclusion of air space as a part of the volume of the geometry. As quoted, this slight variation of volume for the actual simulated total pressure sensor structure may provide a resonance frequency not exactly equal to the correct expected one, however, this effect has been ignored relying on the fact that the real part of the resonance frequency should be scaled of a factor that is extremely close to 1, or, in other words, the correspondent resonance frequencies difference is close to 0:

$$Scaling\ factor = \frac{\frac{1}{2\pi}\sqrt{\frac{k_2}{m_2}}}{\frac{1}{2\pi}\sqrt{\frac{k_1}{m_1}}} = \sqrt{\left(\frac{k_2}{k_1}\frac{m_1}{m_2}\right)} \cong 1$$

(28)

Where m_1 and k_1 are the mass and the stiffness of the composite central resonator and m_2 and k_2 are the mass and the stiffness of the homogeneous that includes the air gaps as if they belong to the single block.

4.2. Simulation on the theoretical Pre-Fabricated Capacitive Resonant Pressure sensor 180nm TSMC

The first simulation performed in order to detect the resonance frequency, the quality factor, the capacitance and the pull-in voltage of the geometry has been done for the most ideal theoretical structure. This case represents the pressure sensor if no variations would have been introduced by the fabrication process in terms of thickness or other kind of contributions, such as temperature dependency. In particular, the dimensions of the Top Metal 6 and the central resonator have been set respectively to be equal to $h_{springs} = 2.34um$ and $h_{central\ res} = 3.87um$, which are the theoretical original values.

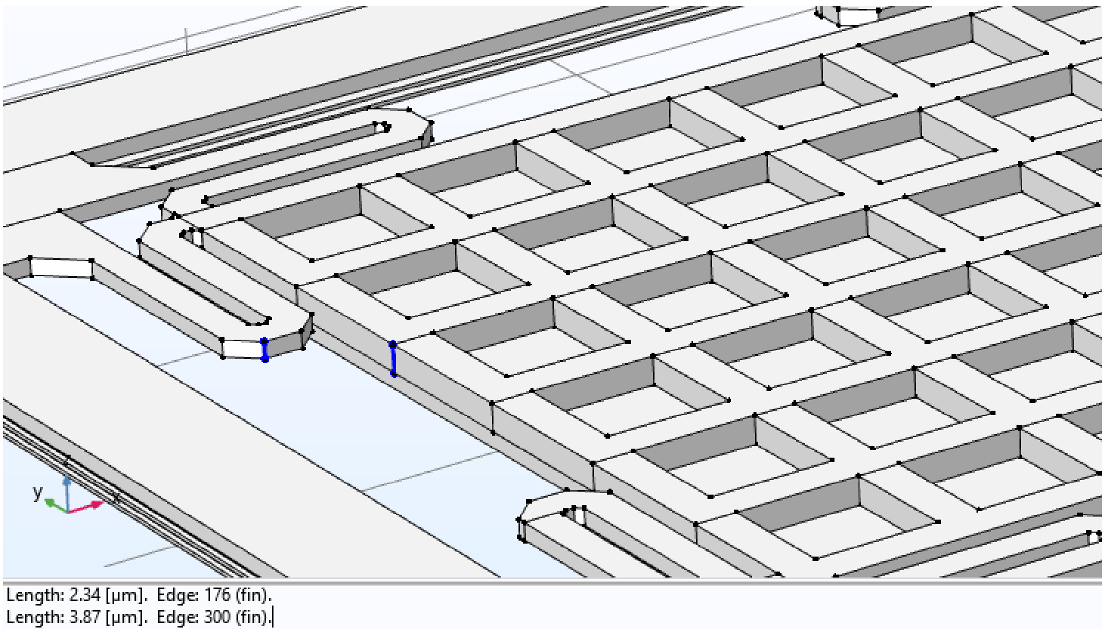

Figure 30 pre-fabrication Pressure sensor dimensions built in COMSOL 5.5

<u>*-Step 1*</u>

As a first step the geometry must be defined in COMSOL in all its parts, springs, external fixed metal layer, external fixed vias, bottom fixed electrode (represented by the Metal3 in the CMOS process) with the correct theoretical values of dimensions and proper thicknesses and elevations in order to define the exact structure as it would be integrated during an ideal CMOS fabrication process (see Figure 30). For the central resonator, the mechanical and electrical parameters found in section 4.1 were substituted in the single homogeneous structure. The most important parameters of the pre-fabricated pressure sensor are then:

$$h_{springs} = 2.34\ um\ (theoretical) \tag{29}$$

$$h_{central\ res} = 3.87\ um\ (theoretical) \tag{30}$$

$$mass_{central\ res\ composite} = 1.824 * 10^{-10}\ kg \tag{31}$$

$$mass_{central\ res\ homogeneous} = 1.8995 * 10^{-10}\ kg \tag{32}$$

$$volume_{central\ res\ composite} = 3.817 * 10^{-14} m^3 \tag{33}$$

$$volume_{central\ res\ homogeneous} = 3.9747 * 10^{-14} m^3 \tag{34}$$

$$Density_{central\ res} = 4778.85\ kg/m\hat{}3 \tag{35}$$

$$E_{central\ res} = 113.59\ GPa \tag{36}$$

$$v = 0.308 \tag{37}$$

$$\varepsilon = 3.714 \tag{38}$$

Coherently with the previous analysis carried out on the central resonator.

-Step 2

Consequently, the proper boundary conditions must be defined. Since most of the interest is in the detection of the resonance frequency of the structure a first *Solid Mechanics physic interface* has been defined in COMSOL. The contours representing the fixed structure that supports the central perforated plate have been defined as "*fixed constraint*" in the *Solid Mechanics physics* and no prescribed displacement has been applied to the central movable parts in order to simulate the most real case of free movement of the proof mass. As a first general approach, Rayleigh damping has been included by defining two material constants $alpha$ and $beta$ under the *Linear Elastic Material* section of the *Solid Mechanics physics interface.*

Indeed, in COMSOL, there are different approaches to model damping in the solid mechanics of a parallel plate structure. The two common methods are:

- Thin Film Damping Node, which is a method that represents the energy dissipation in the structure due to internal damping mechanisms. This method provides a simple and efficient way to account for damping effects and it requires specifying the damping coefficient, which specifically determines the amount of energy dissipated per unit time. This approach is generally suitable for cases where the damping mechanism is not explicitly known or when detailed damping models are not required.
- Damping Based on Rayleigh Parameters, which is a method that involves incorporating damping into the model using Rayleigh damping parameters, namely $alpha$ and $beta$. This second method is a phenomenological damping model that combines mass damping and stiffness damping. The values of the parameters alpha and beta can be derived from experimental data or analytical models, and they represent the ratio of the damping forces to the mass and stiffness forces, respectively. Generally speaking, this second approach is suitable when the specific damping mechanism is known and when more accurate and detailed damping modelling is required.

Due to the know conditions and characteristics of the sensor [1], the second method can be used in order to characterize the structure, hence to be able to define the quality factor of it and to apply similar damping to analog geometries. For instance, for a mass spring damper system with a single degree of freedom the equation of motion with viscous damping is equal to:

$$m\frac{d^2u}{dt^2} + c\frac{du}{dt} + ku = f(t)$$

(39)

Where c is the total damping coefficient, k is the stiffness, m is the mass, u is the displacement, t is the time and $f(t)$ is the driving force. Now, in literature the parameter $alpha$ and $beta$ are not always available, that is why a relation between the damping factors and the Rayleigh damping parameters help to define these contributions. In particular, more details are reported in the "Frequency Response of a Biased Resonator" COMSOL tutorial [15, 16], in which the relation between $alpha$, $beta$ and the damping factor is provided at two different frequencies:

$$\begin{bmatrix} \frac{1}{4pif_1} & pif_1 \\ \frac{1}{4pif_2} & pif_2 \end{bmatrix} \begin{bmatrix} \alpha \\ \beta \end{bmatrix} = \begin{bmatrix} \xi_1 \\ \xi_2 \end{bmatrix}$$

(40)

Where ξ_1 and ξ_2 are the two damping factors.

For this particular case, knowing that the approximated quality factor of the pressure sensor obtained by the experimental results is equal to 87.65 and knowing that the approximated resonance frequency f_0 which is characterizing this pre-fabricated structure is around $148kHz$ (computed performing a first simulation with no damping applied), it is possible to estimate the $alpha$ and the $beta$ coefficients:

$$\alpha = 4 * \mathrm{pi} * \frac{\mathrm{f_0}}{3 * \mathrm{Q}} = 7072.9Hz$$

(41)

$$\beta = \frac{1}{6 * \mathrm{pi} * \mathrm{f_0} * \mathrm{Q}} = 4.0896 * 10^{-9}s$$

(42)

Hence, these values will be exploited for the further considerations on this structure. However, an iterative process always more precise may be implemented simply by performing more simulations and finding the actual resonance frequency that characterizes this theoretical case, so the actual quality factor, until stable $alpha$ and $beta$ values are found. Overall, this chosen first values does not provide deeply different results with respect the iterative conservative procedure.

-Step 3

At this point a *Stationary study* can be run for this first case, in order to obtain only the mechanical behaviour of the structure in terms of correct resonance frequency, quality factor and damping coefficient. The correspondent values can be achieved:

$$f_r = 147.16\ kHz$$

(43)

$$Q = 88.46$$

(44)

$$b = \frac{2\,\pi\, mass_{central\ res\ homogeneous}\, f_r}{Q} = 1.985 * 10^{-6} \frac{Ns}{m}$$

(45)

Where the damping coefficient b has been computed with the mass of the homogeneous layer, thus in order to be coherent with the obtained resonance frequency. It is clear, that the damping coefficient value is absolutely coherent with the Bao model study on the central resonator that will be analysed in the successive steps (see section 4.4).

-Step 4

At this point an *Electrostatics interface* is added to the simulation. In particular, since the pressure sensor must work in air, specifically at atmospheric pressures, air must be added to the structure as a single block, or as multiple filling blocks to the general geometry. With the use of the *Electrostatics* and the *Solid Mechanics*, the *Electromechanics Multiphysics* interface is automatically defined by COMSOL, which includes the fundamental equations of both the single physics and also the eventual coupling conditions between the two. In this case an important condition of the tool for a correct simulation, is to define a *Deforming Domain* and a *Moving Mesh*[5] constraints (see *Deforming Domain vs Moving Mesh* in the COMSOL 5.5 Reference Manual) specifying all the domains that will be affected by a possible change in mesh, so affected by deformation. This is a pivotal condition if the aim is to simulate the capacitive pressure sensor actuated by an electrostatic force and/or an external stimulus such as pressure and to see the resultant displacement or value of capacitance that arises between two electrodes of the sensor. Indeed, when an electric field is applied to the electrodes of the sensor, it creates an electrostatic force that causes the sensor to deform. This deformation changes the capacitance that arises in the sensor, which can be measured and used to determine the pressure applied to the sensor as well. However, to achieve this purpose the *Deforming domain* must represent faithfully the shape of the sensor, since it allows the geometry to change shape in response to mechanical or electrostatic force and, when defined, also thermal stresses applied to the sensor, hence leading the possibility to properly predict how the capacitance of the sensor will change as a result of deformation under different pressure and voltage conditions. Moreover, in order to prevent electrical interference and unwanted coupling among different part of the system, the walls of the air blocks must be defined in COMSOL as *non-conductive*, so that no current can flow through them. In order to define this air boundaries as "electrically insulated" a

[5] Features added under Moving Mesh control the spatial frame. They can be used to study both stationary states and time-dependent deformations where the geometry changes its shape due to motion of solid boundaries and deformation of solid domains. The same feature types are also available as Deformed Geometry Features, but there they control the material frame instead. A Deforming Domain feature can be used for fluid domain deformations in fluid-structure interaction (FSI) or electrostatic domain deformations (Electromechanics) in MEMS. The shape of the domain is then governed by the deformation or motion of its boundaries. Other features can specify that parts of the model rotate or that tend to deform.

relative permittivity of 1 is exploited for the definition of the characterizing material, which means that the material does not affect the electric field passing through it, and it does not store any electric charge when an electric field is applied. These are also called non-polar or non-polarizable materials. On the actual real case, air results to be a mixture of gases, like nitrogen (N_2) and oxygen (O_2), which are both nonpolar molecules, but there can be small amounts of polar molecules such as carbon dioxide (CO_2) and water vapor (H_2O) so that air can actually contain some polar molecules. Once, these blocks of air has been defined, these must be excluded from the *Solid Mechanics physic,* otherwise COMSOL will ask for the mechanical properties of this, such as Young's modulus and Poisson's ratio. Now, an additional *charge conservation* must also be added to represent the non-solid air domains, the bottom fixed electrode represented by Metal3 has been defined as the terminal with a specified Bias potential, while the central resonator has been defined instead as ground. The application of a potential difference among two electrodes (central resonator and Metal 3) creates an electrostatic force that bends the grounded beam toward the plane beneath it. The electrostatic field in the air and in the beam is governed by Poisson's equation:

$$-\boldsymbol{\nabla}(\boldsymbol{\varepsilon}\boldsymbol{\nabla}\boldsymbol{V}) = \boldsymbol{0}$$

(46)

where the derivatives are with respect to the spatial coordinates.

It is of interest to know that in COMSOL four frames always exist, with their own separate coordinate names:

- The spatial frame coordinates are by default x, y, z, or r, phi, z in an axisymmetric geometry.

- The material frame coordinates are by default X, Y, Z, or R, PHI, Z in an axisymmetric geometry, which is a coordinate system that identifies material points by their spatial coordinates.

- The geometry frame coordinates are by default Xg, Yg, Zg, or Rg, PHIg, Zg in an axisymmetric geometry, and is a coordinate system that identifies points by their spatial coordinates.

- The mesh frame coordinates are by default Xm, Ym, Zm or Rm, PHIm, Zm in an axisymmetric geometry and is a coordinate system used by the finite element method which identifies mesh points by their spatial coordinates (Xm, Ym, Zm) at the time the mesh was created.

In the proposed case, the numerical model represents the electric potential and its derivatives on a mesh which is moving with respect to the spatial frame. Then the fundamental transformations are carried out by the *Electromechanics Multiphysics* interface, which also contains smoothing equations governing the movement of the mesh in the air domain. The material coordinates and mesh coordinates are exactly the same in order to make the coordinate system to follow and deform with the material. Now, positive feedback between the electrostatic forces and the deformation of the movable plate is created: the gap among the plates is reduced because of the presence of forces and consequently this higher attraction increases the forces. At a certain voltage the electrostatic forces overcome the stress forces and the system becomes unstable making the entire structure to collapse: the Pull-in voltage has been reached. An important aspect is to observe that in COMSOL, for applied voltage higher with respect the pull-in one the solution may not converge since no stationary solution exist, therefore a FEM analysis must be performed. On the contrary, exactly before pull-in voltage, the movable plate is maintained in equilibrium, hence the electrostatics forces balance the stress ones. A general exploitable formula for an estimation of the pull-in voltage in parallel plate geometries is represented by the one proposed by Ville Kaajakari [6], which states that:

$$V_{pull-in} = \sqrt{\frac{\frac{8}{27}(kd^3)}{\varepsilon A_{central\ res}}}$$

(47)

Where k is the spring stiffness, d is air gap among the movable and the fixed plate, ε is the relative permittivity of the material composing the gap (air) multiplied by the void relative permittivity, $A_{central\ res}$ is the sensing capacitive area. However, this formula does not include the non-linearities present in the geometry that COMSOL instead takes into account. In fact, knowing that, for this pre-fabricated case the $k = 162\ N/m$ (see "Comments on the spring Stiffness" successive section), $A_{central\ res} = (146.22um)^2 - (6 * 6 * (17.56\ um)^2) = 10279.558\ \mathrm{um}^2$, $d = 2.23um$ the pull-in is expected to be around $76.5V$ using the quoted formula (47). However, as a first result obtained from the *Electromechanics* COMSOL simulation it is possible to obtain the behaviour of the capacitance for a Bias voltage sweep applied to the fixed electrode, which clearly confirm that the pull-in of the sensor occurs around $80V$ as clear from Figure 31.

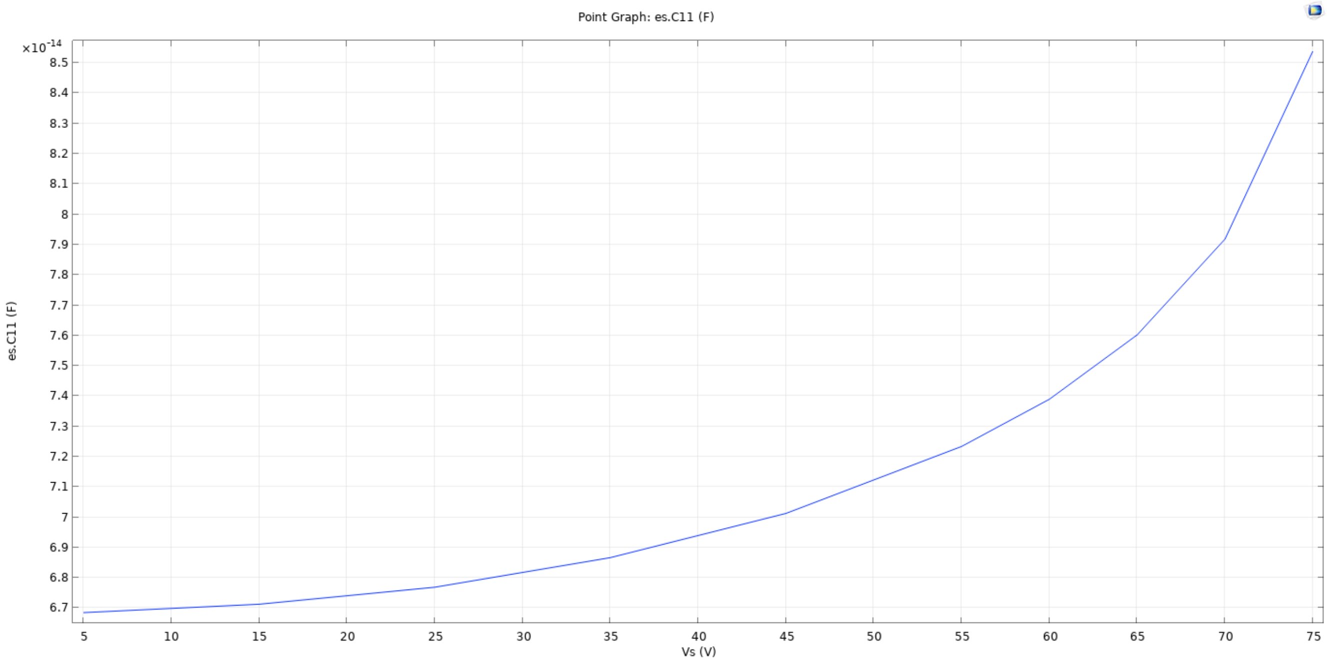

Figure 31 Maxwell Capacitance vs Bias Voltage of pre-fabrication resonant pressure sensor TSMC 180nm (no external pressure variation applied)

$$\boldsymbol{V_{Pull-in} \cong 80V}$$

(48)

$$\boldsymbol{C_{at\,30V} = 68.179\,fF}$$

(49)

It is interesting to observe that, even if the simulation has been set to start from $0V$ of bias applied with a variable step, the simulation starts directly at $5V$ since at $0V$ there is no sensing of capacitance. Indeed, these values are coherent with the ones obtained in the fabricated and tested sample of prototype-A1 [1]. Additionally, the displacement along z of the movable plate can be plotted with respect to the variation of the applied bias voltage. Indeed, the behaviour of one single point belonging to the movable plate has been reported in Figure 32.

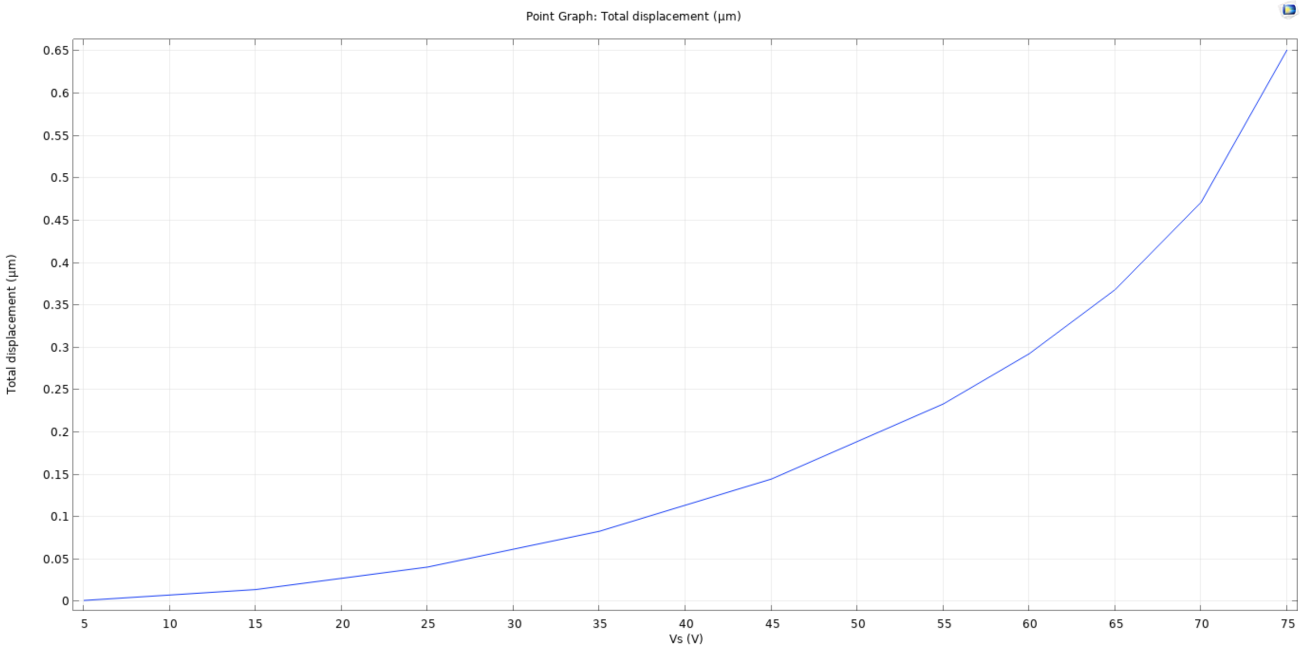

Figure 32 Total displacement point belonging to the central resonator vs Bias Voltage pre-fabrication resonant pressure sensor (no external pressure variation applied)

Since the plot reports the displacement of the movable plate with respect to its zero position it can be confirmed the presence of the pull-in at around $1/3$ of the air gap as the theory of electrostatic actuators states [6]: the plate will move respect its rest position up until a value of $2.23um/3 = 0.74um$, thus resulting in an overall z position of the movable plate in module equal to $2.23um - 2.23um/3 = 1.486um$.

4.3. Comments on the spring stiffness

In order to match the stiffness obtained from the experimental results, the classic formula can be used:

$$f_r = \frac{1}{2\pi}\sqrt{\frac{k}{m_{homogeneous}}} \rightarrow k = (f_r 2\pi)^2 m_{homogeneous}$$

(50)

f_r is the resonance frequency of the structure and m is the mass of the central resonating part. On the contrary a different approach that uses the modal masses that actively contribute to the deformation can be exploited. This second approach is based on the formula reported in Ref. [2], which explicit the stiffness in terms of Young's modulus and that states that:

$$k = \frac{4\pi^2 \beta^2 T_p^2 E m_{composite}}{\rho L^4}$$

(51)

Where β is the dimensionless coefficient dependent on the shape pf vibrating mode, Tp is the central resonator thickness, E is the avarage Young's modulus, m is the mass of the central resonator, ρ is the avarage density and L is the length of the central resonator. This approach exploits the modal mass factor, which is defined as the ratio of the mass participating in a given vibration mode with respect to the total mass of the entire system. This depends on the mass distribution of the system. For the computation of the β contribution, the participation factors must be extrapolated from COMSOL. Particularly, under *Derived value* in the *Global evaluation* section the effective modal masses can be found specifying the following formulas:

$$mpf1.pfLnormX$$

$$mpf1.pfLnormY$$

$$mpf1.pfLnormZ$$

(52)

Then, summing the squares of the obtained values among each other for the same eigenfrequency and dividing this with respect to the total mass, which can be computed in COMSOL with the formula $mpf1.mass$, it can be found the modal mass factor for the resonance frequency:

$$\beta = \frac{mpf1.pfLnormX^2 + mpf1.pfLnormY^2 + mpf1.pfLnormZ^2}{mpf1.mass}$$

(53)

For the average values of Young's modulus and density, COMSOL provides them under the *results*, and more specifically under the *volume integration* section, which will give values that must be after divided by the total volume of the structure. It must be underlined that this second approach tends to be extremely variable with respect to the classic formula for the computation of the stiffness (equation (50). Indeed, the most reliable geometry must be defined in order to compute the correct average values from COMSOL. If one part of the geometry, even if is one not directly acting nor on the mechanical or the electrical behaviour of the resonator device (like the external support structure made of Metal and tungsten Vias), is slightly changed, this formula may not be valid anymore, hence the resulting stiffness may be different or wrong with respect the one obtained from the formula (51). Additionally, for the best matching between the two formulas the *homogeneous mass* of the central resonator should be used for the first case (equation (50)), while the *composite mass* value for the second quoted case (equation (51)). The main reason for this, is that the first case exploits the resonance frequency that is obtained after simulation of the structure with the single homogeneous layer, thus with the inclusion of the additional volumes (so additional mass) of the central resonator to the overall geometry that instead should be made of air; while the second case exploits all mechanical parameters found with the characterization of the composite central resonator part, that indeed, does not include the additional volume (mass) into the overall geometry of the central resonator.

Regarding the pre-fabrication device, the stiffness computed with the second proposed method results to be characterized by the following parameters:

$$L_{res} = 146.22um$$

(54)

$$T_{p\ res} = 3.87um$$

(55)

$$V_{entire\ device} = 1.39230 * 10^{-13}m^3$$

(56)

$$E_{avarage} = \frac{0.019666m^3}{1.39230 * 10^{-13}m^3} = 141.2\ GPa$$

(57)

$$\rho_{avarage} = \frac{8.4348 * 10^{-10}m^3}{1.39230 * 10^{-13}m^3} = 6058.17\frac{kg}{m^3}$$

(58)

$$\beta = \frac{mpf1.pfLnormX^2 + mpf1.pfLnormY^2 + mpf1.pfLnormZ^2}{mpf1.mass} =$$

$$= \frac{(2.3158 * 10^{-10})^2 + (6.7158 * 10^{-11})^2 + (1.4273 * 10^{-5})^2kg}{8.4348 * 10^{-10}kg} = 0.242$$

(59)

$$k = \frac{4\pi^2\beta^2T_p^2E_{avarage}m_{composite}}{\rho_{avarage}L^4} = 160.38\frac{N}{m}$$

(60)

On the other hand, with the classical method the correspondent stiffness results to be equal to:

$$f_r = \frac{1}{2\pi}\sqrt{\frac{k}{m_{homogeneous}}} \rightarrow k = (f_r2\pi)^2m_{homogeneous} = 162.39\frac{N}{m}$$

(61)

The slight difference that is encountered among the two methods is due to approximations during the computation and mesh choices.

4.4. Squeeze film damping study on pre-fabrication Pressure sensor resonant central plate

As mentioned, when two surfaces in a MEMS device are in close proximity and experience a motion, a thin layer of gas (or fluid) is trapped between them. This layer is often referred to as a "squeezed film". As the surfaces move, the fluid undergoes a change in pressure due to the squeezing action, and this pressure change contributes to the damping of the motion. The "relative gas film pressure" represents the pressure of the gas or fluid within this squeezed film, compared to the surrounding environment. This pressure can influence the damping effect, and proper control of the relative gas film pressure can be important for achieving effective vibration damping in MEMS devices. A better characterization of damping mainly affecting the central perforated resonator movable plate could be performed basing on the studies of Bao et. Al [19] and it is possible to exploit the COMSOL tutorial [18] adjusting accordingly the parameters. Indeed, it would be possible to define the squeeze film damping acting on the geometry by using the *Thin film flow physics* present in COMSOL that is described by the Bao's model and formulas. The damping occurs from the squeezing of the thin film of gas material present in the gap between the two surfaces. The squeezing action forces out the gas from the gap, resulting in a damping force that acts to prevent mechanical contact between the two surfaces and also the opposite effect takes place when the surfaces move away from each other as gas is drawn back into the gap. The perforations allow the gas in the gap to escape. For instance, the *Perforations* feature of the *Thin Film Flow* interface has been exploited in COMSOL in order to simulate the effect of the etch holes without explicitly modelling them. Additionally, this feature acts as a sink for gas that is proportional both to the ambient pressure and to the pressure difference between ambient pressure and the ambient on the other side of the perforated surface. Particularly, for the characterization of the behaviour of the film pressure on the central perforated resonator, the geometry has been defined with $6x6$ perforations and the dimensions characteristic of the already described pressure sensor under test. Three cases have been analysed on this geometry: the limiting case of no etch holes, the case with etch holes not explicitly modelled using Bao's formula and the case of zero relative pressure in the etch holes which means that the pressure inside the holes is equal to the pressure outside of them resulting in no pressure difference between the inside and outside, with the holes explicitly modelled. The following studies are the results of the 2D model central resonator structure of the sensor under test, with the surface normal of the plates pointing out of the paper, in this case the plate is assumed to move exclusively in the surface normal direction (z axis in the 3D model), with a prescribed sinusoidal velocity. The applied wall velocity at the frequency of interest has been defined as $2 * pi * f0 * dh$, where $f0$ is the vibrating frequency and dh is the change in the gap air which has been set to be around $1.1 * 10^{-7} um$, which means to define a fractional change in the air gap of about 0.05, so a variation of $1/20$ from the nominal air gap. The boundary conditions for this model have been considered with a vanishing relative pressure at the border of the plate, and, only for the third quoted case, the relative pressure is zero also within every etch holes. The parameters defined in COMSOL for this simulation are reported in Figure 33.

Parameters

Name	Expression	Value	Description
M_h	6	6	num of holes along length
N_h	6	6	num of holes along width
h0	2.23[um]	2.23E-6 m	Gap height
l_h	3.87[um]	3.87E-6 m	length of hole (thickness...
l_pl	146.22[um]	1.4622E-4 m	length of plate
w_pl	146.22[um]	1.4622E-4 m	width of plate
s_h	17.56[um]	1.756E-5 m	Side of square hole
s_1	5.84[um]	5.84E-6 m	distance between holes
s_2	5.84[um]	5.84E-6 m	distance between hole an...
s1p	5.84[um]	5.84E-6 m	
s2p	5.84[um]	5.84E-6 m	
pitch__	s_h+s_1	2.34E-5 m	
l_per	l_pl-2*(s2p-s1p)	1.4622E-4 m	length of perforated region
w_per	w_pl-2*(s_2-s_1)	1.4622E-4 m	width of perforated region
r0	sqrt(l_per*w_per/M_h/N_h/pi)	1.3749E-5 m	unit disc radius
ri	s_h/sqrt(pi)	9.9072E-6 m	equivalent radius of hole
dhND	0.05	0.05	Fractional gap height cha...
dh	dhND*h0	1.115E-7 m	Change in gap height
mu0	1.8e-5[Pa*s]	1.8E-5 Pa·s	Gas viscosity (Air)
f0	147[kHz]	1.47E5 Hz	Vibration frequency
vf	2*pi*f0*dh	0.10298 m/s	velocity of wall
pRef	1[atm]	1.0133E5 Pa	

Figure 33 Parameters set for the simulation of the Squeeze film damping pre-fabrication pressure sensor

Performing the simulations, the relative gas film pressure behaviour resulted to be the highest for the limiting case of no etch holes which it reaches a maximum of $2.5 * 10^3\ Pa$ in the centre of the structure, while the lowest resulted for the limiting case of Bao's model with perforations not explicitly modelled, which reaches a peak of $10\ Pa$. It is curious to observe that the minimum relative film pressure is not reached for the zero relative pressure in the etch holes case (Figure 36) since the space between the holes is still enough to create an important local relative pressure concentration, however the overall average damping coefficient is still the lowest in this last quoted case as visible from Figure 37. The three cases are reported for the central resonator of the pre-fabrication pressure sensor in Figure 34, Figure 35 and Figure 36 respectively, while the damping coefficients are reported in Figure 37.

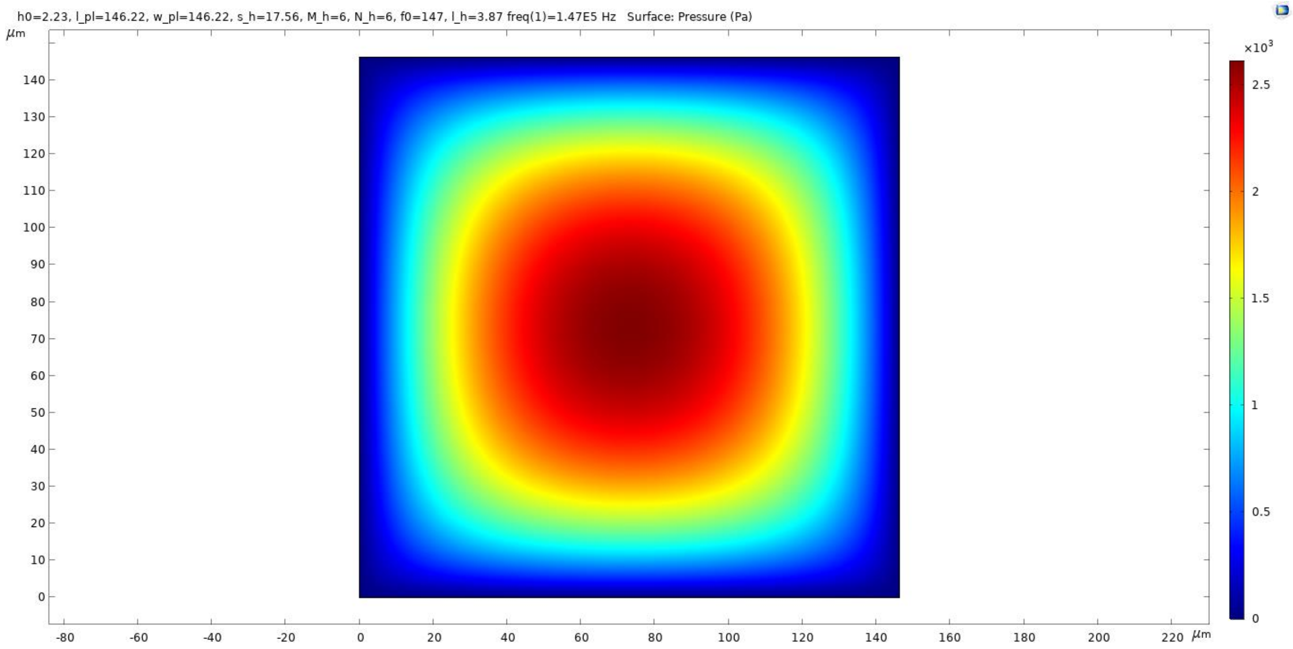

Figure 34 Relative film pressure on the central resonant movable plate pre-fabrication with no perforation

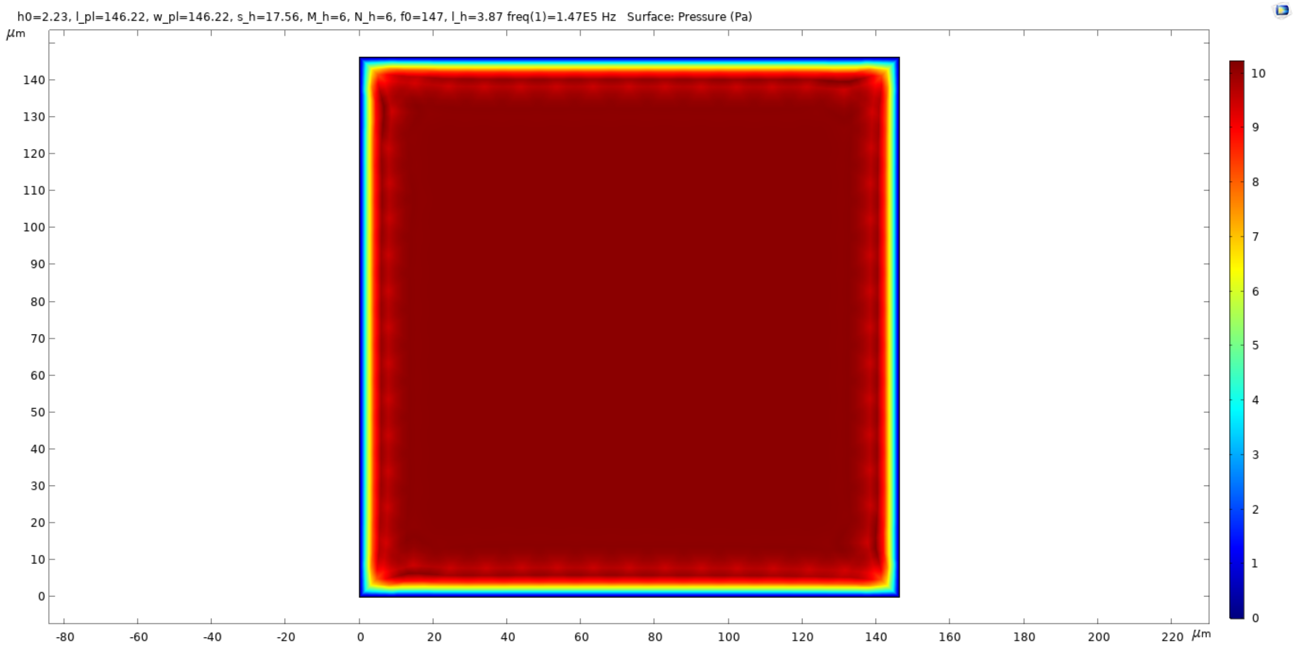

Figure 35 Relative film pressure on the central resonant movable plate pre-fabrication with Bao's Model (perforations not explicitly modelled)

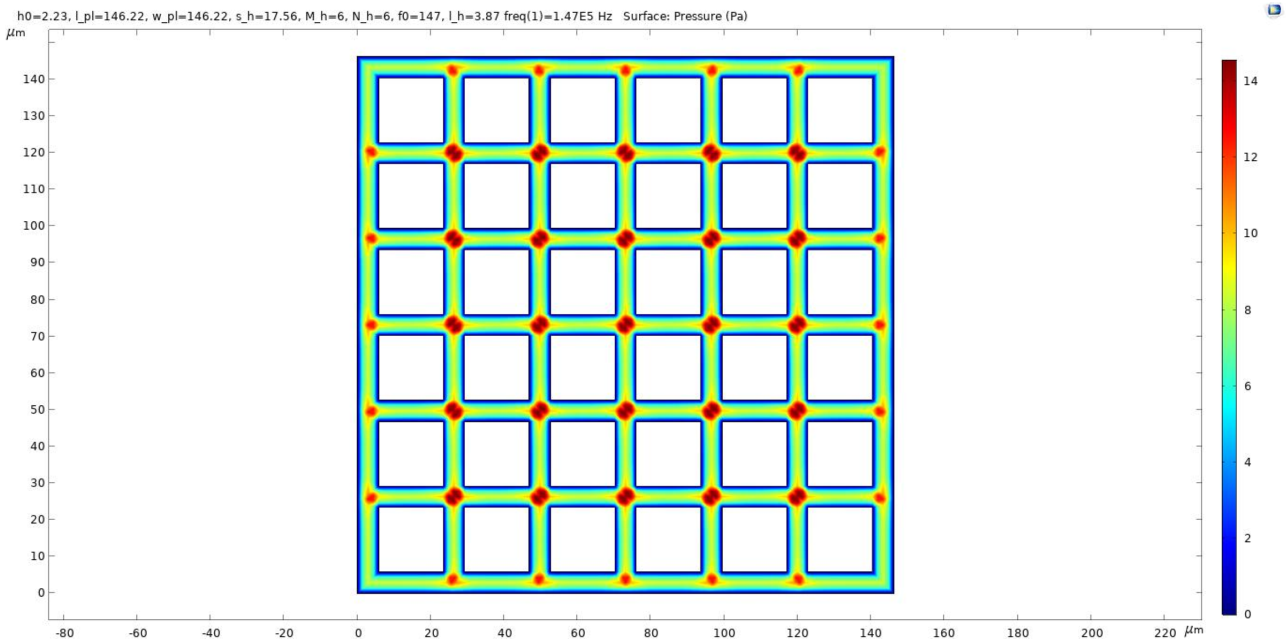

Figure 36 Relative film pressure on the central resonant movable plate pre-fabrication with perforations and zero relative pressure in the etch holes P=0

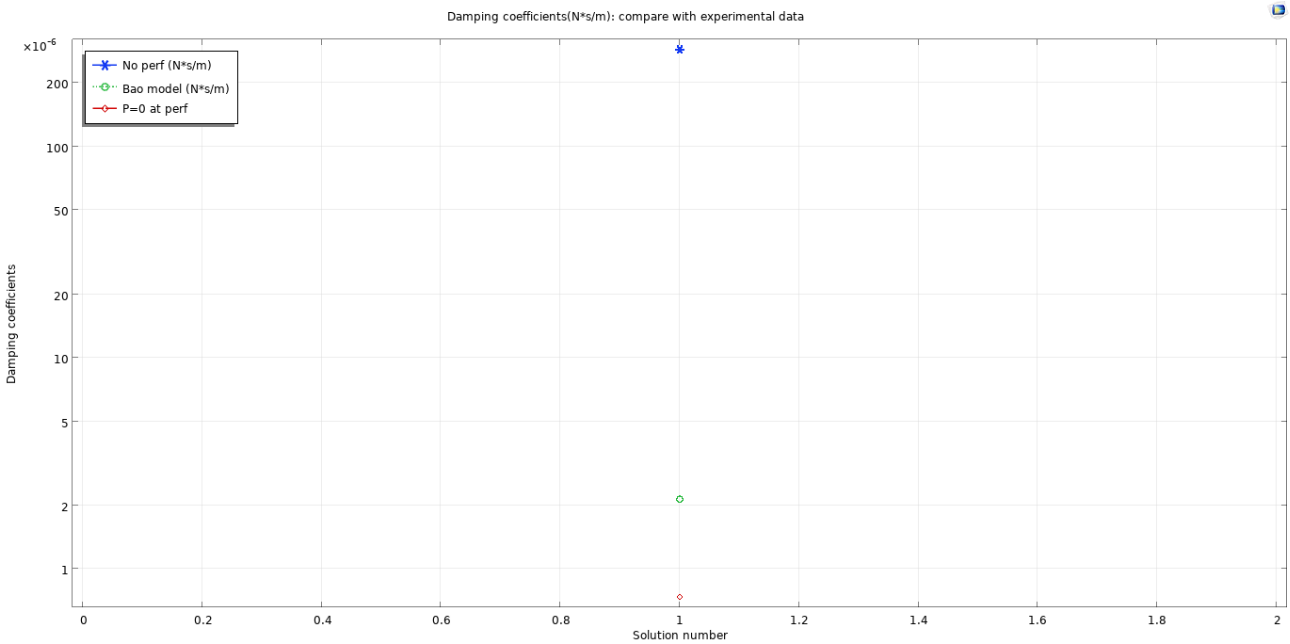

Figure 37 Damping coefficient extrapolated from the three cases

In conclusion, it can be notice that the Bao's model case value of the damping coefficient, which is equal to $2 * 10^{-6}$, results to be coherent with respect to the experimental results found in Bao's real study [18, 19], however in the study it is not present a geometry that perfectly matches the geometry under test, hence a direct comparison with the experimental data is not possible.

4.5. Simulations on the theoretical Post-Fabricated Capacitive Resonant Pressure sensor 180nm TSMC *(based on [Ref. 1])*

The post-fabricated pressure sensor characterization has been basically performed by repeated trials with the principal aim to obtain the most similar characteristics of the already fabricated pressure sensor. In particular, since during the manufacturing procedure it is likely to have a variation on the thickness of the layers mainly based on several factors such as release time, external temperature and conditions, the thickness of the Top metal6 and the central resonator parts have been varied along a wide range until the resulting simulated resonance frequency and stiffness were the closest to the one obtained from the experimental results which are equal to $135kHz$ and $110\ N/m$ according to [1]. The chosen thicknesses are explicated in Figure 38. This sweep corresponds to change the mass of the central resonator and of the entire structure, thus the volume, but maintaining the density equal to the one found in the central resonator characterization, since it represents the closest one to the real case. Additionally, an automatic sweep of the geometry is not possible in COMSOL and would require an incredible amount of simulation time, therefore a manual one has been actuated. Furthermore, in order to be consistent with the reality, the change in the geometrical characteristics has been maintained within the 20%, since this represents the maximum variation that the fabrication process may introduce. A similar approach described in section 4.2 has been used to include the damping contribution, and since for this case all the results are already known by experimental results, more precise values can be specified. Substituting to the central resonator movable part the mechanical and electrical properties found in section 4.1, the thickness and the obtained correspondent parameters required to obtain the wanted experimental resonance frequency of $135kHz$ have been found:

$$h_{springs}\ (Metal6\ height)\ = 2.17um \tag{62}$$

$$h_{central\ resonator}(Central\ resonator\ height)\ 3.494um \tag{63}$$

$$mass_{original\ central\ res\ composite} =\ 1.824 * 10^{-10}\ kg \tag{64}$$

$$mass_{central\ res\ homogeneous}\ = 1.715\ * 10^{-10}\ kg \tag{65}$$

$$volume_{original\ central\ res\ composite} = 3.817 * 10^{-14}\ m^3 \tag{66}$$

$$volume_{central\ res\ homogeneous} = 3.975 * 10^{-14} m^3$$

(67)

$$Density_{central\ res} = \frac{m}{V} = \frac{1.824088112 * 10^{-10} kg}{3.817 * 10^{-14}\ m^3} = \ 4778.85\ kg/m^3$$

(68)

$$E_{central\ res} = \frac{0.0043361\ J * m^3}{3.817 * 10^{-14}\ m^3} = \ 113.59\ GPa$$

(69)

$$v_{central\ res} = \frac{1.1742 * 10^{-14} m^3}{3.817 * 10^{-14} m^3} = 0.308$$

(70)

$$\varepsilon_{central\ res} = \frac{1.4175 * 10^{-13}\ m^3}{3.817 * 10^{-14}\ m^3} \ = \ 3.714$$

(71)

$$Q = 87.584$$

(72)

$$b = \frac{2\ pi\ mass_{central\ res\ homogeneous} f_r}{Q} = 1.657 * 10^{-6} \frac{N\ s}{m}$$

(73)

$$\boldsymbol{fr = 134.69 kHz}$$

(74)

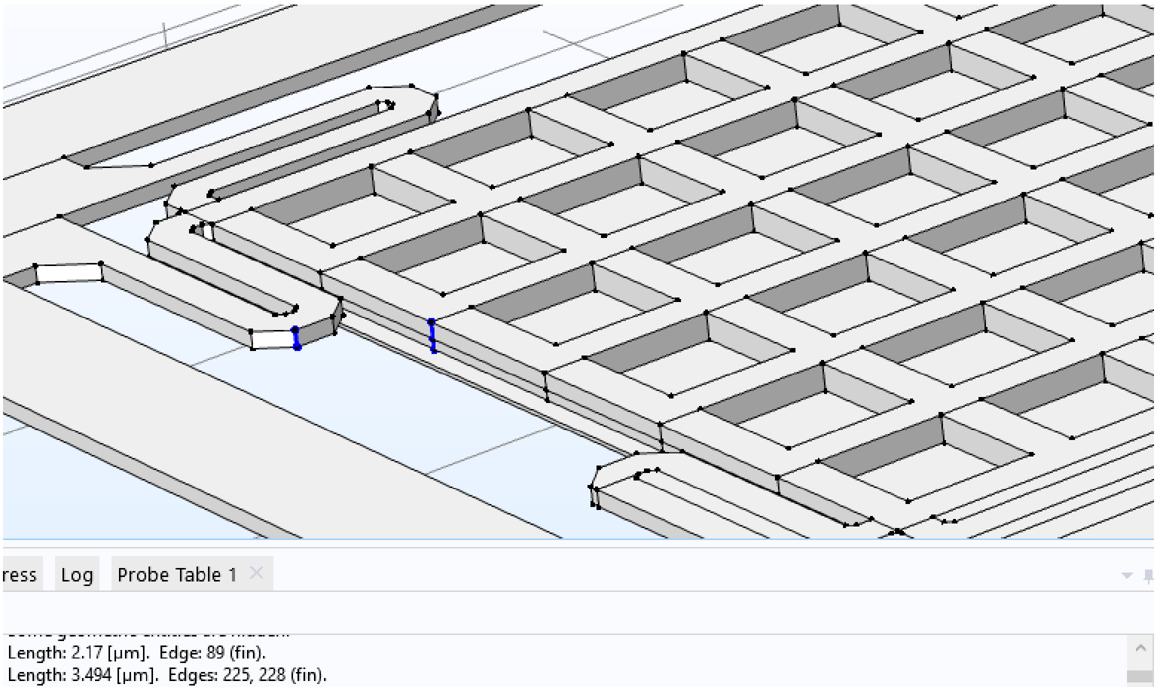

Figure 38 Thicknesses of the springs (Metal6) and the central resonator of the post fabricated case of the resonant capacitive pressure sensor TSMC

All the obtained results are coherent with the experimental ones. The interesting aspect to this approach based on the estimation of the possible variations from the pre-fabricated case to the post fabricated one is that a precise correction factor on the thickness (which as well, acts on the volume and the mass of the simplified homogeneous geometry) can be extrapolated for the structure. Therefore, the same correction may be applied on another sensor that has not been fabricated yet, for instance, an accelerometer, which is made with the same technology $180nm$, same materials, and analogue dimensions as will be seen in further sections of this document. Indeed, the characterization of an accelerometer will be performed in the following paragraphs, and the same thicknesses variation will be applied from the pre to the post-fabricated case, in order to consider the possible similarities and differences present between the two sensors in terms of mechanical and electrical parameters. Providing a comparison among the masses in the pre and post fabrication cases of the central resonator of the pressure sensor, it can be observed that, since $\boldsymbol{m_{pre}} = \mathbf{1.8995} * \mathbf{10^{-10}}\ \boldsymbol{kg}$ and $\boldsymbol{m_{post}} = \mathbf{1.7149} * \mathbf{10^{-10}}\ \boldsymbol{kg}$**,** a correction factor of $\mathbf{1.1076}$ (a change of 11% in terms of masses) must be applied from the ideal case to the real one. Additionally, this variation that occurs has been accurately chosen in order to be within the 20% of variation that a fabrication step may introduce, in fact regarding the thicknesses chosen:

$$2.34um \rightarrow 2.17um \rightarrow\ 7.265\% \text{ of variation}$$

$$3.87um \rightarrow 3.494um \rightarrow 9.716\% \text{ of variation}$$

On the other case, it is possible also to detect a certain correction factor that describes how the post-fabrication case provided by the simulation (which is the only case that can be directly compared with the real experimental one described in the document [1]) changes with respect the real experimental one. For instance, the mass obtained by simulation for the post case is $\boldsymbol{m_{post} = 1.7149 * 10^{-10}\, kg}$, while the real experimental one results to be $\boldsymbol{m_{exp} = 1.53 * 10^{-10} kg}$, thus showing a correction factor of $\boldsymbol{1.12}$.

- Post-fabrication Pressure sensor *Simulations: No external pressure applied, Bias Voltage sweep*

Using the tool, it is also possible to plot some behaviours of the post fabrication structure. The pull-in voltage can be visually inspected from the behaviour of the capacitance with respect the applied bias voltage (Figure 39 and Figure 40), as well as from the overall total displacement of the movable plate with respect the applied bias voltage (Figure 41).

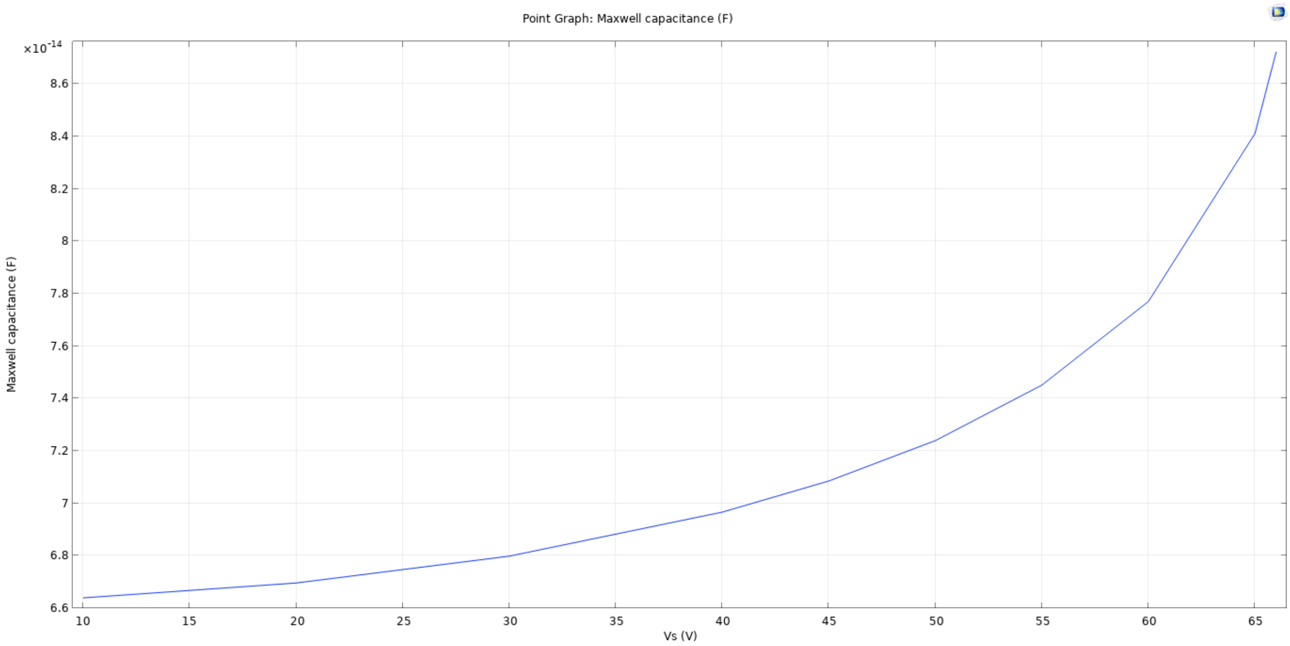

Figure 39 Maxwell Capacitance vs Bias Voltage of post-fabrication resonant pressure sensor TSMC 180nm (no external pressure variation applied)

From the behaviour of the capacitance curve with respect the bias voltage applied it is clear that the pull-in voltage occurs around $67V$. This result is smaller with respect the pre-fabrication case ($\cong 80V$), demonstrating that with a less rigid structure the pull-in effect in a parallel plate structure occurs at lower bias voltage. On the contrary, the sensed capacitance remains practically unchanged with respect the previous case.

$$\boldsymbol{V_{Pull\,in} \cong 67V} \tag{75}$$

$$C_{\text{at } 30\text{V}} = 67.979\, fF$$

(76)

The simulation starts directly at $10V$ since at $0V$ there is no sensing of the capacitance. Moreover, some more detailed simulations reported in Figure 40 have been carried out showing the behaviour of the sensed capacitance for a range of Bias voltage from $2.5V$ to $10V$.

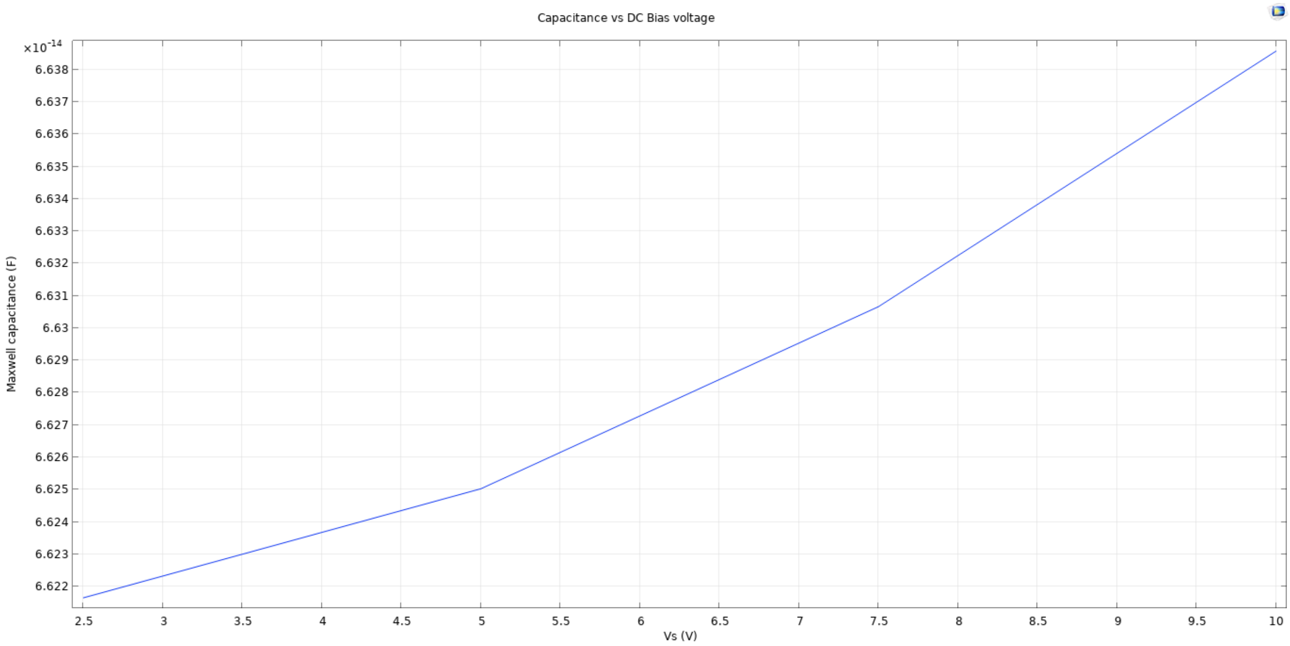

Figure 40 Maxwell capacitance between the movable (Grounded) and the fixed electrode (Biased) with respect the bias voltage range 2.5V-10V

Since the air gap has not change with respect the pre-fabrication characterization the displacement plot of the movable plate with respect to its zero position confirms again the presence of the pull in around $1/3$ of the air gap, thus after a displacement of about $0.743um$. This is clear from Figure 41.

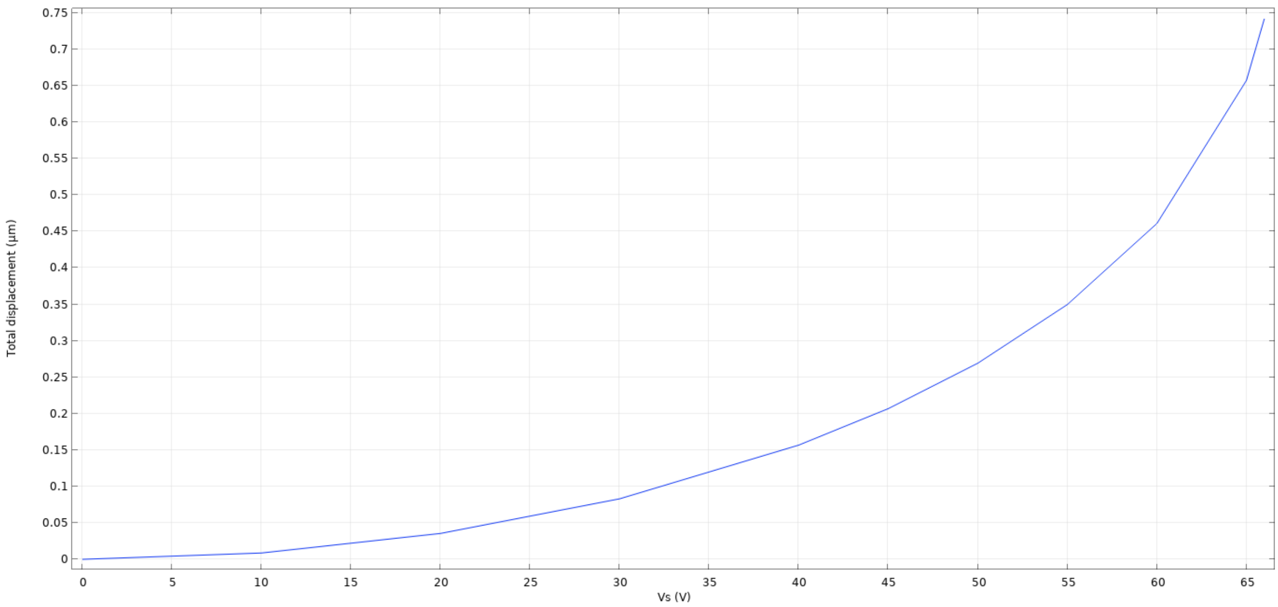

Figure 41 Total displacement central resonator vs Bias Voltage post-fabrication resonant pressure sensor (no external pressure variation applied)

Additionally, a frequency domain simulation has been performed on COMSOL in order to plot the behaviour of the RMS displacement with respect the resonance frequency (Figure 42). It is clear that the highest peak of RMS is achieved exactly at the expected resonance frequency of $134.69kHz$ reaching a maximum value of around $0.8\ um\ RMS$.

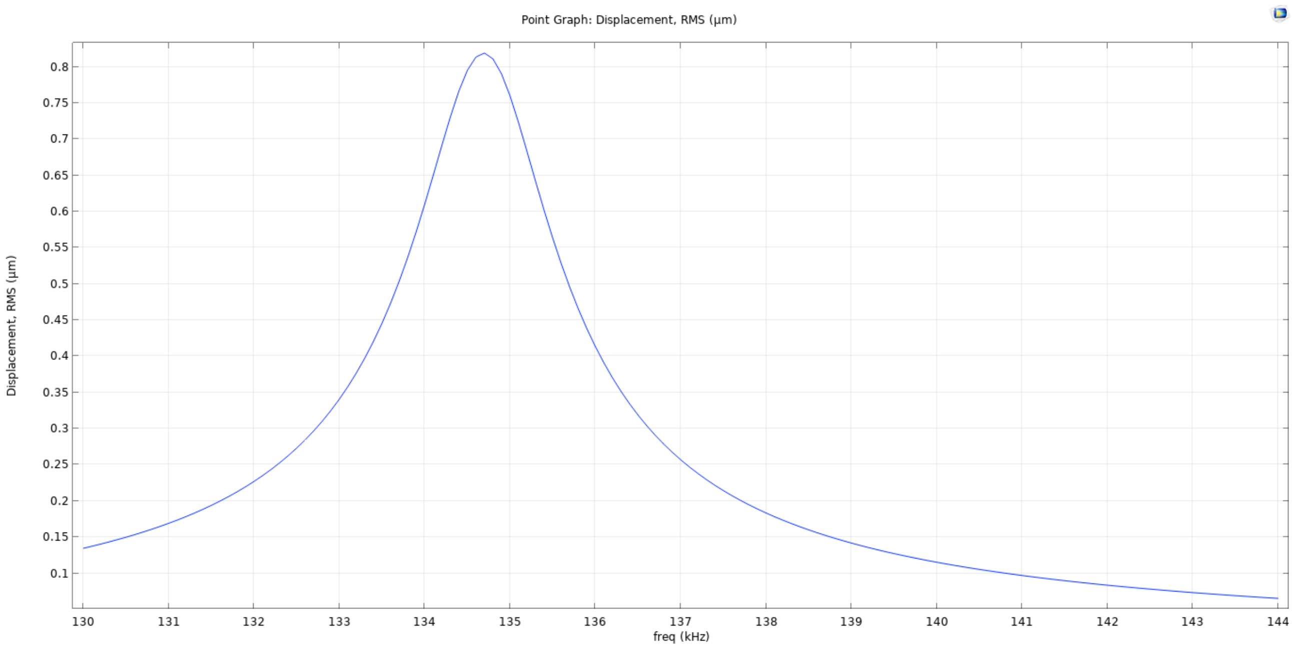

Figure 42 RMS displacement of the movable plate (Grounded) in the frequency range post-fabrication pressure sensor

4.6. External pressure applied, Bias Voltage sweep

A relative external pressure variation can be applied on the structure by including a *Boundary Load* node in the *Solid Mechanic* physic acting on the surface of the movable central resonator and the springs. Particularly, the force per unit of surface variation applied to the structure has been set to sweep from different values with distinct stationary voltages applied. The entire structure has been surrounded by air in order to specify in COMSOL that the sensor is surrounded by the standard atmospheric pressure at sea level under normal conditions. The relative pressure variation applied to the surface of the pressure sensor is positive, therefore an estrangement with respect the bottom fixed electrode, hence a decrement in the capacitance behaviour is expected. For instance, biasing the fixed bottom plate with $30V$ and applying a pressure variation in the range from $0Pa$ to $50kPa$ with a $10kPa$ of step (Figure 43) and a voltage of $5V$ with a pressure variation from $30kPa$ to $50kPa$ with a $2kPa$ of step (Figure 44), it is clear that the displacement becomes very important approaching higher values of variation of pressure.

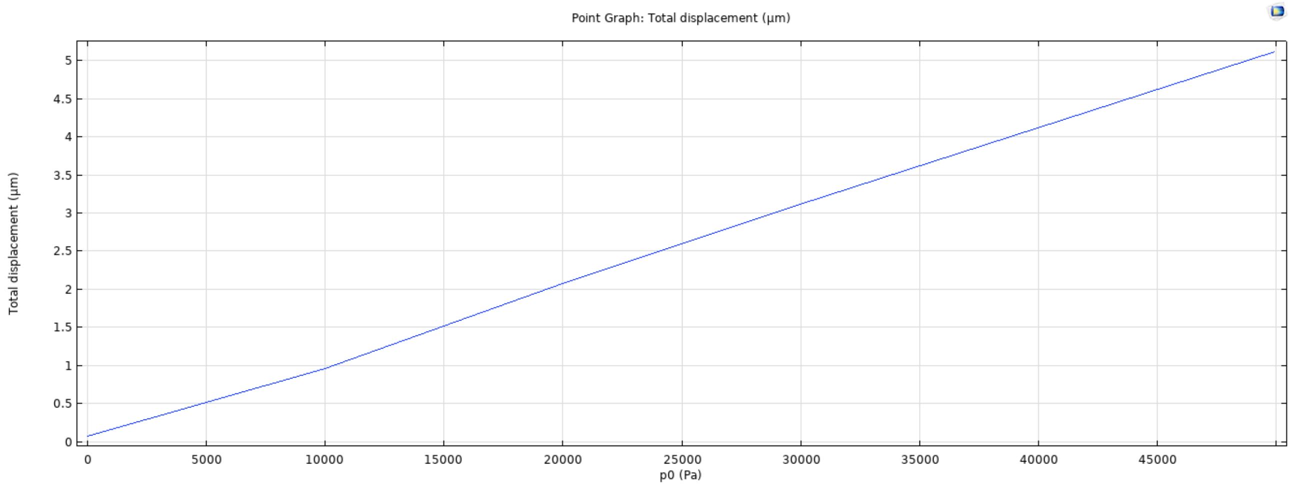

Figure 43 Total displacement of the movable plate of the pressure sensor at 30V of Biasing with respect the variation of the external pressure from 0Pa to 50kPa

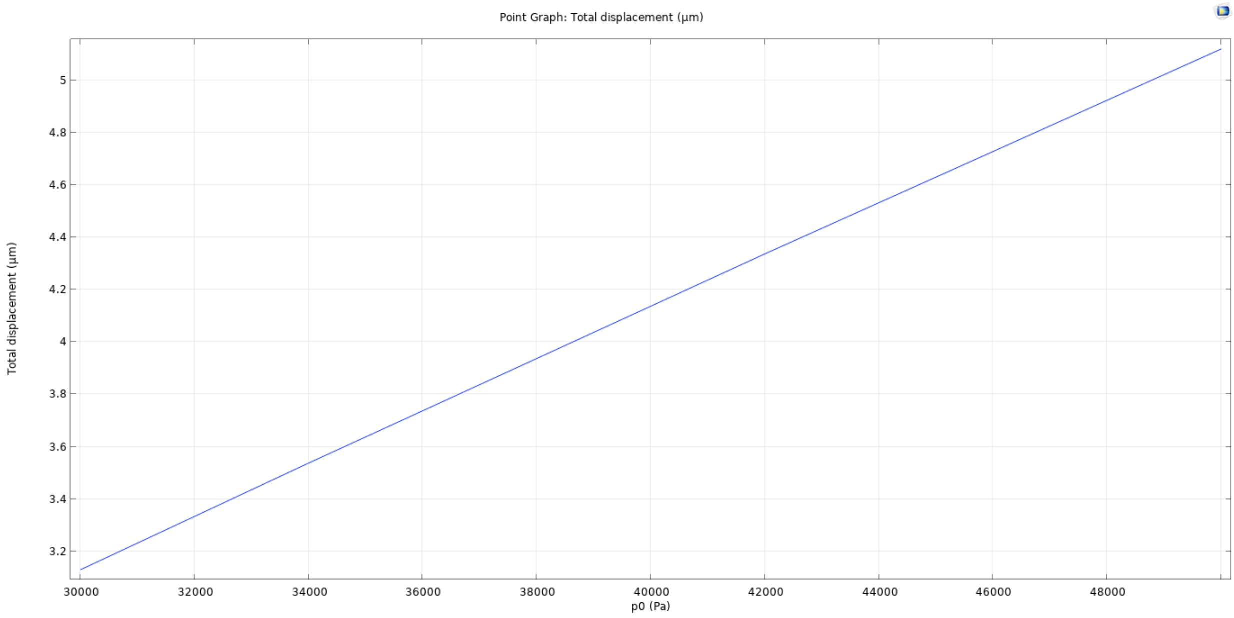

Figure 44 Total displacement of the movable plate of the pressure sensor at 5V of Biasing with respect the variation of the external pressure from 30kPa to 50kPa

From the reported plots the mechanical sensitivity obtained results to be around $0.1 nm/Pa$. Moreover, at high variation pressure the stresses on the structure become dominant. Indeed the Von Mises stresses, which are a measure of the combined effect of normal and shear stresses in a material and that are used to evaluate the possible failure or deformation of a particular structure acting on the structure when $50kPa$ of pressure variation is applied, show a maxumum of $6.78 * 10^8\ N/m^2$ of stress (Figure 45), which is mainly present on the folding of the springs and that is indeed far above the ultimate tensile strenght of Aluminium, thus a break will probably occurs at the springs under extremely high external excitation.

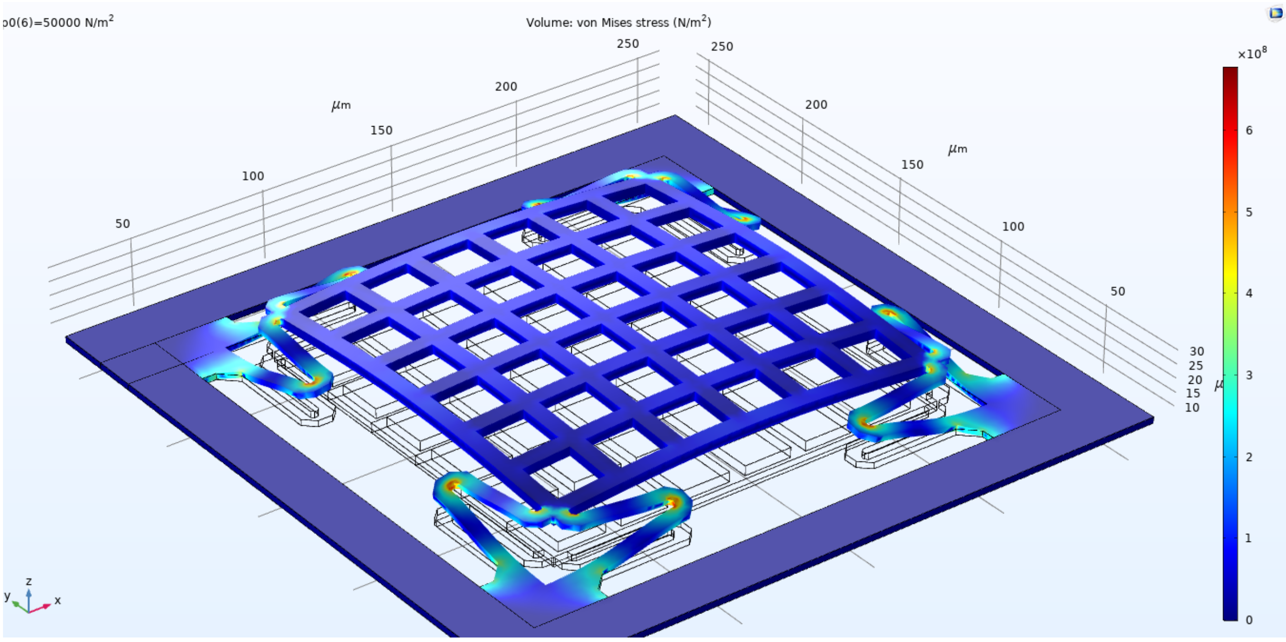

Figure 45 Von Mises stresses on the movable plate of the pressure sensor at 5V of Biasing with 50000Pa of external variation of pressure

It's fundamental to note that the ultimate tensile strength of a certain material is variable on different factors such as manufacturing processes, heat treatment or the presence of any impurities in the material. Additionally, COMSOL does not directly provide the tensile strength of materials as a built-in material property, in fact the material properties must be provided as input by the user that will depend on the exploited material. The tensile strength of materials must be provided from reliable sources such as material specification or material databases. Thus, the material specifications must be consult for accurate estimation of the maximum Von Mises stress withstand of a certain alloy. Indeed, this study has been performed with the main purpose to make aware about the importance of simulations also in terms of stresses and how to prevent the break or permanent deformation of a device by observing the responding behaviour of the geometry under the presence of certain external strains. Putting the attention towards the behaviour of the capacitance, the plot reported in Figure 46 is obtained when $5V$ of biasing are applied with the correspondent sweep of external variation in pressure is present.

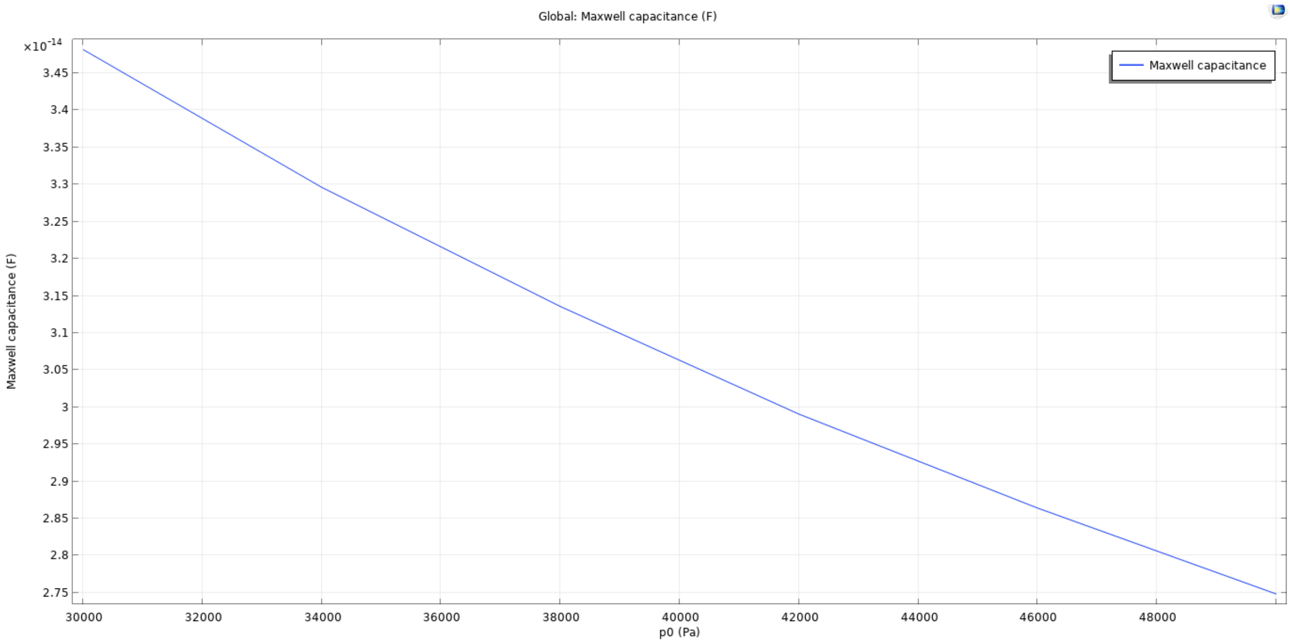

Figure 46 Maxwell Capacitance between the movable and the fixed plate at 5V of Biasing with respect the variation of the external pressure

The plot shows an important variation in the static capacitance as a response to a big variation in pressure. It must be underlined that, applying higher biasing voltages the displacement diminishes very slightly and not significantly with respect the behaviour at $5V$. However, since it has been started from $0Pa$ it is interesting also to observe the biasing at $30V$ where it can be confirmed that when no external variation of pressure is applied on the movable domains the value of the capacitance is exactly equal to the one obtained at $30V$ during the evaluation of the Pull-in and capacitances of the pressure sensor post-fabrication case, that is in fact equal to $67.98fF$, as previously stated in Figure 39. Therefore, this behaviour can be observed in Figure 47 and Figure 48 where the region of interest of $0Pa$ has been zoomed for a better visualization.

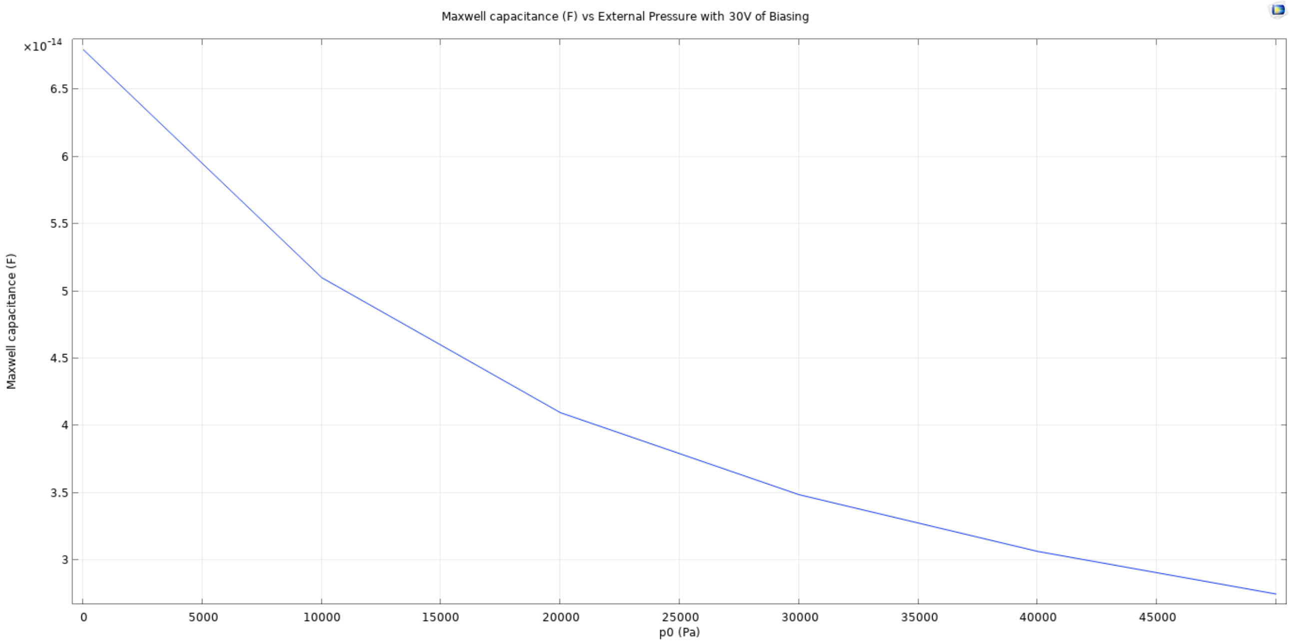

Figure 47 Maxwell Capacitance between the movable and the fixed plate at 30V of Biasing with respect the variation of the external pressure. Less points of step have been exploited; therefore, the plot does not show a good quality

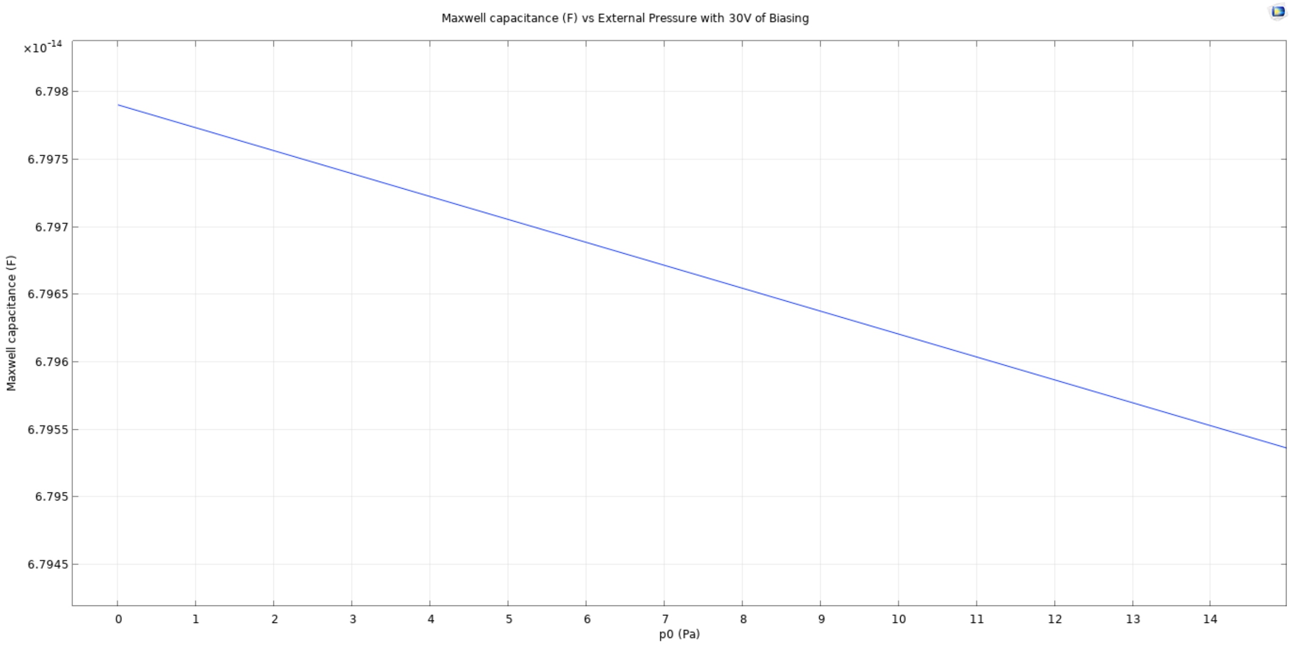

Figure 48 Maxwell Capacitance between the movable and the fixed plate at 30V of Biasing with respect the variation of the external pressure zoomed around 0Pa

Even if this kind of behaviours are non-realistic in real devices, since such high variation in pressure will never actually occur, it could be of interest observing the behaviour of it to have clear in mind what kind of applications could be suitable for the device under test and which material is more suitable for the type of application chosen.

4.7. Squeeze film damping study Post-Fabrication Pressure sensor

The squeeze film damping study on this new geometry, as performed for the pre-fabrication case, provided the results reported in Figure 49, Figure 50, Figure 51 for each of the already quoted case in section 4.4 and Figure 52.

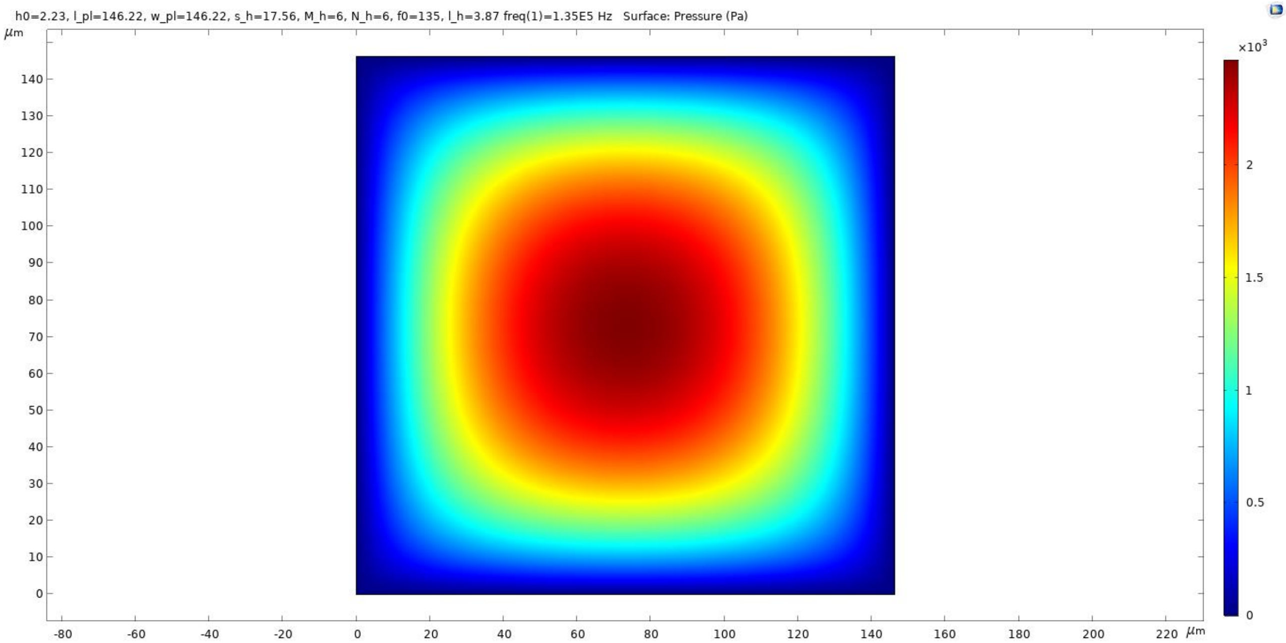

Figure 49 Relative film pressure on the central resonant movable plate post-fabrication with no perforation

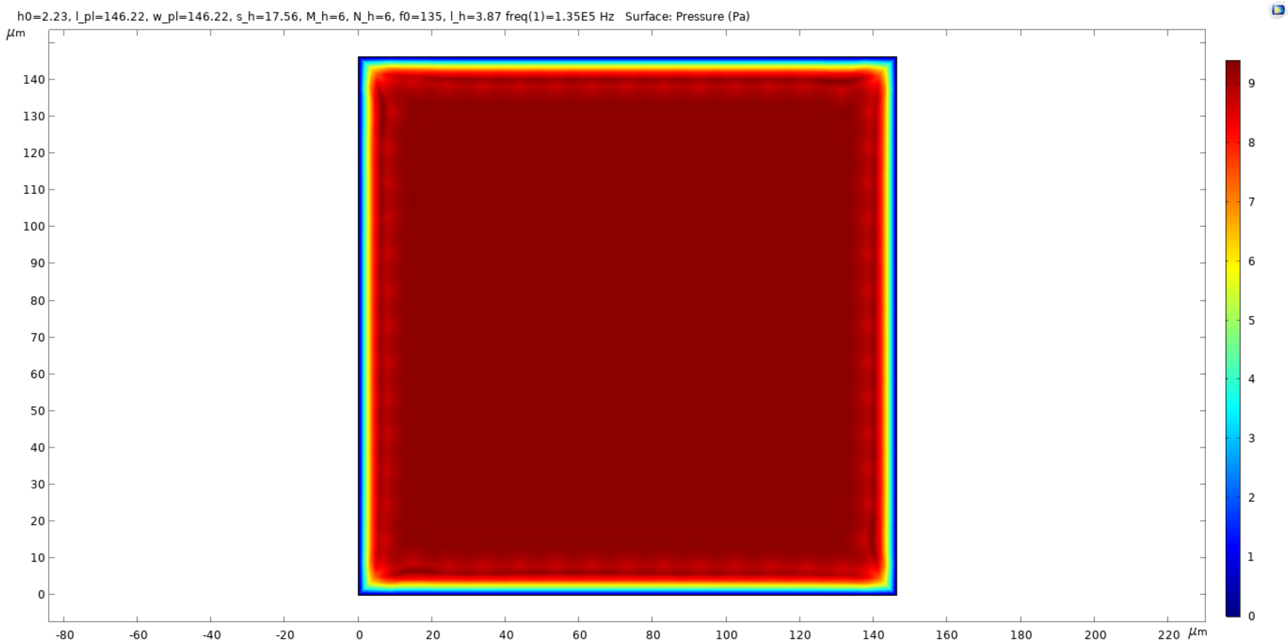

Figure 50 Relative film pressure on the central resonant movable plate post-fabrication with Bao's Model (perforations not explicitly modelled)

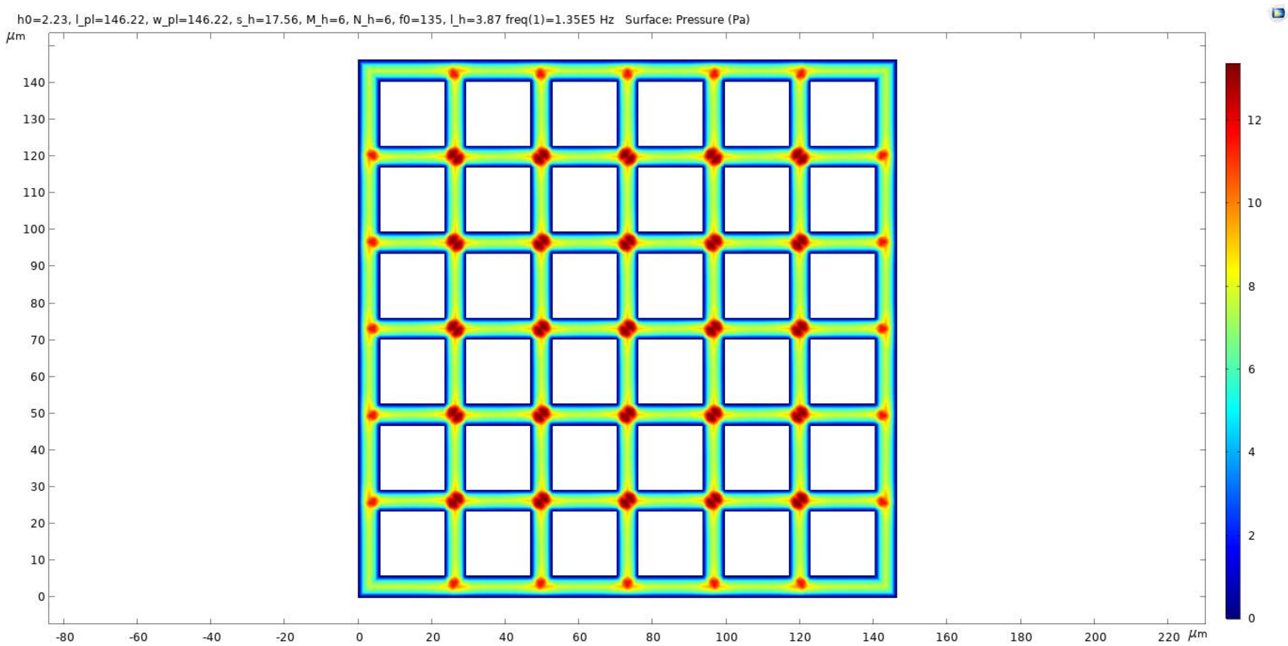

Figure 51 Relative film pressure on the central resonant movable plate post-fabrication with perforations and zero relative pressure in the etch holes P=0

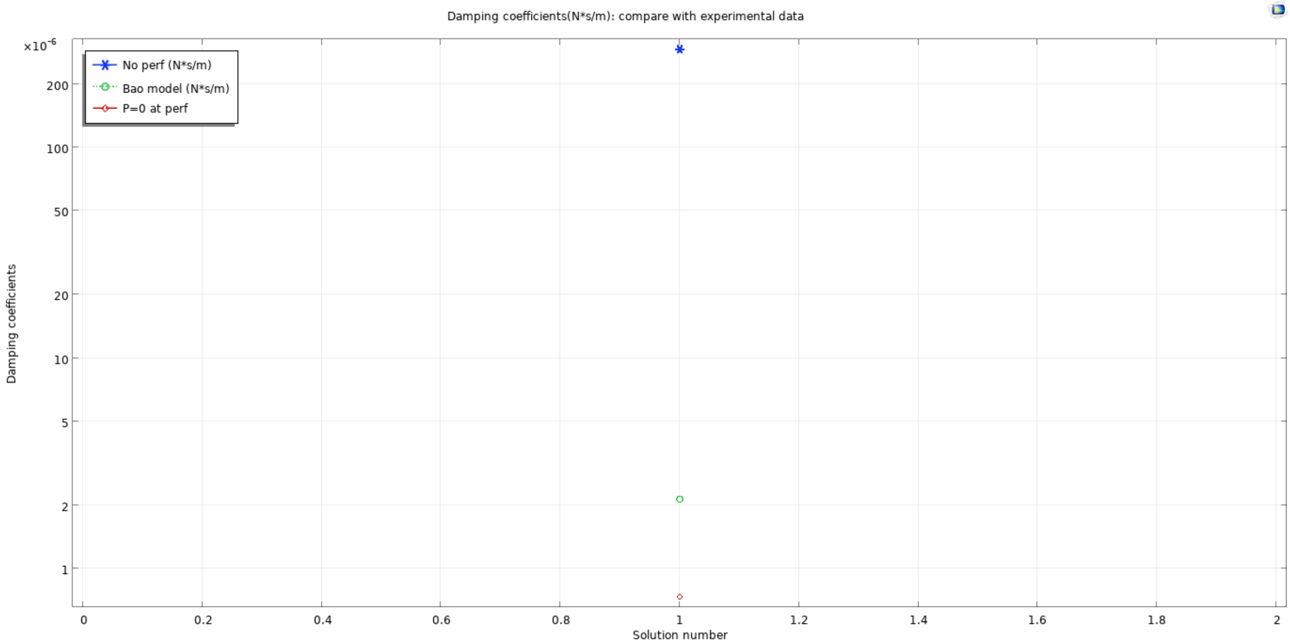

Figure 52 Damping coefficient extrapolated from the three cases. The Bao model result is extremely similar to the actual experimental results related to a 6x6 perforation structure analysed in Bao's work

This case results to be extremely similar with the one obtained in section 4.4. However, due to the lower thickness used in the post-fabrication central resonator, the relative film pressure is slightly lowered with respect the pre-fabrication case. Almost identical observations made on the pre-fabrication case can be re-proposed for this case.

4.8. Spring Stiffness computation for the post-fabrication device

From the classic formula for the computation of the stiffness it is clear that:

$$f_r = \frac{1}{2\pi}\sqrt{\frac{k}{m_{homogeneous}}} \rightarrow k = (f_r 2\pi)^2 m_{homogeneous} = (2\pi\ 134.69kHz)^2 * 1.7149 * 10^{-10}kg =$$

$$= 122.82\ N/m$$

(77)

This result is coherent with the one obtained from the experimental study performed by Mata et. Al. [1]. This stiffness results to be smaller with respect the pre-fabrication case, demonstrating that reducing the thickness of Metal6 layer, the springs thickness is affected in an important way. The stiffness reduction is the dominant contribution affecting the reduction of the resonance frequency for this new geometry. More flexibility is guaranteed and, as a consequence, the proof mass resonates more slowly and the pull-in is reached earlier with respect the theoretical case.

In conclusion, the pre-fabrication and the post-fabrication reproductions of the resonant pressure sensor have been successfully modelled in COMSOL. The most important mechanical and electrical parameters have been obtained, and it has been proven that all of them resides in a coherent range with respect the experimental ones. The overall behaviour of the simulated structure is extremely similar to the real case, hence the proper correction factors from pre-fabrication to the post-fabrication can be properly determined. This particular resonant capacitive pressure sensor will be mostly exploited in the atmospheric environment ($27000Pa$-$272000Pa$), therefore, this device can cover a huge amount of several applications. For instance, CMOS-MEMS resonant pressure sensors can be used in weather monitoring systems to measure atmospheric pressure changes. Indeed, real-time pressure readings can be easily provided, which it may results to be fundamental for weather forecasting, climate studies, and more generally meteorological research. Moreover, resonant pressure sensors can be employed in altimeters to measure changes in atmospheric pressure and determine altitude. Additionally, heating, ventilation, and air conditioning systems (HVAC) utilize pressure sensors to monitor and control air pressure within buildings. CMOS-MEMS resonant pressure sensors can be integrated into HVAC systems to ensure proper ventilation, optimize energy efficiency, and maintain air quality. In industrial settings, CMOS-MEMS resonant pressure sensors can be also utilized for process control and monitoring since they can measure and regulate pressure in various applications such as gas pipelines, manufacturing processes, chemical plants, and food processing industries. In conclusion, medical devices such as respiratory equipment, anaesthesia machines, and blood pressure monitors exploit this kind of devices, in fact, these sensors can accurately measure pressure changes and provide vital information for diagnosis, treatment, and patient monitoring. However, better performances need to be obtained from CMOS-MEMS pressure sensors if these are dedicated for a medical use purpose.

4.9. Composite Central resonator capacitive pressure sensor UMC characterization

After the migration from the TSMC to the UMC technology, an analogue characterization of the central resonator of the pressure sensor can be performed in the new technology to detect eventual differences with the TSMC one. The foremost characteristic hides under the fact that more Vias (Via5) are present in the central resonator part of the UMC device as quoted in section 3. This higher integration is possible because of the smaller width that the UMC technology accepts for the Vias between metal 5 and metal 6 with respect the original one. This possibility, not only add a higher robustness to the central resonator part, but also it decreases the possibility of detachment of the metal5 and metal6 among each other. However, a similar simplification used for the TSMC case has been performed. Due to the higher computational complexity that governs this new structure more steps have been performed. Particularly, always utilizing an iterative process for the simulation of the mechanical and electrical parameter, COMSOL was not able this time to perform the simulation of the entire complex structure made of a complex patterned layer of vias, thus a more complex patterned layer of oxide between them with respect the TSMC case. Therefore, to opt this issue it has been decided to use the same geometry (same pattern of vias and oxide) used for the TSMC central resonator characterization, in order to not add complexity, but substituting the mechanical and electrical parameters related to each UMC layer, studied separately and singularly among the others. Thus, each layer such as vias5, oxide between vias, metal6 and metal5 of the UMC central resonator, has been studied separately and the Young's modulus, Poisson's ratio, normalized relative permittivity and density of each has been extrapolated. After, obtained the required values, these values have been substituted in the original TSMC central resonator geometry, so that the results obtained after the simulation of this last one belongs to the actual characterization of the UMC project. Besides all of these considerations, it has been proven that the final results of the central resonator part from the UMC are almost completely identical with respect the TSMC ones. This, is because the only change that occurs from one technology to another is the variation in volume and in mass, which are higher for the UMC case, however the actual density results to be constant due to the same material choices w.r.t the TSMC case. The values obtained for each layer of interest (central vias and dielectric layers, since Metal6 and Metal5 are identical w.r.t the TSMC case) of the UMC design central resonating part are reported below, and also a visual comparison among the pattern utilized for the UMC and TSMC central vias (Figure 53) and central dielectric (Figure 54) respectively.

- *UMC ViasM5M6 layer's parameters:*

$$Volume = 4.943\ 10^{-15}\ m^3 \tag{78}$$

$$Mass\ =\ 9.565\ 10^{-11}\ kg \tag{79}$$

$$Density = \frac{m}{V} =\ 19349{,}977\ kg/m^3 \tag{80}$$

$$E = 410.99\ GPa \tag{81}$$

$$v = 0.28 \tag{82}$$

$$\varepsilon = 1 \tag{83}$$

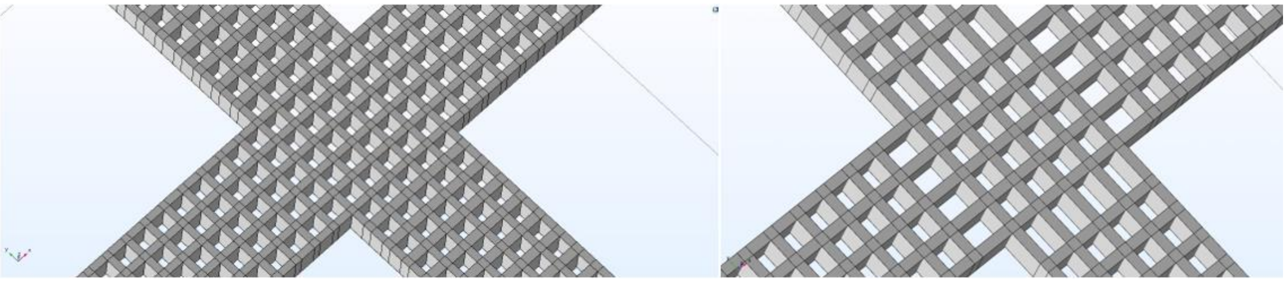

Figure 53 Central Vias pattern for UMC technology (left) and TSMC technology (right) design zoomed

- *UMC Dielectric layer's parameters:*

$$Volume: 3.653\ 10^{-15}\ m^3 \tag{84}$$

$$Mass: 8.037\ 10^{-12}\ kg \tag{85}$$

$$Density = 2200\ kg/m^3 \tag{86}$$

$$E = 69.99\ GPa \tag{87}$$

$$v = 0.1699 \tag{88}$$

$$\varepsilon = 4.2 \tag{89}$$

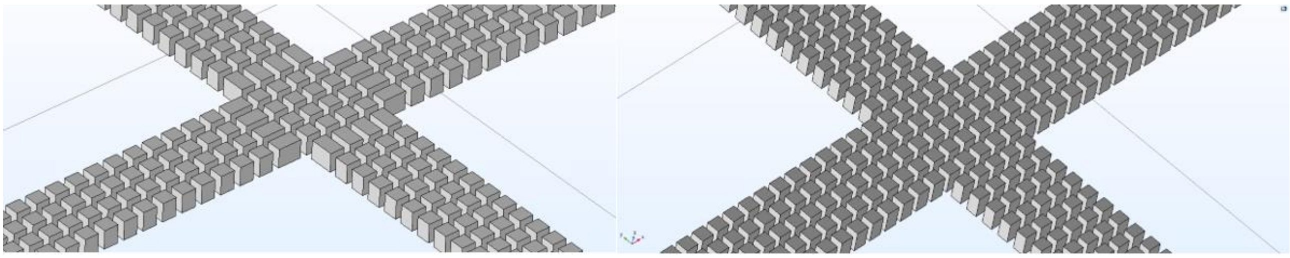

Figure 54 Central Dielectric pattern for UMC technology (right) and TSMC technology (left) design zoomed

Replacing the acquired parameters of each layer of the UMC technology in each correspondent layer of the composite TSMC geometry that COMSOL is able to simulate without high computational effort, the same final results already obtained for the composite central resonator part in the TSMC technology (section 4.1) are achieved. Therefore, the new mechanical and electrical parameters that can be extrapolated from this last simulation could be utilize to define a homogeneous layer representing the UMC central resonator part, and also the same steps performed in section 4.1 for the TSMC case can be carried out. However, since the results are almost identical this may represent the catalyst for the assumption for which the sensor fabricated in UMC should behave similarly to the one made in TSMC if exactly the same variation introduced by the fabrication process are applied, hypothesis that however still remain ideal and affected instead by random factors such as temperature variation, noises etc…. Moreover, thermal stresses have not been analysed for either the structures, but variations are expected also due to these reasons.

5. Accelerometer 180m, TSMC COMSOL Multiphysics Characterization

The interdigitated comb accelerometer principal behaviour is based on the measuring of the external acceleration by detection changes in the resonance frequency of its mechanical structure. Similarly with respect to the resonant capacitive pressure sensor, it consists of a composite proof mass suspended within a mechanical structure in most of the case in form of a spring-mass system. As clear from this kind of system, the mechanical structure is characterized by a resonance frequency at which it tends to vibrate more efficiently at its maximum amplitude variations and that depends mostly on the resonator mass and the stiffness of the structure. In order to provide the necessary energy input to sustain the oscillation, a voltage is applied between the movable and the fixed structure, hence allowing the geometry to resonate and to maintain its resonance at its fundamental frequency. However, when an external force acts on the accelerometer the proof mass moves leading to a shift in the resonance frequency. Indeed, this change in resonance frequency can be detected through different sensing mechanism such as piezoelectric or piezoresistive sensing, however in this proposed case a general simplified capacitive sensing is analysed and characterized on COMSOL. The gap space between the movable (belonging to the central resonant mass) and the fixed electrodes is altered by means of the external acceleration, thus a variation in the capacitance occurs in between. This output capacitance variation can then be detected and translated into an electrical signal which is related to the external input acceleration; thus, the sensitivity of the device can be defined. In conclusion, by monitoring the capacitance or other sensing parameters associated with the resonant structure, it is possible to detect and to measure the external acceleration variations in terms of changes in the resonant frequency. This kind of sensors are usually characterized by high sensitivity and precision; however, a good design is required in order to optimize their performance. As for the pressure sensor, two main designs of the accelerometer have been performed and simulated in terms of their mechanical and electrical parameters on COMSOL, the pre-fabrication and the post-fabrication case. Indeed, all the variations from one design to another rely on the well-founded variations obtained from the previously analysed resonant capacitive pressure sensor transition, which mainly act on the thicknesses. However, the TSMC version of the accelerometer has not been fabricated yet, hence no experimental data are available for this design. The principal purpose then, is to make assumptions on how the accelerometer will behave after fabrication if the same identical variations with respect the pre to post pressure sensor model will be introduced during its fabrication. The original theoretical dimensions of the accelerometer are reported in Table 3.

Table 3 Parameters 180nm TSMC Accelerometer prototype-A1 pre-fabrication

$W = 142.5um$	Width central resonator plate
$L = 142.5um$	Length central resonator plate
$W_{tot} = 256.12um$	Total width central resonator plate
$L_{tot} = 256.12um$	Total length central resonator plate
$L_h = 1.5um$	Perforation length
$s = 3um$	Spacing between perforations
$T_p = 3.87um$	Thickness central plate resonator
$L_{finger} = 29.81um$	Length movable fingers
$W_{finger} = 2.1um$	Width movable fingers
$L_{finger\ active} = 26.81um$	Fingers length participating to the sensing
$h_0 = 1.5um$	Horizontal air gap

Where W and L are the width and length of the central movable plate with no sides included respectively, W_{tot} and L_{tot} are the width and length of the central movable plate with sides and movable fingers included respectively, L_h is the length of the perforations, s is the spacing among central perforations, L_{finger} and W_{finger} are the length and the width of the movable fingers, $L_{finger\ active}$ is the length of the movable fingers that actively participates to the capacitance sensing (area of the parallel plate) and T_p is the thickness of the central movable plate that, since the considered tecnhology is always TSMC, does not change with respect the original one of the TSMC pressure sensor and that includes the thickness of the Metal5-Via5-Metal6 respectively for the central proof mass resonator and finally h_0 which is the air gap between the movable and the fixed electrodes.

5.1. Central Resonator TSMC characterization Accelerometer

The first characterization to perform in COMSOL is the simplification of the central resonant proof mass structure and the other blocks in order to reduce as much as possible the computation of the entire structure. Indeed, also for the accelerometer, the movable plate is made sequentially by Metal5-Vias5-Metal6, were Aluminium (Al) and Tungsten (W) are the materials used for the metal and the vias respectively. Between the vias there is Oxide (SiO_2). Even in this case there is the presence of many patterned vias between the two metal layers, moreover, an additional high number of small perforations with respect the pressure sensor is present. Additionally, a separate characterization of each of the single block that compose the entire accelerometer structure, such as fixed sensing electrodes, fixed support blocks and resonant central part, has been performed to simplify the computational effort. The principal aim of this simulation is to extract the most important parameters (Young's modulus, Poisson's ratio, density, permittivity, electrical conductivity) of each block of the entire structure and to describe a single central resonating homogeneous block that includes all the parameters and characteristics of each single layer of the composite version as performed in section 4.1 for the pressure sensor. For instance, the outermost blocks that act as the supporting structure of the springs are represented with a *transparency view* in COMSOL in Figure 55 and Figure 56 as well as the single fixed external sense electrode shown in Figure 57.

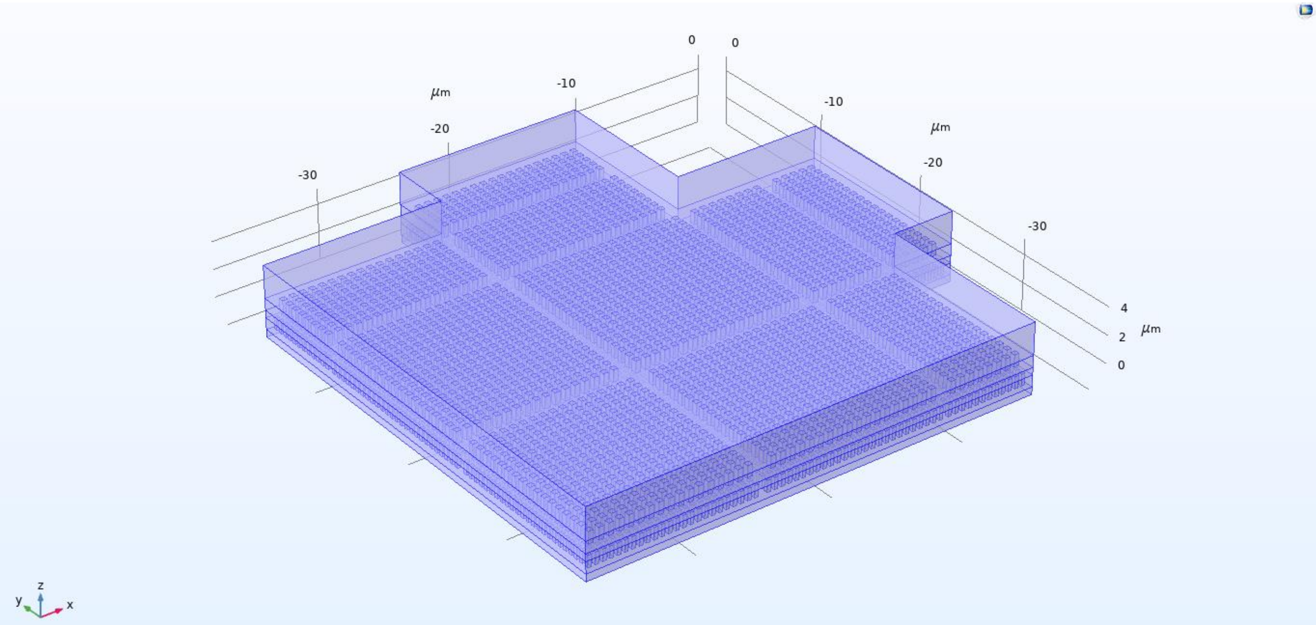

Figure 55 transparent view of the supporting outermost block for the springs that carries the central resonator proof mass. It can be clearly seen the path of the Vias below the Metal6

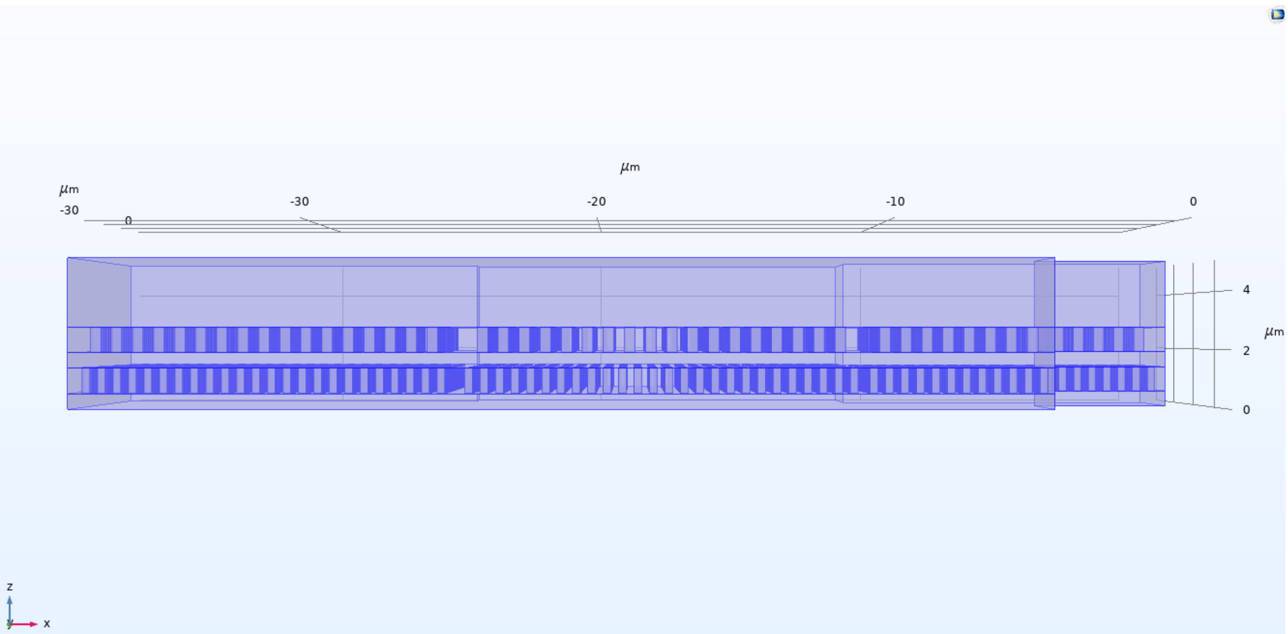

Figure 56 clear prospective of the vias by means of transparent side view of the supporting outermost block for the springs that carries the central resonator proof mass. In sequence from the bottom there is metal4-Via4-Metal5-Via5-Metal6, between the vias there is the presence of oxide

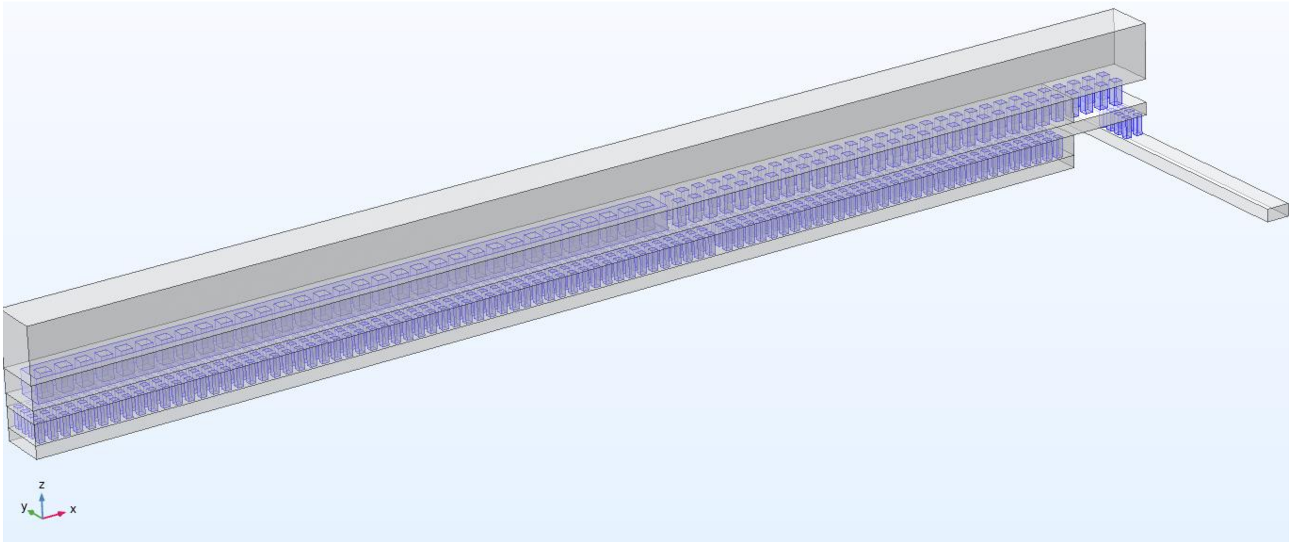

Figure 57 Single Fixed sense electrode, underlined in blue colour the Vias4 and Vias5 from the bottom to the top, between the vias the presence of oxide

The central resonator proof mass part has been minutely characterized by all its layers. A general view, a clipping plane view and a top view with hidden Metal6 layer have been reported accordingly in Figure 58, Figure 59 and Figure 60.

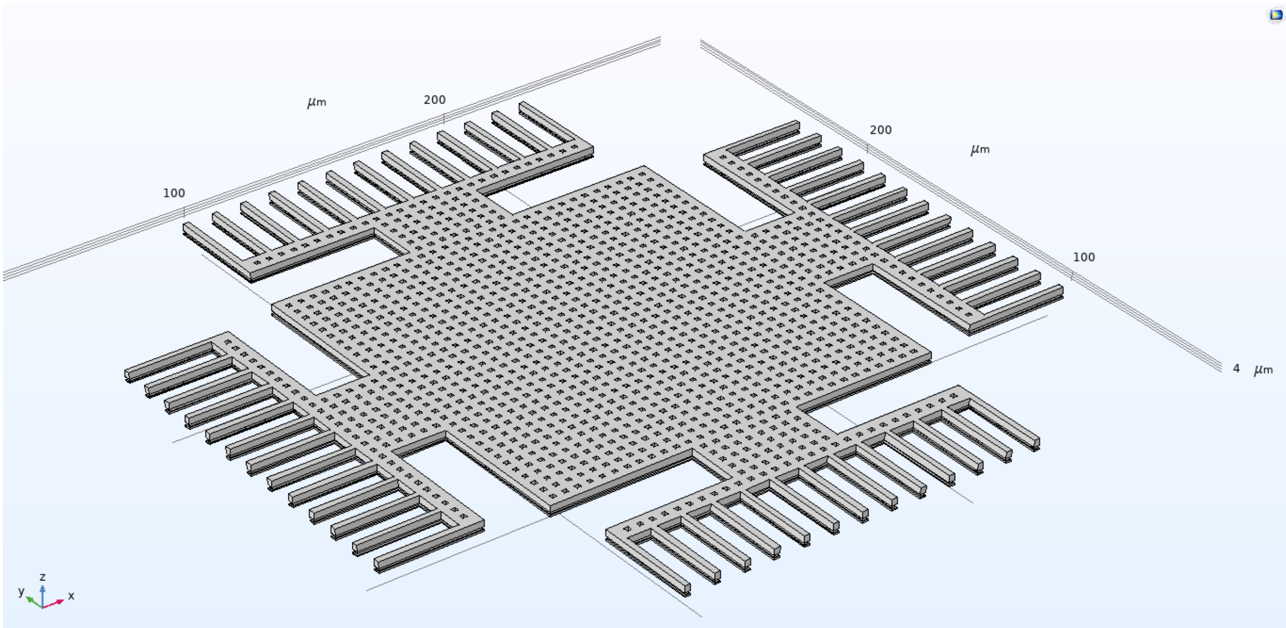

Figure 58 General view of the Central resonator proof mass part of the CMOS-MEMS Accelerometer

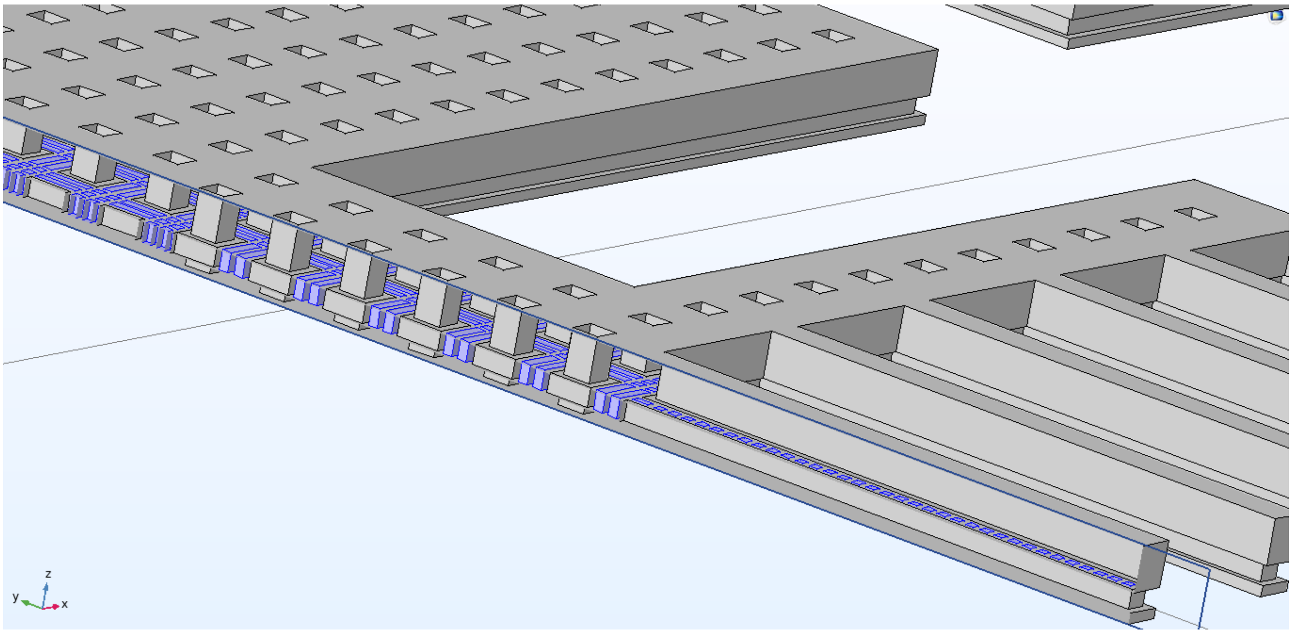

Figure 59 Zoomed Clipping plane view of the Central resonator proof mass part of the CMOS-MEMS Accelerometer. In blue is underlined the oxide layer that must exist within the metal layers and between the Vias. The thickest top layer is the Metal6 while the thin bottom layer is Metal 5

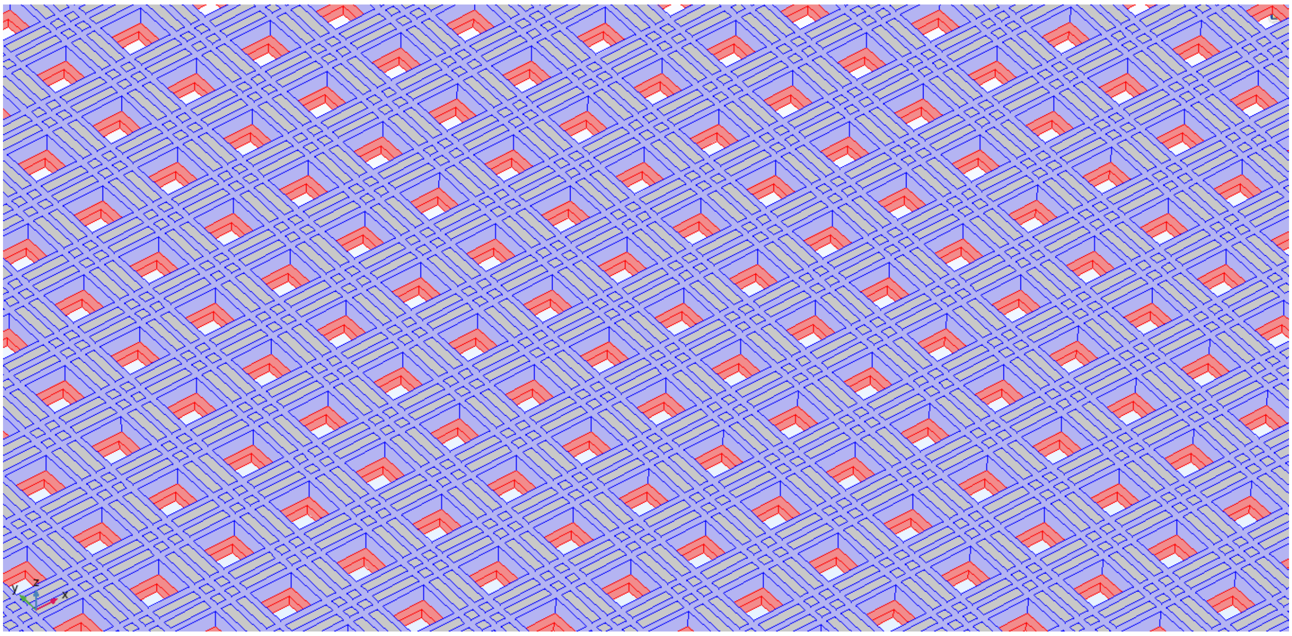

Figure 60 Zoomed top view of the Central resonator proof mass part of the CMOS-MEMS Accelerometer with hidden TOP Metal6 layer. Underlined in blue the Vias (Vias5) that exist between Metal6 and Metal5, while in red the bottom Metal5 layer

Similarly to the previous analysed structure, it is important to be aware about the difference between the simplified and composite structure which relies mainly on the variation among the volumes of those, this as a consequence of choosing a single homogeneous block with respect to a composite one: despite the exact same thickness exploited for both the geometries, the total structure does not include in the volume the spaces present next to the outermost vias, which indeed are represented by air; on the contrary, the simplified version includes this spaces in its geometry due to the intrinsic simplification as a single block layer as was for the pressure sensor central resonator. Figure 61 and Figure 62 clarify this concept.

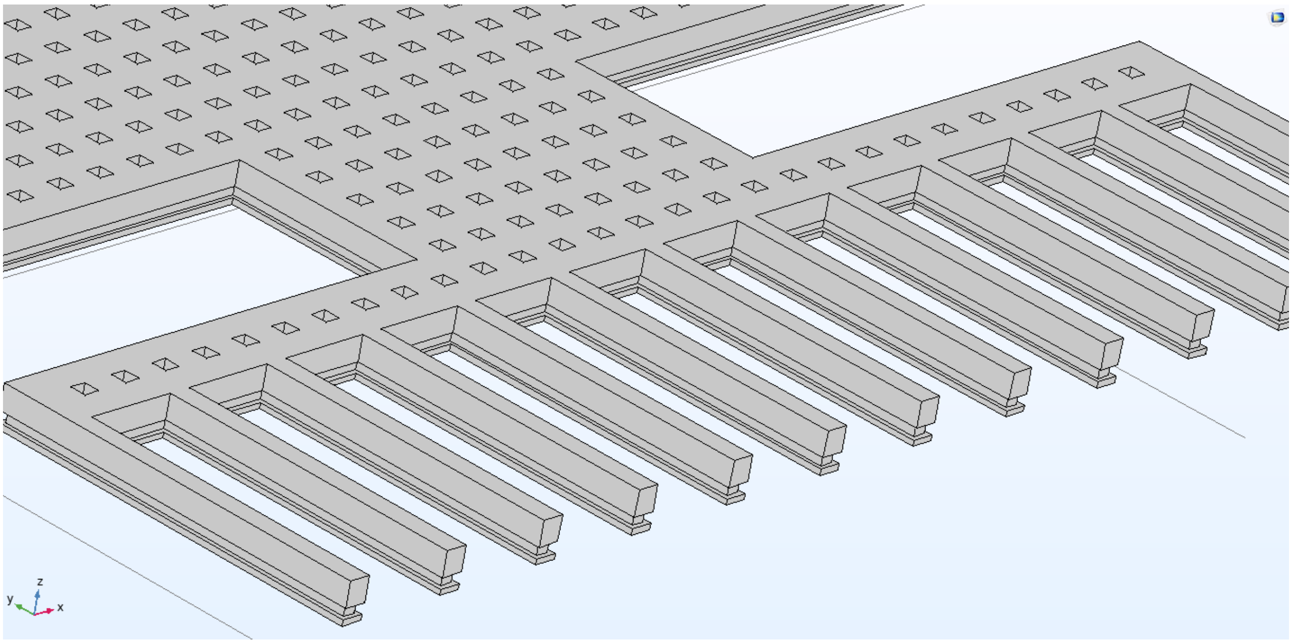

Figure 61 Composite central resonator proof mass

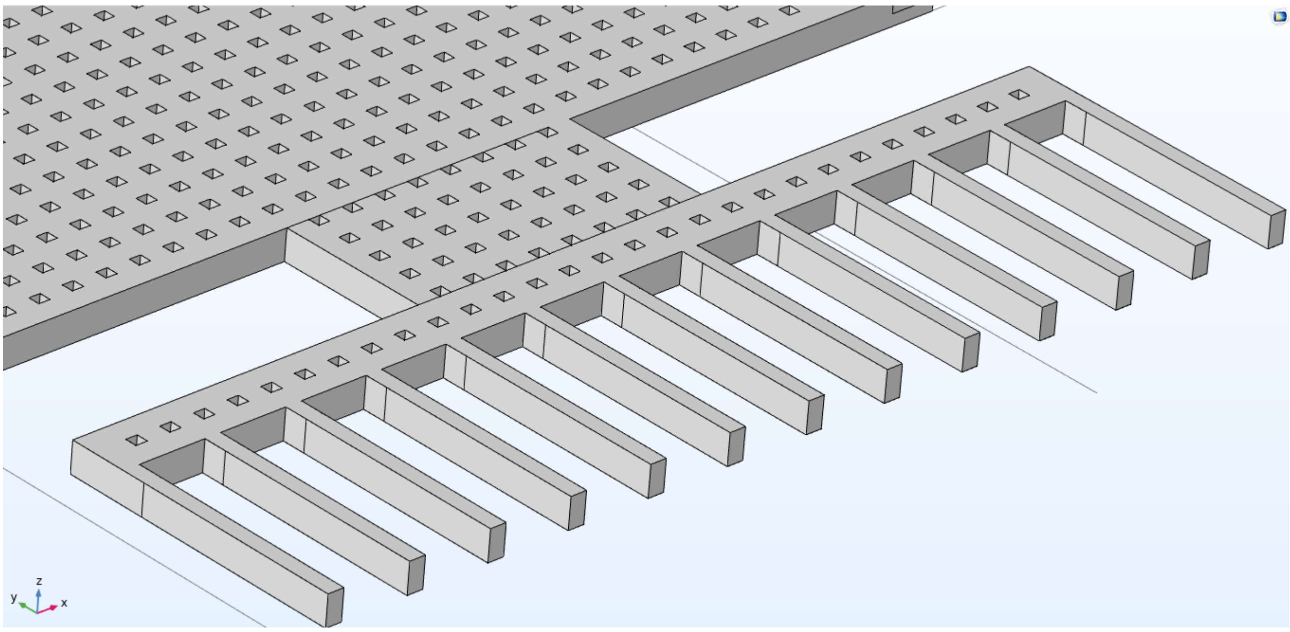

Figure 62 Homogeneous central resonator proof mass

Figure 62 reports the homogeneous central resonant plate with the same mechanical and electrical property of the composite one “mounted” on the total structure. Figure 61 reports the composite (M5-Vias5+SiO_2-M6) central resonant plate were clearly no volume is present nearby the most external vias nor within the small perforations that characterize the entire structure. Nevertheless, the density of the two is the same, thus a very small variation on the resonance frequency with respect the one that is obtained from the simulation should be taken into account due to this simplification, mainly due to the effect of damping acting on the highly perforated structure. Utilizing the proper materials for each layer, hence each characterized by their own density, Young’s modulus and Poisson’s ratio, the correspondent volume and the mass can be achieved:

$$Volume_{composite\ central\ res} = 101100.0um^3 = 1.011 * 10^{-13}\ m^3$$

(90)

$$mass_{composite\ central\ res} = 4.853 * 10^{-10}\ kg$$

(91)

Once defined the proper boundary conditions the mechanical properties of the entire central resonating part are obtained:

$$Density_{composite} = \frac{m}{V} = 4800.593\ kg/m^3$$

(92)

$$E_{composite} = \frac{0.011512\ J * m^3}{1.011 * 10^{-13}\ m^3} = 113.867\ GPa$$

(93)

$$v_{composite} = \frac{3.1374 * 10^{-14}\ m^3}{1.011 * 10^{-13}\ m^3} = 0.31$$

(94)

As described in section 4.1, the values at the numerator of the Young’s modulus and Poisson’s ratio obtained from COMSOL must be divided by the volume of the structure itself. It must be underlined that the volume used in this case is exclusively the one of the composite geometry. Once set the relative standard permittivities of SiO_2 and aluminium, and a relative permittivity of 1 for the tungsten, the relative permittivity (relative dielectric constant) of the central resonator has been extrapolated from COMSOL:

$$\varepsilon_{composite} = \frac{1.2787 * 10^{-13} m^3}{1.011 * 10^{-13}\ m^3} = 1.265$$

(95)

Similarly, the value of the electrical conductivity that characterize the central resonator has been found performing an *average* evaluation among the whole geometry:

$$\sigma_{avarage} = 3.234 * 10^{7} S/m$$

(96)

While the maximum one is the aluminium's which is equal to:

$$\sigma_{max} = 3.774 * 10^{7} S/m$$

(97)

Since the permittivity is very close to 1, it seems that this structure is more conducting with respect the one of the pressure sensors, this behaviour is likely to be due to the higher integration of vias and high volume covered by the metals, which indeed show a relative permittivity close to the one of air. As stated, isotropic values of permittivity have been considered. At this point a new homogeneous material can now be exploited in the general geometry of the resonant capacitive accelerometer as the central perforated plate. On the contrary, leaving unchanged the dimensions in terms of length, thickness, width and spacing, the volume and the mass of the homogeneous central structure with original theoretical thickness results to be respectively equal to:

$$Volume_{homogeneous} = 1.075 * 10^{-13}\, m^{3}$$

(98)

$$mass_{homogeneous} = 5.161 * 10^{-10} kg$$

(99)

Those values are higher with respect the ones obtained in the composite case coherently to the pressure sensor resonator. Regarding the fixed sense electrodes and the fixed supporting blocks, the correspondent extrapolated parameters are:

$$Volume_{fixed\ electrodes\ composite} = 541.77 um^{3}$$

(100)

$$mass_{fixed\ electrodes\ composite} = 2.211 * 10^{-12}\, kg$$

(101)

$$Density_{fixed\ electrodes\ composite} = \frac{m}{V} = 4080.698\, kg/m^{3}$$

(102)

$$E_{fixed\ electrodes\ composite} = 98.785\, GPa$$

(103)

$$v_{fixed\ electrodes\ composite} = 0.287$$
(104)

$$\varepsilon_{fixed\ electrodes\ composite} = 1.756$$
(105)

$$Volume_{fixed\ block\ composite} = 6510.8um^3$$
(106)

$$mass_{fixed\ block\ composite} = 2.241 * 10^{-11}\ kg$$
(107)

$$Density_{fixed\ block\ composite} = \frac{m}{V} = 3442.894\ kg/m^3$$
(108)

$$E_{fixed\ block\ composite} = 85.306\ GPa$$
(109)

$$v_{fixed\ block\ composite} = 0.265$$
(110)

$$\varepsilon_{fixed\ block\ composite} = 1.7002$$
(111)

All the obtained values for each component of the accelerometer have then been substituted in the respective homogeneous structure, in order to form the general homogeneous version of the accelerometer. As quoted, this slight variation of volume for the actual simulated total accelerometer structure may provide a resonance frequency not exactly equal to the correct expected one. This effect has been neglected as small and not significant. Figure 63 shows the general sensor formed by the different homogeneous blocks.

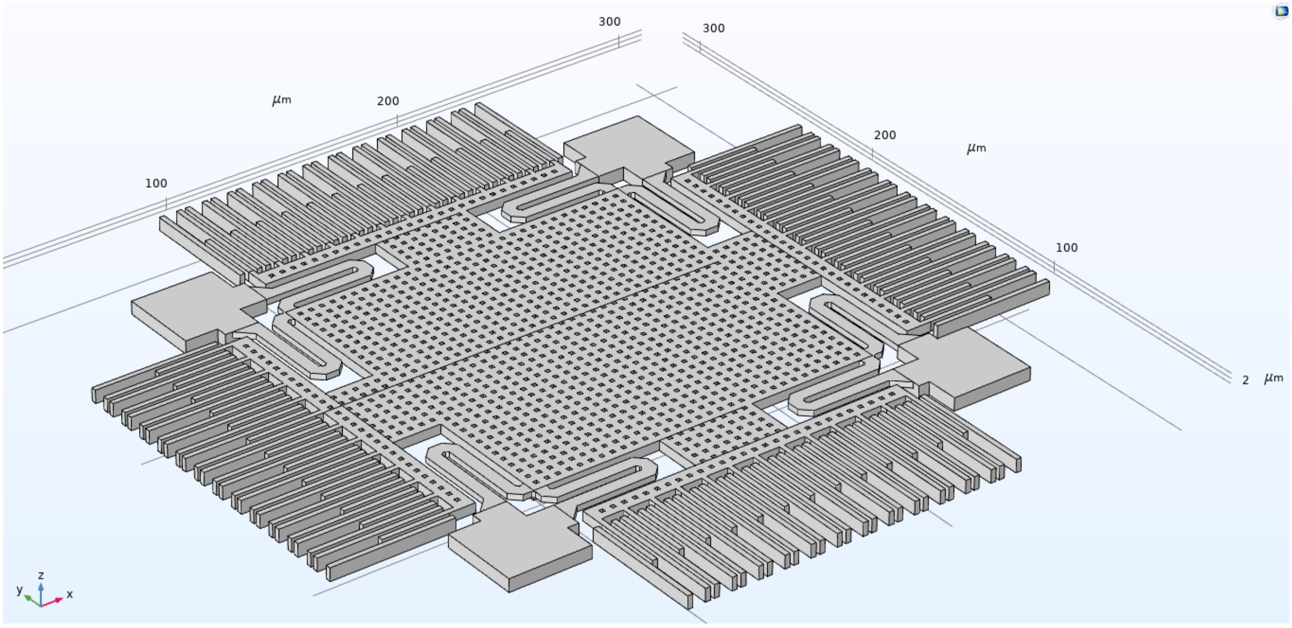

Figure 63 General homogeneous accelerometer structure

6. Accelerometer Technical implementation in COMSOL

The structure analysed in this proposed study is made of four springs characterized by the same dimensions of the ones exploited in the resonant capacitive pressure sensor. When the device is subjected to an external acceleration the restoring force from the springs induces a displacement of the proof mass. To model this behaviour in COMSOL the *Electromechanics* interface has been used similarly as for the pressure sensor, with air deforming gaps between the electrodes in which the applied physic tends to model the electric field and it tends to apply the appropriate deformation as a consequence to the electrostatic forces. Indeed, the deformation of the gaps between electrodes results in nonlinear geometrical effects, which are included in the Electromechanics Multiphysics interface by default. Particularly, the entire geometry has been characterized with a *Body Load* constraint in the *Solid Mechanics* physic interface with an acceleration acting on the x direction only and that depends on the density of the total structure including the resonator itself ($solid.rho$) as:

$$Force\ per\ unit\ of\ volume = \ acceleration * solid.rho * g\_const \left[\frac{N}{m^3}\right]$$

(112)

Where the g_const is COMSOL's default name for $9.81\ [m/s^2]$. With the exception of the movable central resonating part, all the other components, such as fixed electrodes and spring support blocks have been mechanically anchored with a *Fixed constraint* node. In the *Electrostatics* physic interface, the fixed electrodes (in charge of capacity sensing) have been set at constant potentials, and more in particular, the left ones with respect the movable mass have been set to $+0.5mV$ while the right ones to $-0.5mV$. On the contrary, the proof mass has been set to ground. Now, in a real device, the proof mass with its attached moving electrodes is generally floating at a potential close to one half of the supply voltage, and also, instead of a DC, a high frequency square wave swinging between zero and the full supply voltage is applied with opposite phase to the fixed sense electrodes on each side of the moving electrodes during normal operation, and this is done in order to reduce eventual parasitic capacitance that may acquire during the sensing. For the proposed study, only the stationary part of the square wave is modelled, hence a *Stationary* study is used. Therefore, a $1V$ supply voltage applied to the entire device corresponds to a $+0.5mV$ and $-0.5mV$ to the alternated fixed sense electrodes giving the possibility to detect the corresponding static capacitance.

6.1. Fringing fields effect

Most of the standard accelerometer MEMS use the parallel plate configuration. XY-axis (in-plane) accelerometers are built with many parallel plates capacitors in order to increase the amount of overall capacitance change that occurs between the fingers at different potential. The most generic formula for the computation of the capacitance may be exploited

$$C = \varepsilon \frac{S}{d}$$

(113)

With S the overlapping area and d the air gap distance between the movable and fixed fingers. However, whenever the dimensions of this devices are comparable with the air gap between the movable and the stationary fingers, this formula is not appropriate anymore since it takes into account exclusively the uniform electric field that arises between overlapping surfaces, hence underestimating the actual capacitance value. In the real conditions, electric fields that arises outside the overlapping surfaces (Figure 64) must be taken into account, this are called fringing fields. Depending on the length of the field line, a higher capacitance value occurs with respect the one computed with the classic formula (113).

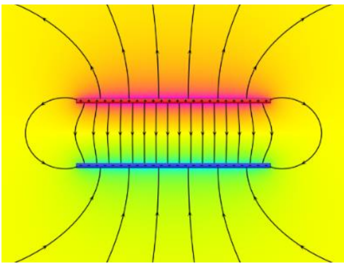

Figure 64 Fringing fields effect on a capacitance

FEM simulations are crucial for the evaluation of this effect. In fact, COMSOL uses finite element methods (FEM) to numerically solve the governing equations for electric fields, which includes the Poisson's equation or the Laplace equation depending on the setup. Therefore, an accurate computation of the electric field distribution, potential distribution, and subsequently, the capacitance of the system can be easily performed without the need of external manual computation. However, if the problem is complex the results may be provided after a very high computation time, that is the main reason why geometries are often defined with simplified shapes, hence their behaviour can be defined by easier formulas. In some cases, doing so, an important underestimation can cause the final results to be wrong. Cezary Maj and Michal Szermer [23] have provided the underestimation when no fringing fields are taken into account under various geometrical conditions for a parallel plate configuration accelerometer and proper sizing equation for comb-drive accelerometer. The geometry under test must be properly modelled in COMSOL in order to observe the behaviour of fringing fields, thus in order to correctly deduce the capacitance among the fingers. COMSOL provides a tutorial on how to observe the effect of fringing fields acting on a parallel plate capacitance [24], however during the computation of the sensed capacitance COMSOL takes automatically into account this effect.

6.2. Simulations on the theoretical Pre-Fabrication Capacitive Accelerometer

The geometrical characteristics used for the pre-fabrication accelerometer characterization are the following:

$$T_{fixed\ blocks} = 5.25um \tag{114}$$

$$T_{springs} = 2.34um \tag{115}$$

$$T_p = 3.87um \tag{116}$$

$$m_{homog} = 5.161 * 10^{-10} kg \tag{117}$$

$$\boldsymbol{f_{r_{generic}} = 106.89\ kHz} \tag{118}$$

$$k_{generic} = 232.796\ N/m \tag{119}$$

$$\boldsymbol{f_{r_{horizontal}} = 471.46\ kHz} \tag{120}$$

$$k_{horizontal} = 4528.889\ N/m \tag{121}$$

$$Q_{at\ f_{r_{generic}}} \cong 80.5 \tag{122}$$

$$Q_{at\ f_{r_{horizontal}}} \cong 48.6$$

(123)

Where $f_{r_{generic}}$and its correspondent $k_{generic}$ are the first resonance frequency and stiffness that COMSOL specifies for the geometry, hence the mechanical properties that include principally the vertical movement. On the contrary, $f_{r_{horizontal}}$ is exclusively resonance frequency dedicated to the horizontal movement, thus the one of interest, since is the direction on which the capacitance will be detected. Particularly, to simulate the effect of an external acceleration acting on the movable resonant part the most real condition has been used giving the possibility of free movement in all direction to the movable central mass, hence resulting in a worst-case condition regarding the sensing operation. Considering that the accelerometer is made of 13 movable fingers at each lateral side, the value of the non-differential sensed capacitance, with acceleration acting on x (or y), is estimated from the movement of $13 * 2$ movable fingers. However, for the computation of the overall sensed capacitance, so for the estimation of the electrical sensitivity, it will be exploited the total surface charge density (reported in COMSOL in $Coulomb$) of all the surfaces that actively contribute to the sensed capacitance (blue areas highlighted in Figure 65, to be added to the ones on the other side of the accelerometer, see section 3.5), since they take into account the deformations induced by the applied acceleration and the resulting redistribution of charges: subtracting the value of the surface charge density of the specified $13 * 2$ surfaces obtained at $50g$ of acceleration with the value obtained at $0g$ and dividing the result for the voltage applied across the terminals ($0.5mV$), and after dividing again the result for the range of acceleration used in the simulation ($50g$), the gradient, hence the sensitivity of the accelerometer in that direction, can be estimated in $Farad/g$. The estimation of the surface charge density change (as a consequence of the displacement induced by the acceleration/deceleration) can be easily achieved in COMSOL. For the following simulations, the sensed capacitance is related to an external acceleration acting exclusively on the x direction.

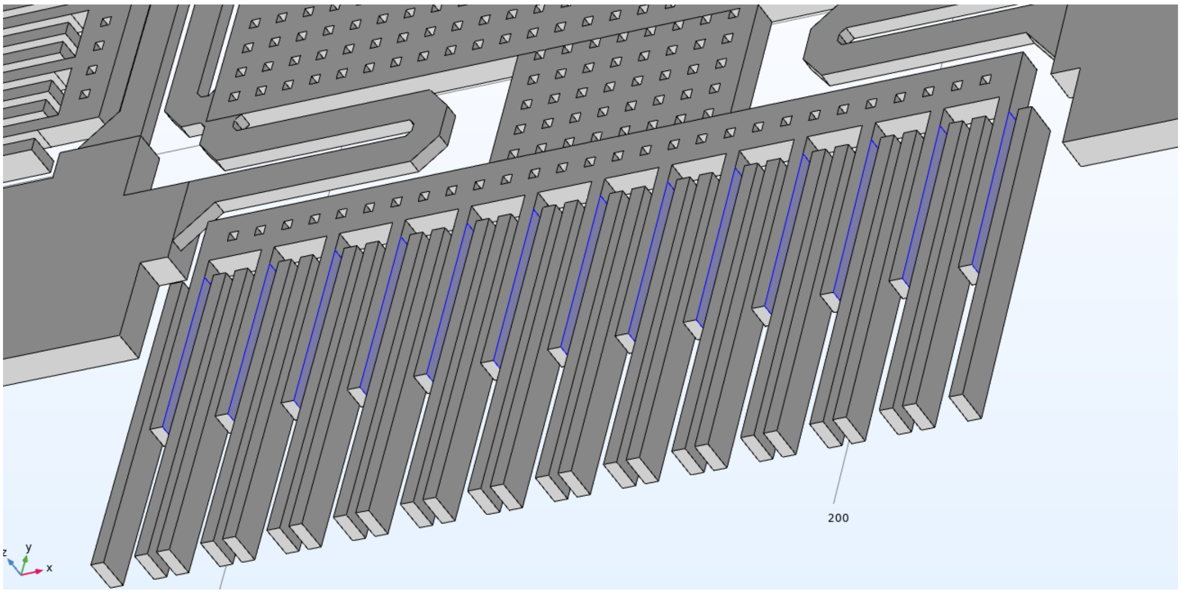

Figure 65 The blue areas are the surfaces that actively contribute to the sensed capacitance. These must be added to the ones on the other side of the accelerometer if acceleration/deceleration along x is the one to be estimated

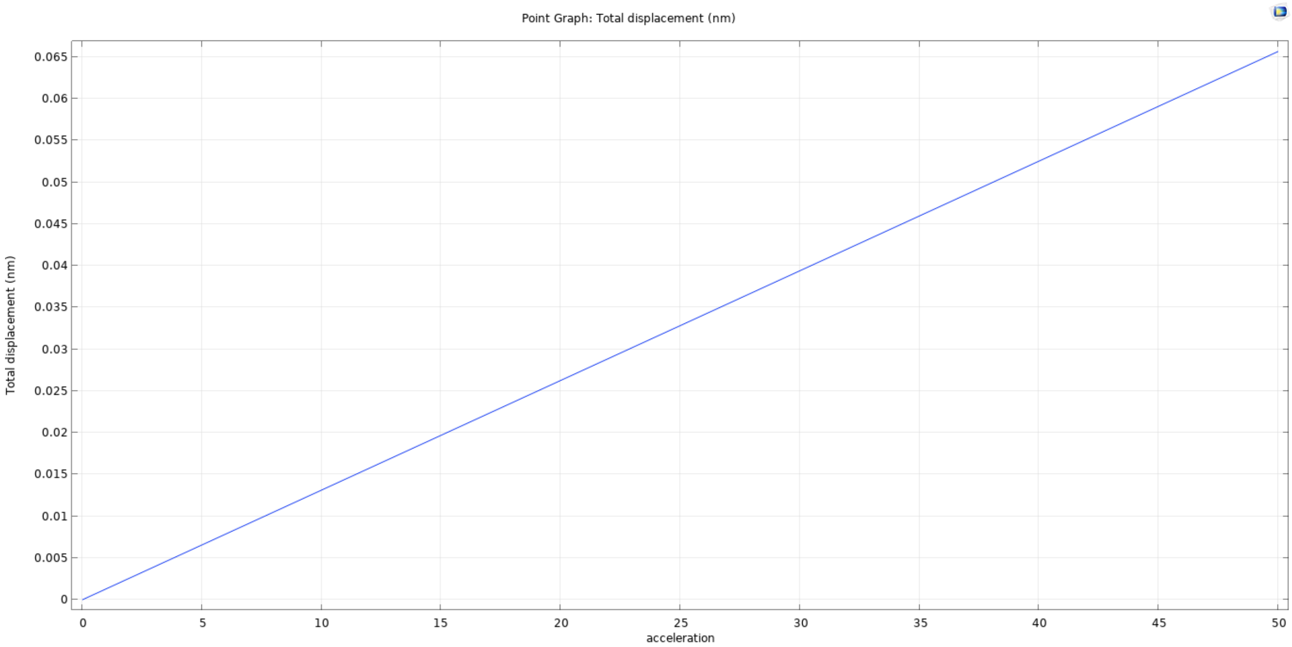

Figure 66 Pre-fabrication accelerometer displacement of a point belonging to one movable finger vs acceleration at +-0.5mV of Biasing. From it the mechanical sensitivity can be estimated

From an ideal theoretical aspect, the formula to compute the mechanical sensitivity of an accelerometer is

$$S = \frac{1}{f_r^2}$$

(124)

Where f_r is the estimated resonance frequency in Hz. Particularly, this formula relates to the mechanical sensitivity of an idealized resonant accelerometer under specific assumptions. For instance, it models the device when it operates in its resonant mode and exhibits a linear response over a certain range of frequencies. Therefore, this formula may not accurately reflect the behaviour of real-world accelerometers that instead are characterized by more complex design features, non-linearities, and variations in their mechanical response. The actual mechanical sensitivity of an accelerometer will depend on its specific design, materials, and operating conditions. However, as a first approach, and in order to check if COMSOL is computing properly the behaviour of the accelerometer, this formula can be used to have an initial idea on the mechanical sensitivity of the design. In fact, the horizontal resonance frequency must be taken into account since the horizontal motion (in-plane) of the structure is the one of interest for the sensing of capacitance, hence the value of the horizontal resonance frequency of value $471kHz$ it is used to find the theoretical mechanical sensitivity which is on the order of $4.5 * 10^{-12} \frac{1}{Hz^2}$. This is indeed comparable to the mechanical sensitivity obtained from the displacement of the proof mass under the external acceleration as visible in Figure 66, and that it is equal to:

$$S = \frac{0.065nm}{50g} = 1.3 * 10^{-12} ms^2/m$$

(125)

Therefore, while the first formula provides a simplified relationship between mechanical sensitivity and resonance frequency in some ideal cases, it is crucial to consider the specific characteristics and limitations of the accelerometer in question for accurate predictions and measurements of mechanical sensitivity.

In section 2.4 and 4.1 the concept of getting a good trade-off between mesh and computational time in COMSOL has often been reiterated. Due to the choice of measuring the sensed capacitance exploiting the surface charge density present on smaller repeated surfaces of the accelerometer, a good mesh in the $x - y$ directions (in-plane movement) is necessary to have reliable results. However, in order to not increase hugely the computational time, a simple way to provide a better mesh localized in a specific volume of the structure is to add a smaller block of air that contains the sides of the accelerometer where the surface charge will be detected, with movable and fixed fingers included in it (see Figure 67). This simulation is extremely sensitive to the chosen mesh, mostly affecting the order of magnitude expected of the charge density.

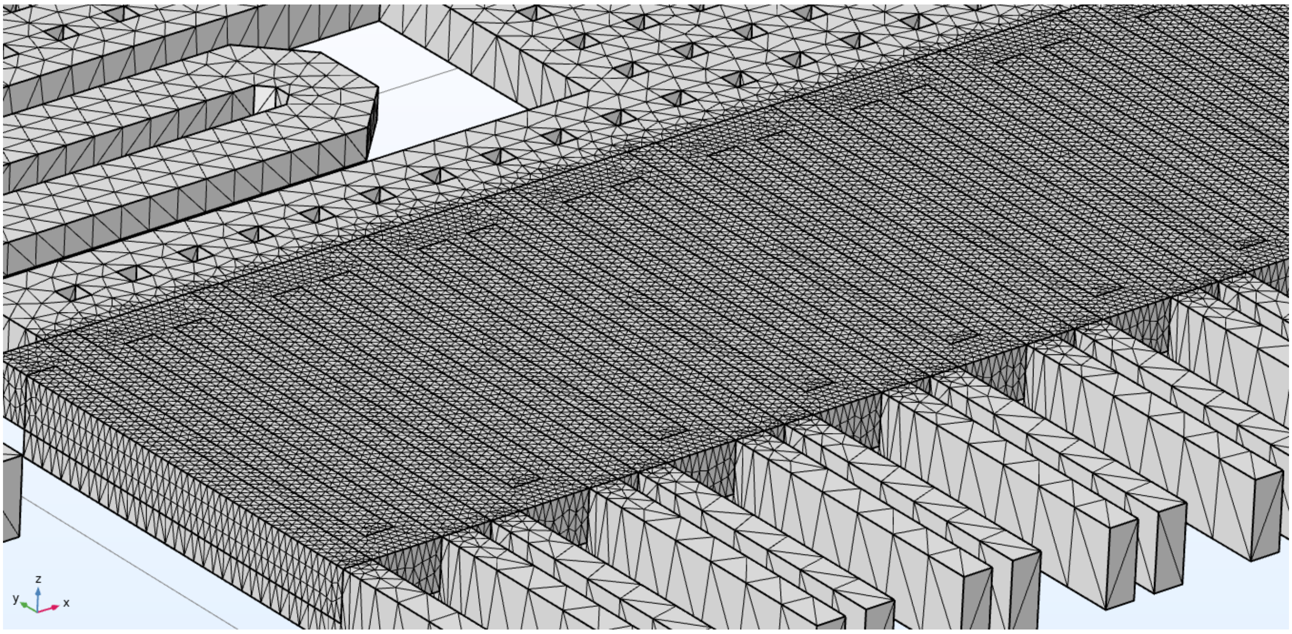

Figure 67 Optimized mesh localized in the region for the sensing of surface charge density performed with a block of air. As can be observed the vertical mesh is less complex with respect to the horizontal one.

Additionally, thanks to the use of a finer mesh, it is also possible to appreciate a proper effect of fringing fields acting on the side of structure. The peak of fringing fields results very high with a maximum value of $700\,V/m$. Additionally, this effect seems to be the highest between the fixed electrodes and it seems to decrease between the fixed and the movable ones, but it remains still significant and around $100 - 200\,V/m$ as visible in Figure 68 where the red areas represent the more concentrated effect.

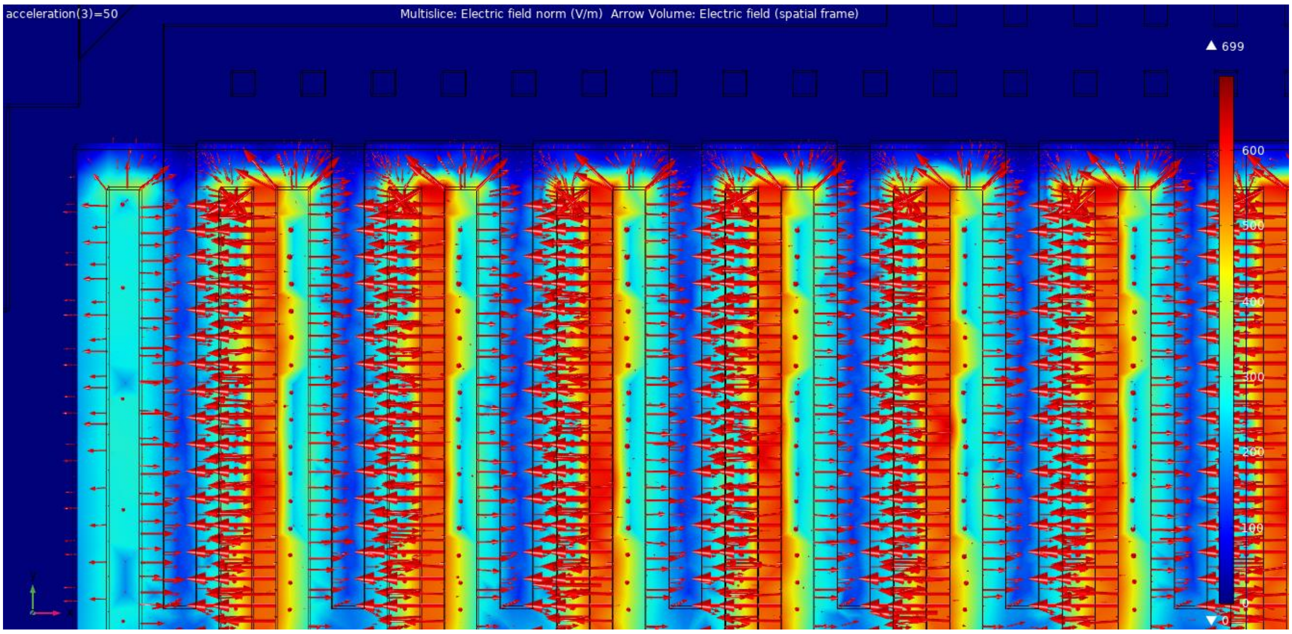

Figure 68 Pre-fabrication accelerometer, effect of fringing fields at 50g and +-0.5mV of bias

Regarding the values of the charge density computed on the quoted surfaces with no prescribed displacement defined for the central movable part, it is possible to obtain the capacitance and the sensitivity vs the acceleration applied at $+-0.5mV$ of biasing:

$$Surface\ charge\ at\ 0g = 8.11881 * 10^{-18}C \tag{126}$$

$$Surface\ charge\ at\ 50g = 8.11914 * 10^{-18}C \tag{127}$$

$$Capacitance\ sensed\ at\ 0g = 1.62376 * 10^{-14}F \tag{128}$$

$$Capacitance\ sensed\ at\ 50g = 1.62383 * 10^{-14}F \tag{129}$$

$$Sensitivity = \frac{6.6188 * 10^{-19}F}{50g} = \mathbf{1.324 * 10^{-20}F/g} \tag{130}$$

The sensitivity obtained with working accelerometers manufactured in the past also for z-axis acceleration detection [21, 25], resulted to be of the order of aF/G ($G \approx 9.81\,m/s^2$). It is clear that the accelerometer under test does not provide such sensitivity, hence the capacitance change in response to the external acceleration may be too small to be detected by the read-out, which means that the sensor is too little sensitive. The main reason for this is the used springs arrangement, which is optimized for a vertical movement of the proof mass and not for a horizontal one. Indeed, the horizontal displacement is extremely smaller with respect the vertical one, thus a new typology of arrangement may be taken into account to improve the sensitivity. Another factor hides under the variation of the charge density. A bigger variation should occur when an acceleration different from $0g$ is applied, to achieve this it is plausible to use a greater active area, therefore involving movable fingers with a greater area. An alternative to the latter quoted reason, is to decrease the gap between the movable and the fixed fingers, but this can be achieved exclusively whenever the manufacturer's design rules allow it.

6.3. Simulations on the theoretical Post-Fabrication Capacitive Accelerometer 180nm TSMC

To be consistent with the variation introduced by the pressure sensor post-fabrication case, the used characteristics of the post-fabrication accelerometer geometry are the following:

$$T_{fixed\ blocks} = 5.08um \tag{131}$$

$$T_{springs} = 2.17um \tag{132}$$

$$T_p = 3.494um \tag{133}$$

$$m_{homog} = 4.6596 * 10^{-10}kg \tag{134}$$

$$f_{r_{generic}} = 100.52kHz \tag{135}$$

$$k_{generic} = 185.874\ N/m \tag{136}$$

$$f_{r_{horizontal}} = 477.23\ kHz$$

(137)

$$k_{horizontal} = 4189.516N/m$$

(138)

$$Q_{at\ f_{r_{horizontal}}} \cong 48$$

(139)

Similarly with respect to the pre-fabrication case, the mechanical sensitivity can be evaluated form the Total displacement with respect the acceleration plot reported in Figure 69.

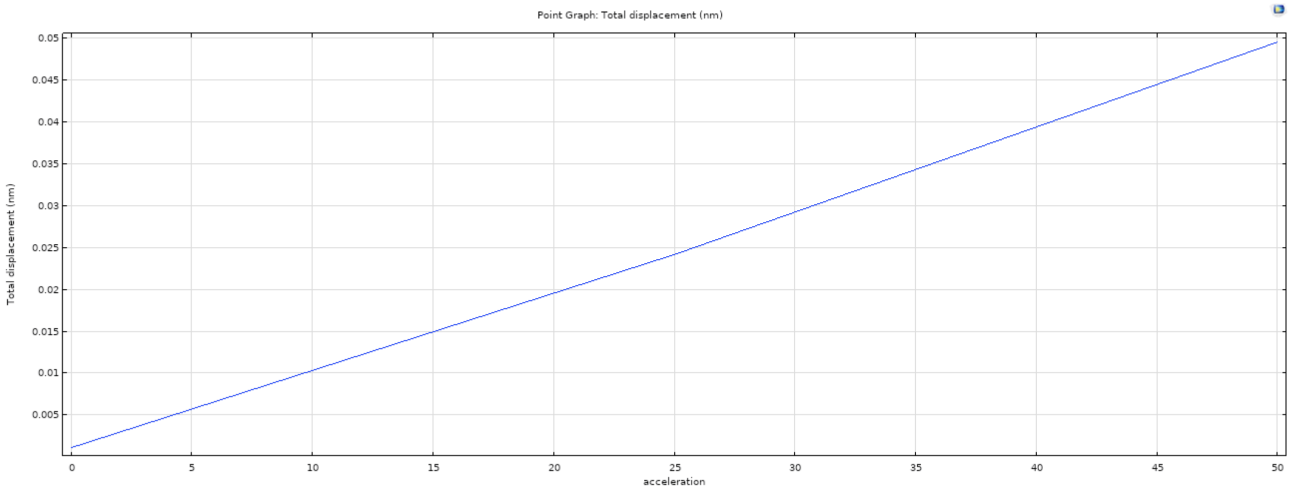

Figure 69 Post-fabrication accelerometer displacement of one movable finger vs acceleration at +-0.5mV of biasing

From the obtained displacement looks that the mechanical sensitivity is comparable to the pre-fabrication case. A simulation related to the effect of fringing field is performed. The maximum value results to be much higher with respect the previous case as a possible consequence of the *Proximity Effect* and the *Electric field concentration*. Regarding the former, the closer proximity results in stronger electric field interactions between adjacent elements and the distance between conducting elements (such as electrodes) is reduced in thinner structures. The electric field lines tend to curve or "fringe" outward from the edges of these elements, resulting in higher field strength at the edges and in the regions between them; the latter is the effect for which the electric field concentrates mostly in specific regions, particularly near the edges or corners of conductive elements. The concentration of electric field lines in these areas can result in higher fringing fields. The maximum fringing field value is around $1000V/m$ ($0.001V/um$) with similar considerations of the pre-fabrication case (Figure 70, Figure 71).

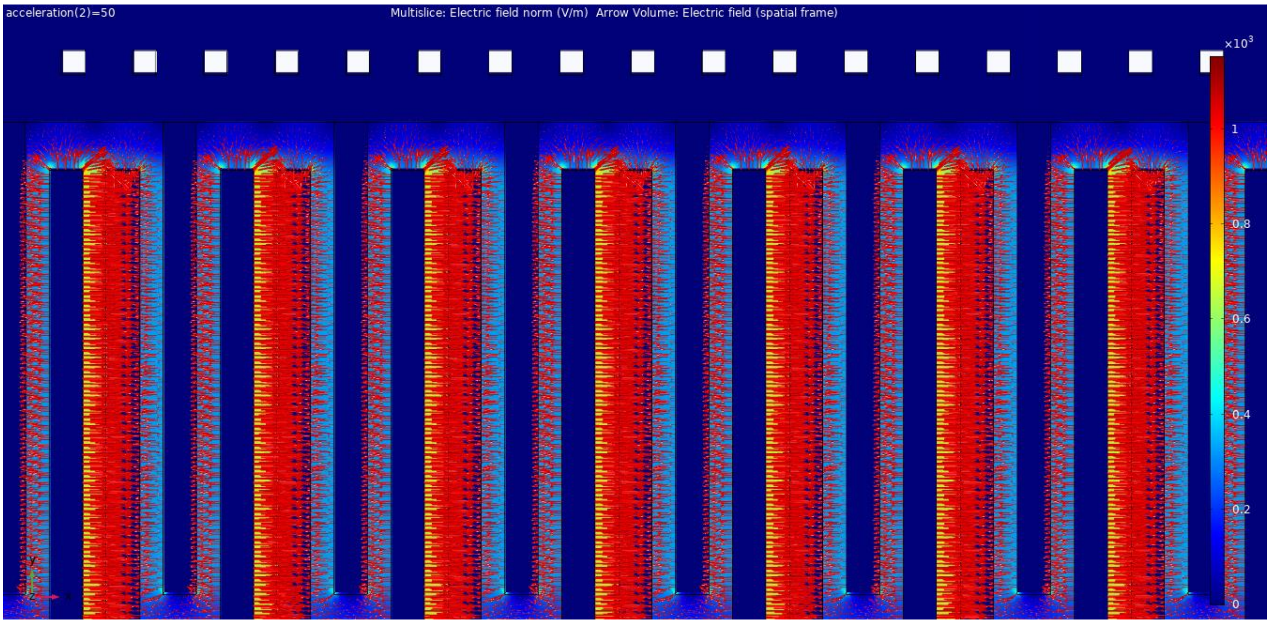

Figure 70 Post-fabrication accelerometer, effect of fringing fields at 50g and +-0.5mV of bias

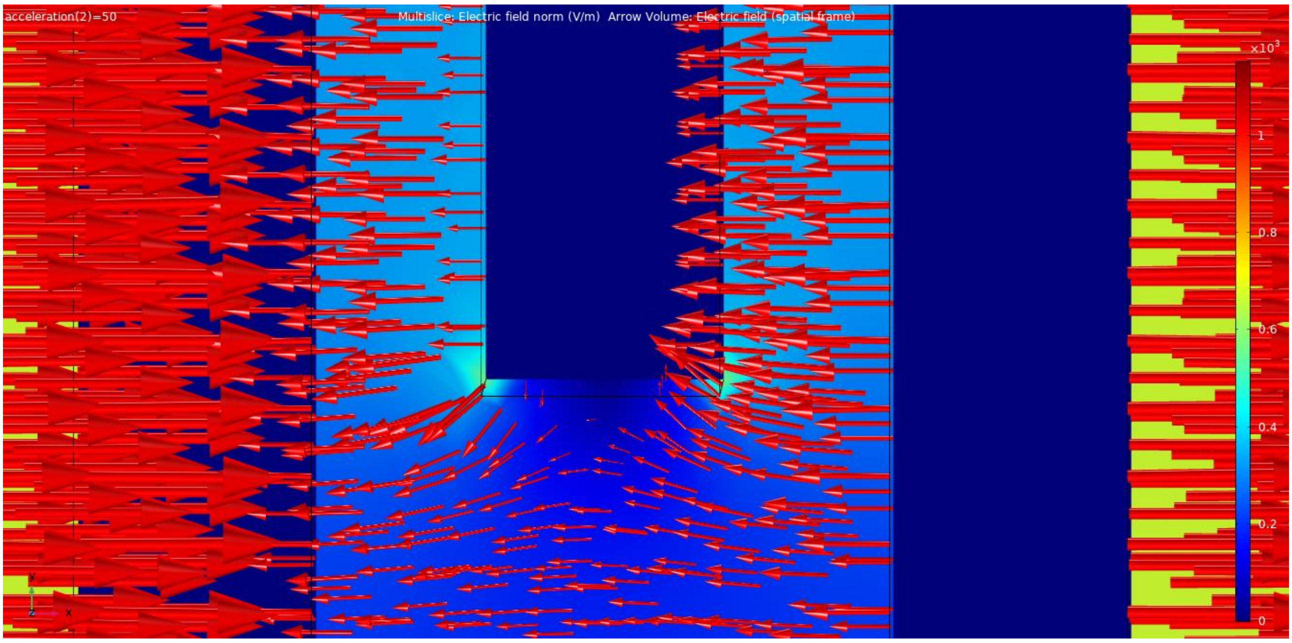

Figure 71 Post-fabrication accelerometer, effect of fringing fields at 50g and +-0.5mV of bias zoomed on the movable finger

Due to the difference between the pre and post-case, it is fundamental to take into account the effect of fringing field in this second case, else a higher error on the computation of the capacitance may occur. Of course, also in the pre-fabrication case is compulsory to take into account this effect, but comparing the two geometries, a lower error on the computation of the capacitance will be present in the pre-fabrication case due to a slightly smaller electric field acting on the structure with respect the post-fabrication one. However, COMSOL takes automatically care of the effect of fringing fields in the computation of other parameters, such as surface charge density.

Regarding the values of the charge density computed on the surfaces specified in section 6.2, with no prescribed displacement defined for the central movable part, it is possible to obtain the capacitance and the sensitivity vs the acceleration applied at $+-0.5mV$ of biasing:

$$Surface\ charge\ at\ 0g = 7.26144 * 10^{-18}C \tag{140}$$

$$Surface\ charge\ at\ 50g = 7.26172 * 10^{-18}C \tag{141}$$

$$Capacitance\ sensed\ at\ 0g = 1.45229 * 10^{-14}F \tag{142}$$

$$Capacitance\ sensed\ at\ 50g = 1.45234 * 10^{-14}F \tag{143}$$

$$Sensitivity = \frac{5.65908 * 10^{-19}F}{50g} = \mathbf{1.132 * 10^{-20}F/g} \tag{144}$$

It has been proven that also in this case the sensitivity is low, hence both the versions of the sensor are too few sensible to acceleration variation. In this post-fabrication case, the sensitivity is even smaller with respect the previous case, this is a result to the fact that less area is involved in the sensing of the capacitance, since the thickness during the fabrication has decreased.

In conclusion, it is possible to state that for the best possible sensing some adjustments may be considered on the geometry of the accelerometer. For instance, in order to optimize the effect of fringing fields, thus to increase the sensed capacitance, the length of the side movable fingers could be increased. However, since this device is a parallel plate and not a comb drive, the lower stiffness of the single finger due to the increment of length could lead to possible unwanted effect (such as break, or mechanical attachment to the fixed electrodes), therefore a decrement in the width, with a decrement on the gap between the fingers, may be taken into account instead, in order that the fringing fields acting on the geometry are mostly perpendicular to the surface and their effect is not underestimated. Finally, a possible improvement could hide on the rise of the thickness of the movable resonator part. This will allow, not only to increase the stiffness of the single fingers, hence giving the possibility to increase their length or decrease their width, but also to increase the area of sensing and leading to a higher sensed capacitance. The main drawback of this is that Metal4 with Via4 layers should be considered as part of the resonator movable plate (with consequent variation in the design, release etching time and temperature and so on…), so the masses, the stiffness and the resonance frequency of the whole geometry can significantly change with respect the considerations made so far.

6.4. Simulation Pull-in as if the accelerometer is a simple parallel plate

With the aim to compare the pull-in behaviour between the sensors, it is possible to suppose the model of the accelerometer under test as a simple parallel plate configuration, where the bias voltage is present only on one of each couple of fixed fingers, while the other is grounded for a total of $13 * 2$ fingers and no acceleration is applied. This kind of implementation in COMSOL, with no external forces and sweeping the bias voltage, has provided a maximum displacement with an initial exponential increase to be around $0.55um$ (Figure 72), which indeed correspond exactly to $1/3$ of the gap ($1.5um$), hence it appears at $1um$ of the remaining gap.

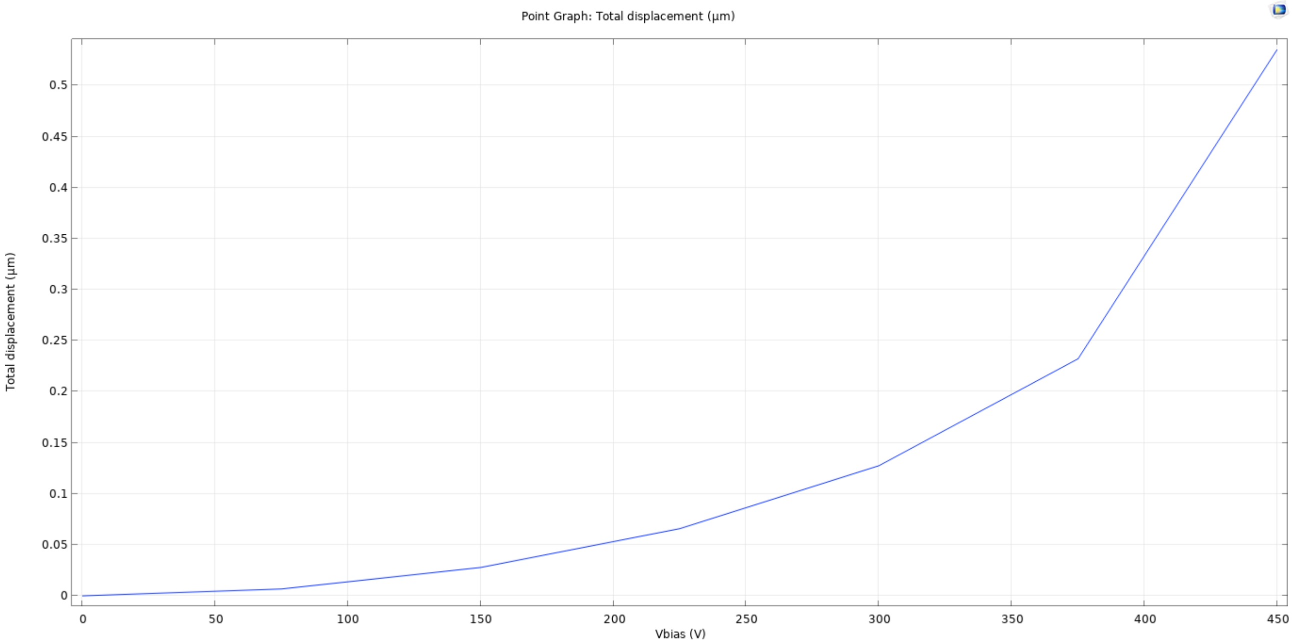

Figure 72 Exponential increase in displacement. It can be observed that at 450V a displacement of 0.55um (≅1/3 of the gap) is achieved

Theoretically speaking, this behaviour is still the expected one. Indeed, the pull-in, given the approximated horizontal stiffness that is characterizing the structure that is around $4200\ N/m$ (see the following section for more details), the overlapping area and the gap, should appear with a voltage of $450V$. In fact, exploiting the formula (12) related to the parallel plate, it is possible to detect the theoretical pull-in voltage in this kind of condition. Plotting both the theoretical electrostatic and mechanical forces that characterize the geometries in MATLAB it is possible to have theoretical estimation on the ideal pull-in condition in absence of non-linearities as if modelling as a simple parallel plate. The correspondent result has been reported in Figure 73.

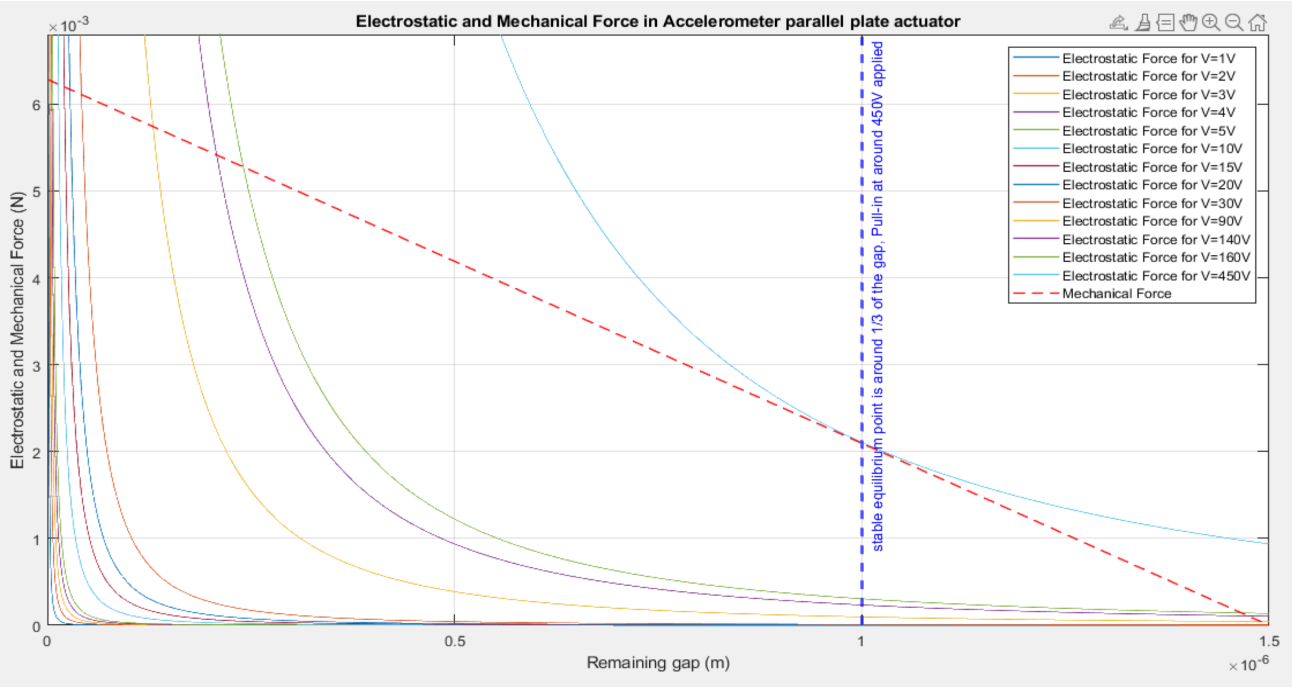

Figure 73 Linear pull-in in the pre-fabricated accelerometer, as clear the pull-in occurs at 0.5um, thus at 1um of remaining gap

From it, it is clear that the ideal pre-fabricated accelerometer theoretical voltage at which a snap between the fixed and movable fingers is expected is around $450V$, which is coherent with the simulated result. Similarly, for the supposed post-fabrication device, the pull-in is likely to be very close to this value, but slightly lowered due to the smaller area involved, since the resonator has characterized by a smaller thickness. Overall, the actual expected $1/3$ of the gap is reached both in simulation and in the theoretical approach at around the same voltage equal to $450V$. This high value of voltage required to snap the fingers even for a parallel plate like structure is due to the high value of the horizontal stiffness characterizing the structure. The stiffness related to the movement of the pressure sensor and the accelerometer are very different, hence the pull-in voltages for the parallel plate configuration are not comparable among each other.

The overall displacement of the entire central mass in scale can be observed in Figure 74 and Figure 75.

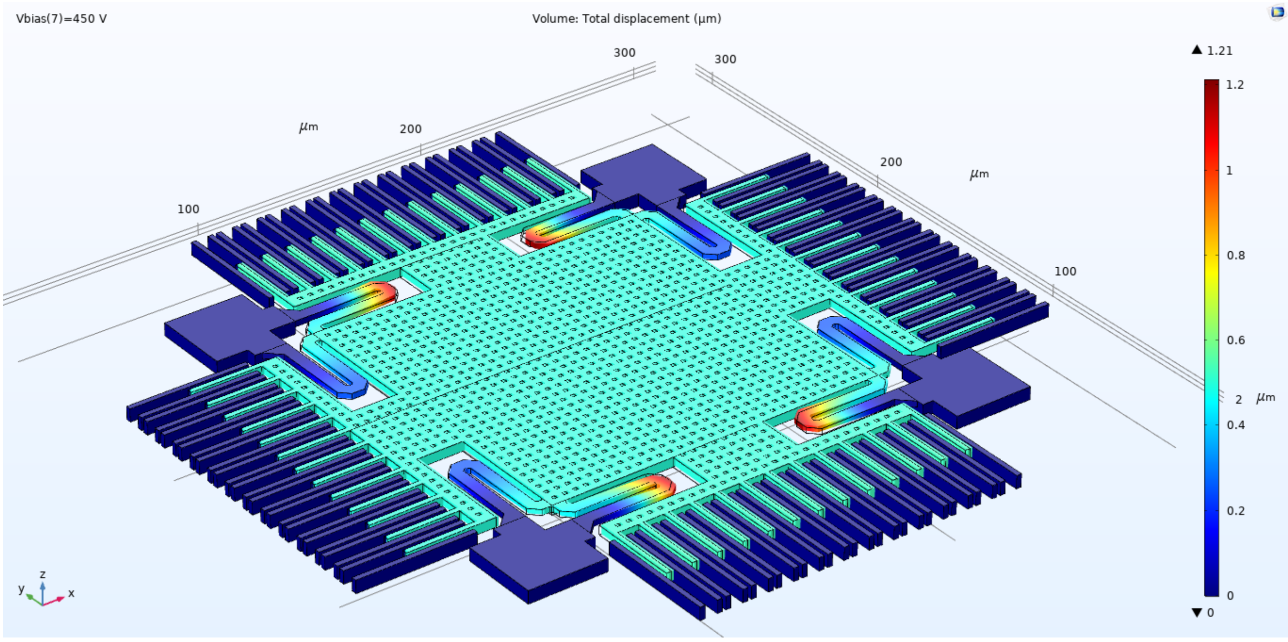

Figure 74 Displacement of sensor at 450V applied to one only of the fixed electrodes in both sides in scale

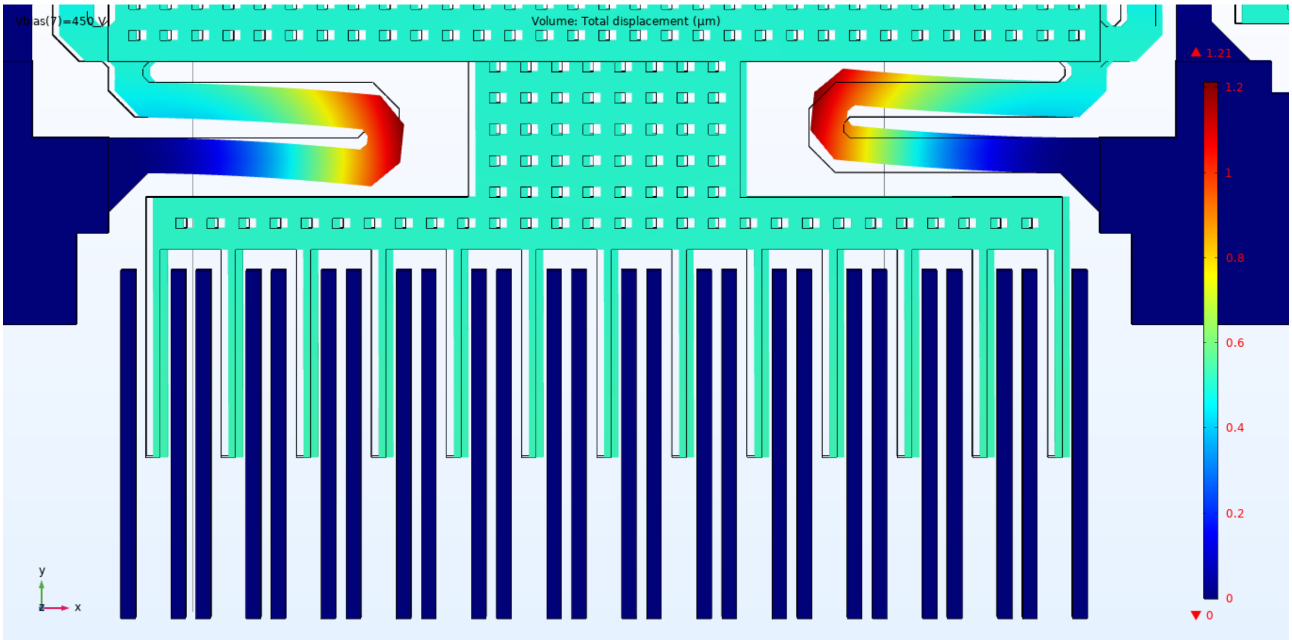

Figure 75 Displacement of sensor at 450V applied to one only of the fixed electrodes in both sides in scale zoomed

The maximum displacement of $1.21um$ occurs at the springs, while a displacement of about $0.5um$ characterizes the movable fingers. Overall, this kind of modelling was performed just to provide some comparisons between the pressure sensor and accelerometer parallel-plate-like response to the pull-in. From the previous statements it is clear that the pull-in is no-likely to happen in the accelerometer unless huge voltages are exploited. However, the actual behaviour of the accelerometer consists of a bias present on both the fixed electrodes of a couple, hence defining an interdigitated structure which indeed describes a specific pattern or layout where two sets of complementary structures, such as fingers or electrodes, are interleaved or interlocked with each other, hence pull-in is likely to happen rarely.

6.5. Vertical Squeeze film damping study on Accelerometer resonant central plate

The accelerometer is characterized by a movable central resonator plate with $31x31$ central perforations plus the perforations present on the sides. In particular, it is possible to perform a simplified study of the vertical and horizontal squeeze film damping of the central square only just by observing how surface pressure tends to change in a structure of this dimensions and with the quoted number of perforations. For instance, this simulation has been carried out similarly to the one of the pressure sensor, hence modelling the movable surface with respect a stationary surface placed at the bottom that are distant among each other $2.23um$ (same air gap used for the pressure sensor). The *Thin Film Flow* physic has been exploited. Particularly, the following studies are the results of the 2D model structure, with the surface normal to the plates pointing out of the paper, indeed also in this case the plate is at first assumed to move exclusively in the surface normal direction, with a prescribed sinusoidal velocity equal to

$$2 * pi * f_0 * dh$$

(145)

where f_0 is the vibrating frequency set at $105kHz$ and dh is the change in gap height defined as $dhND * h0$, with $h0$ the air gap and $dhND$ the fractional variation of the air gap which has been set to 0.05, thus correspondent to $1/20$ of the air gap. The simulation covers the already quoted case of no etch holes, the case with etch holes using Bao's formula (perforations not explicit) and the limiting case of zero relative pressure in the etch holes (perforations explicitly modelled). The output results obtained from the simulation are reported for the no perforation (Figure 76), Bao's Model (Figure 77) and perforations and zero relative pressure (Figure 78, Figure 79) are reported as well as the correspondent damping coefficients (Figure 80).

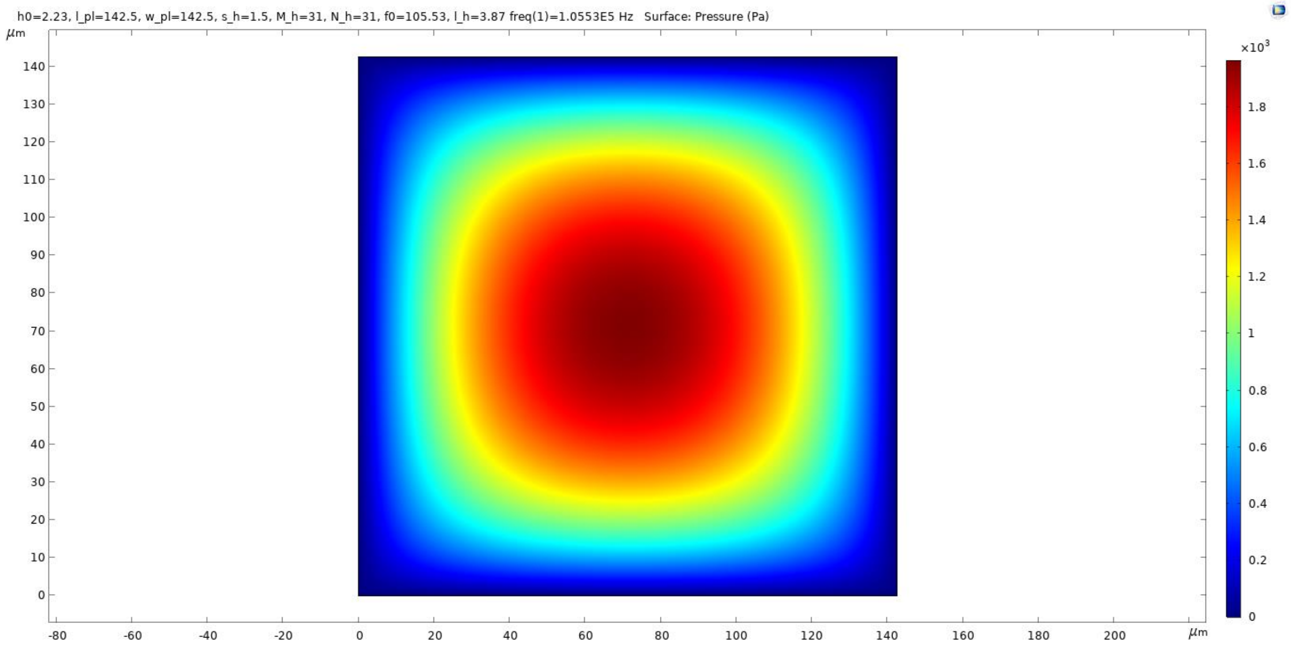

Figure 76 Relative film pressure on the central resonant movable plate pre-fabrication with no perforation

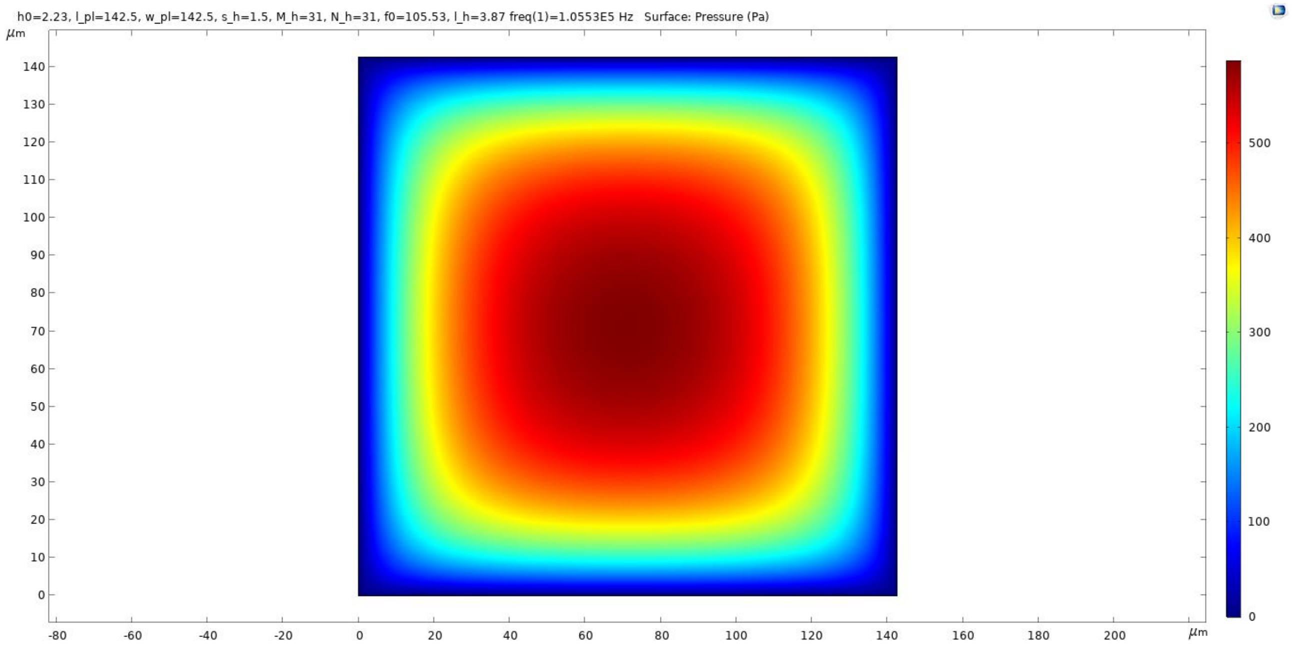

Figure 77 Relative film pressure on the central resonant movable plate pre-fabrication with Bao's Model (perforations not explicitly modelled)

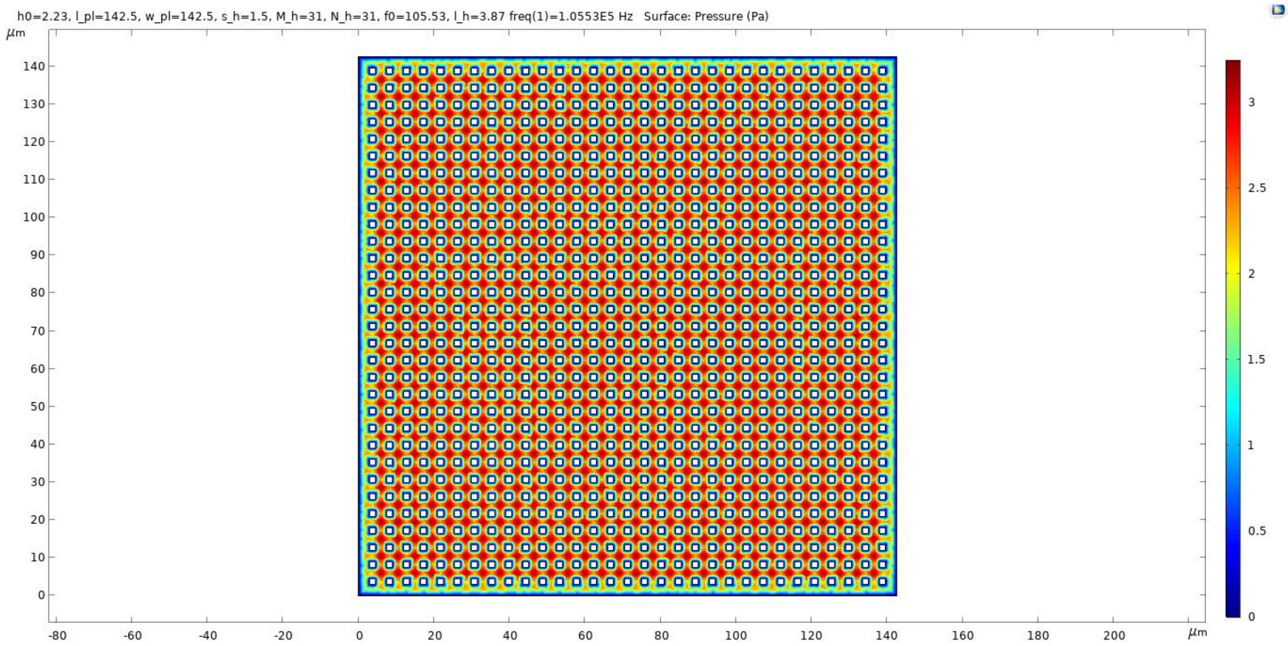

Figure 78 Relative film pressure on the central resonant movable plate pre-fabrication with perforations and zero relative pressure in the etch holes $P=0$

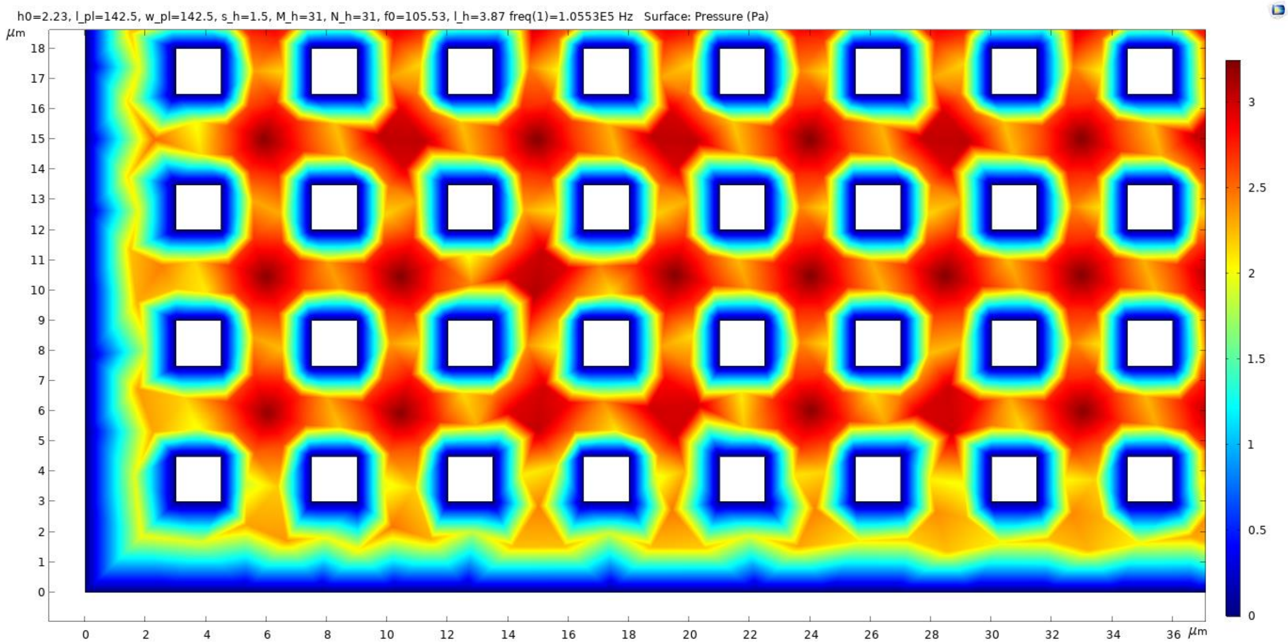

Figure 79 Relative film pressure on the central resonant movable plate pre-fabrication with perforations and zero relative pressure in the etch holes $P=0$ zoomed

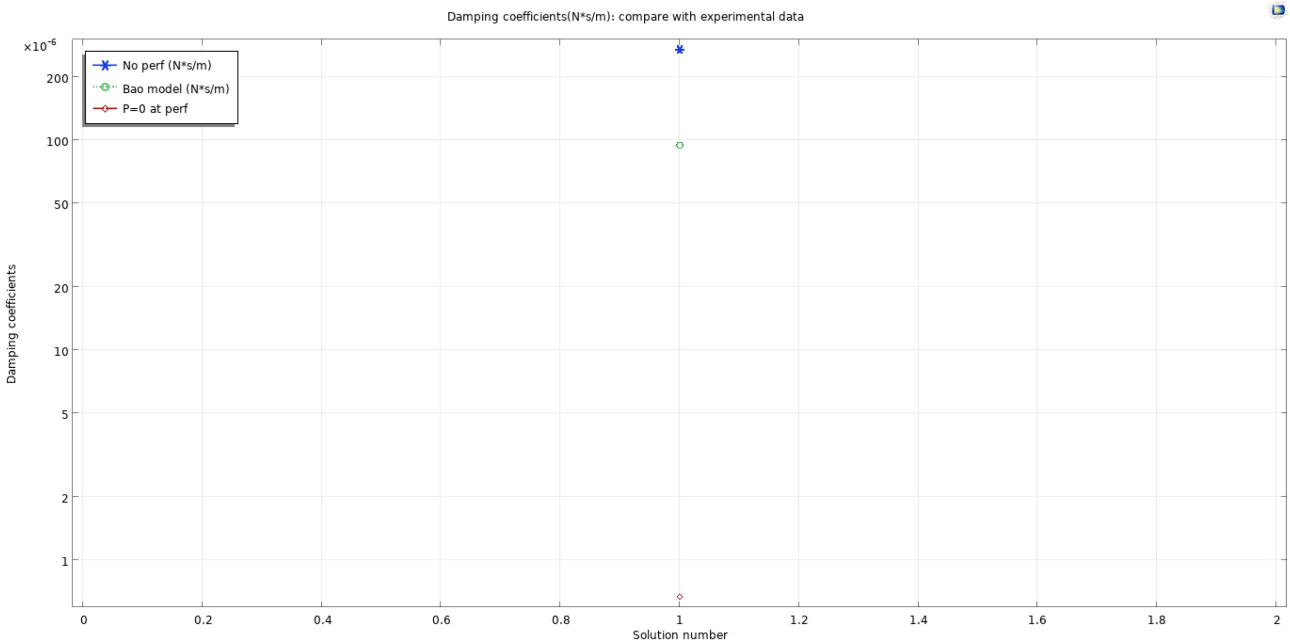

Figure 80 Damping coefficient extrapolated from the three cases pre-fabrication

Principally from Figure 80, it is clear that the vertical damping affecting this structure is much higher if compared to the one affecting the pressure sensor (see section 4.4 and 4.7), this as a consequence of the higher but smaller in size number of holes that characterize the accelerometer central resonator. From the pre to the post fabrication case of accelerometer the only significant change that can be detected in the flow of the structure is in the Bao's model (Figure 81), where the pressure results to be more spread from the centre with respect the pre-fabrication case that instead is concentrated mostly in the centre as can be with accurate attention from Figure 82. However, the difference among the two is very small and not significant.

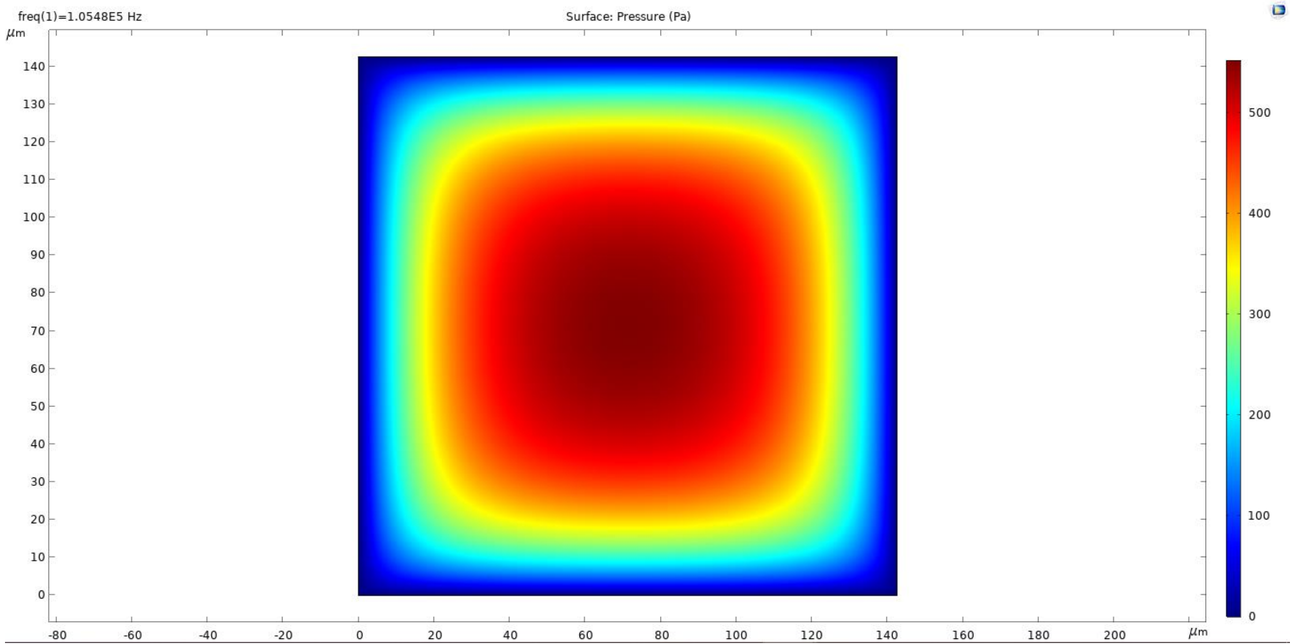

Figure 81 Relative film pressure on the central resonant movable plate post-fabrication with Bao's Model (perforations not explicitly modelled)

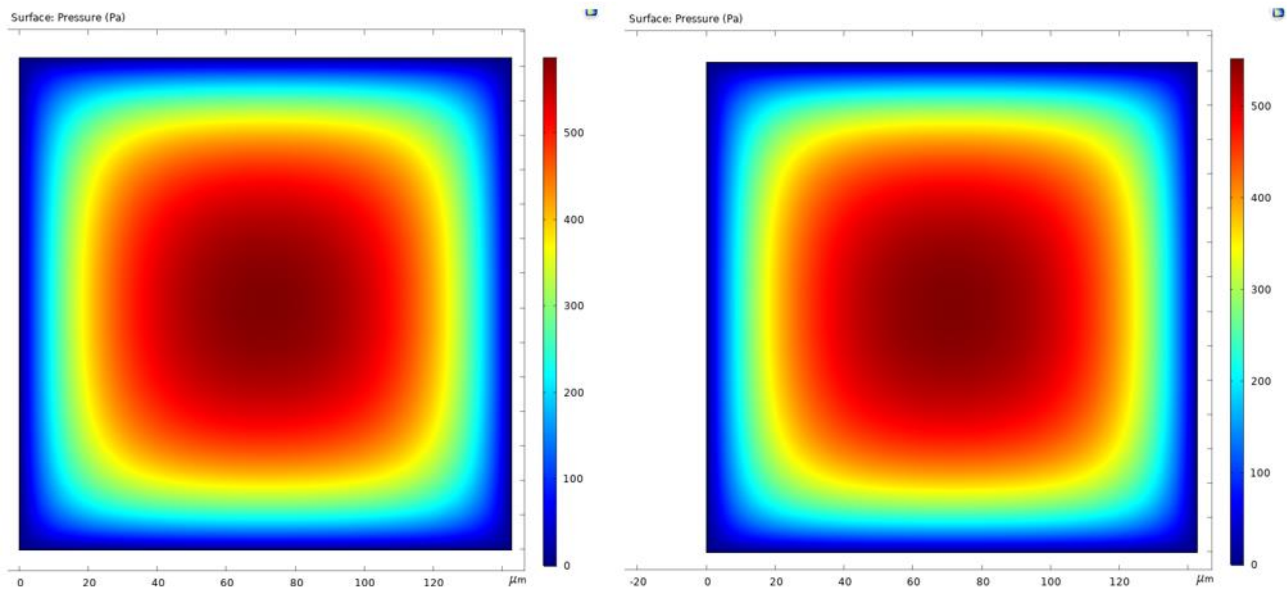

Figure 82 Relative film pressure on the central resonant movable plate comparison pre and post-fabrication with Bao's Model (perforations not explicitly modelled). On the left the pre-fabrication case, on the right the post fabrication case of the accelerometer. They are practically identical.

It is interesting to observe also the behaviour of a prescribed movement exclusively on the y and on the x direction which is the one more of interest for the accelerometer, since it represents the in-plane movement. By applying a velocity only in these directions, the behaviour of the relative film pressure it can be observed in Figure 83 and Figure 84.

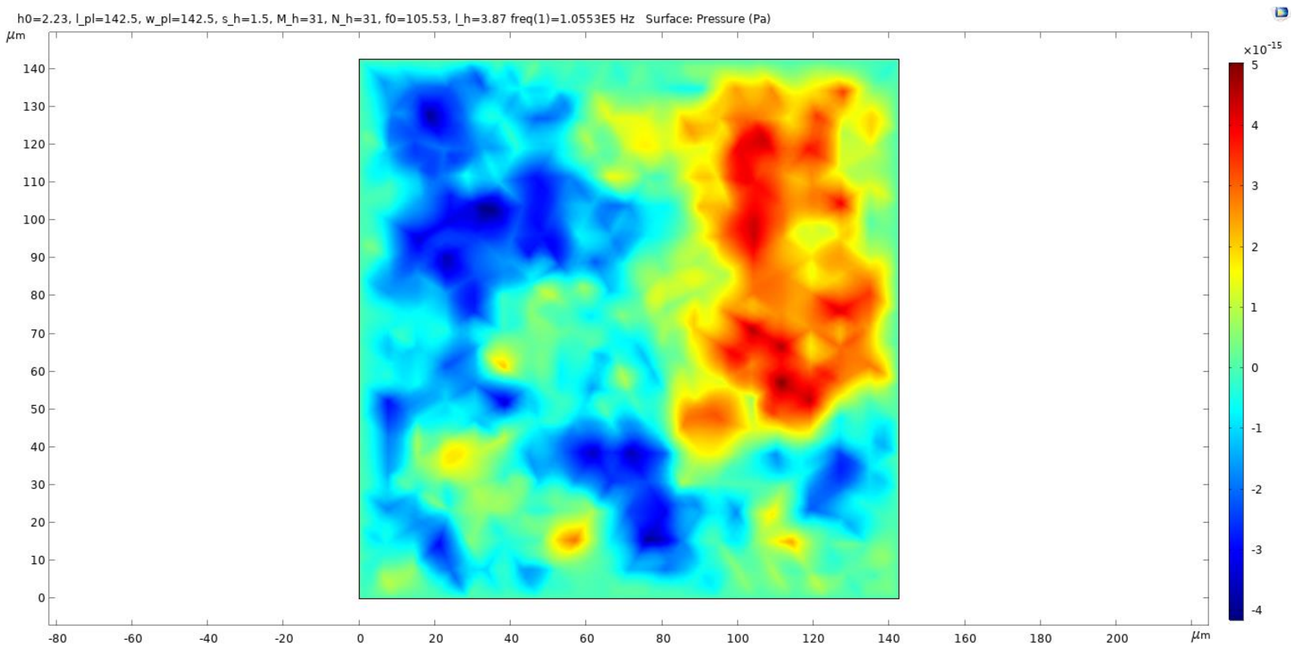

Figure 83 Relative film pressure on the central resonant movable plate pre-fabrication with Bao's Model (perforations not explicitly modelled), with prescribed displacement only along y and x with z=0

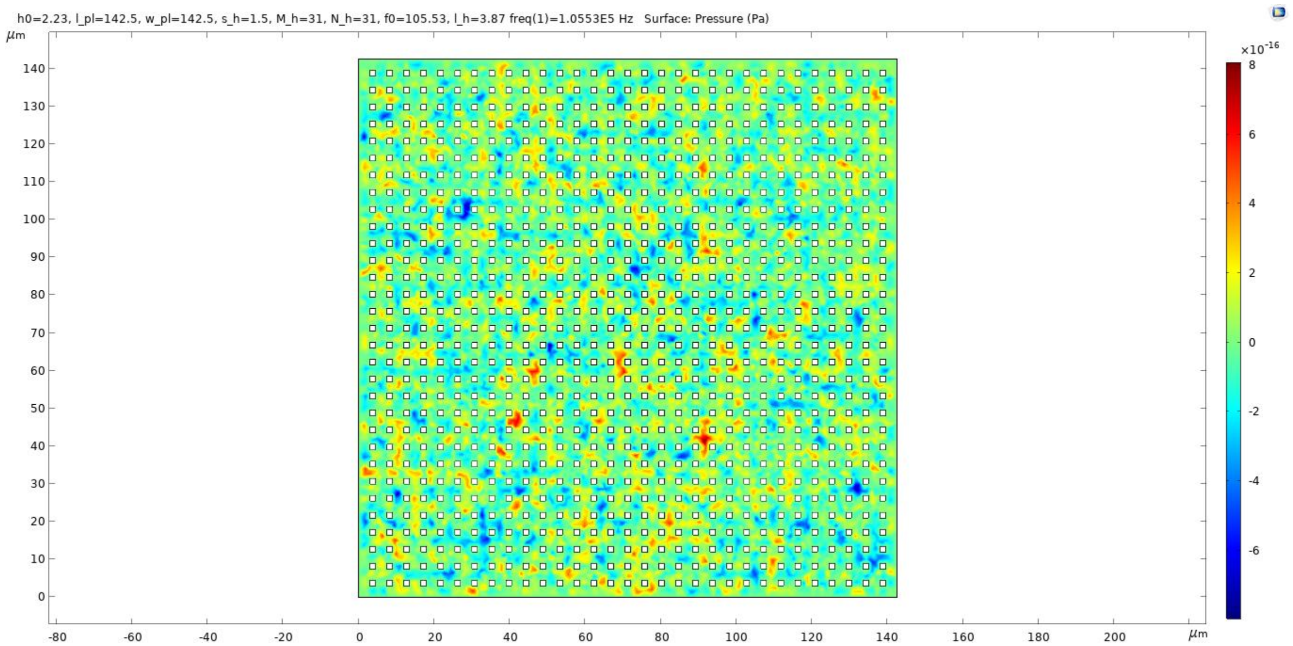

Figure 84 Relative film pressure on the central resonant movable plate post-fabrication with perforations and zero relative pressure in the etch holes P=0 zoomed, with prescribed displacement only along y and x with z=0

Figure 83 shows that the higher relative pressure is on the top right corner coherently to the movement of the mass. On the contrary, the effect of perforations in the case of zero relative pressure in the etch holes (Figure 84) provides almost a random distribution of pressure among the rectangular structure.

7. Mechanical differences Pressure sensor vs Accelerometer

An interesting aspect to take into consideration is the reason why the stiffness between the accelerometer and the pressure sensor is not similar although the same geometric dimensions of the springs have been used.

Figure 85 TSMC layout with Metal6, Metal5 and Metal4 layers respectively of pressure sensor and accelerometer designs

As clear from Figure 85, the springs arrangement is different from one sensor to another. The accelerometer (right) has been designed with its metal 4 (that is not part of the movable central resonator) and metal5 layers with the correspondent vias below metal6 up until the beginning of the springs itself. On the contrary, for the case of the pressure sensor (left) a good area of metal 6 (violet area) appears to float with nothing below (no metal5, hence no vias), thus contributing in an important way to the vertical change of stiffness from one sensor to another. Indeed, the stiffness of the accelerometer results to be higher for both the pre and post-fabrication case with respect its counterpart, hence defining a more rigid structure due to the less area available that contributes to the oscillation. In particular, the mass distribution actively participating to the vertical movement is smaller in the accelerometer, therefore, a lower vertical resonance frequency is expected to characterize the entire structure and indeed this has been demonstrated in the previous sections. Moreover, the mass (both homogeneous and composite ones, but the former still remains the one of interest for the characterization of the resonance frequency) of the central resonator plate of accelerometer is higher with respect the one of the pressure sensor, and this is affecting with a much more important contribution with respect the stiffness the overall resonance frequency. This is the reasons why even if the stiffness of the accelerometer results to be higher compared to the one of the pressure sensor, the mass effect is the main consequence of the decrement of the resonance frequency. The main differences in the vertical resonance frequency among the sensors are reported in Table 4.

Table 4 Mechanical differences between Pressure sensor and Accelerometer in the pre and post-fabrication cases

SENSORS DIFFERENCES:	***PRESSURE SENSOR TSMC***			***ACCELEROMETER TSMC***		
	Pre	***Post***	***Correction factor pre-post***	***Pre***	***Post***	***Correction factor pre-post***
MASS HOMOGENEOUS *(10^{-10}KG)*	1.8995	1.7149	1.1076	5.1611	4.6596	1.1076
VERTICAL RESONANCE FREQUENCY *(KHZ)*	147.16	134.69	1.093	106.89	100.52	1.063
VERTICAL STIFFNESS*(N/M)*	162.39	122.82	1.322	232.796	185.87	1.252

In fact, the *weight factors,* intended as the contributions of both the stiffnesses and the masses on the resonance frequency of the structures are:

For the pre-fabrication case:

$$k_{change} = \frac{k_{accelerometer}}{k_{pressure\ sensor}} = \frac{232.796 N/m}{162.39\ N/m} = \mathbf{1.434}$$

(146)

$$m_{change} = \frac{m_{homog\ accelerometer}}{m_{homog\ pressure\ sensor}} = \frac{5.1611 * 10^{-10} kg}{1.8995 * 10^{-10} kg} = \mathbf{2.717}$$

(147)

For the post-fabrication case:

$$k_{change} = \frac{k_{accelerometer}}{k_{pressure\ sensor}} = \frac{185.87\ N/m}{122.82\ N/m} = \mathbf{1.513}$$

(148)

$$m_{change} = \frac{m_{homog\ accelerometer}}{m_{homog\ pressure\ sensor}} = \frac{4.6596 * 10^{-10}kg}{1.7149 * 10^{-10}kg} = \mathbf{2.717}$$

(149)

Therefore, the contributions of correction related to the resonance frequencies from the pressure sensor to the accelerometer for the pre-fabrication and the post-fabrication cases respectively are the following:

$$Correction_{pre} = \sqrt{\frac{\mathrm{k_{change}}}{\mathrm{m_{change}}}} = \sqrt{\frac{1.434}{2.717}} = \mathbf{0.7265}$$

(150)

$$Correction_{post} = \sqrt{\frac{\mathrm{k_{change}}}{\mathrm{m_{change}}}} = \sqrt{\frac{1.5134}{2.717}} = \mathbf{0.7463}$$

(151)

As a proof, the same resonance frequencies found in sections 6.2 and 6.3 are found:

$$f_{r\ acc\ post\ expected} = 0.7463\ f_{r\ press\ post} = 0.7463 * \ 134.69kHz = 100.5kHz$$

(152)

$$f_{r\ acc\ pre\ expected} = 0.7265\ f_{r\ press\ pre} = 0.7265 * 147.16kHz = 106.9kHz$$

(153)

A direct linear estimation of the resonance frequency of the accelerometer based on the pressure sensor one is not possible due to dependency on both the mass and the stiffness contributions. The masses variations between the sensors affect much more the resonance frequency as noticeable from the computed weight factors, but the effect of the stiffnesses variations due to the change in the springs' arrangement must be taken into consideration as well. However, it is fundamental to notice that the behaviour of interest for the accelerometer is related to its horizontal motion with respect its vertical one. Therefore, the accelerometer resonates horizontally with the resonance frequencies reported in Table 5.

Table 5 Horizontal resonance frequency and stiffness for the pre and post-fabrication accelerometer

ACCELEROMETER	PRE-FABRICATION	POST-FABRICATION
HORIZONTAL FR (KHZ)	471.46	477.23
HORIZONTAL K (N/M)	4528.889	4189.516

The stiffnesses in both the cases seem very high, therefore a very small displacement occurs in the horizontal direction as demonstrated in previous sections (see 6.2 and 6.3).

8. Alternative design of the post-fabrication Accelerometer

From the COMSOL simulations of the accelerometer design it has been proven that the sensitivity affecting the structure is incredibly low. This is mainly due to the fact that the external force acceleration does not move the central proof mass enough in order to provide a significant redistribution of the charges on the surfaces of the movable fingers, hence the horizontal stiffness of this configuration of springs does not allow enough horizontal displacement. The capacitance variation is extremely small as a consequence of the small change in the charges distribution which in turn is due to the small displacement detected. The increasing of the bias voltage applied at the fixed fingers does not represent a suitable solution to the problem. Instead, a possible solution hides in the modification of the geometry itself. For instance, in the following sections a new version of the accelerometer is proposed. Particularly, the most important changes are on the springs structure and in the air gap between the fixed and the movable electrodes. Everything will be checked by recreating a new layout in UMC on Cadence and performing the DRC, to be sure that the applied variations are compatible with the manufacturer constraints.

8.1. New springs configuration and new arrangement of fixed electrodes

Using a particular configuration of springs and decreasing the gap between the movable fingers and the fixed electrodes to $1.1um$ instead of $1.5um$, the total capacitance sensed by the two sides increases up to $20fF$, which is higher with respect the $14.5fF$ of the previous version. Indeed, the charges at one side of the surfaces of the movable fingers sensed at $0g$ and $50g$ resulted to be respectively the following:

$$Surface\ charge\ at\ 0g = 4.75508 * 10^{-18}C \tag{154}$$

$$Surface\ charge\ at\ 50g = 4.77719 * 10^{-18}C \tag{155}$$

Hence, the total sensed capacitances are:

$$Capacitance\ sensed\ at\ 0g = 1.90203 * 10^{-14}F$$

(156)

$$Capacitance\ sensed\ at\ 50g = 1.91088 * 10^{-14}F$$

(157)

Most importantly the sensitivity results to be on the order of $1 * 10^{-18}F/g$ since the distribution of charges changes in a more important way during the variation from $0g$ to a higher value of acceleration with respect the original design.

$$Sensitivity = \frac{8.845134 * 10^{-17}F}{50g} = \mathbf{1.769 * 10^{-18}F/g}$$

(158)

Now, this happens thanks both to the new springs' configuration, for which the displacement on the central mass is much higher ($4nm$ under $50g$ acting horizontally) with respect the original case ($0.05nm$ with $50g$ acting horizontally), and the smaller gap between fixed and movable electrodes. The Figure 86 exhibits the metal6 layer only, showing the new design with the new arrangement of the springs and the fixed electrodes.

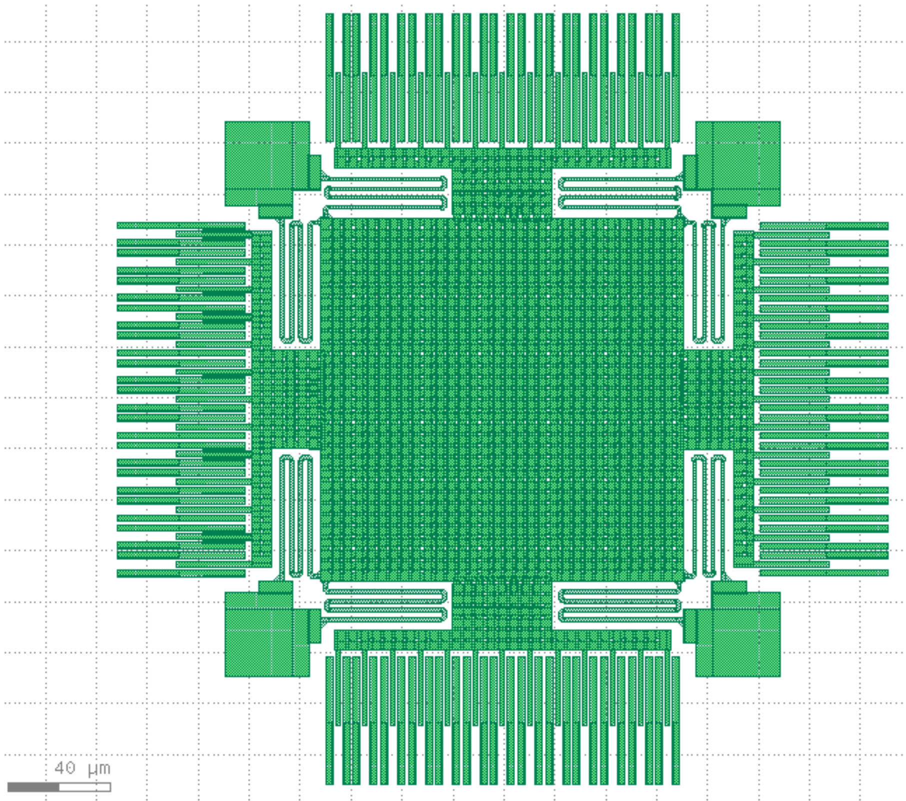

Figure 86 Klayout view metal6 layer of the new design of the post-fabrication accelerometer UMC 180nm

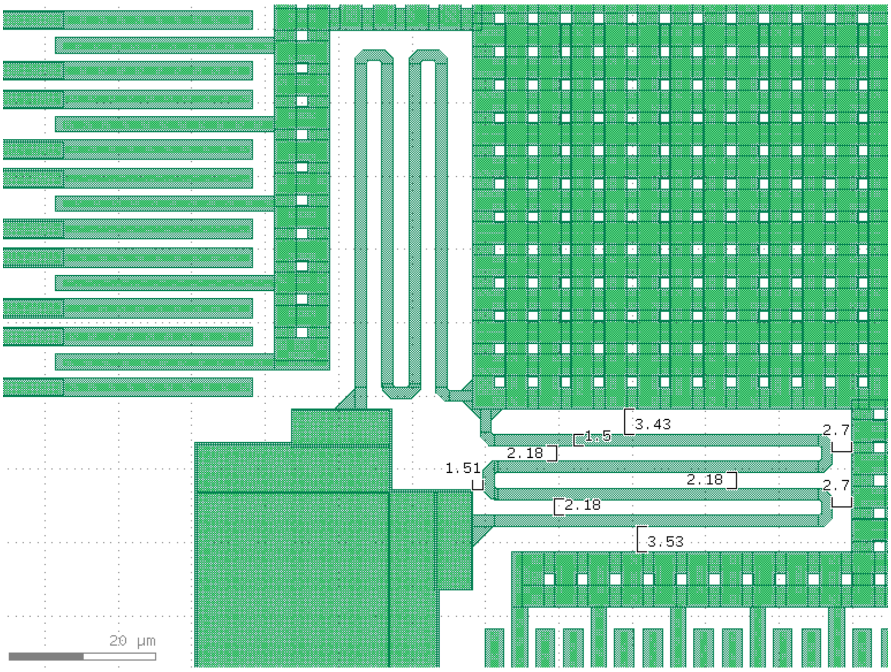

Figure 87 Klayout view metal6 layer of the new design of the accelerometer UMC 180nm zoomed. The dimensions are explicit.

The dimensions exploited for this new version are reported in Figure 87 and are detailed in the following table:

Table 6 Dimensions Accelerometer new springs and electrodes arrangement

$b \cong 44um$	Single arm length
$c = 2.18um$	Spacing between arms
$a = 1.5um$	Single arm width
$h_0 = 1.1um$	Horizontal air gap between fixed and movable electrodes

It is likely to suppose that a similar arrangement could be found for the TSMC technology. For instance, the width of the fixed electrodes depends on the technology exploited since dissimilar constraints may require different width for the Metal6 in particular. In UMC technology, those constraints on the Top Metal are easier to bypass.

The actual displacement of the proof mass of the new geometry can be appreciated in Figure 88.

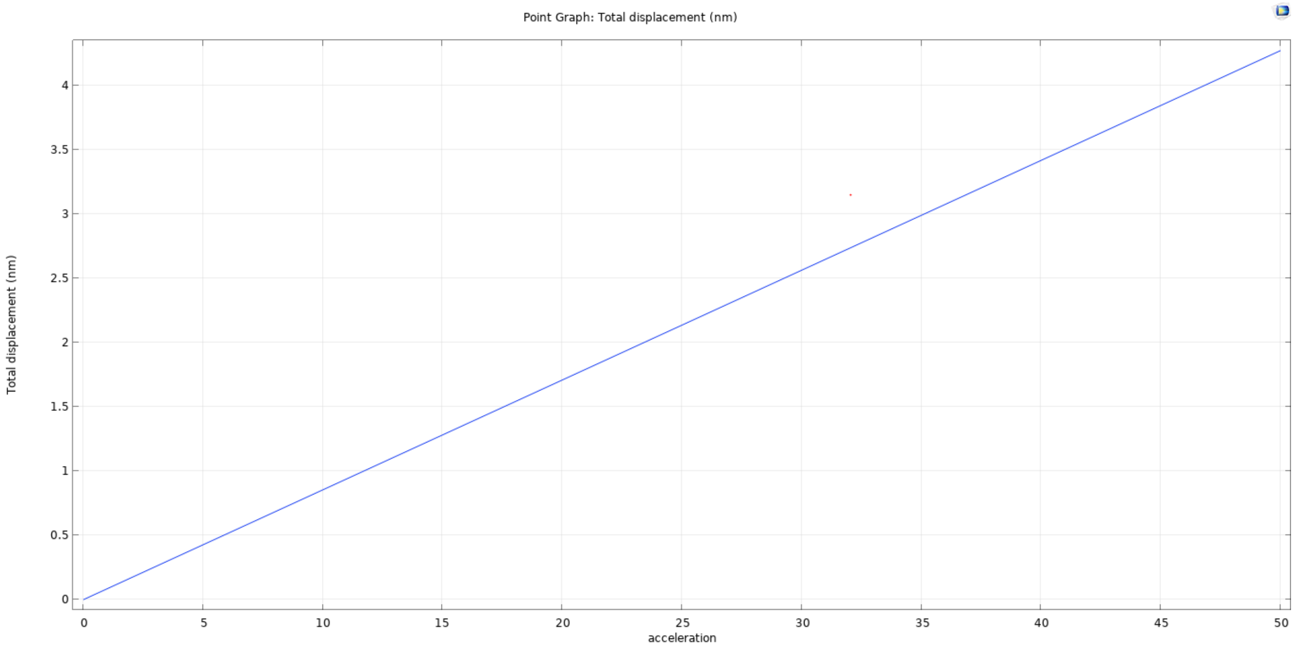

Figure 88 Displacement of the point belonging to the movable finger of the new geometry vs External Acceleration

The highest displacement does not belong to the proof mass, but to the springs itself, which show a maximum displacement under $50g$ of external acceleration of $0.01\ um$, as clear from Figure 89:

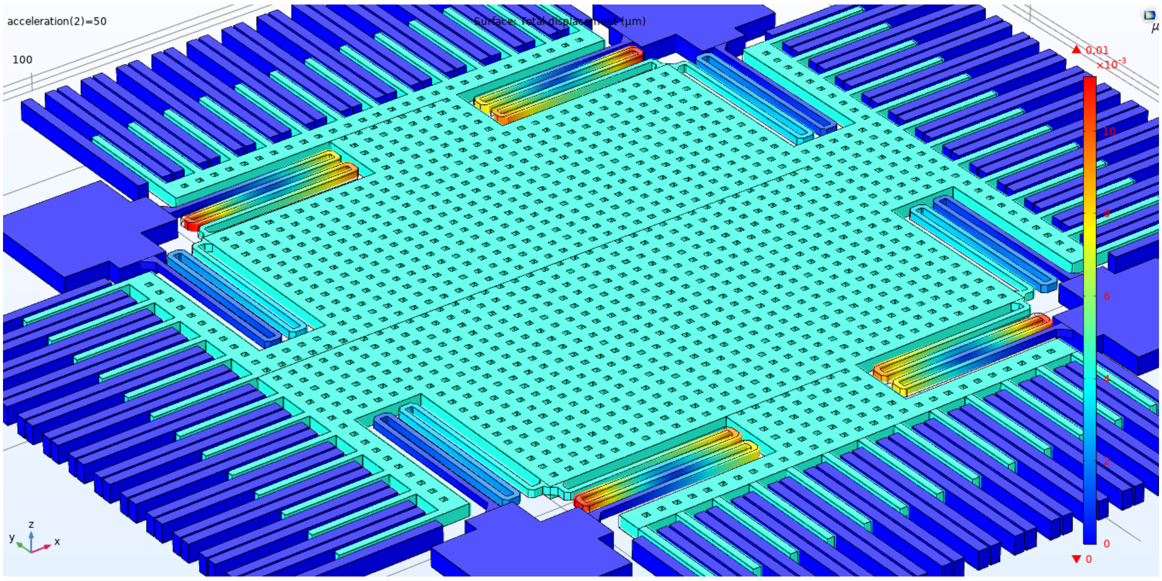

Figure 89 Maximum Total Displacement of the new geometry under 50g of external acceleration and $\pm 0.5mV$ of bias voltage

The compromises of this new design are mainly on the resonance frequencies, which result to be $26kHz$ regarding the vertical one (with a correspondent stiffness of $k = 14N/m$) and $53kHz$ regarding the horizontal one (the one of interest, corresponding to a stiffness of $k = 58\,N/m$, hence much smaller with respect the original case and providing the possibility for a higher displacement).

Table 7 - Differences on the horizontal and vertical resonance frequency and stiffness for the old and new designs of the accelerometer

	NEW VERSION(POST-FABRICATION)	***OLD VERSION (POST-FABRICATION)***
HORIZONTAL FR (KHZ)	$\cong 53$	477.23
HORIZONTAL K (N/M)	$\cong 58$	4189.516
VERTICAL FR (KHZ)	$\cong 26$	134.69
VERTICAL K (N/M)	$\cong 14$	122.82
HORIZONTAL Q	$\cong 53.8$	$\cong 48$
VERTICAL Q	$\cong 29$	$\cong 80$

In Table 7 are reported the characteristics of the new and old versions of the post-fabrication accelerometer design. Particularly, it is clear how in both the designs the horizontal resonance frequency and stiffness are higher with respect the vertical case, however the new arrangement exploited shows much lower values with respect the original arrange, hence providing higher displacements and, as quoted, a higher change during the distribution of charges on the surfaces of interest. The stresses on the new design have also been analysed to check that no break may occur during the proper behaviour. From the simulations obtained it is possible to state that under high variation of acceleration the maximum Von Mises stresses are on the order of $10^4\,N/m^2$ acting horizontally while of the order of $10^6\,N/m^2$ acting vertically under the influence of $50g$ simulated horizontally and vertically separated. Since aluminium (material's springs) should be able to sustain stresses around $10^6\,Pa$ (tensile strength or yield strength of aluminium) of higher without undergoing significant deformation or failure, we are in the limit for the vertical case, however this could be fix with dimples or just by stating that this kind of solicitudes such as $50g$ will never actually be case of sensing from this kind of device.

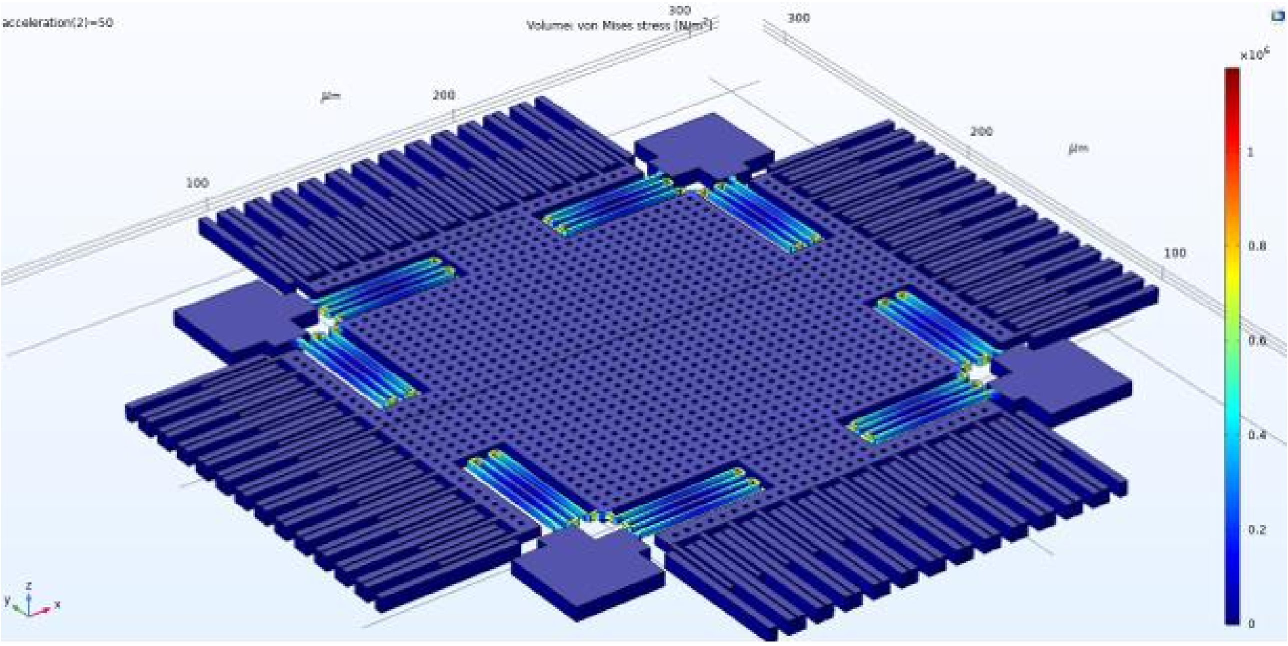

Figure 90 Vertical Von Mises stresses on the new version design of the accelerometer 180nm with vertical acceleration of 50g

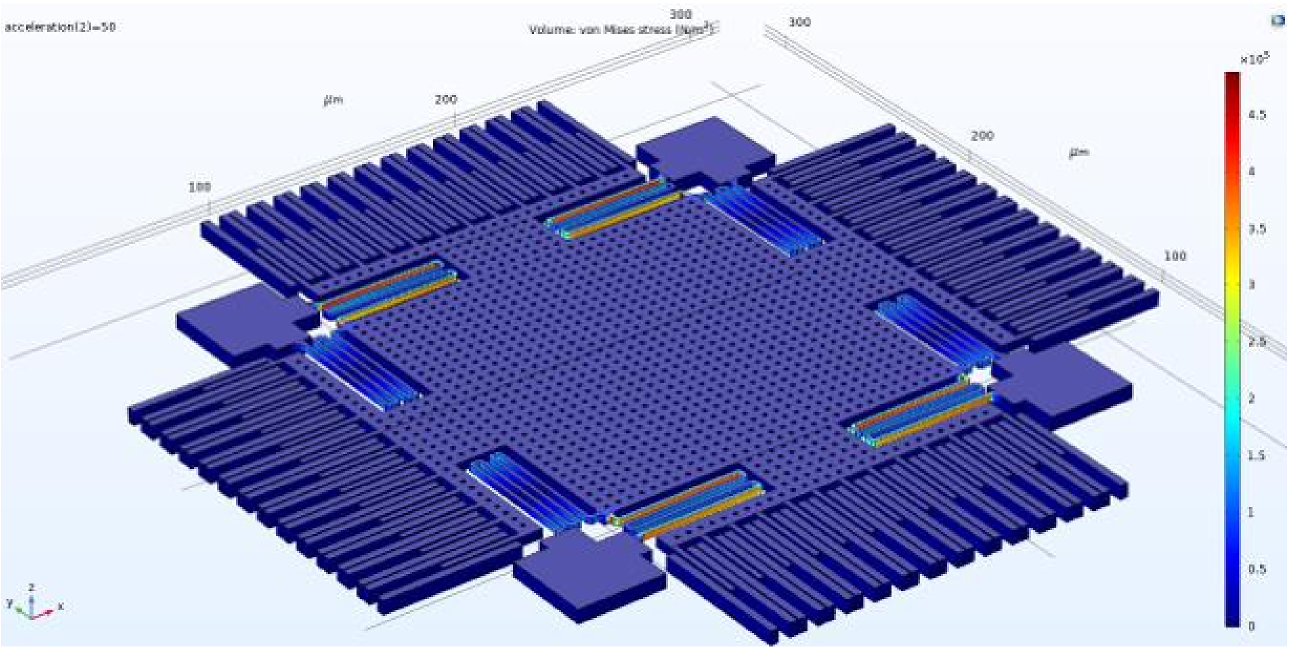

Figure 91 Horizontal Von Mises stresses on the new version design of the accelerometer 180nm with horizontal acceleration of 50g

Indeed, from Figure 90 and Figure 91 appears that the highest stress is present on the springs and, in particular, during the vertical excitation ($10^6\ N/m^2$ if compared to the $5 * 10^5 N/m^2$ during the horizontal excitation). The maximum vertical displacement of the structure results to be much higher with respect the horizontal case due to the significantly smaller stiffness that acts vertically on the structure. Indeed, the maximum vertical displacement of the structure results to be equal to $18nm$, which is very high if compared to the horizontal movement. Additionally, since also the vertical case may be of interest for measuring of the capacitance, it is possible to detect also a slight variation of charge whenever a vertical acceleration act on the structure. Indeed, the sensed distribution of charge in this case are respectively:

$$Surface\ charge\ at\ 0g\ acting\ vertically = 4.75508 * 10^{-18}C \tag{159}$$

$$Surface\ charge\ at\ 50g\ acting\ vertically = 4.75658 * 10^{-18}C \tag{160}$$

Hence the variation in this case outcomes to be small with respect the horizontal case and it is not significant for the capacitance measurement, but still, a slight change with respect the case of pure horizontal acceleration only could be expected if vertical accelerations act on the proof mass.

In conclusion, the effect of fringing fields under $\pm 0.5mV$ of bias voltage applied at the fixed electrodes can be described also for this structure (Figure 92). Those result to be higher with respect the original case principally between the fixed electrodes showing a maximum value of $0.0012\,V/um$; indeed, the distance between those has decreased as a consequence of the reduction in the gap and technology constraints.

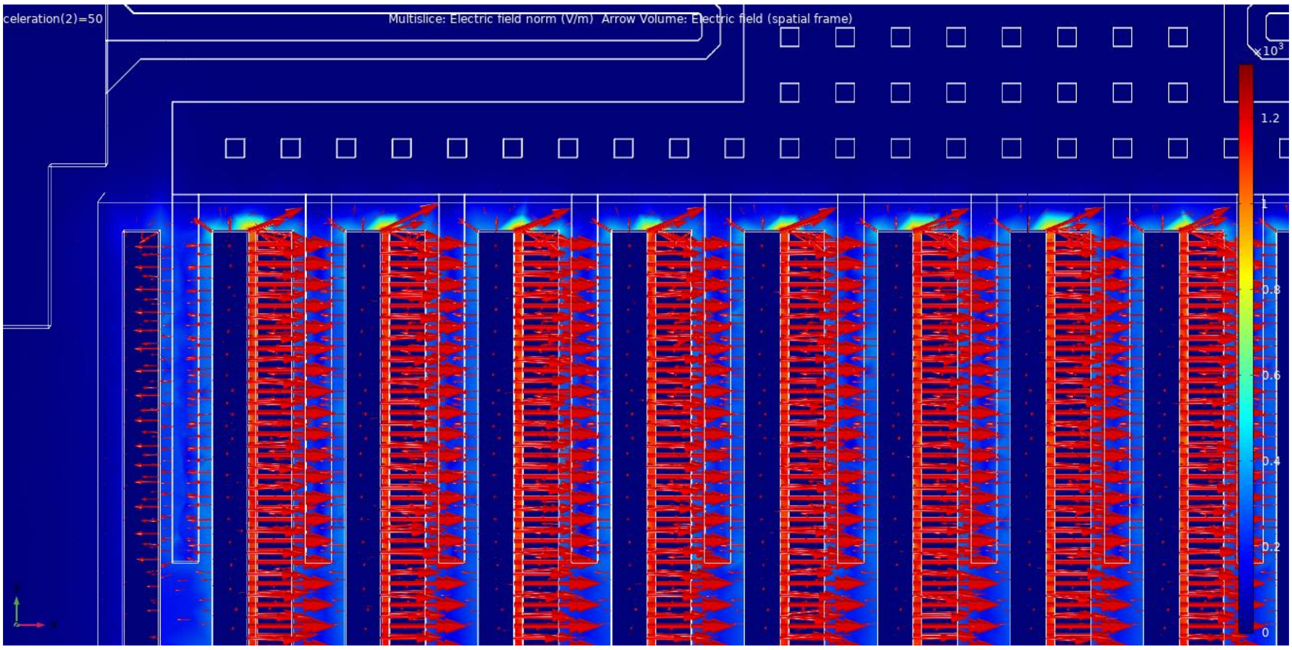

Figure 92 Fringing fields effect of the new design accelerometer with 0.5mV of Biasing at 50g

In conclusion, the DRC with the new quoted variations has been successfully performed for the UMC technology. It showed the usual expected errors (as slotting and vias width/length constraints) and no unexpected ones, hence this solution could actually represent an excellent outcome. From the simulation point of view, the new design seems to be more sensitive for horizontal acceleration with respect its older version, however the TSMC design of this exact new version is more complex to model due to the stricter constraints on the TOP metal6. Therefore, it has been also proven that UMC technology provides the possibility to design layouts that are instead limited in TSMC technology; this may represent a pivotal reason during the choice of the technology to exploit for a project.

9. Electronics read-out: comparison between TSMC and UMC

9.1. Introduction

Capacitive MEMS sensors operate based on changes in capacitance, and the measured capacitance values are typically analog signals. After the capacitance value is detected in the sensor, it needs to be processed and converted into a meaningful digital format for further analysis or utilization [2, 5]. This conversion typically involves analog-to-digital conversion (ADC), where the analog signal is converted into a digital representation that can be processed and manipulated by digital circuits or microcontrollers. In some cases, a low-noise amplifier (LNA) may be employed in the readout circuitry of the sensor since it amplifies weak signals from the sensor, particularly when the signal-to-noise ratio is low or when the sensor output needs to be conditioned for improved sensitivity or accuracy. The LNA can boost the signal level while minimizing additional noise contributions, enhancing the overall performance of the readout circuitry. In particular, an operational amplifier plays a crucial role in amplifying this signal to a usable level. Therefore, in order to have a more general view on the development of a sensor in all its part, an essential electronic read-out part has been also analysed: an operational amplifier. As a starting point, the main differences between the transistors of the two technologies have been discussed. The analysis has been followed by the migration of already existing operational amplifier design originally made in TSMC technology. The resizing of the transistors in this case represents a crucial part during the migration into UMC were the achievement of the most similar performances with respect the original design represents the main purpose of the migration. Both the TSMC and UMC schematic have been tested by the exploitation of a test bench, in which driving current have been set to be identical in order to make the most correct comparison among the two. Later, after achieving satisfactory performance, the design layout of the UMC operational amplifier version was completed, hence, both the DRC (Design rule checking) and LVS (Layout Versus Schematic) have been checked in order to validate the migration.

9.2. Comparison between UMC and TSMC transistors

The comparisons between the two manufacturers have been performed exploiting the *Cadence tool* and it has been carried out between the following transistors:

- nmos2v (TSMC) and N_18_MM (UMC)
- pmos2v (TSMC) and P_18_MM (UMC)
- nmosnvt2v (TSMC) and N_ZERO_18_MM (UMC)

As a first approach to the comparison, the gate voltage, the early voltage, the overdrive voltage, the threshold voltage, the transconductance gain and the output resistance for each transistor have been measured and compared among them with $10\,uA$ drain current applied in a diode-like connection, with source and bulk placed at the same potential. Indeed, MOSFETs have voltage ratings that define the maximum allowable voltages that can be applied to different terminals of the device. The voltage ratings are typically specified for the drain-source voltage (Vds), gate-source voltage (Vgs), and sometimes the bulk or substrate voltage ($Vbs\ or\ Vsub$). For a "$1.8V\ MOS$" the MOSFET is designed to operate within a maximum drain-source voltage of 1.8 volts. It indicates that the voltage across the drain and source terminals of the MOSFET should not exceed 1.8 volts to ensure proper operation and avoid potential damage to the device itself. Exceeding the specified voltage limits can lead to device failure, breakdown, or other undesirable consequences. Therefore, it is crucial to choose MOSFETs with voltage ratings that match the requirements of the intended application to ensure reliable operation. On the contrary, the gate source could be lower with respect the specific, but since a diode like connection has been exploited, this has not been taken into consideration, hence the only present DC generator that defines the supply voltage has been set to $1.8V$. Therefore, the maximum applicable V_{ds} from the DC generator for the devices under test is $1.8V$. When the drain-source voltage exceeds the specified limit, it can cause various undesirable effects, such as excessive leakage current, breakdown of the oxide layer, or even permanent damage to the transistor.

The relation between the gate source voltage and the drain current is the following:

$$I_d = \beta\left(V_{gs} - V_{th}\right)V_{ds} - \frac{V_{ds}^2}{2}$$

(161)

and

$$\beta = \mu * Cox * \left(\frac{W}{L}\right)$$

(162)

Where β is the transconductance parameter, V_{th} is the threshold voltage and V_{ds} is the drain-source voltage.

For the n-mos cases, a current source has been added to the drain node of the transistor and has been set to a current of $10uA$. The source of each n-mos has been set to ground in order to enhance the flow of current and reduce the susceptibility to voltage fluctuations or variation of power supply, and similarly, the drain of each p-mos has been set to the power supply voltage. Every transistor has been classified in terms of the most important parameters with different specified length and width for a proper characterization. Specifically, the TSMC transistor nmos2v, pmos2v and nmosnvt2v have minimum length in Cadence respectively of $180nm$, $180nm$ and $500nm$, while the minimum width is $220nm$ for the first two quoted and $420nm$ for the latter; on the other case the UMC transistors N_18_MM, N_ZERO_18_MM, P_18_MM and P_LV_18_MM have respectively minimum length of $180nm$, $300nm$, $180nm$ and $240nm$ and all present a minimum width equal to $240nm$. However, the default Cadence widths of the TSMC transistor are $2um$. In order to observe the schematic exploited for the comparison, the correspondent DC Bias operating points for each transistor with Cadence defaults length and width respectively (see Table 11 for specific values) for the UMC and TSMC have been simulated and reported in Figure 93 and Figure 94.

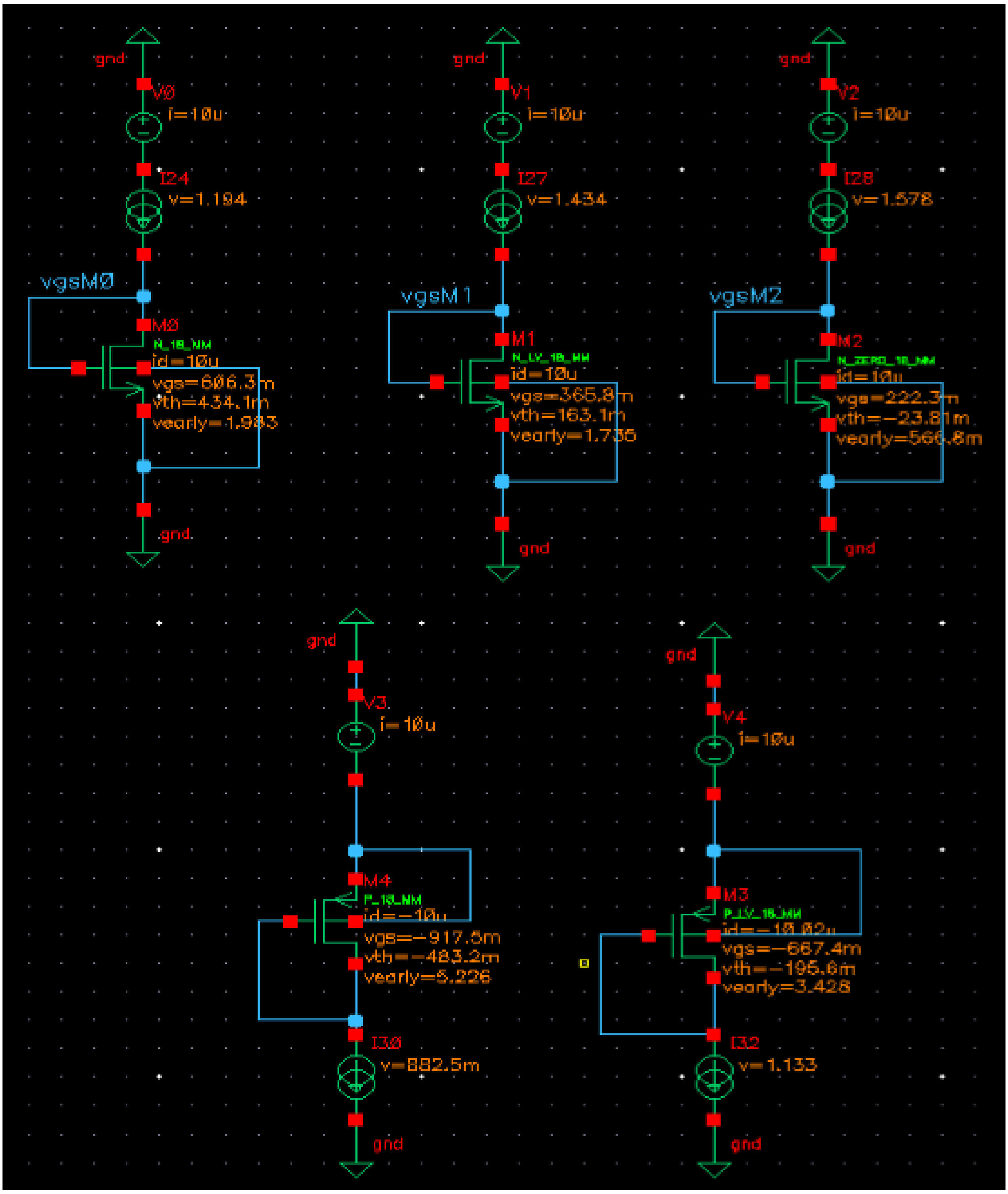

Figure 93 UMC transistors under test schematic representation with Cadence default sizes. From left to right and up to down: N_18_MM, N_LV_18_MM, N_ZERO_18_MM and P_18_MM, P_LV_18_MM. The operating bias points of each transistor can be appreciated

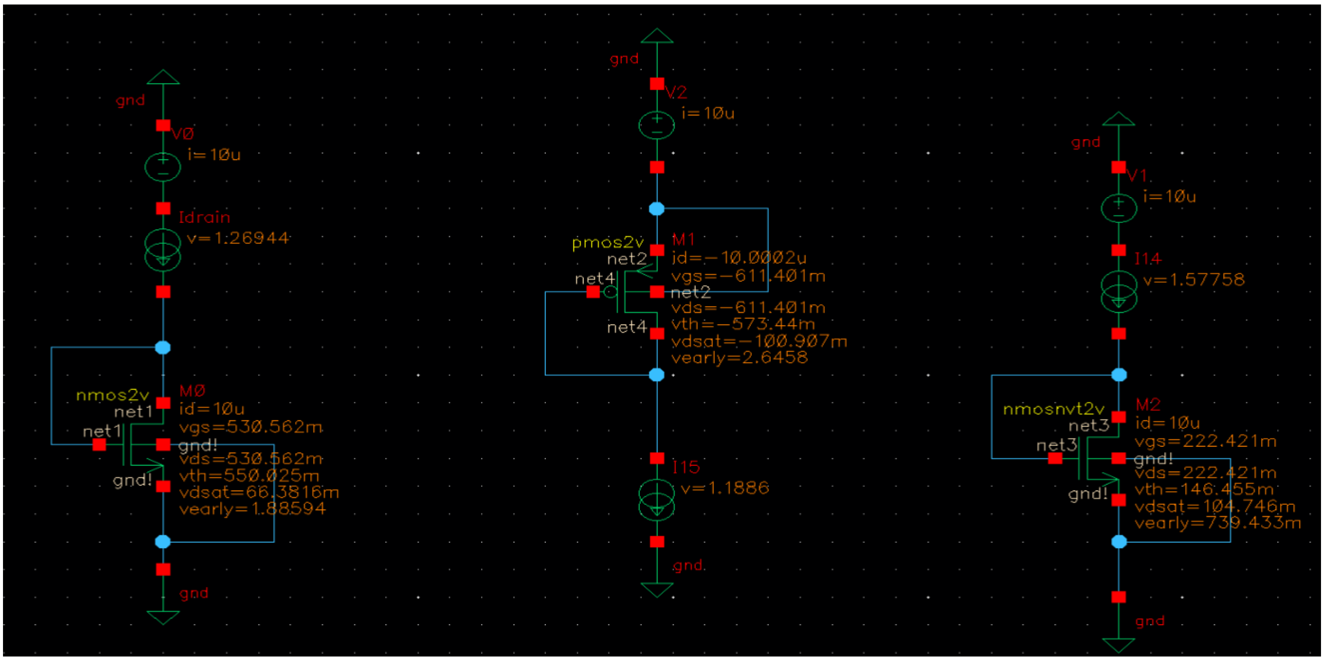

Figure 94 TSMC transistors under test schematic representation with Cadence default sizes. From left to right: nmos2v, pmos2v and nmosnvt2v. The operating bias points of each transistor can be appreciated

A better overview on the comparisons between the transistors also resides observing different cases: with minimum size, with ten times the sizes with respect the minimum one and with standard $180nm$ process size ($2um$ length and $10um$ width). All of them have been characterized in terms of the previously quoted electrical parameters. A DC analysis exploiting the *Maestro tool* in Cadence allowed the achieving of the results obtained for each transistor and size in the diode connection configuration. The following tables represent all the collected data.

Table 8 Minimum length and width size (the same colour on columns has been used for a direct comparison between transistors)

Outputs		**TSMC**			**UMC**			
	nmos2v	**pmos2v**	**nmosnvt 2v**	**N_18_MM**	**N_LV_18_MM**	**N_ZERO_18_MM**	**P_18_MM**	**P_LV_18_MM**
minimum length	180nm	180nm	500nm	180nm	240nm	300nm	180nm	240nm
minimum width	220nm	220nm	420nm	240nm	240nm	240nm	240nm	240nm
Idrain	10uA	-10.0052 uA	10uA	10uA	10uA	10uA	-10uA	-10.02uA
Vgs	648.839 mV	-909.85mV	353.743 mV	606.3mV	365.8mV	222.3mV	-917.5 mV	-667.4mV
Vearly	3.584V	5.671V	1.519V	1.983V	1.735V	566.8mV	5.226V	3.428V
Vth	485.653 mV	-548.054 mV	157.507 mV	434.1mV	163.1mV	-23.81mV	-483.2 mV	-195.6mV
gm	75.095uS	45.0216uS	80.972uS	78.93uS	75.43uS	50.7uS	34.11uS	34.24uS
gds	2.789uS	1.764uS	6.580uS	5.043uS	5.765uS	17.64uS	1.913uS	2.923uS
Vov=Vgs-Vth	163.186 mV	-361.796 mV	196.236 mV	172.2 mV	202.7mV	246.11mV	-434.3 mV	-471.8mV
op. region	2	2	2	2	2	2	2	2

Politecnico di Torino

Table 9 Standard technology sizes

Outputs		TSMC			UMC			
	nmos2v	pmos2v	nmosnvt2v	N_18_MM	N_LV_18_MM	N_ZERO_18_MM	P_18_MM	P_LV_18_MM
length standard at 180nm	2um	2um	2um	2um	2um	2um	2um	2um
width standard at 180nm	10um	10um	10um	10um	10um	10um	10um	10um
Idrain	10uA	-10.0014uA	10uA	10uA	10uA	10uA	-10uA	-10uA
Vgs	553.822mV	-694.04mV	152.234mV	457.1mV	149.8mV	34.98mV	-744.7mV	-452.1mV
Vearly	21.495V	30.3472V	888.713mV	8.281V	1.248V	38.68mV	40.74mV	20.1V
Vth	468.762mV	-479.05mV	63.361mV	348.5mV	67.76mV	-143.5mV	-481.5mV	-223mV
gm	125.158uS	70.551uS	183.97uS	135.2uS	164.6uS	46.61uS	67.61uS	74.85uS
gds	465.23nS	329.565uS	11.252uS	1.208uS	8.016uS	258.5uS	245.4nS	497.4nS
Vov=Vgs-Vth	85.06mV	-214.99mV	88.873mV	102.6mV	82.04mV	178.48mV	-263.2mV	-229.1mV
op. region	2	2	2	2	2	1, Vds=Vgs<Vov	2	2

Politecnico di Torino

Table 10 Sizes ten times the minimum ones

Outputs		TSMC			UMC			
	nmos2v	pmos2v	nmosnvt 2v	N_18_ MM	N_LV_18_ MM	N_ZERO_18_ MM	P_18_ MM	P_LV_18_ MM
length 10 times minimum one	1.8um	1.8um	5um	1.8um	2.4um	3um	1.8um	2.4um
width 10 times minimum one	2.2um	2.2um	4.2um	2.4um	2.4um	2.4um	2.4um	2.4um
Idrain	10.0004 uA	-10uA	10uA	10uA	10uA	10uA	-10uA	-10uA
Vgs	706.489 mV	- 975.517 mV	251.821 mV	596.4 mV	266.6mV	163.5mV	-1.035V	-779.3mV
Vearly	27.345V	35.841V	1.348V	12.27V	2.295V	254.8mV	44.63V	30.25V
Vth	476.304 mV	- 478.178 mV	32.6877 mV	357.8 mV	46.96mV	-158.7mV	-485.2 mV	-217.6mV
gm	72.0356 uS	34.694uS	83.599 uS	75.98uS	76.94uS	38.85uS	32.7uV	31.57uS
gds	365.709 nS	279.013n S	7.419uS	815.3nS	4.357uS	39.25uS	224.1nS	330.7nS
Vov=Vgs-Vth	230.185 mV	- 497.339 mV	219.133 mV	238.6m V	219.64mV	322.2mV	-549.8 mV	-561.7mV
op. region	2	2	2	2	2	1, Vds=Vgs<Vov	2	2

Table 11 Default Cadence sizes

Outputs		TSMC			UMC			
	nmos2v	pmos2v	nmosnvt 2v	N_18_MM	N_LV_18_MM	N_ZERO_18_MM	P_18_MM	P_LV_18_MM
CADENCE default length	180nm	180nm	500nm	180nm	240nm	300nm	180nm	240nm
CADENCE default width	2um	2um	2um	240nm	240nm	240nm	240nm	240nm
Idrain	10uA	10uA	10uA	10uA	10uA	10uA	-10uA	-10.02uA
Vgs	530.562 mV	-611.401 mV	222.421 mV	606.3 mV	365.8mV	222.3mV	-917.5 mV	-667.4mV
Vearly	1.886V	2.645V	739.433 mV	1.983V	1.735V	566.8mV	5.226V	3.428V
Vth	550.0.25 mV	-573.44 mV	146.455 mV	434.1 mV	163.1mV	-23.81mV	-483.2 mV	-195.6mV
gm	167.304uS	121.499 uS	156.448 uS	78.93uS	75.43uS	50.7uS	34.11uS	34.24uS
gds	5.302uS	3.779uS	13.524uS	5.043uS	5.765uS	17.64uS	1.913uS	2.923uS
Vov=Vgs-Vth	-19.463 mV	-37.961 mV	75.966 mV	172.2 mV	202.7mV	246.11mV	-434.3 mV	-471.8mV
op. region	3	2	2	2	2	2	2	2

Observing the standard sizes used at $180nm$ (Table 9), where a direct comparison can be made, it is clear that the transconductance gain results comparable between the two technologies, with slightly lower values for the UMC p-mos and native mos. Moreover, the threshold voltages of the UMC transistors seems to be smaller, specifically for the n-mos case ($Vth_{umc} = 348.5mV$, $Vth_{umc} = 468.76mV$) and the native case, while it tends to marginally increase for the p-mos one. Indeed, a smaller Vth allows to enhanced device performance by enabling lower power consumption, faster switching speeds, and reduced leakage currents also as a result that a smaller gate voltage is required to turn on the device. Additionally, a smaller Vth enables better linearity, it provides a wider dynamic range and it improves signal-to-noise ratio specifically in analog circuits. However, it is also true that MOS devices with smaller Vth values may be more susceptible to increased sensitivity to process variations, and reduced threshold voltage stability, hence careful optimization and design considerations are necessary to achieve the desired balance between performances and reliability. These factors are critical for applications such as amplifiers, analog-to-digital converters, and data communication systems. Furthermore, the behaviour of the overdrive voltage is an important aspect to analyse. It includes both the variation of the gate-source voltage and the threshold voltages. Therefore, observing the overdrive voltages of the UMC transistors it is clear that they are always higher in module with respect their counterparts. As a matter of fact, the standard UMC n-mos shows a $Vov = 102.6mV$, while the one of TSMC counterpart is instead equal to $Vov = 85.06mV$; the UMC pmos shows a $Vov = -263.2mV$, while the TSMC one is equal to $Vov = -214.99mV$ and finally the UMC native has a $Vov = 178.58mV$, while the TSMC one is equal to $Vov = 88.87mV$. The overdrive voltage directly affects the operation and performance of a MOS device. When this parameter results to be larger, it indicates that the voltage applied to the gate terminal is significantly higher than the threshold voltage, resulting in increased carrier (electron or hole) injection into the channel region of the transistor. This enhances conduction and improve switching characteristics. Thus, among the main catalysts of a high overdrive voltage could be annoverated: a stronger electric field, which allows for increased carrier mobility and higher current flow through the device, a faster charge/discharge times, which leads to quicker switching transitions in the MOS device and a reduction of the resistance, resulting in lower on-resistance and improved overall device efficiency. On the contrary, a smaller Vov can reduce power dissipation and energy consumption and also it may provide a more precise channel modulation of the output current or voltage. Regarding the transconductance gm, it indicates how effectively the transistor can amplify and control the output current based on changes in the input voltage. A high gm allows for a more significant change in the output current for a given change in the input voltage. This translates to increased amplification capability, enabling the transistor to provide stronger signal amplification in applications such as amplifiers and signal processing circuits, on the other hand, this could lead to higher dissipation and noise level. With a high gm the output current tends to follow the input voltage more faithfully in a wide range. Moreover, a high value of this parameter positively affects the gain bandwidth of the transistor, thus allowing the amplification of higher frequency without introducing important distortion. MOSFETs in general, shows a gm range that variates from $0.1mA/V$ to $10mA/V$, but this depends mainly on the manufacturer and on the typology of the transistor. In the proposed case all the transconductance gain results to fall in the quoted range. As quoted, the UMC n-mos exhibits a higher transconductance gain, while the p-mos a smaller one with respect the TSMC transistors in fact $gm_{nmos_{umc}} = 135.2uS$, $gm_{nmos_{tsmc}} = 125.158uS$ and $gm_{pmos_{umc}} = 67.61uS$, $gm_{pmos_{tsmc}} = 70.551uS$. However, those values still result comparable among each other. In general, considering all the data extrapolated from Cadence seems that the UMC n-mos has rather slightly better performance with respect the TSMC one, while an opposite consideration can be carried out for the p-mos case. However, it must be underlined that all the considerations made describe the effect that a single parameter variation has on the transistor, hence the overall effect that act on a transistor may be very different and it may affect the total circuit in which is part in a different way with respect the considerations made. Analogue inspection may be performed for all the other proposed cases, which however show differences between the sizes of transistors belonging to the different manufacturers. Particularly, providing some feedback between the TSMC minimum size and the ten times the minimum size values in the tables (Table 8 and Table 10), seems that for both the n-mos and p-mos cases an increment on the sizes enhance the overdrive voltage, reducing the threshold voltage and increasing the gate-source voltage, at the same time the transconductance gain appear to get worse. This behaviour may be due to an increment of the channel length modulation, hence due to a larger effective channel length, which reduces the electric field and the carrier mobility in the channel region. Also, with larger transistor sizes, the threshold voltage may increase, resulting in a higher Vov requirement to achieve the desired operation point. This increase in Vov can lead to a decrease in the transconductance gain as it becomes more challenging to achieve higher amplification levels. On the contrary, for the UMC case the Vth of the n-mos transistor seems to be much more affected with respect the TSMC one by the variation of the sizes of the device. In fact, even if the gate-source voltage in this technology reduces, the threshold voltage decrement is so important to lead anyway to an increment in the overdrive voltage. This high variation of the threshold voltage is not found in the UMC p-mos case. Furthermore, the larger size results in larger gate-source and gate-drain capacitances, which can cause increased charging and discharging delays which can limit the speed and performance of the transistor, impacting the transconductance gain. Regarding the Early voltage, which represents the slope of the output characteristics curve in the active region of the transistor and that is defined as the change drain current with respect to the change in the drain voltage, while keeping the gate voltage and other operating conditions constant, it is clear that, in all the cases with the exception of the default Cadence size case, is much smaller for the UMC n-mos transistors with respect the TSMC n-mos ones of at least a factor of 2. On the contrary, the UMC p-mos shows a higher Early voltage with respect the TSMC devices with the exclusion of the minimum size case, where the parameter is instead slightly smaller. A higher Early voltage can be beneficial in applications where a high output impedance is desired, such as in amplifiers or voltage buffers, and it can contribute to a higher voltage gain improving the linearity of the transistor by reducing distortion effects. Observing the minimum size and the ten times the minimum cases, it can be stated that the Early voltage for almost each case tends to change coherently between the transistors, it always increases with the increase of sizes, the only exception is represented by the native transistor.

Overall, increasing the size of a transistor can lead to an increase in Vov and a decrease in transconductance gain for the nmos case. Moreover, it has been proven that the n-mos UMC case tends to be more sensible to size variation, hence during the migration process this behaviour should be taken into consideration mainly because it could cause an important effect on noise itself.

9.3. UMC transistors width modulation to get same TSMC transistors performance

It is of interest to observe how the width of each UMC transistor could be modified with the aim to get the most similar results in terms of operating voltages with respect the TSMC devices. To achieve this, a sweep on the width of each transistor have been performed, observing if and when the correspondent TSMC gate-source/overdrive voltage were reached. It must be underlined that, not in all the cases this condition could be accomplished due to the early saturation of the voltage of the UMC transistor. In this latter case, a variation on both the length and width may be required. In the following tables, the width to get the same gate-source/overdrive voltage of the TSMC devices have been reported for each correspondent UMC transistor.

Table 12 Minimum sizes, width variation to get same vgs of the TSMC version

		UMC	
Transistors sizes to get:	**Vov(N_18_MM)=Vov(nmos2v)**	**Vov(N_ZERO_18_MM)=Vov(nmosnvt2v)**	**Vov(P_18_MM)=Vov(pmos2v)**
length	180nm	300nm	180nm
width	263.173nm	385.801nm	296.1468nm
Transistors sizes to get:	**Vgs(N_18_MM)=Vgs(nmos2v)**	**Vgs(N_ZERO_18_MM)=Vgs(nmosnvt2v)**	**Vgs(P_18_MM)=Vgs(pmos2v)**
length	180nm	300nm	180nm
width	max achivable Vgs=606.2842mV ! (unable to reach 648.839mV only by changing the width)	max achivable Vgs=222.332mV ! (unable to reach 353.743mV only by changing the width)	245.86nm

Table 13 Standard technology, width variation to get same vgs of the TSMC version

		UMC	
Transistors sizes to get:	**Vov(N_18_MM)=Vov(nmos2v)**	**Vov(N_ZERO_18_MM)=Vov(nmosnvt2v)**	**Vov(P_18_MM)=Vov(pmos2v)**
length	2um	2um	2um
width	14.021um	minimum achivable Vov=146.7mV ! (unable to reach 88.8728mV)	14.271um
Transistors sizes to get:	**Vgs(N_18_MM)=Vgs(nmos2v)**	**Vgs(N_ZERO_18_MM)=Vgs(nmosnvt2v)**	**Vgs(P_18_MM)=Vgs(pmos2v)**
length	2um	2um	2um
width	max achivable Vgs=457.1mV ! (unable to reach 553.822mV)	max achivable Vgs=34.98mV ! (unable to reach 152.234mV)	14.554um

Table 14 Ten times sizes, width variation to get same vgs of the TSMC version

		UMC	
Transistors sizes to get:	**Vov(N_18_MM)=Vov(nmos2v)**	**Vov(N_ZERO_18_MM)=Vov(nmosnvt2v)**	**Vov(P_18_MM)=Vov(pmos2v)**
length	1.8um	3um	1.8um
width	2.562um	7.565 um	2.875um
Transistors sizes to get:	**Vgs(N_18_MM)=Vgs(nmos2v)**	**Vgs(N_ZERO_18_MM)=Vgs(nmosnvt2v)**	**Vgs(P_18_MM)=Vgs(pmos2v)**
length	1.8um	3um	1.8um
width	max achivable Vgs=596.4mV ! (unable to reach 706.489mV)	max achivable Vgs=163.5mV ! (unable to reach 251.821mV)	2.943um

Table 15 Default Cadence sizes, width variation to get same vgs of the TSMC version

		UMC	
Transistors sizes to get:	**Vov(N_18_MM)=Vov(nmos2v)**	**Vov(N_ZERO_18_MM)=Vov(nmosnvt2v)**	**Vov(P_18_MM)=Vov(pmos2v)**
length	180nm	300nm	180nm
width	3.742um	1.64001um	4.35239um
Transistors sizes to get:	**Vgs(N_18_MM)=Vgs(nmos2v)**	**Vgs(N_ZERO_18_MM)=Vgs(nmosnvt2v)**	**Vgs(P_18_MM)=Vgs(pmos2v)**
length	180nm	300nm	180nm
width	1.697um	max achivable Vgs=222.3mV ! (unable to reach 222.421mV)	2.4003um

The formula that relates the gate-source voltage (Vgs) and width (W) of a n-mos transistor is the following:

$$Vgs = Vth + \frac{2 * Id * L}{\beta * W}$$

(163)

where Vgs is the gate-source voltage, Vth is the threshold voltage of the n-mos transistor, Id is the drain current, L is the length of the n-mos transistor and β is the transconductance parameter. It is clear that the gate source voltage variates with the width proportionally to $\frac{1}{W^2}$, therefore, the behaviour for the n-mos transistors would be a classic negative exponential. On the other hand, the behaviour of the curves of the p-mos, since the gate-source voltage (not the source-gate one) is plotted, is represented as a logarithmic and indeed the voltage on the y axis is negative. As a visualization of the expected curves, some plots of the gate-source voltages (y-axis) with variation on the width (x-axis) have been reported for the case of the default Cadence sizes for the different transistors in Figure 95, Figure 96 and Figure 97.

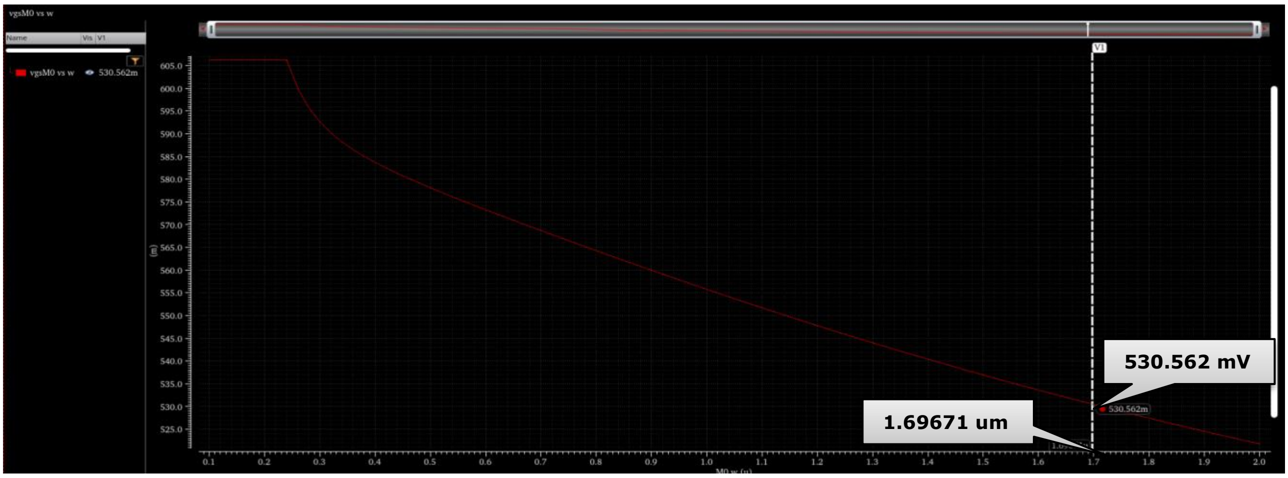

Figure 95 N_18_MM width required to get the same vgs of the correspondent nmos2v TSMC

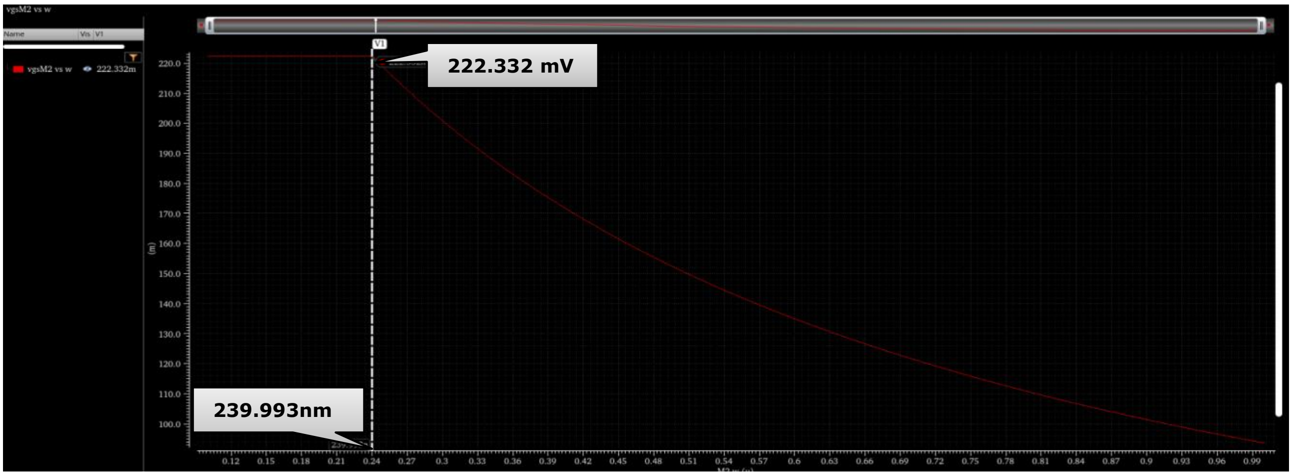

Figure 96 N_ZERO_18_MM width required to get the same vgs of the correspondent nmosnvt2v TSMC (since it should reach the value of 222.421mV, correspondent to the TSMC gate-source voltage of the nmosnvt2v, the achievable gate-source voltage results to be close to this, but still, it is not possible for this UMC transistor to obtain the same gate source voltage only by changing its width)

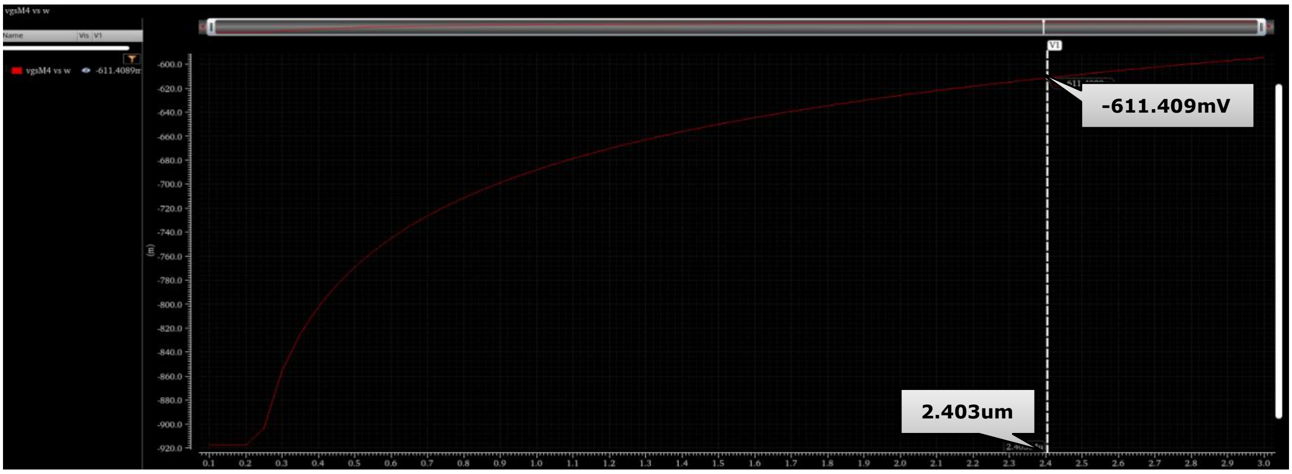

Figure 97 P_18_MM width required to get the same vgs of the correspondent pmos2v TSMC

As already quoted, is not always possible to obtain a proper exact value of width for the UMC transistors able to show a gate-source or overdrive voltage which are comparable to the TSMC ones. In particular, this occurs in the case of the N_ZERO_18_MM (UMC) transistors if compared to the nmos2v (TSMC) one (Figure 96) where a value of gate-source voltage of $222.421mV$ represents the goal to reach, but the maximum voltage achievable is instead equal to $222.332mV$. In this latter case the variation is practically negligible, but on other cases previously reported in the tables this effect is much more important. An identical approach has been exploited also for the overdrive voltage comparison among transistors.

In conclusion, modifying the channel width primarily affects the channel conductance and, consequently, the transconductance gain. Indeed, a wider channel width increases the channel conductance, allowing for higher output currents and higher gm values. However, wider channel widths may lead to larger parasitic capacitances, slower switching speeds, and increased power consumption. On the contrary, the change on the channel length affects the channel resistance and the threshold voltage. A shorter channel length reduces the channel resistance, allowing for higher drive currents and faster switching speeds, however it may increase leakage currents and susceptibility to short-channel effects. Shorter channel lengths can result in improved performance in terms of speed and power consumption, making them desirable for high-speed and low-power applications. On the other hand, manufacturing accuracy and fabrication costs, represent limitations that may impose constraints on how short the channel length can be. During the migration process have been exploited sizes much higher with respect the minimum one, hence no problems of this nature have been encountered. The information collected in this section will be useful for the next section where the migration of an operational amplifier is performed from the TSMC to the UMC technology.

9.4. TSMC Operational amplifier migration to UMC

To start the migration of an operational amplifier from the TSMC to the UMC technology, the TSMC schematic and the correspondent electrical characteristics must be analysed at first. As a general approach, as it can be visualized in Figure 98, the TSMC operational amplifier design is made of a differential pair, current mirrors, a bottom switch to turn on the amplifier after a certain voltage level is reached and some input and output capacitances.

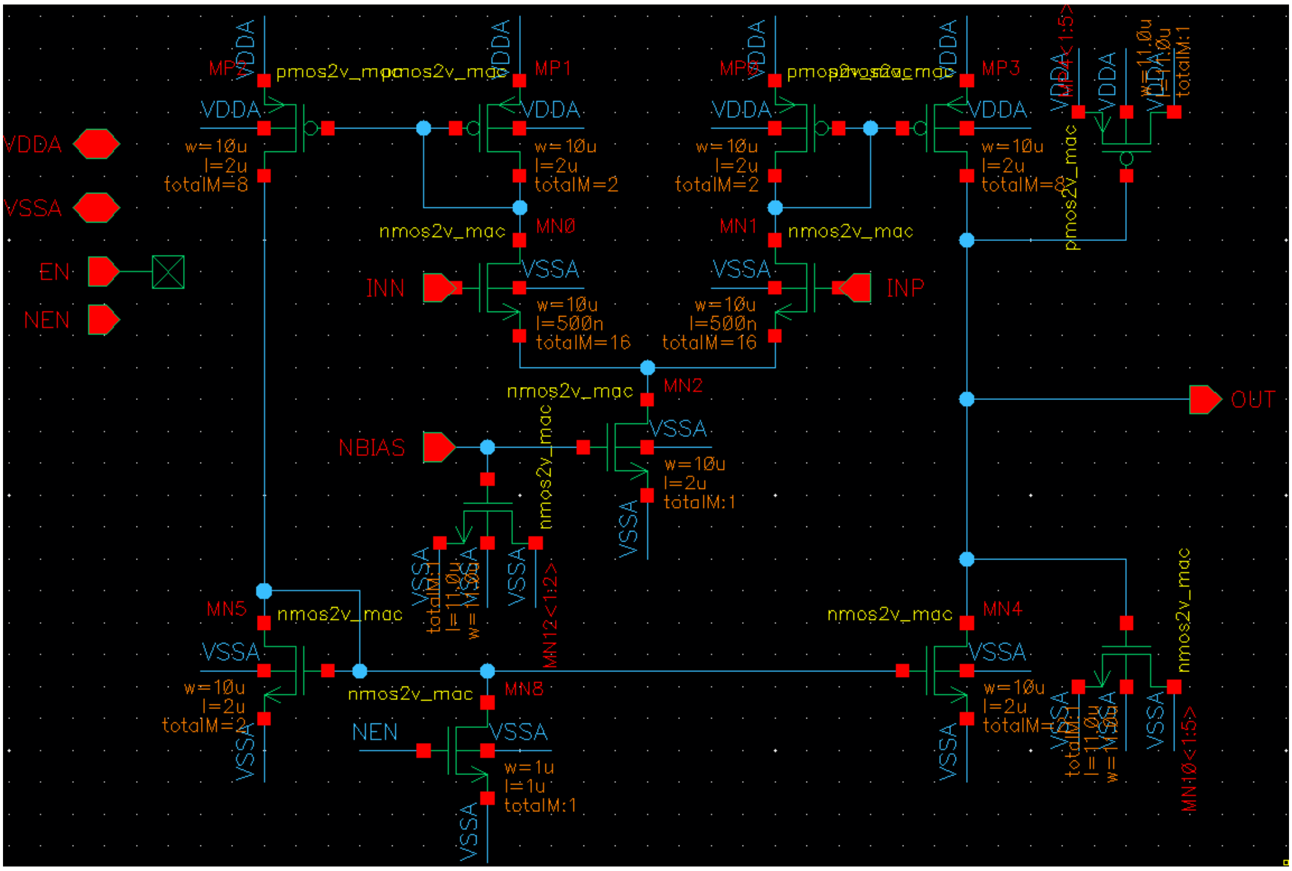

Figure 98 Operational amplifier TSMC schematic Cadence view

This configuration is a classic two stages amplifier where the first stage is represented by the differential pair, and the second by the right transistors, which in turn have a current defined by the left transistors due to the current mirror configuration. Indeed, current mirrors are exploited to assure the most similar driving current among transistors. Since providing a positive step to the INN node the output results to be negative, this signal represents the negative differential input. Similarly, providing a positive step to the node INP, the output will result to be positive due to the fact that the common source is acting as an inverting cell, hence INP is the positive differential input. Moreover, in order to detect the behaviour in terms of electrical parameters, the testbench reported in Figure 99 has been used.

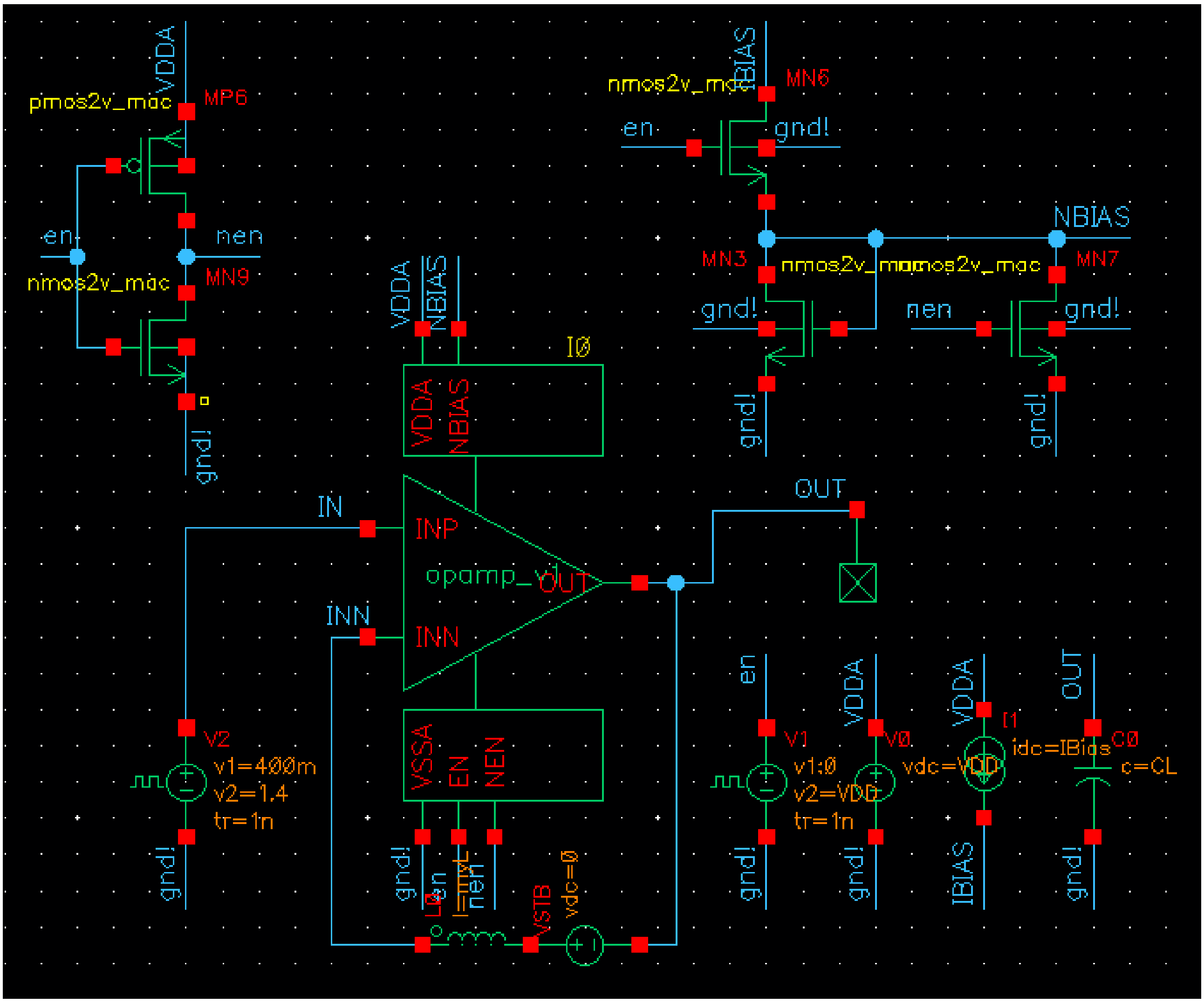

Figure 99 test bench operational amplifier TSMC Cadence view

In this case a voltage follower configuration has been exploited for simplicity. Some components have been added in order to ease the process of detection of the electrical behaviour of the circuit. For instance, the *VSTB* generator has been placed in the feedback loop as a probe to detect the Loop Gain. The UMC test bench has been replicated almost in an identical way. The sizes of the UMC transistors in the migrating version of the test bench have been chosen in order to provide the most similar value for the *nen* and *NBIAS* signals with respect the one obtained in the TSMC version without caring too much about other parameters since they are not part of the operational amplifier under test. The variables present in the test bench used for the comparison of the operational amplifier in the two technologies are the following:

$$CL = 10pF \tag{164}$$

$$en = 1V \tag{165}$$

$$Frec = 100kHz \tag{166}$$

$$IBias = 2.5uA \tag{167}$$

$$myL = 0H \tag{168}$$

$$VDD = 1.8V \tag{169}$$

$$Vin = 1.4V \tag{170}$$

$$VSSA = ground \tag{171}$$

In particular, the CL is the load capacitance, $Frec$ is the frequency of operation necessary to define the pulse width of the input signal, $IBias$ is the driving current, VDD is the power supply for this technology node and Vin is the signal that defines the DC voltage. The parameters of the V2 generator have been set as following:

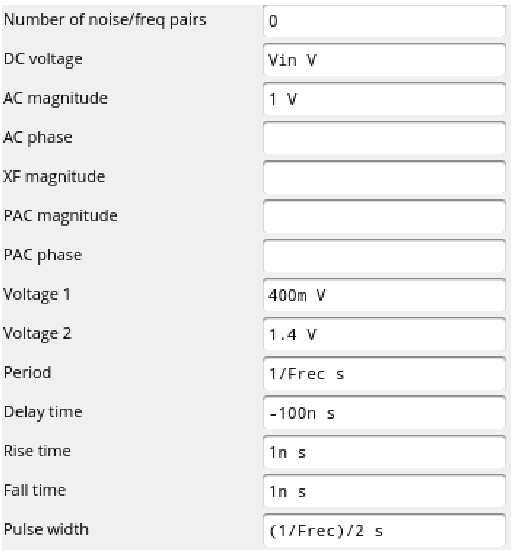

Number of noise/freq pairs	0
DC voltage	Vin V
AC magnitude	1 V
AC phase	
XF magnitude	
PAC magnitude	
PAC phase	
Voltage 1	400m V
Voltage 2	1.4 V
Period	1/Frec s
Delay time	-100n s
Rise time	1n s
Fall time	1n s
Pulse width	(1/Frec)/2 s

Figure 100 V2 generator parameters Cadence window view

Performing some simulations on the circuit, it has been noticed that a simple 1:1 scaling from one technology to another on the operational amplifier in terms of sizes of transistors is not possible in order to reproduce with fidelity the most similar characteristics of the TSMC design; this is due to the differences between the transistors of the two technologies. A trial with the UMC design with *identical sizes* with respect the TSMC one provides similar, but not close results, which have been reported below and that are also visible in Figure 101 taken directly from Cadence plots:

$$Power\ consumption_{UMCopamp} = 24.42uW\ (in\ TSMC\ resulted\ to\ be\ 24.5uW) \tag{172}$$

$$Loop\ Gain_{UMCopamp} = 44.22dB\ (in\ TSMC\ resulted\ to\ be\ 49dB) \tag{173}$$

$$Phase\ Margin_{UMCopamp} = 63.36deg\ (in\ TSMC\ resulted\ to\ be\ 70.0deg) \tag{174}$$

$$Band\ Width\ closed\ loop_{at\ -3dB\ UMCopamp} = 2.25116MHz\ (in\ TSMC\ resulted\ to\ be\ 1.83846MHz) \tag{175}$$

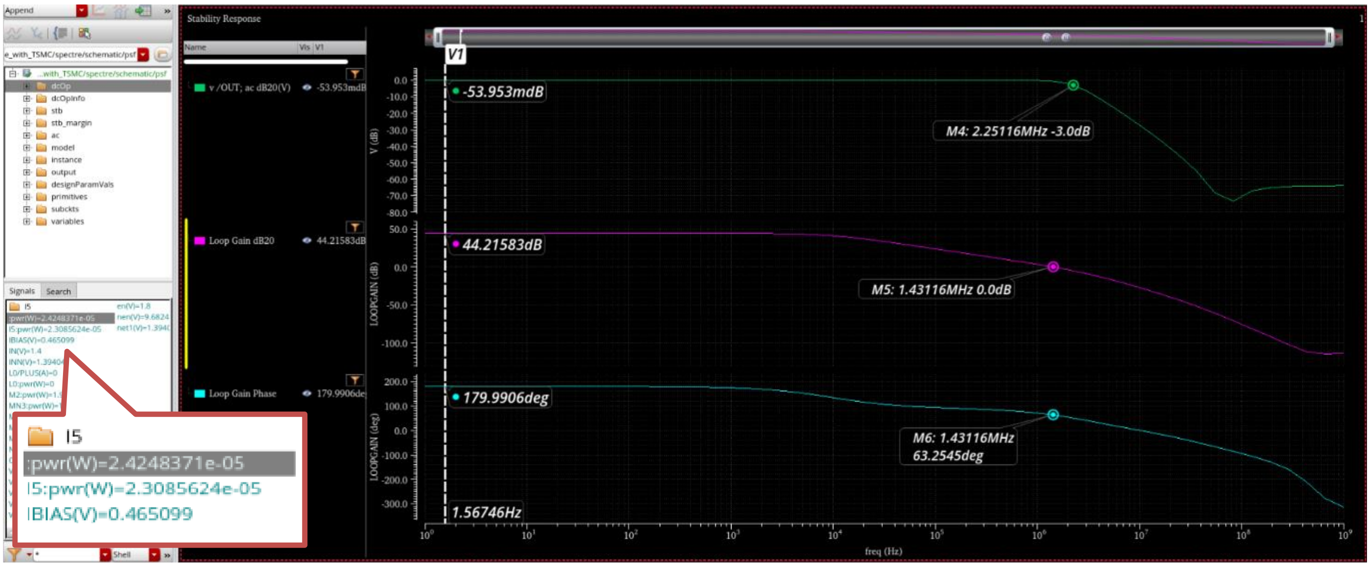

Figure 101 UMC operational amplifier characteristics in terms of Open and Closed loop gain, phase margin, power consumption, with transistors with identical sizes with respect the one used in TSMC operational amplifier

It is clear how the highest difference is in the phase margin, which in UMC it results to be much lower, hence increasing the possibility to obtain an unstable circuit. Therefore, some adjustments on the sizes of the transistors have been necessary in order to enhance stability and to get closer results to the TSMC values. The final choice made can be appreciated in Figure 102 which shows the UMC schematic, where width (w), length (l) and multiplier (m, which identifies the actual width of the transistor) of each transistor have been noted on it.

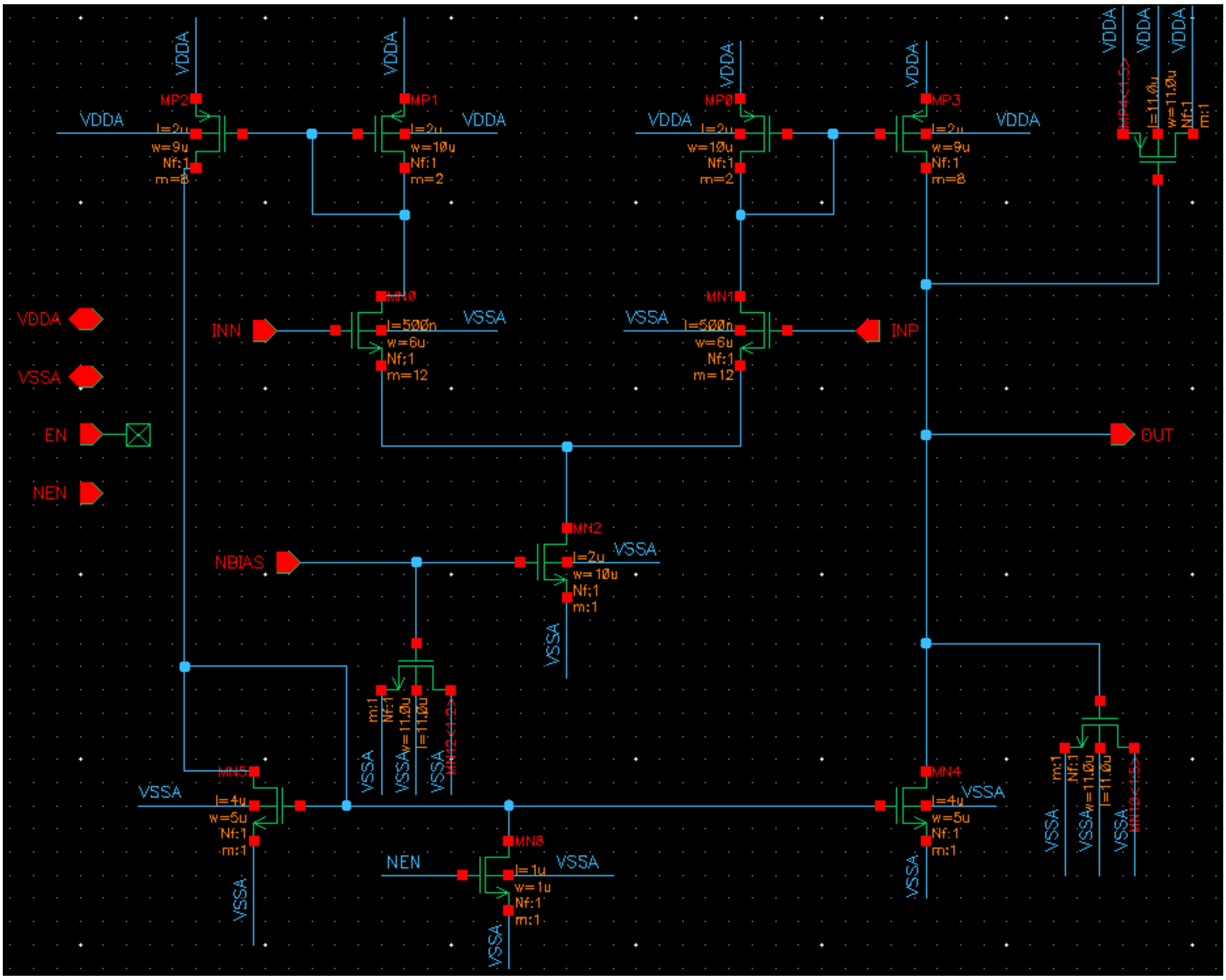

Figure 102 Operational amplifier UMC schematic Cadence view. The chosen width, length and multiplier are visible on each transistor

In this case the chosen UMC width, length and the multiplier for each transistor have been specified in Table 16.

Table 16 Width, length and multiplier chosen for the transistors dedicated to the UMC version of the operational amplifier

Transistors	Width	Length	Multiplier
MP2, MP3	$9um$	$2um$	8
MP1, MP0	$10um$	$2um$	2
MN0, MN1	$6um$	$500nm$	12
MN2	$10um$	$2um$	1
MN5, MN4	$5um$	$4um$	1
MN8	$1um$	$1um$	1
MP4<1:5>	$11um$	$11um$	1
MN10<1:5>	$11um$	$11um$	1

With this choice of sizes, the corresponding results from the UMC operational amplifier resulted to be the following:

$$Power\ consumption\ =\ 21.114uW\ (in\ TSMC\ resulted\ to\ be\ \ 24.5uW) \tag{176}$$

$$Loop\ Gain\ =\ 49.13dB\ (in\ TSMC\ resulted\ to\ be\ 49dB) \tag{177}$$

$$Phase\ Margin\ =\ 69.49deg\ (in\ TSMC\ resulted\ to\ be\ \ 70.0deg) \tag{178}$$

$$BWclosed\ loop_{at-3dB}\ =\ 1.82358MHz\ (in\ TSMC\ resulted\ to\ be\ \ 1.83846MHz) \tag{179}$$

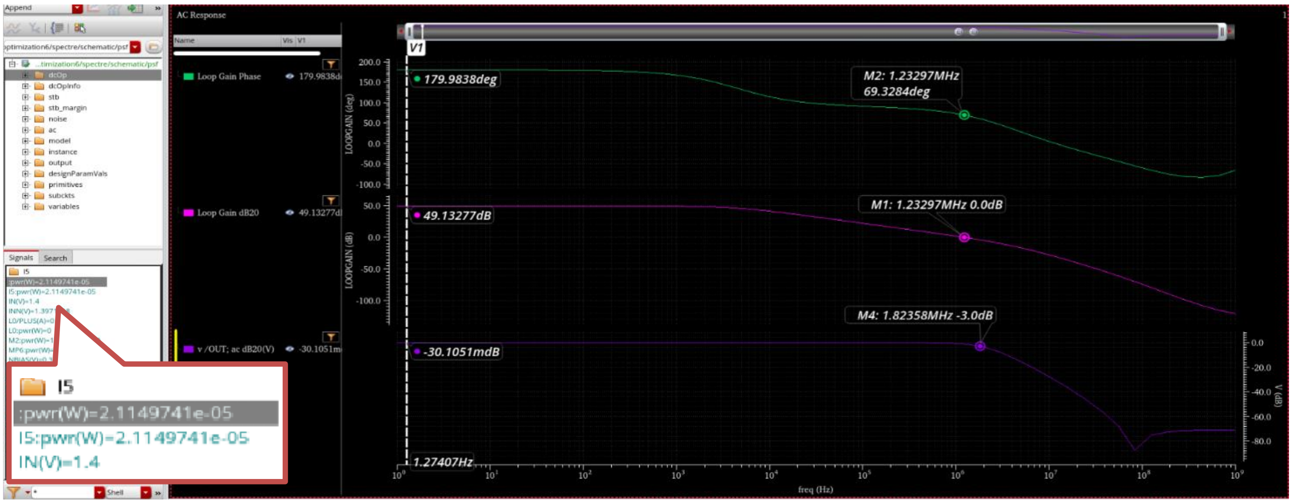

Figure 103 Optimized UMC operational amplifier total results

Much closer results to the original TSMC design have been obtained (Figure 103). The only relevant change is in the noise, which resulted to be slightly higher in this UMC design with respect the TSMC one. The following pictures (Figure 104, Figure 105) underline the effect of noise, showing the behaviour on both the TSMC and UMC designs.

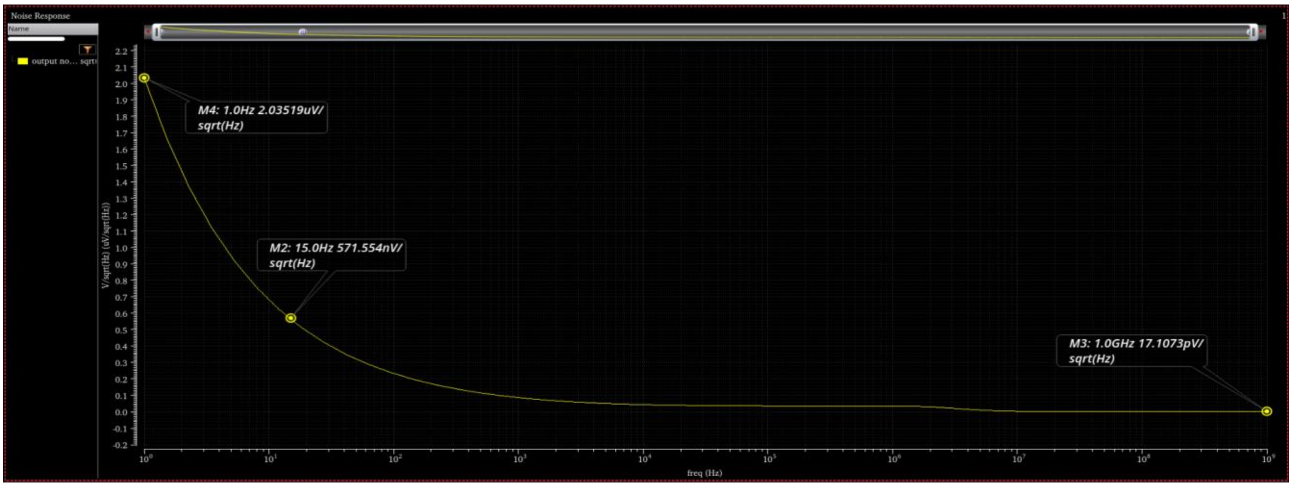

Figure 104 TSMC operational amplifier noise

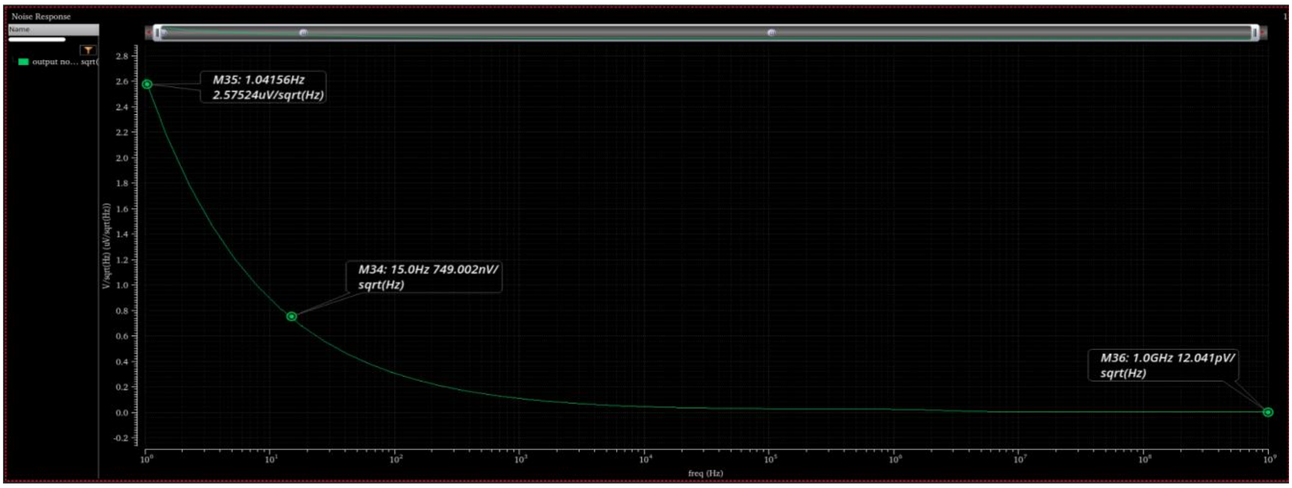

Figure 105 UMC operational amplifier noise

Additionally, the comparison between the dynamics of the original TSMC and the UMC operational amplifier design have been obtained in Cadence (Figure 106, Figure 107), where has been noticed that the one belonging to the TSMC resulted to reach a minimum value of around $19mV$ and a maximum one of $1.77V$, while the UMC dynamic reached a minimum and maximum value of output voltage respectively of $17mV$ and $1.75V$, thus slightly lower with respect its antagonist.

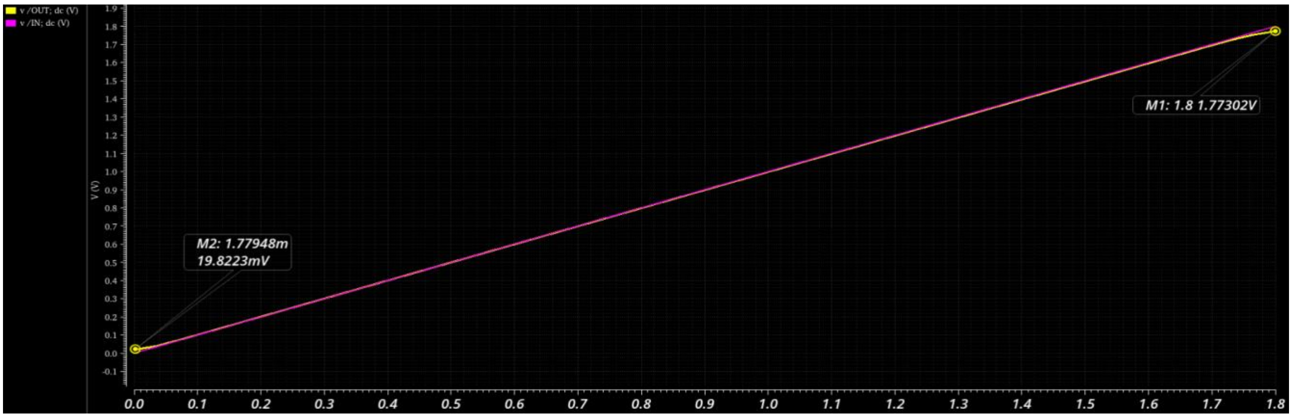

Figure 106 TSMC operational amplifier dynamic in DC

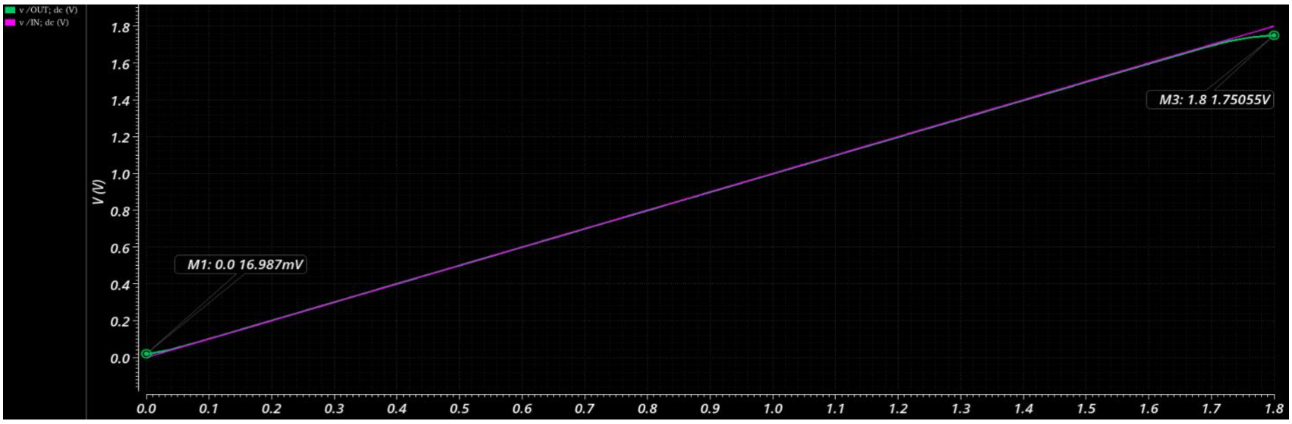

Figure 107 UMC operational amplifier dynamic in DC

The slew-rate parameter may represent an important parameter of comparison between the optimization and the original design. This represents the maximum amount of output swing achievable from the circuit. In Figure 108 has been reported the time analysis of of the input and output of the UMC optimization for one particular cycle. It is clear that the slew rate can be estimated exploiting the gradient, hence using the following computation:

$$SR_{UMC} = \frac{1.2819\,V - 548.12\,mV}{11.88153\,us - 10.23648\,um} = 0.446\frac{V}{us} \quad (180)$$

The value of the slew-rate of the TSMC version is instead equal to $0.488\frac{V}{us}$, therefore, it is higher with respect the UMC version, which means that the output can follow more faithfully the input with the drawback of a higher contribution of ringing effect.

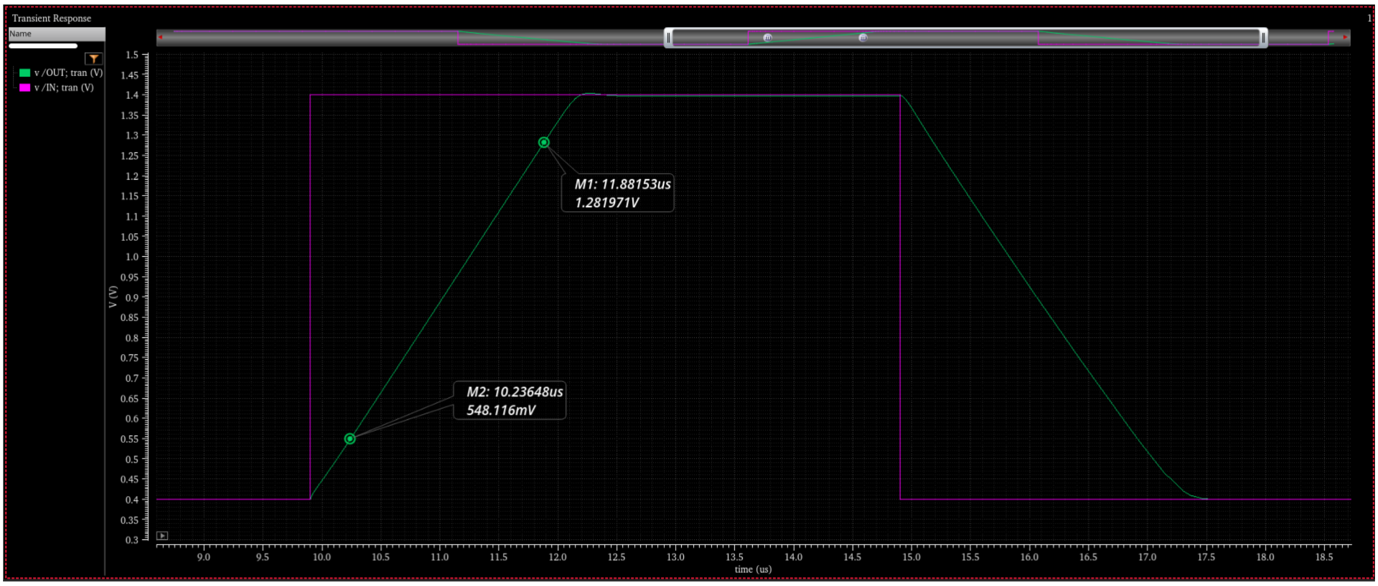

Figure 108 UMC operational amplifier time analysis for slew rate computation. In green line the output signal, in pink the input signal

In conclusion, very similar and acceptable electrical results have been obtained in the UMC version of the operational amplifier with the transistors size choice made. At this point, once the schematic is defined, the design can then continue outlining the correspondent layout.

9.5. UMC layout design operational amplifier

Once satisfactory electrical results have been obtained from the schematic, the following step see the implementation of the actual layout migration in UMC performed in *Cadence XLayout*. Cadence XLayout provides the possibility to generate an initial layout with all the fundamental pins and transistors and capacitors by exploiting the "*Generate selected from source*" default setting. At this point, transistors, contacts, additional layers, interconnections and the proper pin labels have been drawn in order to completely match the schematic. The UMC schematic layout has been then faithfully recreated and similarly for the layout of the pressure sensor and the accelerometer designs, the DRC of the UMC has been completed with success. Regarding the final dimensions of the entire operational amplifier chip, the length resulted to be $L = 90.3um$ and the height $h = 102.84um$, which are indeed higher with respect the TSMC design that are instead equal to $L = 76.46um$ and $h = 92.33um$ respectively. This variation was expected due to the higher limitation in constraints from the UMC manufacturer. In addition to the DRC check, also the Layout vs schematic (LVS) check has been performed and successfully completed with no errors.

For instance, all the nets, power supplies and instances included in the layout must perfectly correspond to the schematic ones. To complete the entire layout, it has been taken advantage of only two levels of hierarchy which are visible in Figure 110. At the occurrence, both n-ring and p-ring have been exploited for capacitors and set of transistors with the principal aim to isolate the N-well and poly-gate regions from neighbouring components, hence to prevent unwanted interactions between different circuit elements. The following figures represent the Cadence view of the UMC operational amplifier layout with the exploited layers. Reported on the top and bottom of the layout, there are the power rails which are made of metal 1 and that indeed, define the height and length of the entire cell. These blocks have been drawn with the respective power pins. All the layout has been designed trying to maintain the minimum occupied space possible while achieving the minimum tracks length of interconnections between the signals. In particular, Figure 109 and Figure 110 shows the lower and the highest level of hierarchy of the final implementation of the UMC operational amplifier respectively in all its components made with the different layers, which are shown on the right.

Politecnico di Torino

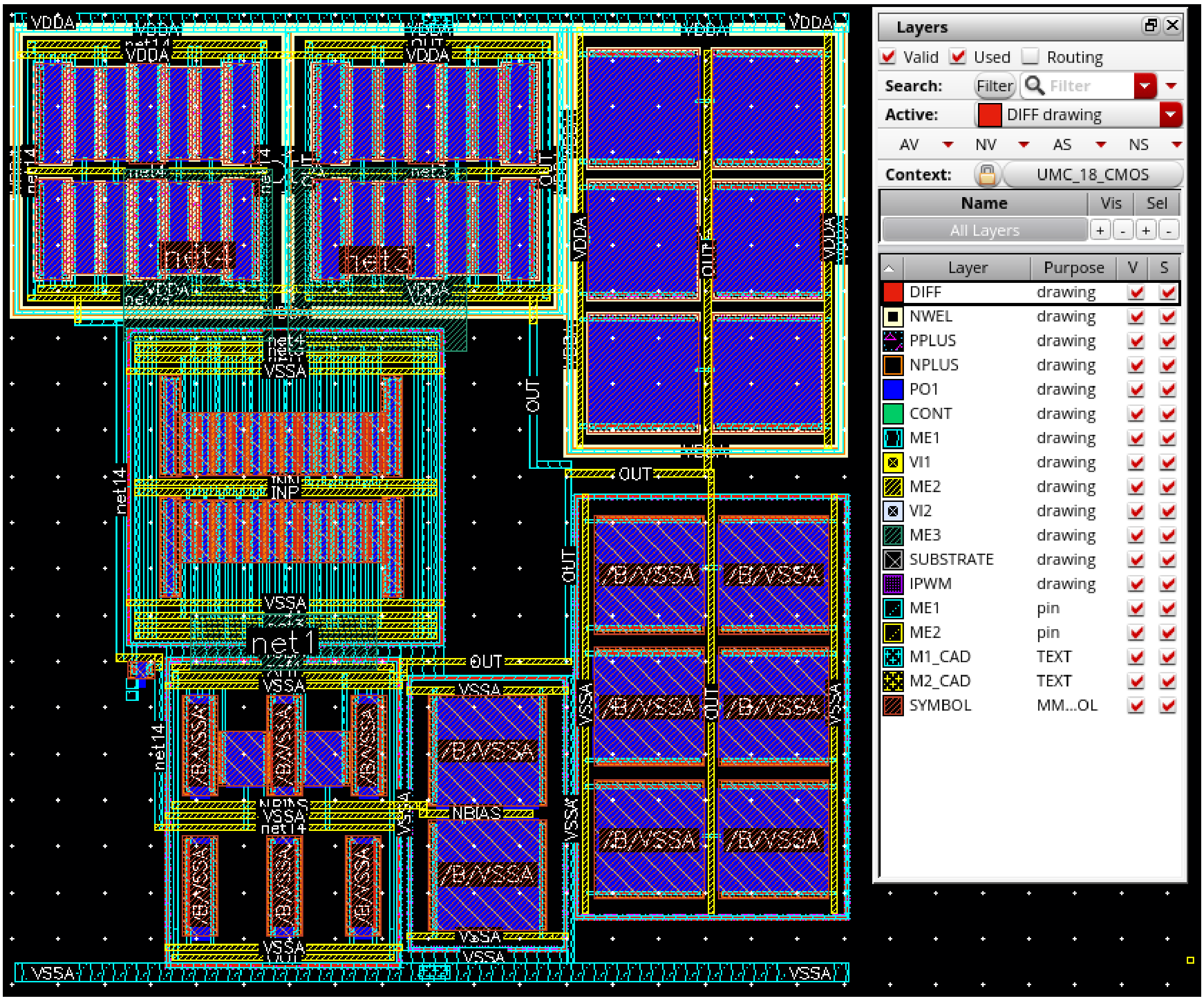

Figure 109 UMC operational amplifier Layout design complete view

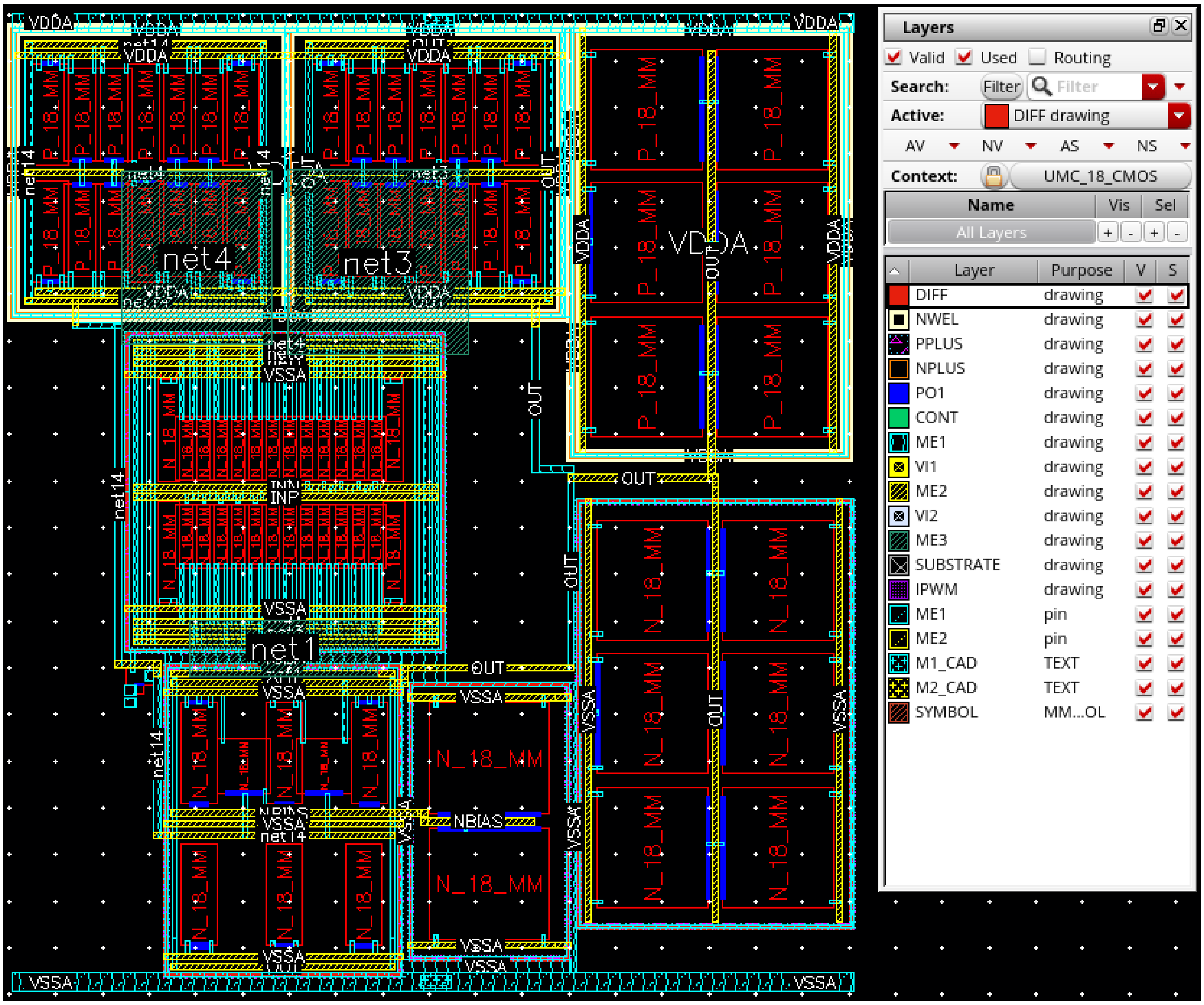

Figure 110 UMC operational amplifier Layout design higher level of hierarchy

Finally, Figure 111 shows the log file related to the LVS which states that no errors have been detected during the check, hence the cell is suitable to be used in further implementation and circuits as a part of the UMC read-out of a sensor.

```
              CELL COMPARISON RESULTS ( TOP LEVEL )


                 #       ###################       _   _
                #        #                 #        *   *
            #   #        #     CORRECT     #          |
             # #         #                 #        \___/
              #          ###################


LAYOUT CELL NAME:        opamp_v1_UMC_optimization6
SOURCE CELL NAME:        opamp_v1_UMC_optimization6

--------------------------------------------------------------------------------

INITIAL NUMBERS OF OBJECTS
--------------------------

                Layout    Source         Component Type
                ------    ------         --------------
 Ports:              8         8

 Nets:              12        12

 Instances:         45        45         MN (4 pins)
                    34        34         MP (4 pins)
                ------    ------
 Total Inst:        79        79

NUMBERS OF OBJECTS AFTER TRANSFORMATION
---------------------------------------

                Layout    Source         Component Type
                ------    ------         --------------
 Ports:              8         8

 Nets:              12        12

 Instances:          9         9         MN (4 pins)
                     6         6         MP (4 pins)
                ------    ------
 Total Inst:        15        15
```

Figure 111 LVS results log file of the UMC operational amplifier optimization

10. Conclusions and recommendations

The following four major milestones have been covered in this thesis.

Firstly, the most important theoretical aspects related to the pressure sensor and accelerometer have been carried out as an introduction to the work. This has been followed by the migration from the TSMC to the UMC technology of the prototypes-A1 of a pressure sensor and an accelerometer. The achievement of this was initially possible thanks to the study of the design processes and the rules of the individual manufacturers. The simplicity of migrating an existing design in one technology to another, while maintaining the same technological node, has been demonstrated, provided that the rules of the new manufactures allow for easy migration, otherwise greater precautions must be taken when designing the layout. Klayout and Cadence layout tools have been used for the purpose of this objective, proving to be excellent and simple tools and also giving the possibility to easily analyse the DRC of each layout.

Secondly, the characterization of the pressure sensor and the accelerometer have been performed exploiting the COMSOL 5.5 tool. Two cases for each sensor have been discussed and distinguished in terms of mechanical and electrical parameters: the pre-fabrication and post-fabrication cases. The simulations of the post fabrication case have been based on the study already made by *Diana Mata-Hernandez* et. Al. *[1]. B*ased on this last quoted work and on the theoretical pre-fabrication case, some ideal and constant correction factors have been extrapolated in order to be applied afterwards for the simulations and characterization of the accelerometer, which instead has not been released at the moment. The effect of squeeze film damping has been carried out on all the different kind of central resonators to study the behaviour of the relative film pressure acting on the proof mass, particularly distinguishing the horizontal and vertical movement whenever required. A new version of the accelerometer has been proposed with the aim to enhance the sensitivity of it. Final comparison among the sensors have been discussed, underlying the main differences that brought to the obtained results. All has been corroborated with information related to the COMSOL tool and the highlights to carry a good analysis of MEMS mainly exploiting *the Electromechanics physic interface*.

Thirdly, a direct comparison between the primary transistors belonging to the TSMC and UMC have been presented with the aim to extrapolate the differences and the similarities of the devices under identical conditions. The UMC transistors width has been modified in order to emulate the behaviour of the TSMC devices. Overall, all the devices resulted to be slightly different with respect the original manufacturer.

Finally, a further migration from TSMC to UMC was successfully completed. The scheme of an operational amplifier has been reproduced in UMC technology in order to obtain characteristics as much similar as possible to the TSMC ones, and, once this has been obtained, the layout has been defined and controlled through the DRC and LVS procedure using the Cadence tool.

The key performance parameters of the CMOS-MEMS sensors have been deeply analysed, thus demonstrating the feasibility of migrating both pressure sensors and accelerometers layouts from one technology to another and to integrate them together with other electronics. The presented work does not fulfil all the requirements to develop a final product, however it encompasses the initial most interesting aspects related to the CMOS-MEMS design development in terms of design, migration and simulation.

Politecnico di Torino

1859

References

[1] "*Resonant MEMS Pressure Sensor in 180 nm CMOS Technology Obtained by BEOL Isotropic Etching" Diana Mata-Hernandez, Daniel Fernández, Saoni Banerji and Jordi Madrenas, 23 October 2020, Sensors 2020, 20, 6037; doi:10.3390/s20216037*

[2] "Development of System-on-Chip CMOS-MEMS Pressure Sensors", Saoni Banerji, Ph.D. dissertation, Barcelona, September 2017

[3] H. Qu, "CMOS MEMS fabrication technologies and devices," Micromachines, vol. 7, p. 14, Jan. 2016, doi: 10.3390/mi7010014.

[4] "Manufacturing issues of BEOL CMOS-MEMS devices," J. Valle, D. Fernandez, O. Gibrat, and J. Madrenas, IEEE Access, vol. 9, pp. 83149–83162, 2021. [Online]. Available: https://ieeexplore.ieee.org/document/9447709.

[5] "*Monolithic Sensor Integration in CMOS Technologies" Daniel Fernández , Piotr Michalik, Juan Valle , Saoni Banerji , Josep Maria Sánchez-Chiva , and Jordi Madrenas, IEEE SENSORS JOURNAL, VOL. 23, NO. 2, 15 JANUARY 2023*

[6] "MEMS Tutorial: Pull-in voltage in electrostatic microactuators", Ville Kaajakari, Tutorials: http://www.kaajakari.net/~ville/research/tutorials/tutorials.shtml

[7] "Analytical solution of the modified Reynolds equation for squeeze film damping in perforated MEMS structures", Ashok Kumar Pandey, Rudra Pratap, Fook Siong Chau, Available online at www.sciencedirect.com, 23 October 2006

[8] "Monolithic Multi-sensor Design with Resonator-Based MEMS Structures" F. Y. Kuo, C. Y. Lin, P. C. Chuang, C. L. Chie, Y. L. Yeh, and Stella K. A. Wen, DOI 10.1109/JEDS.2017.2666821, IEEE Journal of the Electron Devices Society, 2016

[9] "Experiments on MEMS Integration in 0.25 um CMOS Process", Piotr Michalik, Daniel Fernández, Matthias Wietstruck, Mehmet Kaynak and Jordi Madrenas, Sensors 2018, 18, 2111; doi:10.3390/s18072111

[10] "The challenges and solutions of building MEMS devices using the BEOL metal layers of a solid-state CMOS semiconductor process", Nanusens, Josep Montanyà i Silvestre

[11] "A Comprehensive High-Level Model for CMOS-MEMS Resonators", Saoni Banerji, Daniel Fernández, and Jordi Madrenas, IEEE SENSORS JOURNAL, VOL. 18, NO. 7, APRIL 1, 2018

[12] "Best Practices for Compact Modeling in Verilog-A", Colin C. McAndrew et al. JOURNAL OF THE ELECTRON DEVICES SOCIETY, 21 August 2015

[13] "COMSOL Multiphysics 5.5 Reference Manual", COMSOL

[14] “Introduction to MEMS module”, COMSOL

[15] “Frequency Response of a Biased Resonator — 3D”, COMSOL tutorial

[16] “Stationary Analysis of a Biased Resonator — 3D”, COMSOL tutorial

[17] “Pull-In Voltage for a Biased Resonator — 3D”, COMSOL tutorial

[18] “Squeeze-Film Damping of Perforated Plates”, COMSOL tutorial

[19] M. Bao and H. Yang, “Squeeze film air damping in MEMS,” Sensors and Actuators A: Physical, vol. 136, no. 1, pp. 3 – 27, 2007, 25th Anniversary of Sensors and Actuators A: Physical. [20] “Modelling and validation of air damping in perforated gold and silicon MEMS plates” Giorgio De Pasquale et al 2010 J. Micromech. Microeng. 20 015010

[21] “Design and Prototyping of BEOL-Embedded CMOS-MEMS Accelerometers”, Piotr Michalik, Barcelona, October 2015

[22] “FRINGING FIELD MODELLING IN MEMS CAPACITIVE COMB-DRIVE ACCELEROMETERS”, Cezary MAJ, Jacek NAZDROWICZ, Adam STAWIŃSKI, DOI: 10.24427/978-83-66391-87-1_02

[23] “Influence of Fringing Fields on Parallel Plate Capacitance for Capacitive MEMS Accelerometers”, Cezary Maj, Michał Szermer, IEEE 2020

[24] “Computing the Effect of Fringing Fields on capacitance”, COMSOL tutorial

[25] “CMOS BEOL-embedded z-axis accelerometer”, P. Michalik, J.M. Sánchez-Chiva, D. Fernández and J. Madrenas, ELECTRONICS LETTERS 28th May 2015 Vol. 51 No. 11 pp. 865–867

[26] “Dependence of the quality factor of micromachined silicon beam resonators on pressure and geometry”, F. R. Blom, S. Bouwstra, M. Elwenspoek, et al., Journal of Vacuum Science & Technology B: Microelectronics and Nanometer Structures Processing, Measurement, and Phenomena 10, 19 (1992); doi: 10.1116/1.586300, View online: https://doi.org/10.1116/1.586300

[27] ”Temperature dependent Young's modulus and quality factor of CMOS-MEMS resonator: Modelling and experimental approach”, Mohammad Tariq Jan, Farooq Ahmada, Nor Hisham B. Hamid, Mohd Haris B. Md Khir, Khalid Ashraf, Muhammad Shoaiba, Microelectronics Reliability 57 (2016) 64–70

[28] “E. J. Hearn, Mechanics of Materials 1: The mechanics of elastic and plastic deforma-tion of solids and structural materials. Butterworth-Heinemann, 1997, vol. 1. 16, 17”

[29] “CMOS MEMS Fabrication Technologies and Devices”, Hongwei Qu

[30] “Simulation of microelectromechanical systems,” G. K. Fedder, Ph.D. dissertation, University of California at Berkeley, 1994.

[31] “Surface Micromachined Accelerometer”, COMSOL Tutorial

[32] “MEMS Tutorial: Nonlinearity in Micromechanical Resonators”, Ville Kaajakari (ville@kaajakari.net) Homepage: http://www.kaajakari.net Tutorials: http://www.kaajakari.net/~ville/research/tutorials/tutorials.shtml

[33] “Behavioural modelling and system-level simulation of micromechanical beam resonators”, Lynn Khine and Moorthi Palaniapan 2006 J. Phys.: Conf. Ser. 34 1053

[34] “Behavioral Modeling of a CMOS–MEMS Nonlinear Parametric Resonator”, Congzhong Guo, Gary K. Fedder

[35] “Gas Ambient Dependence of Quality factor in MEMS resonators”, Q. Li, Q. Li, J.F.L. Goosen, F. van Keulen J.T.M. van Beek

[36] “A Micromachined Pressure Sensor with Integrated Resonator Operating at Atmospheric Pressure” Sen Ren, Weizheng Yuan, Dayong Qiao, Jinjun Deng and Xiaodong Sun, Sensors, December 2013 DOI: 10.3390/s131217006

[37] “MEMS resonators with electrostatic actuation and piezoresistive readout for sensing applications”, Claudia Coelho, George Machado Jr, Jorge Cabral, Luís Rocha, MNE 16 (2022) 100158

[38] “Temperature Dependence of Quality Factor in MEMS Resonators”, Bongsang Kim et al., JOURNAL OF MICROELECTROMECHANICAL SYSTEMS, VOL. 17, NO. 3, JUNE 2008

[39] “Molecular dynamics of ows in the Knudsen regime”, Marek Cieplaka, Joel Koplik, Jayanth R. Bavanar, Physica A 287 (2000) 153-160

[40] “A High-Q Resonant Pressure Microsensor with Through-Glass Electrical Interconnections Based on Wafer-Level MEMS Vacuum Packaging”, Zhenyu Luo, Deyong Chen, Junbo Wang, Yinan Li, Jian Chen, Sensors 2014, 14, 24244-24257; doi:10.3390/s141224244

[41] ”Electrical Control of Effective Mass, Damping, and Stiffness of MEMS Devices”, Jason V. Clark, Oleksandr Misiats, Shehrin Sayed, IEEE SENSORS JOURNAL, VOL. 17, NO. 5, MARCH 1, 2017

[42] “Modelling the electrostatic actuation of MEMS:state of the art 2005.” A. Fargas Marquès, R. Costa Castelló and A.M. Shkel, IOC-DT-P-2005-18, Setembre 2005

[43] “Resonant silicon sensors”, G Stemme 1991 J. Micromech. Microeng. 1 113

[44] “Microresistor Beam”, COMSOL Tutorial

[45] “Electrostatically Actated Cantilever”, COMSOL Tutorial

[46] "Capacitive pressure sensor", COMSOL Tutorial

[47] "Stationary Analysis of a Biased Resonator — 2D", COMSOL Tutorial

Glossary

CMOS (Complementary metal–oxide–semiconductor)

MEMS (Micro-electromechanical systems)

CMOS-MEMS

DRC (Design Rule Checks)

capacitive pressure sensor

BEOL (Back end of life)

FEOL (Front end of line)

Electronics

Resonance frequency

Frequency response

Quality factor

TSMC (Taiwan Semiconductor Manufacturing Company)

UMC (United Microelectronics Corporation)

LVS (Layout Versus Schematic)

NMOS

PMOS

Micromachined

Fringing Fields

Hierarchy

Squeeze damping